

AD-A119 286

AIR FORCE WEAPONS LAB KIRTLAND AFB NM
EXPLOSION AND EARTHQUAKE SOURCE DISCRIMINATION. (U)
MAY 82 B W STUMP, R E REINKE

F/G 18/3

AFOSR-PO-82-00004

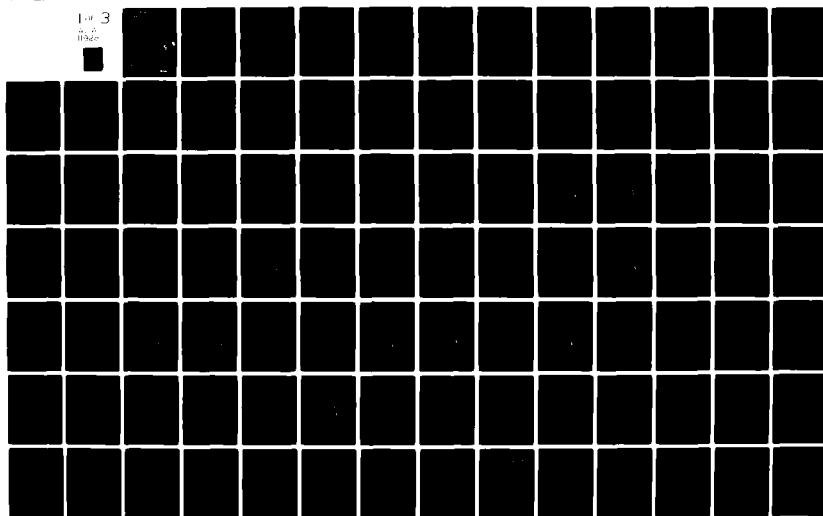
UNCLASSIFIED

AFOSR-TR-82-0733

NL

1 of 3

AD-A119 286



UNCLASSIFIED

SECURITY CLASSIFICATION OF THIS PAGE (When Data Entered)

REPORT DOCUMENTATION PAGE		READ INSTRUCTIONS BEFORE COMPLETING FORM
1. REPORT NUMBER AFOSR-TR- 82-0733	2. GOVT ACCESSION NO. AD-A119286	3. RECIPIENT'S CATALOG NUMBER
4. TITLE (and Subtitle) Explosion and Earthquake Source Discrimination		5. TYPE OF REPORT & PERIOD COVERED Technical Report 01 April 81 - 01 April 82
		6. PERFORMING ORG. REPORT NUMBER
7. AUTHOR(s) B. W. Stump R. E. Reinke		8. CONTRACT OR GRANT NUMBER(s) AFOSR-P0-82-00004
9. PERFORMING ORGANIZATION NAME AND ADDRESS Air Force Weapons Laboratory Kirtland AFB NM 87117		10. PROGRAM ELEMENT, PROJECT, TASK AREA & WORK UNIT NUMBERS 2309/A1 62714E, 42550101
11. CONTROLLING OFFICE NAME AND ADDRESS Air Force Office of Scientific Research Bolling AFB Washington DC 20301		12. REPORT DATE May 1982
		13. NUMBER OF PAGES 241
14. MONITORING AGENCY NAME & ADDRESS (if different from Controlling Office)		15. SECURITY CLASS. (of this report) Unclassified
		15a. DECLASSIFICATION/DOWNGRADING SCHEDULE N/A
16. DISTRIBUTION STATEMENT (of this Report) Approved for public release; distribution unlimited.		
17. DISTRIBUTION STATEMENT (of the abstract entered in Block 20, if different from Report)		
18. SUPPLEMENTARY NOTES		
19. KEY WORDS (Continue on reverse side if necessary and identify by block number) Underground Nuclear Explosion, Body-Waves, Synthetic Seismogram, Moment Tensor, Accelerometer, Surface Explosion		
20. ABSTRACT (Continue on reverse side if necessary and identify by block number) This report summarizes work accomplished by the Air Force Weapons Laboratory during the period May 1981 to April 1982. The purpose of this work has been to focus on seismic source characterizations of explosive sources. Specifically, we have investigated the usefulness of the moment tensor representation in modeling near-field recordings of contained nuclear explosions (Paper 1). Extension of the source representation to surface explosions utilizing the zeroth order moment has also been accomplished (Paper 2).		

AD A119286

DTIC FILE COPY

DTIC
ELECTE
SEP 14 1982
H

UNCLASSIFIED

In an attempt to investigate the possibility of using small scale high-explosive tests in studying source characterization problems, a 256-pound fully contained chemical explosion was instrumented and detonated. A preliminary data report (Paper 3) is included while data analysis is ongoing. Further studies of small scale surface and buried chemical explosions are outlined in Paper 4. Reflectivity modeling of the observational data was attempted.

Finally, an effort was made to field the original Leet seismographs (along with modern digital equipment) from the first nuclear shot, Trinity, on the DNA sponsored MILL RACE shot (620 tons ANFO, surface burst). The purpose of this task was to validate the early nuclear ground motion data and attempt to model it. Paper 5 documents the experiment and the resulting data.

DTIC
COPY
SELECTED
2

Accession For	
NTIS GRA&I	<input checked="" type="checkbox"/>
DTIC TAB	<input type="checkbox"/>
Unannounced	<input type="checkbox"/>
Justification	
By	
Distribution/	
Availability Codes	
Dist	Avail and/or Special
A	

✓ . AFOSR-TR- 82 - 0733

AFOSR/DARPA PROGRESS REPORT

Explosion and Earthquake Source Discrimination

Brian W. Stump and Robert E. Reinke

Cost: \$30,000

Duration: 2 years

This report summarizes work accomplished by the Air Force Weapons Laboratory during the period May 1981 to April 1982. The purpose of this work has been to focus on seismic source characterizations of explosive sources. Specifically, we have investigated the usefulness of the moment tensor representation in modeling near-field recordings of contained nuclear explosions (Paper 1). Extension of the source representation to surface explosions utilizing the zeroth order moment has also been accomplished (Paper 2).

In an attempt to investigate the possibility of using small scale high-explosive tests in studying source characterization problems, a 256-pound fully contained chemical explosion was instrumented and detonated. A preliminary data report (Paper 3) is included while data analysis is ongoing. Further studies of small scale surface and buried chemical explosions are outlined in Paper 4. Reflectivity modeling of the observational data was attempted.

Finally, an effort was made to field the original Leet seismographs (along with modern digital equipment) from the first nuclear shot, Trinity, on the DNA sponsored MILL RACE shot (620 tons ANFO, surface burst). The purpose of this task was to validate the early nuclear ground motion data and attempt to model it. Paper 5 documents the experiment and the resulting data.

Approved for public release;
distribution unlimited.

82 00 10 194

PAPERS AND TALKS PRESENTED

Stump, B.W. and L.R. Johnson, 1981. The Effect of Green's Functions on the Determination of Source Mechanisms by the Linear Inversion of Seismograms, Identification of Seismic Sources - Earthquake or Underground Explosion, Edited by Dr Eystein Husebye and S. Mykkelveit, D. Reidel Publishing Co, Dordrecht, Holland.

Stump, B.W., 1981. Synthetic Modeling of Explosive Surface Sources, EOS, Transactions American Geophysical Union, 62, December 1981.

Reinke, R.E., B.W. Stump, K.H. Olsen, 1981. Observed and Computed Seismograms from Small Yield High-Explosive Events, EOS, Transactions American Geophysical Union, 62, Dec 1981.

Stump, B.W. and L.R. Johnson, 1982. Higher Degree Moment Tensors - The Importance of Source Finiteness and Rupture Propagation on Seismograms, Geophys. J. Roy. Astr. Soc., accepted for publication.

Reinke, R.E., B.W. Stump, K.H. Olsen, 1982. Trinity - MILL RACE Seismic Experiment, DNA Proceedings of the MILL RACE Experiment, in press.

AIR FORCE OFFICE OF SCIENTIFIC RESEARCH (AFSC)
NOTICE OF TRANSMITTAL TO DTIC

This technical report has been reviewed and is
approved for public release IAW AFR 190-12.
Distribution is unlimited.

MATTHEW J. KERPER

Chief, Technical Information Division

NEAR FIELD SOURCE CHARACTERIZATION
OF
CONTAINED NUCLEAR EXPLOSIONS IN TUFF

BRIAN W. STUMP
Air Force Weapons Laboratory
Kirtland AFB NM 87117

ABSTRACT

The seismic source of three contained nuclear explosions in tuff at Pahute Mesa is characterized by applying the moment tensor source representation to near-field accelerometer recordings of the events. Propagation path effects are accounted for in the study by generalized ray calculations for several plane layered models. Synthetic seismograms generated from the predicted sources model well the distance and azimuthal variations in the data. The moment tensors are dominated by the isotropic component with the absolute ratio of isotropic to deviatoric component varying between 2 and 20, depending on the particular Green's function. The isotropic sources indicate the procedure is a good measure of relative yield while the absolute yield is dependent upon the exact Green's function. Source time functions indicate the possibility of a double pulse source separated by 1.0 to 1.5 seconds. This interpretation is bounded by the fact that phase information is the least well resolved in the study. In contrast, the stability of the spectral characteristics, such as corner frequency, high frequency roll-off, and peak value suggest the use of the moment tensor in the frequency domain for yield and discrimination studies.

SOURCE CHARACTERIZATION

Given a set of observed waveforms from an explosion or an earthquake and knowing the propagation path effects of the geological material, a quantitative procedure for determining the source function in space and time is desirable. The moment tensor source representation is such a formulation (Gilbert, 1970; Gilbert and Dziewonski, 1975; Backus and Mulcahy, 1976 a and b; Stump and Johnson, 1977; Backus 1977 a and b; Strelitz, 1977).

Assuming an explosion or earthquake source can be represented as a set of equivalent body forces, then the source can be written as a series of moments. For small sources or large wavelengths, only the first term of the series is retained, and the displacement at any point and time can be written as:

$$U_k(x',t') = G_{kij}(x',t';Q,0) \otimes M_{ij}(Q,t') \quad (1)$$

Where U_k is the displacement in the k direction, G_{kij} is the Green's function, M_{ij} is the moment tensor, $,j$ indicates derivative with respect to x_j and \otimes represents temporal convolution. A more complete derivation of (1) is given in Stump and Johnson (1977).

In the frequency domain, the equation reduces to:

$$U_k(x',f) = G_{kij}(x',f;Q,0) \cdot M_{ij}(Q,f) \quad (2)$$

Knowing the propagation path effects (G_{kij}), one can determine the source (M_{ij}) from a set of observational data (U_k).

In this study, the moment tensor formulation will be applied to three sets of data from contained nuclear explosions. The sum of the diagonal elements of the moment tensor, the isotropic component, is proportional to volume changes in the source region and will be interpreted as the explosion component of the source. This component can then be compared to the remaining

portion of the moment tensor, its deviatoric component, to analyze that portion of the source not accounted for by a symmetric explosion.

$$M_{TR} \text{ (isotropic)} = 1/3 M_{ij} \delta_{ij} \quad (3)$$

$$D_{ij} \text{ (deviatoric)} = M_{ij} - M_{TR} \delta_{ij} \quad (4)$$

If one has some idea of the source characterization, then constraints can be placed on Equation 2. One such constraint is that the source is a symmetric explosion, but the time function is unknown. Equation 2 reduces to:

$$U_k(x', f) = M_0(G_{k1,1} + G_{k2,2} + G_{k3,3}) F(f) \quad (5)$$

$F(f)$ is the unknown source time function in the frequency domain.

DATA ANALYSIS

This report will discuss the analysis of near-field accelerometer data from three nuclear explosions detonated in Pahute Mesa at the Nevada Test Site. The three shots studied are: Handley with a Wood-Anderson magnitude determined by the U.C. Berkeley seismographic station of 6.3, Pipkin with a Wood-Anderson magnitude of 5.5, and Farm which is similar in size to Pipkin.

The instrumentation arrays for Handley and Pipkin are illustrated in Figure 1. Eight 3-component accelerometers were fielded over a 180° arc at 8 kilometers from the Handley event. Stations 1, 2, 4, and 5 operated properly yielding twelve components of motion. A similar array to Handley was installed for the Jorum event. While the equipment was operating, the Pipkin explosion was detonated yielding data at a variety of azimuths (80° arc) and ranges (2-14 km). Stations 1, 2, 3, 4, 5, and 6 operated for a total of 14 components of motion (not all accelerometers functioned properly).

The Farm instrumental array is given in Figure 2. The 3-component accelerometers spanned 135° in azimuth and varied in range between 2 and 10 kilometers. Of the six stations, only four operated--2, 4, 5, and 6--yielding twelve components of data.

Figure 3 illustrates the three instrumental arrays with respect to one another and the Silent Canyon Caldera, the major structural feature of Pahute Mesa. The Pipkin and Farm events are both within the caldera, while Handley is out. The accelerometers for Farm are all within the caldera, while those for Pipkin and Handley Farm are inside and outside.

The instruments used in all three of these experiments were force-balance accelerometers with a flat response between 0.02 to 50 Hz. The outputs of the gages are 5 volts/g for the verticals and 7.5 volts/g for the horizontals.

For Pipkin and Handley, the data was recorded on analog tape at NTS. The seismograms were low pass filtered at 10 Hz with a 4-pole Butterworth filter. The data was then digitized at a rate of 54 samples/second.

Digital recording of the data for the Farm test utilizing Sprengnether DR-100 digital event recorders was accomplished. The data was filtered with a 2-pole low pass Butterworth at 30 Hz and a 2-pole high pass Butterworth at 5 seconds prior to digitization at 100 samples per second.

Analysis of the data and noise samples in the frequency domain indicates that there are problems with the long period data between 2 and 5 seconds from all three events. This noise becomes increasingly evident as one tries to calculate velocities and displacements. Since the source studies using this data will essentially deconvolve the instrument and propagation path effects out of the data, one must be careful with the data at long periods. In order to avoid long period problems, some post processing of the observational data was done. First a high pass Butterworth filter was applied to the data. The slope and corner frequency of the filter was determined from the noise estimate, a desire to eliminate the rise of the spectra at long periods, and an attempt to yield realistic velocity and displacement records free of ramps, steps, and very long period noncausal signals. Typically, the filter corners were between 2 and 5 seconds with 1 or 2 slopes at high frequencies. After application of these filters, the data were corrected for a DC offset in velocity or a ramp in displacement.

It is this corrected data in velocity and acceleration which were used for the source study. The corrected acceleration, velocity, and displacement records from the Handley event are given in Figures 4 and 5. The uncorrected displacement spectra for each observation are given in Figures 6 through 17. The rise of the spectra at long periods can be noted in these figures. The

time domain data yields vertical components of motion which are quite correlatable while the coherence of the radial and transverse motions is less. The transverse motions in acceleration are comparable in size to the vertical and radial in many cases. In velocity and displacement, the transverse motions are on the average comparable in size to the radial motion and half the size of the vertical.

Unlike the Handley data which were all at the same radial distance, the Pipkin data span distance 2 to 14 km from the source (Figure 1). The data were post processed in the same manner as that for Handley. The corrected accelerations, velocities, and displacements for Pipkin are given in Figures 18 through 20. The displacement spectra prior to correction are given in Figures 21 through 35. The frequency content of the waveforms apparently increases with range. This observation is quite apparent when comparing the vertical acceleration at Station 1 (2.77 km) and the vertical acceleration at Station 6 (13.55 km) (Figures 18 and 20). Again, the relative ratios of the radial, transverse, and vertical motions are similar to those observed for Handley.

The Farm data was the only digitally recorded set. Again, the data were post processed in the same manner as the previous two data sets. The corrected ground motion data are given in Figures 36 and 37 with the accompanying spectra in Figures 38 through 49. The data set has transverse motions which are comparable to the radial and vertical. The accelerograms indicate a good deal of complexity. There is the indication of a fairly large, long period secondary arrival on the displacement records at approximately four seconds. This arrival is particularly apparent on the vertical components of Stations 4 and 6 (Figure 36).

Summarizing the observational data, we have good quality accelerometer

data from three explosions that have been corrected for long period noise. The accelerations yield transverse motions which are comparable to the radial and vertical records. At longer periods, as exemplified by the velocity and displacement records, the vertical motions are on the average a factor of two larger than the radial and transverse. The data appear to increase in frequency with range over 2-14 km. For data at the same range, the vertical records from varying azimuths are quite correlatable, while the radial and transverse motions are much less so.

PROPAGATION PATH EFFECTS

Utilizing geological maps, geophysical explorations, and the observational ground motions from the three explosions, a propagation path model for Pahute Mesa at NTS was developed. Even though there are great geological variations across Pahute Mesa--water table fluctuations, terrain differences, and structural boundaries, such as the Silent Canyon Caldera (Figure 3)--it was our desire to check the feasibility of producing an average plane layered model for the mesa.

The construction of the model began with the early work of Hamilton and Healy, 1969. Their initial velocity model for the Benham explosion on Pahute Mesa was supported by a 4.1 km deep well log, geologic data, and long line refraction studies of NTS. Their model is reproduced in Table 1. Although this model is good at deep depths, we were interested in the fine structure above one km since two of the shots studied were emplaced in this depth range.

Figure 50 is the well log above the Farm working point. The acoustic log indicates a gradual increase in velocity with depth from about 2.0 to 3.4 km/sec with the possibility of a velocity jump at the water table. One must keep in mind that the logging method changes at the water table. Using this data and that from additional drill holes at NTS, an initial velocity model was developed. The model is very close to that of Helmberger and Hadley (1981).

The complexity in the velocity model of interest is controlled by the wavelengths of energy leaving the explosive source. Although the velocity log of Figure 50 shows great variability on a local scale, we wish some type of average structure. In order to help further constrain the Pahute Mesa velocity model for the wavelengths of the nuclear sources, the accelerometer data from the Farm and Pipkin experiments were used to obtain arrival time data.

TABLE 1

<u>Depth to Layer (km)</u>	<u>Layer Velocity (km/sec)</u>
0.0	2.7
0.94	3.4
1.33	3.8
2.14	4.4
2.50	5.1
5.00	6.1
25.00	7.0
35.00	8.0

This time data, in conjunction with travel time curves from the Pahute Mesa model, were utilized to refine the structure. Farm and Pipkin were detonated at similar depths, but Pipkin was just above the water table while Farm was just below it. Since the water table is associated with a velocity jump in our model, the travel time curves for the Pipkin and Farm shots are quite different, and the effect must be taken into account when analyzing the travel time data. The finalized velocity model structure, along with the explosion locations, is given in Figure 51. The travel time curves for a source just above the water table with the Pipkin arrival time data are given in Figure 52. The travel time curve for a source below the water table with the Farm arrival time data is given in Figure 53. The observational data fit the predictions of the models quite well. The change in crossover distance from 5 km to 9.5 km as one moves down across the water table at 0.65 km seems to match the observed arrival time differences for the two shots. In the ray tracing, the second interface at 1.45 km was ignored as we feel the layering at this point replicates a gradient in velocity. Inclusion of this interface as a refraction led to predicted arrivals before those observed in the actual arrival time data.

The interpretation of the proposed structure is that the 0.65 km interface represents the water table depth and is constrained by well levels in the caldera. As one moves out of the caldera near the Handley site, the water moves to half this depth. Since we are interested in an average velocity model and that the ray paths to the Handley gages propagate both in and out of the caldera, the average depth of 0.65 km to the water table will be used. As we already discussed, the interface at 1.45 km replicates the velocity gradient with a two-layer structure. Finally, the 2.50 km interface represents the turning point of the downgoing energy in the structure. Its depth and

velocity are constrained by the arrival time data beyond 6 km. We feel the essential elements of this model are the water table, the velocity gradient below the source, and the turning point of the rays at 2.50 km.

Up to this point, the focus has been upon the compressional velocity structure. The constraints upon the shear velocity are much less. As we shall see later, the shear structure is important in the Green's functions for they control the ratio of the energy from isotropic to deviatoric sources. The shear wave velocity also controls the importance of P to S conversions at the interfaces. The shear velocities were determined from both arrival time data and frequency-wave number analysis of small array data recording explosion data at Pahute Mesa (K. McLaughlin, U.C. Berkeley, personal communication). The β -news model (Figure 51) involved material with an average Poisson's ratio of 0.28. Since we are very interested in the ratio of P to S, a slow shear model-- β -olds--was also investigated. This model began with a Poisson's ratio of 0.45 in the surface layer and slowly decreasing to 0.26 in the half-space.

Using the velocity structure of Figure 51, synthetic Green's functions were calculated. Models utilizing both β -news and β -olds were included. Synthetics were run, including turning rays and conversions at interface two and not including them. The Green's functions were run for a source just above and just below the water table to replicate the Pipkin and Farm emplacements. All the synthetics for the layered structure were calculated using the generalized ray method (Helmberger, 1968; Pao and Gajewski, 1977). For comparison, half-space Green's functions were also calculated (Johnson, 1974). The half-space propagation path was included because: (1) it is the simplest of all path corrections, (2) the results include near-field effects, and (3) Rayleigh wave contributions are included.

The Green's functions for a source just below the water table (Farm, Figure 51) are given in Figures 54 through 65. We will use this source configuration to investigate the various velocity models. All the results are delta function responses passed through the accelerometer. As we noted in the theory section, to completely characterize the material response, ten sources are needed. Primary emphasis shall be placed on the radial and vertical response to an explosive source.

Figures 54 and 55 are the radial and vertical explosive Green's functions for the structure of Figure 51 (β -news) ignoring conversions and turning rays at the second interface. Motions between 2 and 12 kilometers are given. A total of 31 rays were included in the calculation. The travel time curves indicate a crossover distance between 9 and 10 km (Figure 53) and this can be seen in the synthetics. The radial and vertical components are similar in both amplitude and wave shape. The complete set of ten Green's functions and their spectra for a 6.34 km range are given in Figure 56. Radial and vertical Green's functions result from all sources while the transverse contribution comes only from the strike-slip and dip-slip sources. Comparison of peak time amplitudes and spectral estimates indicates transverse motions which are 13.6 to 7.6 times larger than the energy from the explosive source. In order to explain observed transverse motions equal in size to the vertical, one needs a source only 7.6 to 13.6 times smaller than the explosion. As we will see, this ratio varies for the set of Green's functions used in this study. The vertical to radial ratio for the explosive source for this propagation path model is unity.

In order to investigate the effect of the second interface as a turning point, synthetics were run for the model just discussed, but conversions and

turning rays at the second interface were included. A total of 67 rays were calculated. The explosion Green's functions at the 4.20, 6.34, and 9.67 km ranges are illustrated in Figures 57 and 58. Comparison of Figures 54 and 57 indicates that the energy converted and turned at the second interface has a significant contribution to the synthetics. At the 9.67 km range, the energy off the second interface is actually the first arrival. The complete Green's functions for the 6.34 km range are given in Figure 59. The peak transverse motions are 13.2 to 5.3 times larger than the explosive source motions. The vertical to radial ratio for the explosion Green's function is 0.8.

The effect of varying the shear wave velocity is illustrated in Figures 60 through 62. The source structure is the same as before, but with the β -olds shear wave structure, larger Poisson's ratio (0.45) near the surface. The radial accelerations from the explosion Green's function show greatly increased P to S conversions, while the vertical accelerogram shows less change. These conversions are most pronounced at the 6 km or less range. The slow shear velocity yields a vertical explosive Green's function which is 1.7 times larger than the radial. The complete Green's functions (6.34 km range) in both time and frequency are given in Figure 62. The ratio of the transverse body waves to the explosion body waves varies between 13 and 46.

For final comparison, the Green's functions in an elastic half-space are given in Figures 63-65. The direct P wave dominates the explosive source (Figures 63 and 64). Only the upgoing energy is returned to the free surface. This phenomena is unlike that of the previous models. The layering in the three previous models could always return energy to the free surface. The complete Green's functions at the 6.34 km range are given in Figure 65. The seismograms are much simpler than before, consisting of P, SP diffracted, S, and Rayleigh arrivals. The vertical to radial ratio of the P waves from the

explosion is 0.36. The ratio of the transverse waves to the explosive energy is between 1 and 20.

This complete range of Green's functions will be used in the source inversion for the Farm event. The effect of ranging from the simplest propagation path model (elastic half-space) to a fairly complex model (67-News) will be shown. In particular, we wish to investigate the sensitivity of the inversions in determining relative or absolute source strength and the variability of the isotropic/deviatoric source ratios. The high value of the maximum transverse Green's function to the explosive Green's functions seems to indicate that a primarily isotropic source may help explain the large transverse motions observed from contained explosions.

For the Pipkin and Handley studies, a similar set of Green's functions will be utilized. The Pipkin source is just above the water table, while Handley is buried at 1.2 km, some 0.55 km below our water table. Figure 66 gives a comparison for the explosive Green's functions at the Farm, Pipkin, and Handley burial depths and observed at 9.67 km.

MOMENT TENSOR INVERSIONS

Utilizing the data and Green's functions already reviewed in Equation 2, the moment tensor representations of the Farm, Handley, and Pipkin explosions were determined. The inversions were done in the frequency domain and then transformed back into the time domain to yield source time functions. In order to check the adequacy of the resulting source, the moment tensor, along with the appropriate Green's function, is substituted into Equation 1 to yield a calculated seismogram. These predicted seismograms are then cross correlated with the observations to give one a simple measure of the fits.

In addition to using the four sets of Green's functions with each observational data set, various time windows were utilized including the entire waveform and just the P arrivals. Constrained inversions restricting the source to purely isotropic were also conducted. A total of six or more inversions were done on each of the three data sets. This large matrix of inversions was done to investigate the stability of the procedure and its sensitivity to changes in data and Green's functions.

For illustration purposes, the complete moment tensor time functions and the synthetic matches to the observational data for the Farm, Handley and Pipkin explosions will be given for only one Green's function. The Green's function that will be focused upon is the one utilizing the new shear wave velocity, β -news, and excluding conversions and turning rays at interface two (model 31). The results of the inversions using the other three Green's functions are summarized in Table 2.

The observed and calculated seismograms for Farm are given in Figures 66 and 67. A total of 10.24 seconds of data was used in the inversion. The signal to noise ratio in this data is the maximum of three sets and allowed

the study of the long data window. The correlation coefficients for the observed and calculated seismograms are given in the figures. The peak amplitudes and the general decay envelope of the data are well modeled. The maximum correlation coefficients are found for the radial and vertical components, 0.77 and 0.74, while that for the transverse is less, 0.69. As a whole, these fits are quite good.

The complete set of near- and far-field moment tensors from this Farm inversion is given in Figure 68. In addition to the six components of the moment tensor, the sum of diagonal elements, the isotropic moment, is also given. All moment tensor plots are scaled to the maximum of each element, so comparison of component sizes must be done with the numerical values noted in the figures. The moment tensor is dominated by the three diagonal elements of the tensor and, thus, its isotropic component (Equation 3). These elements all have similar time functions and amplitudes. The deviatoric components of the moment tensor (Equation 4) are a factor of 4.4 smaller than the isotropic in the far-field and 3.4 in the near-field. The time functions of the deviatoric components do not resemble each other or the isotropic component. The arrow on the isotropic time function in Figure 68 indicates the predicted source time from the windowing of the data and Green's functions. Taking this reference time, there are two distinct parts to the isotropic time function separated by 1.5 seconds. The first part of the time function is a single pulse in the near-field with approximately 2/3 second duration, while the second part 1.5 seconds later consists of several cycles of 0.67 Hz energy. There is little energy beyond 5 seconds.

The fits to the Handley data using the same layered structure, but accounting for the deeper source, are given in Figures 69 and 70. The data quality limits one to 4.74 second records. As Figure 1 illustrates, the data

from Handley are all at the same range (8 km). The vertical components of velocity are the most correlatable between observations, and the synthetic fits to this data are the best. The average correlation coefficient for the vertical data is 0.90, the radial data is 0.74, and the transverse data is 0.65.

The Handley moment tensors are given in Figure 71. The arrow on the isotropic component of the moment tensor indicates the initiation time for the source as predicted by the data and Green's function windows. The diagonal elements of the moment tensor are all similar in time and amplitude, giving a source dominated by the isotropic moment tensor. In the far-field time functions, the isotropic moment tensor is 7.67 times larger than the deviatoric components. In the near-field, this ratio is 8.33. The isotropic source is a single pulse in this case with a pulse width between 0.67 and 1.00 seconds.

The fits to the final data set, Pipkin, are given in Figures 72 to 74. In the past two data sets, the vertical components of motion were the most correlatable. In this data set, vertical components were lost at two stations. In addition to this loss, great variability in frequency content with range is seen in the data. A total of 4.74 seconds of data are fit in this analysis. The average correlation coefficients for the radial, vertical and transverse data are 0.51, 0.70, and 0.62 respectively.

The moment tensors for this inversion are given in Figure 75. The arrow on the isotropic moment tensor indicates the theoretical source initiation time. The amplitudes of the three diagonal elements of the moment tensor are approximately equal in magnitude but, unlike the previous two data inversions, there is some variability in the time functions. The ratio of the isotropic to the deviatoric moment tensor in the near-field is 1.95 and 2.47 in the far-field.

The isotropic source spectra for the three inversions just discussed are given in Figure 76. The solid lines are the spectral estimates, while the dashed lines are variance estimates. The variances intersect the moment estimates between 10 and 20 Hz. The maximum separation between the spectra and the variances runs between 40 to 60 db near 1 Hz. The high frequency roll-offs for all the sources are between 2 and 3. The corner frequencies vary little between the three sources with a value between 1 and 2 Hz. The spectra decrease at the long periods yielding a peaked spectra around the corner frequency. Although not included in this report, the moment tensor spectra from inversions utilizing the other propagation path models yield spectral characteristics consistent with those reviewed. Of all the moment tensor characteristics, their high frequency slopes, corner frequencies, and maximum values all remain invariant while the phase information varies.

The isotropic near-field moment tensors from the Farm, Handley, and Pipkin inversions utilizing the three, layered Green's functions (31, 67, OLDS) are summarized in Figure 77. The three moments for Farm all indicate a source function with two pulses separated by 1.0 to 1.5 seconds. The period and duration of the second pulse decrease as one moves from the F31 to the FOLDS models. The Handley source also indicates two time functions separated 1.0 seconds in time. These phenomena are particularly apparent for the HOLDS model. There is a hint of two pulses in the Pipkin source too. The period of this source decreases as one moves from the P31 to the POLDS models. Considering the tremendous variations in the observed data from these three explosive sources, the differences in propagation paths, and the physical differences in the sources themselves, the isotropic components of the moment tensor are remarkably consistent.

The absolute size of the moment tensors for all the inversions of this study are summarized in Table 2. The first observation is that the whole record inversions (67, 31, OLDS, HS) yield moments which are nearly the same. The isotropic moments change by a maximum of 52 percent for Farm, 28 percent for Handley, and 121 percent for Pipkin. The largest variation in the source with Green's function is in the ratio of isotropic to deviatoric components. The far-field ratio for Farm varies from 7.33 for the F67 Green's function to 27.3 for the FOLDS model. The ratio of transverse body waves to explosive body waves for the Green's functions varies from 7.6 to 13.6 for the F67 model (Figure 56) to between 13 and 46 for the FOLDS model (Figure 62). As one moves to slower shear wave velocities in the propagation path models, the isotropic to deviatoric ratio in the source function increases due to increased shear wave amplitudes.

The moments of Farm and Pipkin are nearly equal in size. Handley has a moment tensor between 15 and 20 times larger than the two other events.

Since the initial P waves are the most coherent arrivals in the data sets and should be least contaminated by shear waves, inversions were completed using the first second of the Farm data. This source inversion, in conjunction with the earlier whole record studies, will help us understand the importance of P and S waves in constraining the isotropic and deviatoric components of the explosive source.

The observed and calculated seismograms utilizing the Farm data and the F67 propagation model are given in Figures 78 and 79. The fits to the radial and vertical velocities are the best of the trial inversions. The correlation coefficients for the radial velocity is 0.82 and for the vertical velocity is 0.85. The transverse motions are poorly modeled with an average correlation coefficient of 0.23. The inversion window contained no shear arrivals in

TABLE 2

MOMENT TENSORS
x 10²³ dyne cm/sec (10²³ dyne cm)

FARM	M ₁₁	M ₁₂	M ₁₃	M ₂₂	M ₂₃	M ₃₃	M _{TR}	M _{TR} /M _{DEV}
F67	3.72 (0.64)	0.49 (0.05)	0.34 (0.08)	3.55 (0.51)	0.44 (0.11)	3.50 (0.55)	3.59 (0.55)	7.33 (5.00)
F31	2.92 (0.45)	0.61 (0.14)	0.61 (0.13)	2.89 (0.45)	0.61 (0.13)	2.48 (0.56)	2.75 (0.47)	4.50 (3.62)
FOLDS	3.81 (0.79)	0.13 (0.03)	0.14 (0.03)	3.84 (0.79)	0.14 (0.02)	3.84 (0.83)	3.82 (0.81)	27.3 (27.0)
FHS	3.78 (0.79)	0.58 (0.95)	2.61 (0.56)	3.66 (0.68)	0.76 (0.24)	6.18 (1.68)	4.19 (1.04)	1.60 (1.10)
F67-PHAVES	18.40 (2.49)	3.89 (0.88)	8.18 (0.67)	5.68 (0.79)	5.55 (0.47)	13.55 (1.67)	9.37 (1.37)	1.14 (1.55)
HANDLEY								
H67	51.7 (11.9)	6.19 (2.10)	8.37 (2.82)	49.6 (11.2)	12.8 (4.73)	52.5 (13.63)	50.9 (11.7)	3.98 (2.47)
H31	61.6 (12.3)	3.57 (0.88)	3.76 (0.87)	60.9 (11.2)	7.70 (1.33)	55.8 (9.82)	59.3 (11.1)	7.70 (8.34)
HOLDS	63.9 (15.3)	4.58 (2.00)	2.41 (0.54)	63.9 (15.5)	3.96 (1.24)	67.3 (12.9)	65.1 (14.4)	14.21 (7.20)
H67-PHAVES	126.3 (11.2)	47.1 (5.00)	83.2 (9.51)	133.1 (14.4)	107.5 (12.7)	104.5 (13.9)	92.77 (9.7)	0.86 (0.76)
PIPKIN								
P67	2.85 (0.55)	0.81 (0.18)	0.88 (0.22)	2.71 (0.33)	0.46 (0.17)	1.67 (0.27)	2.41 (0.38)	2.74 (1.72)
P31	1.96 (0.54)	0.73 (0.13)	0.75 (0.15)	1.72 (0.24)	0.58 (0.16)	2.05 (0.35)	1.84 (0.32)	2.45 (2.00)
POLDS	5.12 (1.26)	1.04 (0.28)	0.62 (0.14)	3.79 (1.07)	0.52 (0.16)	3.75 (1.17)	4.07 (1.16)	3.91 (4.14)
P67-PHAVES	3.07 (0.66)	3.03 (0.76)	2.21 (0.55)	3.21 (1.02)	1.93 (0.33)	5.36 (1.61)	3.78 (1.07)	1.24 (1.41)

Green's functions, so only near-field components of motion remained to fit the observations. The near-field components from this model are not sufficient to match the transverse observations.

The moment tensors in the near-field from this inversion are given in Figure 80 and summarized in Table 2. The diagonal elements of the moment tensor are no longer equal in magnitude or similar in time function. The isotropic component of the moment tensor is a relatively simple pulse approximately 0.5 to 0.67 seconds in duration. The magnitude of the isotropic source is 2.61 times larger than the whole record inversion. The deviatoric components are more complex with energy spread throughout the time window. The ratio of the isotropic to the maximum deviatoric components is only 1.14. By eliminating the shear waves, the fits are improved, the isotropic source strength increased, and the isotropic to deviatoric ratio decreased. The isotropic source spectrum is given in Figure 81. The high frequency slope is 3 with a corner frequency at 2 Hz.

A summary of similar P wave only inversions for Handley and Pipkin is given in Table 2. As found for Farm, the isotropic source is increased with the short window inversions, while the isotropic to deviatoric ratio decreases dramatically. It appears that the shear arrivals are very important in constraining these sources.

DISCUSSION/CONCLUSIONS

Data from three contained nuclear explosions in tuff at the Nevada Test Site, Pahute Mesa, have been analyzed using the moment tensor source characterization. These explosions included sources just above, just below, and far below the water table. An average velocity model has been developed in order to complete the data analysis. This model utilizes borehole data, geological information, and refraction data. The velocity structure was further refined by the arrival time data from the explosions. The most important features of the model are the compressional velocity jump at the 0.65 km water table followed by a gradient structure (synthesized by 2 layers) down to a 2.50 km interface that acts to return down going energy to the free surface.

The moment tensor source formulation has been used to fit the observational data with Green's functions from the just described velocity model. Frequency domain inversions for the complete moment tensor and just its isotropic component were done. In general, the vertical and, to a lesser degree, the radial velocities were well modeled with the transverse fits slightly degraded. The moment tensor representation can be used to adequately model the observational data in the near-field (2-15 km) from underground explosions.

Comparison of the isotropic moment tensor for Pipkin, Handley and Farm (Figure 82) indicates that this part of the source function may be a good measure of relative explosive yield. The measure is relative if the propagation path is similar for the explosions under study and it can become absolute within the accuracy of Green's functions used to model propagation path effects.

The variety of Green's functions used in this study show shear waves which

average 5 to 15 times larger than the explosion *P* waves. In order to obtain transverse motions comparable to radial and vertical motions, one needs a deviatoric source which is much smaller than the isotropic. In the moment tensor inversions, these phenomena are exactly what occurs. In fitting the Farm, Handley, and Pipkin data the resulting sources are dominated by the isotropic component of the moment tensor. As the transverse shear waves in the Green's functions increased relative to the explosion *P* waves, the dominance of the isotropic moment tensor also increased. The -olds model has the largest shear waves and the largest ratio of isotropic to deviatoric source.

The variation of the resulting source functions between the three explosions and with changing Green's functions was summarized in Figures 76 and 77 and Table 2. Of all the source characteristics, the corner frequency, high frequency roll-off, and spectral peak are least variable. The source phase information is somewhat more changeable and dependent upon the Green's functions. The stability of the spectral information in these few inversions suggests exploration of spectral characteristics of the moment tensor for yield and discrimination studies.

The isotropic time functions for Farm, Handley and Pipkin all suggest the possibility of two source time pulses separated by 1.0 to 1.5 seconds. This observation is particularly apparent in the Farm inversion. The physical interpretation of this mathematical representation of the source is open. The secondary source could be due to nonlinear processes close-in to the explosion, problems in our propagation model, such as improper surface wave calculation or data preparation problems. These areas need to be explored.

The importance of shear waves in controlling the isotropic to deviatoric source ratio has been discussed in the context of the Green's functions. The inversions utilizing only the initial *P* waves from the observational data

further explored this question. The P wave only inversions yielded greatly improved fits, but the isotropic to deviatoric ratio was degraded. It is felt that the inclusion of shear waves in the studies improves our constraints on both the isotropic and deviatoric components of the source.

A preliminary study of the utility of the moment tensor representation in near-field explosion modeling has been completed. The results indicate the method is able to explain the observational data and give insight into relative and possibly absolute yield estimates. The puzzling observation of transverse motions as large as radial and vertical motions may be partially explained in terms of the strength of shear waves from deviatoric sources being much larger than the isotropic P waves. Such models allow sources which are dominated by the isotropic component and have transverse motions equal to observed radials and verticals. The physical interpretation of the source details awaits further study. This interpretation should take advantage of any close-in instrumentation in the nonlinear ground motion regime. Finally, the stability of the source modulus suggests the use of moment tensor spectral characteristics in discrimination and yield studies.

REFERENCES

- Backus, G.E., 1977a. Interpreting the seismic glut moment of total degree two or less, Geophys. J. Roy. Astr. Soc. 51, 1-25.
- Backus, G.E., 1977b. Seismic sources with observable glut moment of spatial degree two, Geophys. J. Roy. Astr. Soc. 51, 27-45.
- Backus, G.E., and M. Mulcahy, 1976a. Moment tensors and other phenomenological descriptions of seismic sources - I. Continuous displacement, Geophys. J. Roy. Astr. Soc. 46, 341-361.
- Backus, G.E. and M. Mulcahy, 1976b. Moment tensors and other phenomenological descriptions of seismic sources - II. Discontinuous displacements, Geophys. J. Roy. Astr. Soc. 47, 301-329.
- Gilbert, F., 1970. Excitation of normal modes of the earth by earthquake sources, Geophys. J. Roy. Astr. Soc. 22, 223-226.
- Gilbert, F., and A.M. Dziewonski, 1975. An application of normal mode theory to the retrieval of structural parameters and source mechanisms from seismic spectra, Phil. Trans. Roy. Soc. London, Ser. A, 278, 187-269.
- HelMBERGER, D.V. and D.M. Hadley, 1981. Seismic source functions and attenuation from local and teleseismic observations of the NTS events Jorum and Handley, Bull. Seism. Soc. Am. 71, 51-67.
- Hamilton, R.M. and J.H. Healy, 1969. Aftershocks of the Benham nuclear explosion, Bull. Seism. Soc. Am. 59, 2271-2281.
- HelMBERGER, D.V., 1968. The crust-mantle transition in the Bearing Sea, Bull. Seism. Soc. Am. 58, 179-214.
- Johnson, L.R., 1974. Green's function for Lamb's problem, Geophys. J. Roy. Astr. Soc. 37, 99-131.
- Pao, Y-H. and R.R. Gajewski, 1977. The generalized ray theory and transient responses of layered elastic solids, Phys. Acous. 13, 183-265, Academic Press.
- Strelitz, R.A., 1977. Moment tensor inversions and source models, Geophys. J. Roy. Astr. Soc. 52, 359-364.
- Stump, B.W. and L.R. Johnson, 1977. The determination of source properties by the linear inversion of seismograms, Bull. Seism. Soc. Am. 67, 1489-1502.

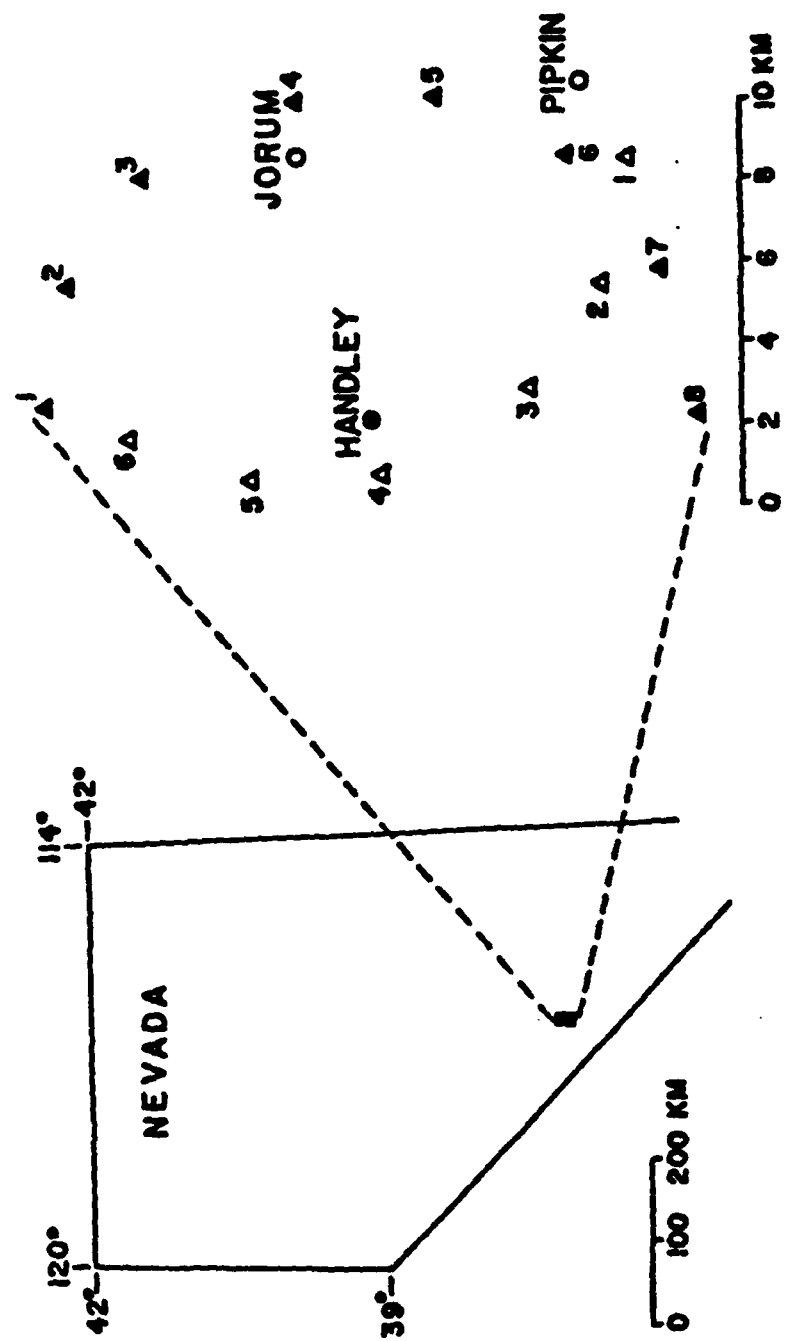
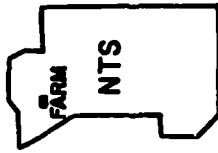


Figure 1



● F3

● F2

● F4

● F5

FARM



SHOT POINT

● F1

● F6

0 1 2 km

Figure 2

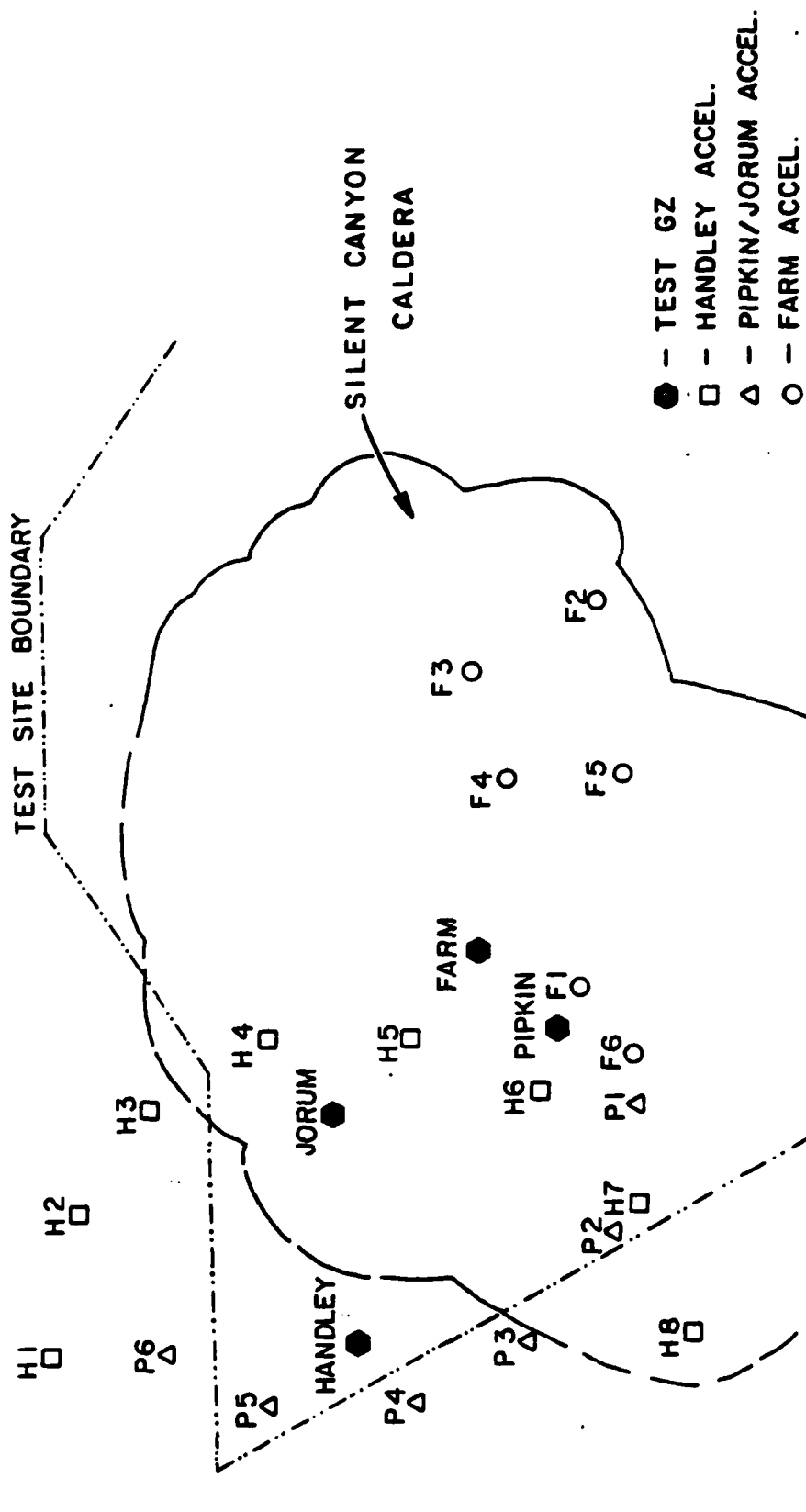


Figure 3

HANDLEY CORRECTED OBSERVATIONS

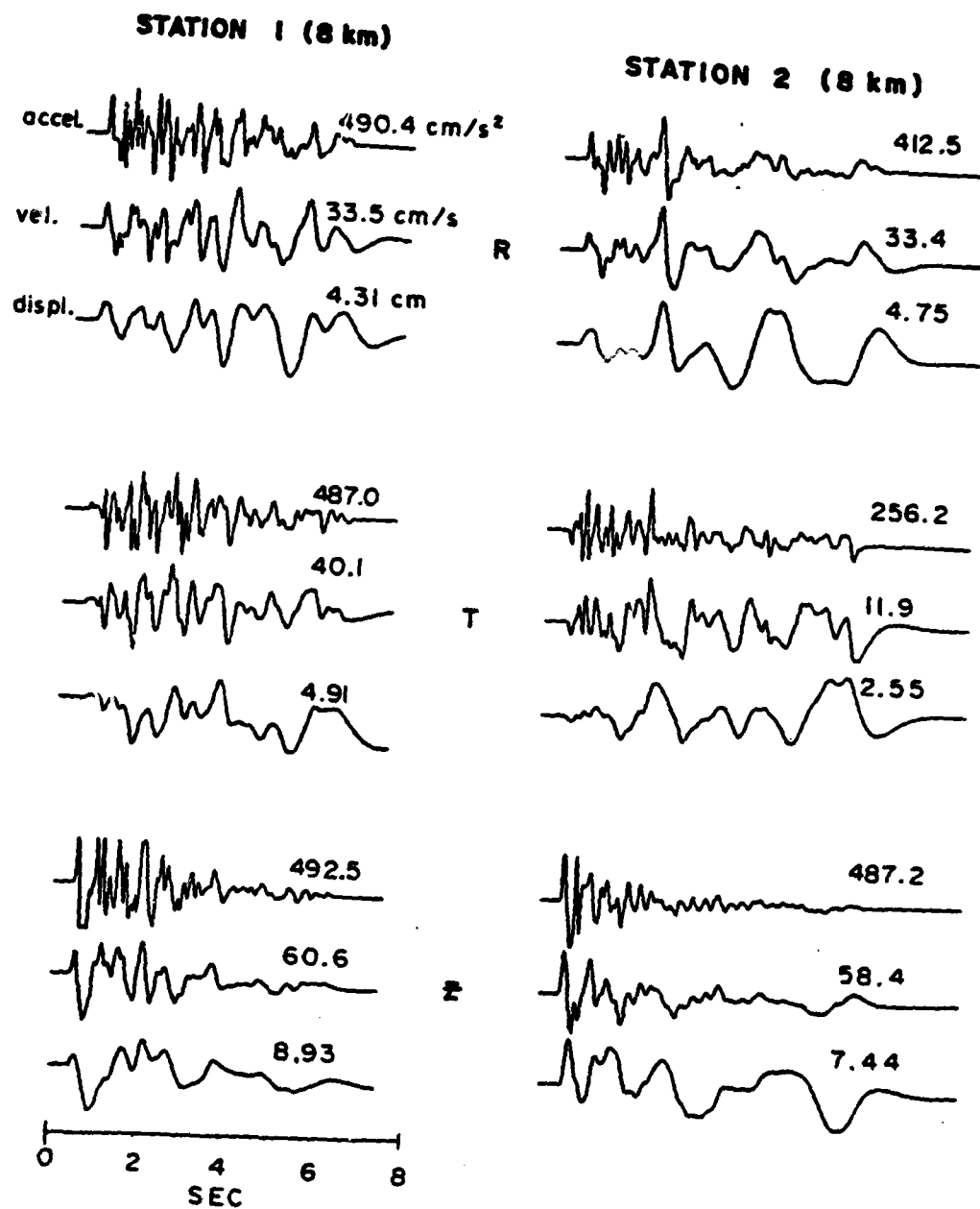


Figure 4

HANDLEY CORRECTED OBSERVATIONS

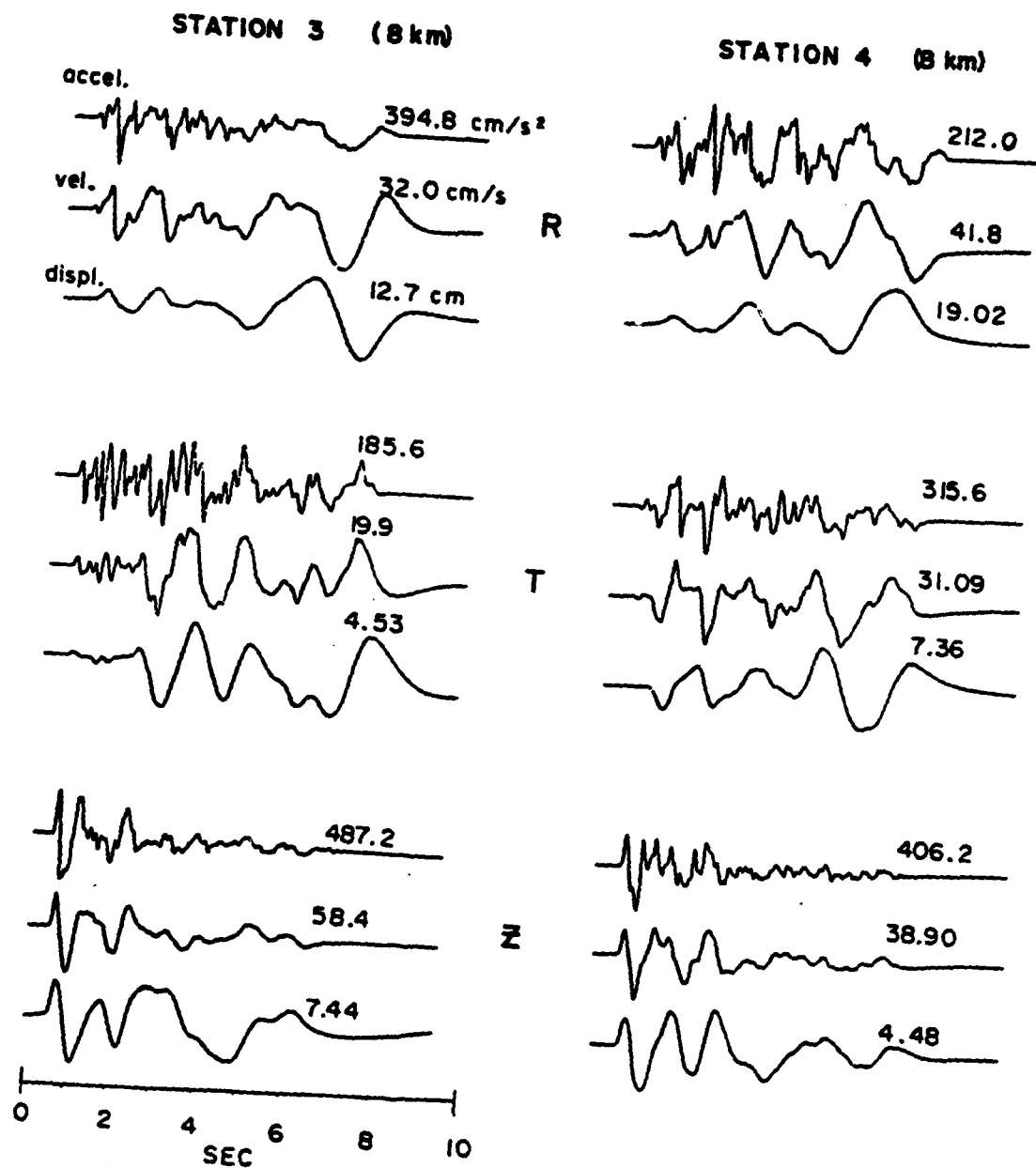


Figure 5

HANDLEY RI SPECTRUM

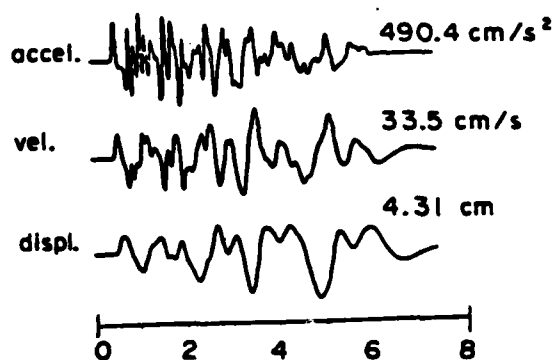
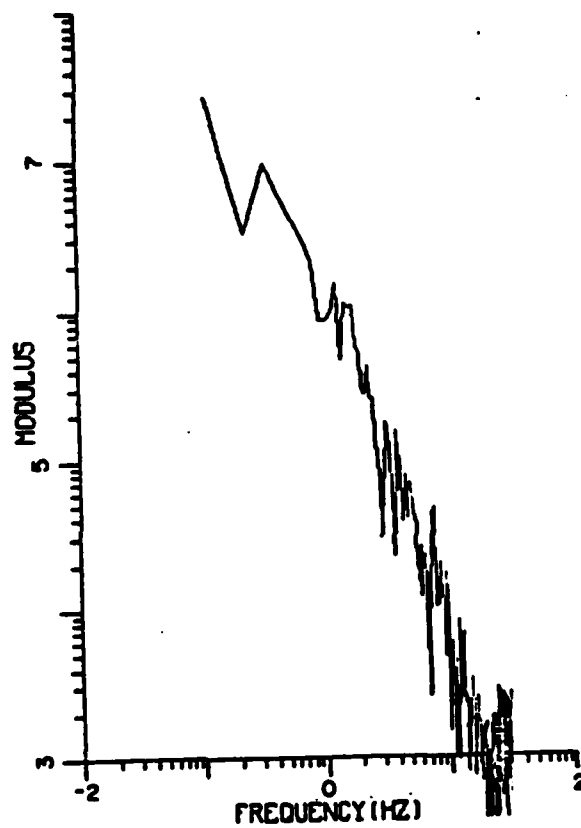


Figure 6

HANDLEY T1 SPECTRUM

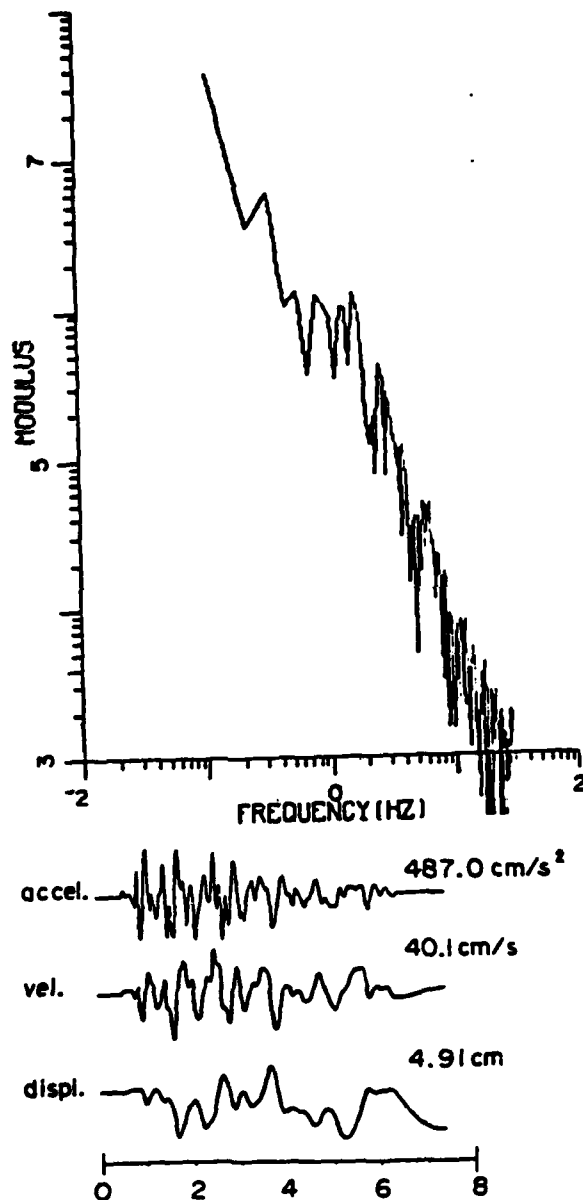


Figure 7

HANDLEY Z1 SPECTRUM

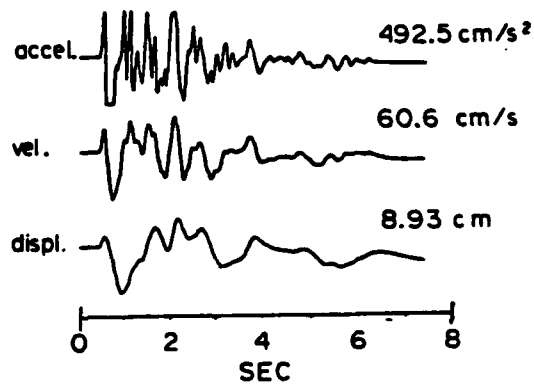
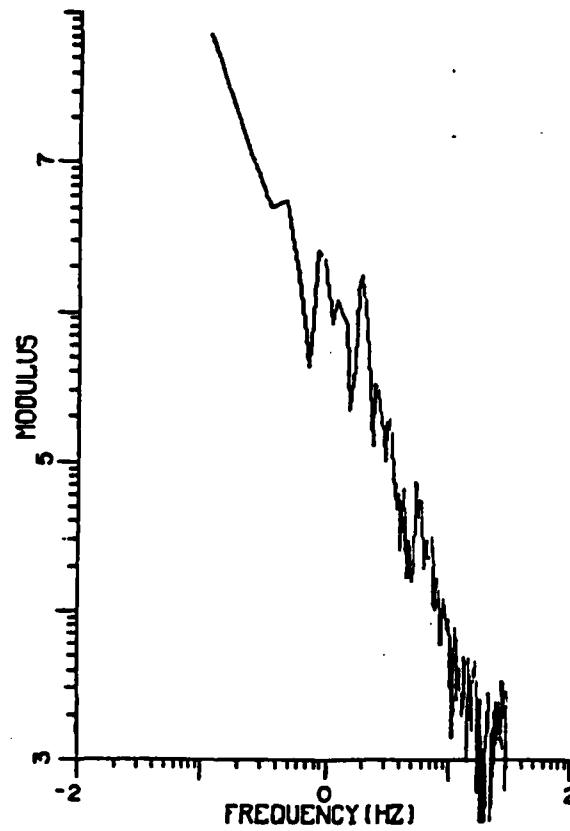


Figure 8

HANDLEY R 2 SPECTRUM

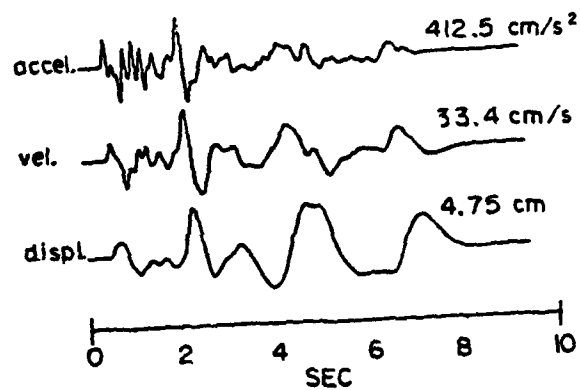
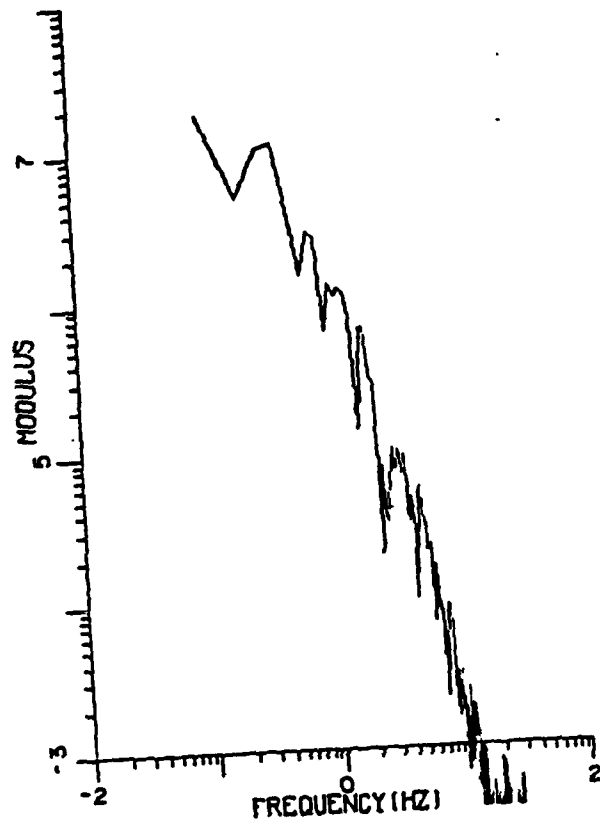


Figure 9

HANDLEY T2 SPECTRUM

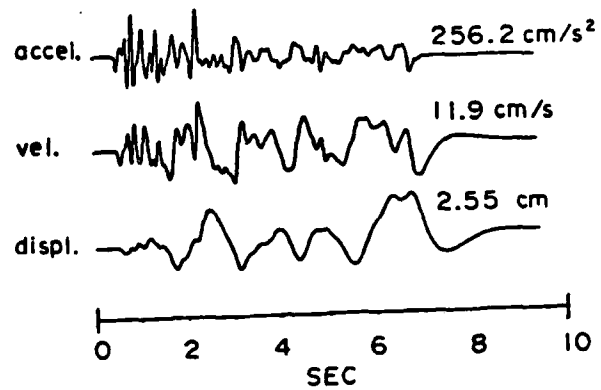
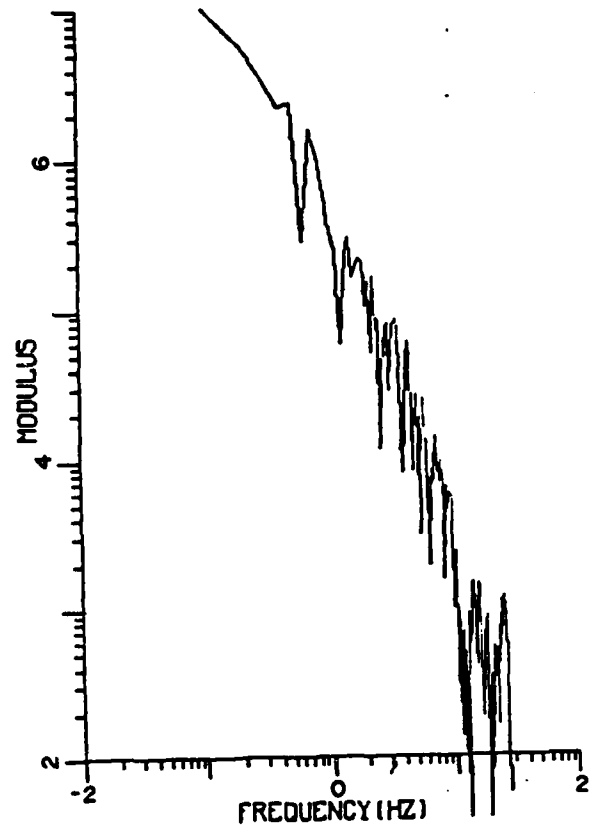


Figure 10

HANDLEY Z2 SPECTRUM

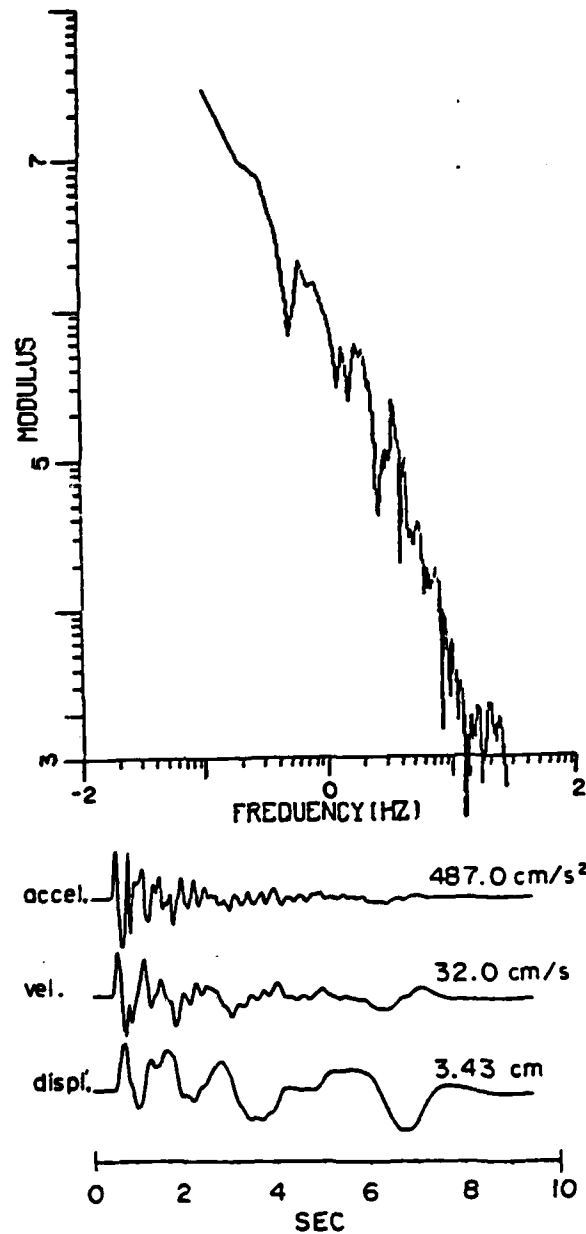


Figure 11

HANDLEY R 4 SPECTRUM

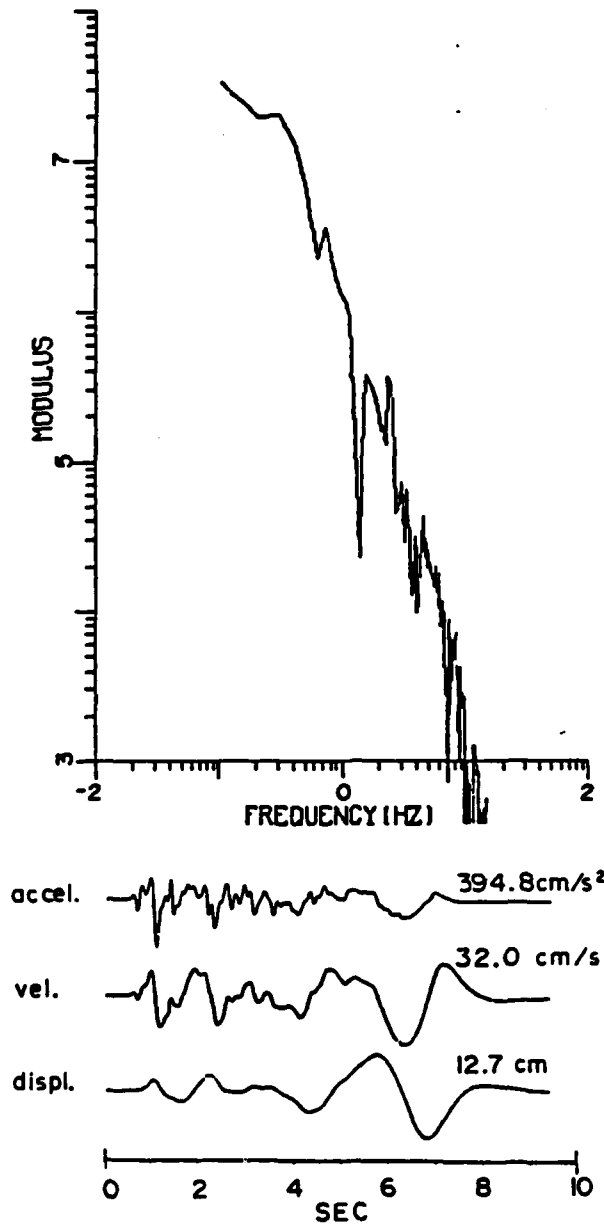


Figure 12

HANDLEY T4 SPECTRUM

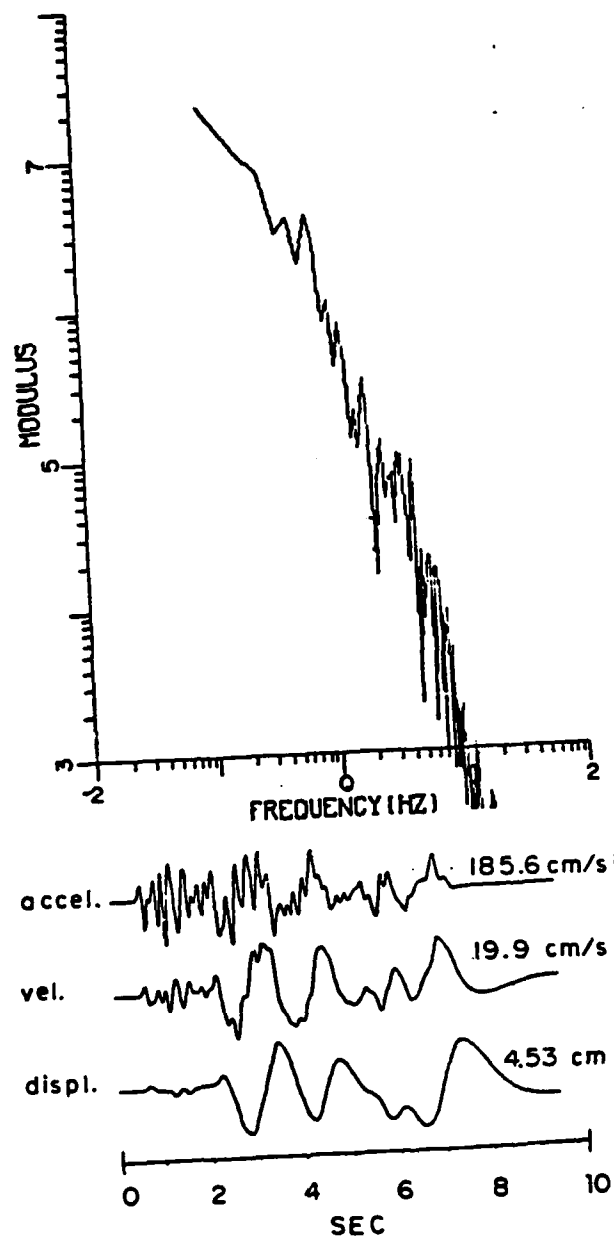


Figure 13

HANDLEY Z4 SPECTRUM

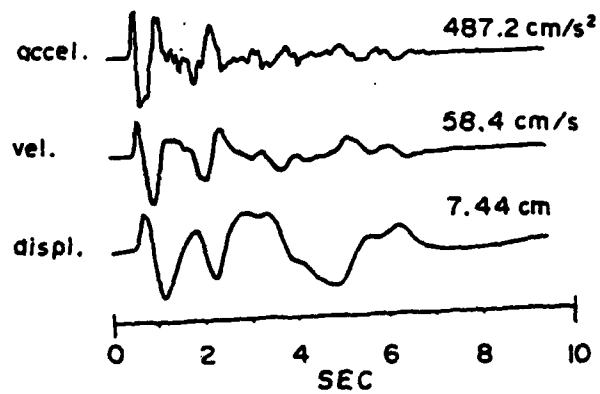
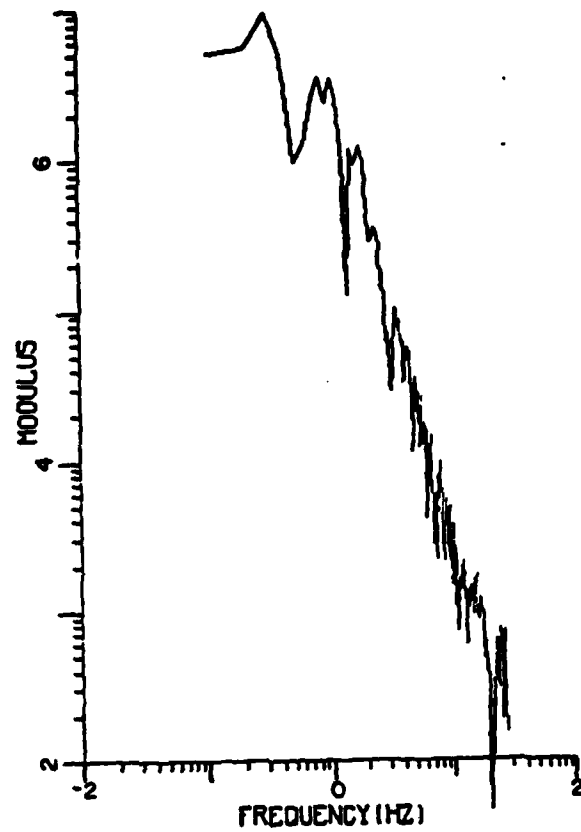


Figure 14

HANDLEY R5 SPECTRUM

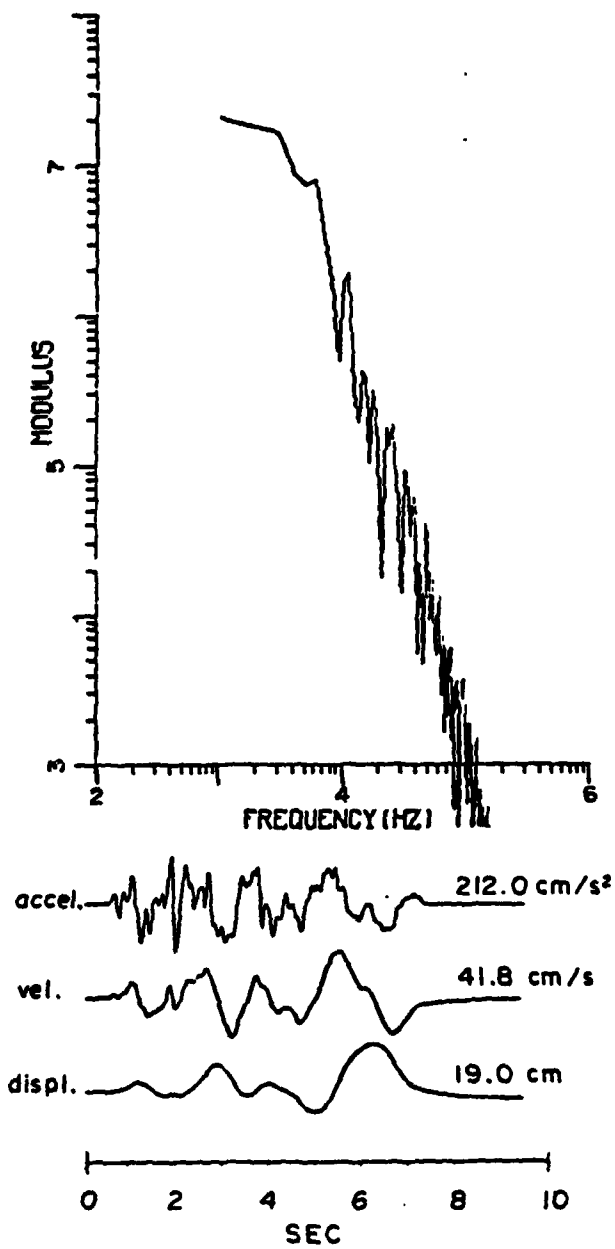


Figure 15

HANDLEY T5 SPECTRUM

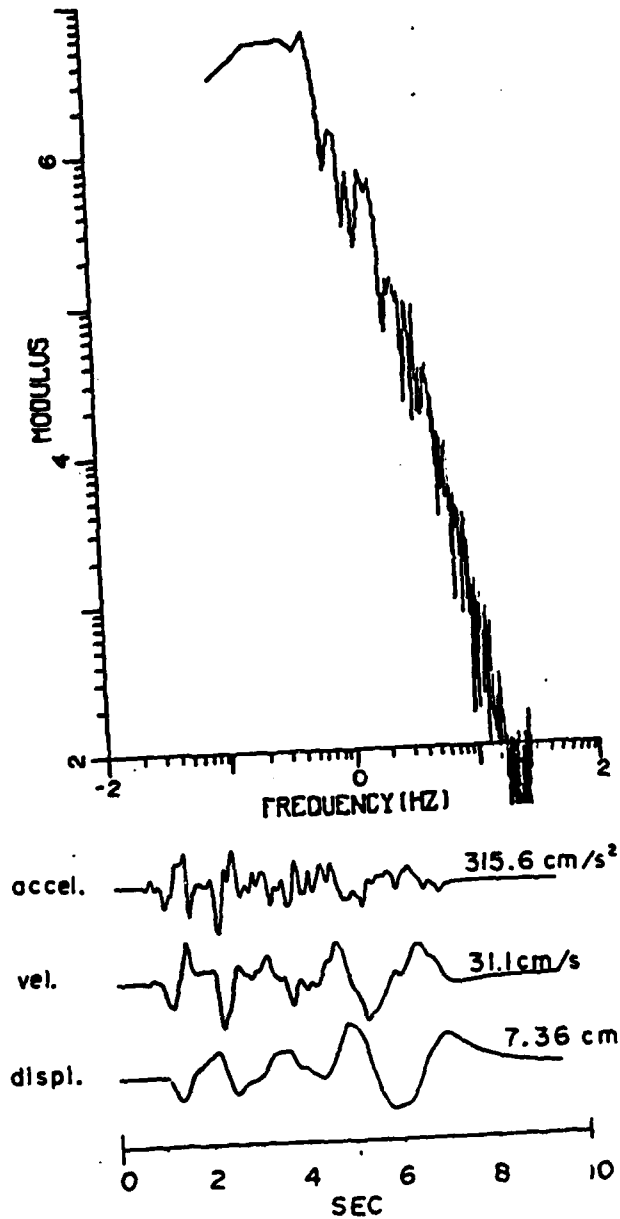


Figure 16

HANDLEY Z5 SPECTRUM

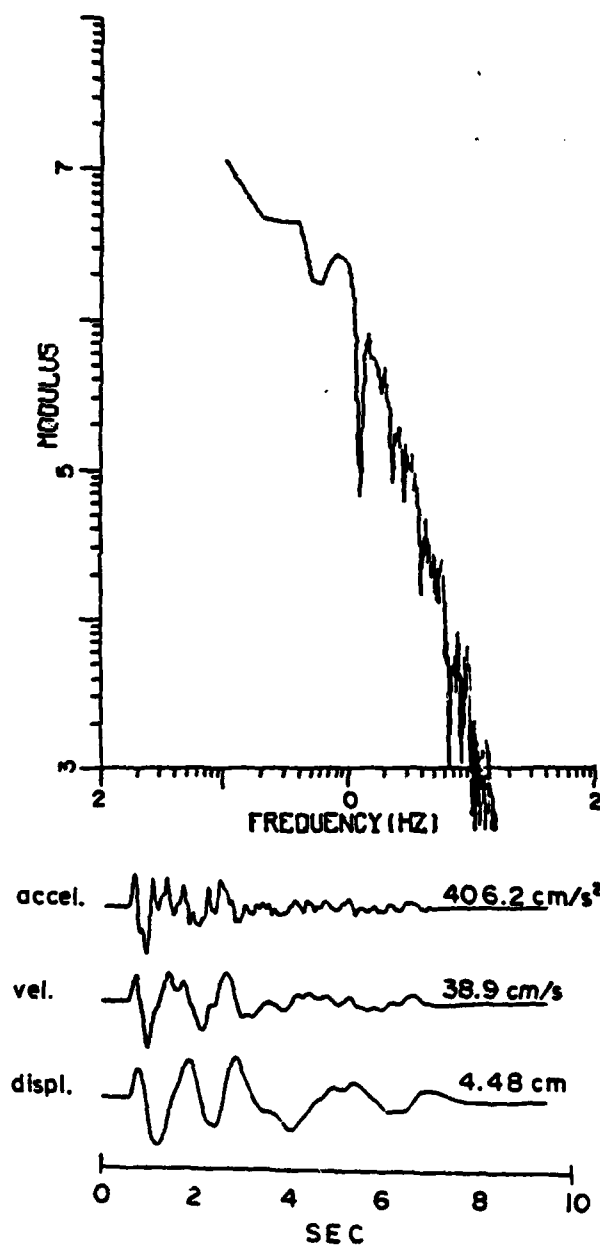


Figure 17

PIPKIN CORRECTED OBSERVATIONS

STATION 1 (2.77km)

STATION 2 (5.60km)

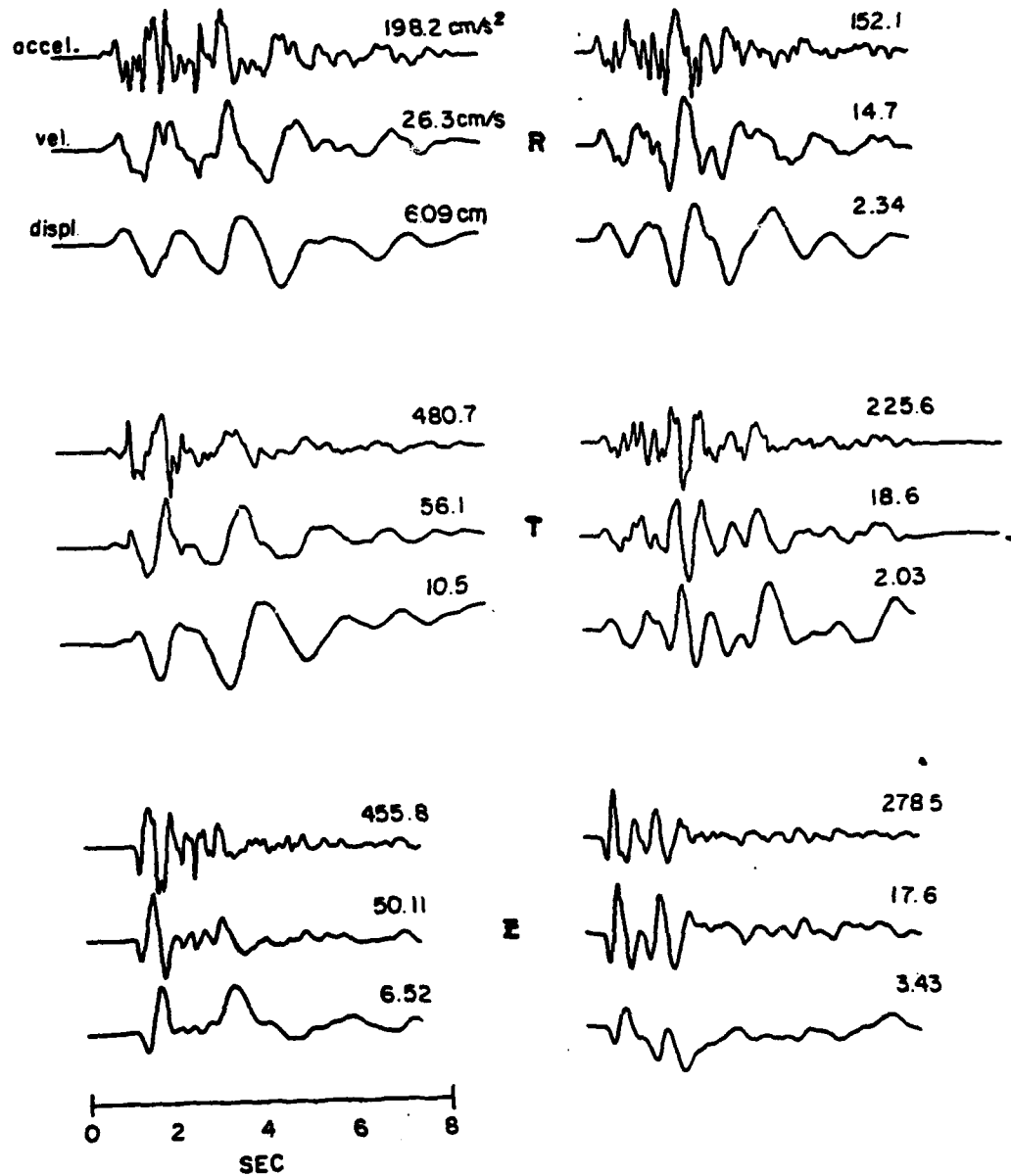


Figure 18

PIPKIN CORRECTED OBSERVATIONS

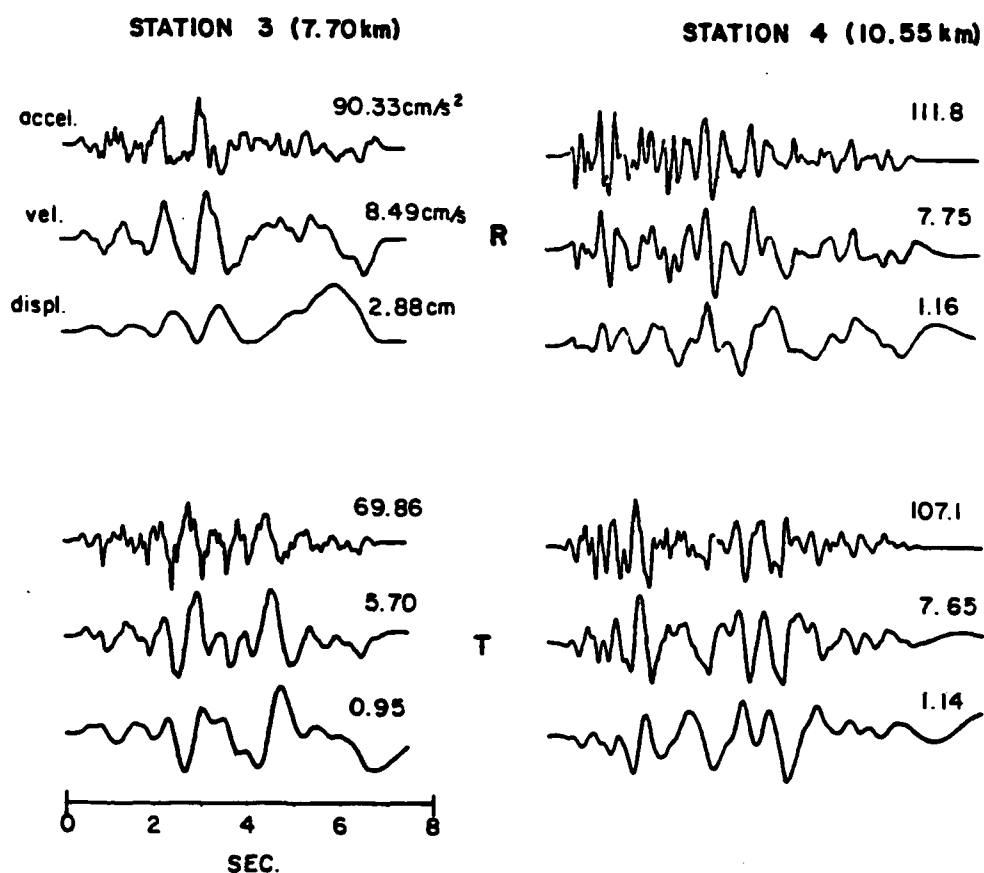
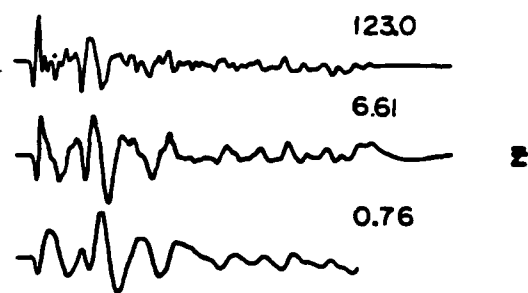
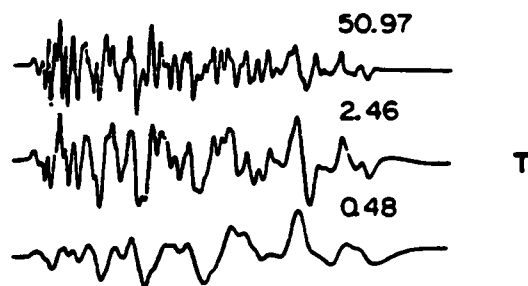
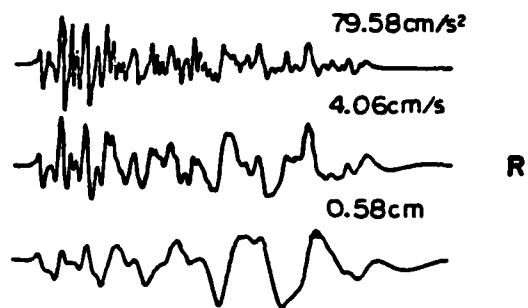


Figure 19

PIPKIN CORRECTED OBSERVATIONS

STATION 5 (1228 km)



STATION 6 (1355 km)

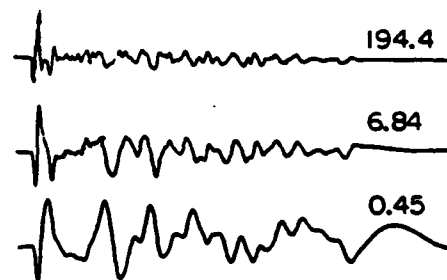


Figure 20

PIPKIN RI
SPECTRUM

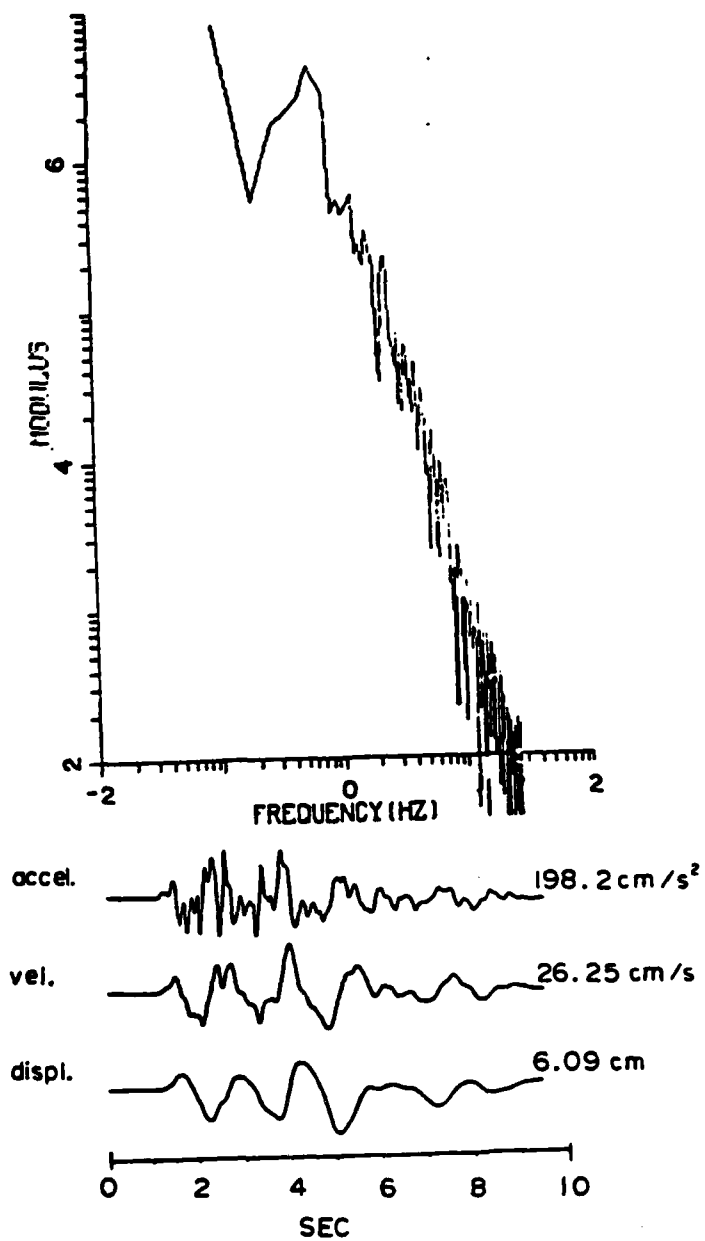


Figure 21

PIPKIN T1 SPECTRUM

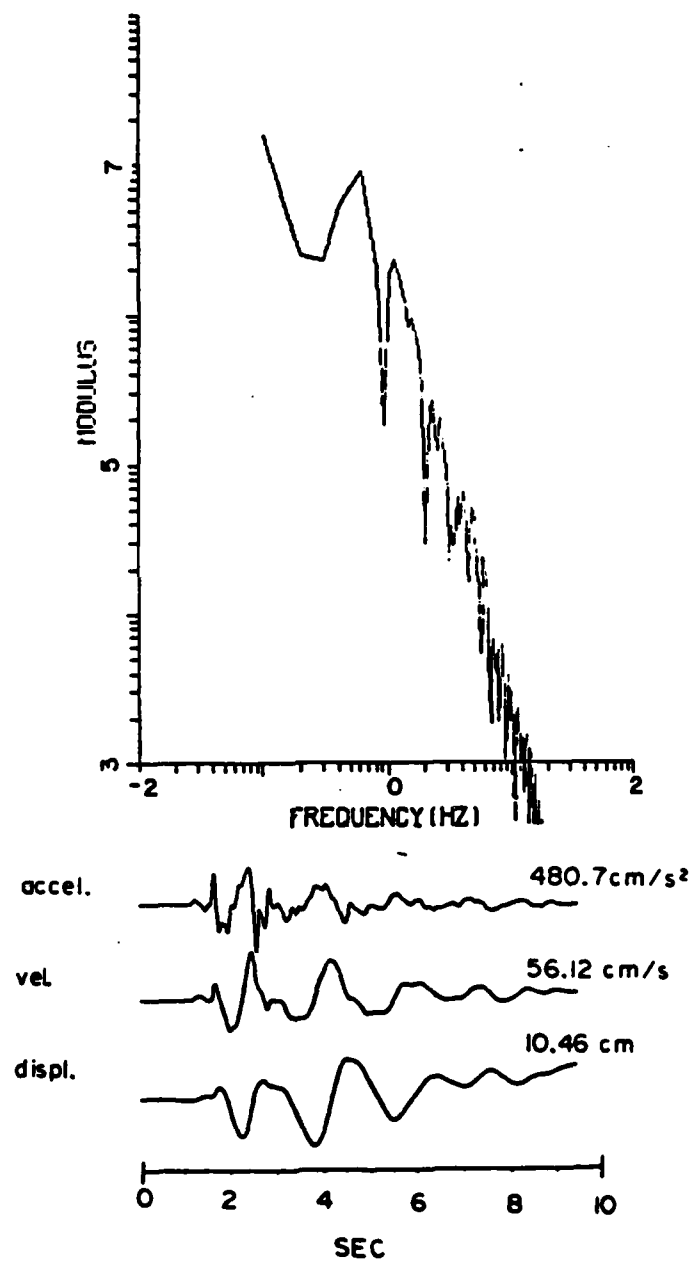


Figure 22

PIPKIN Z1
SPECTRUM

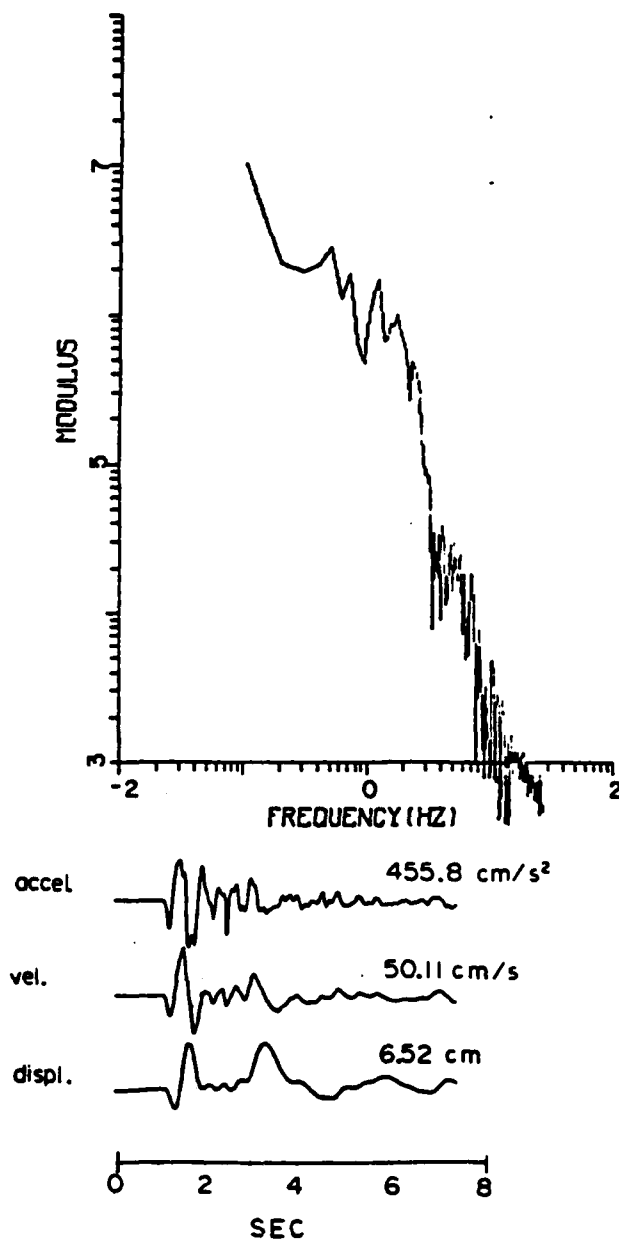


Figure 23

PIPKIN R2 SPECTRUM

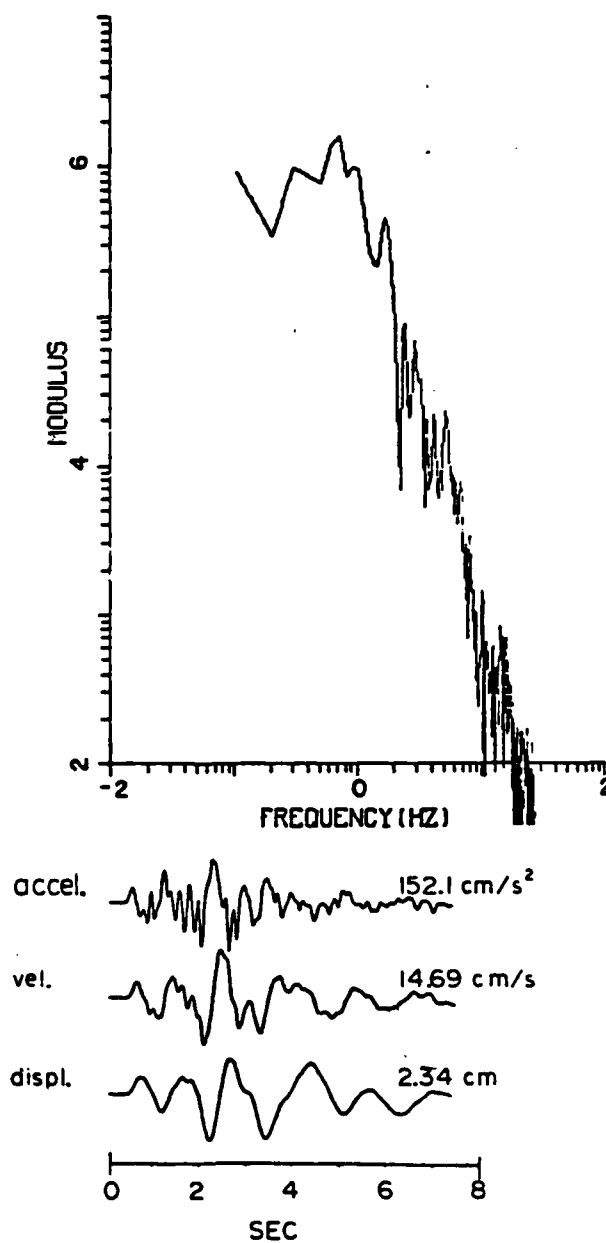


Figure 24

PIPKIN T2 SPECTRUM

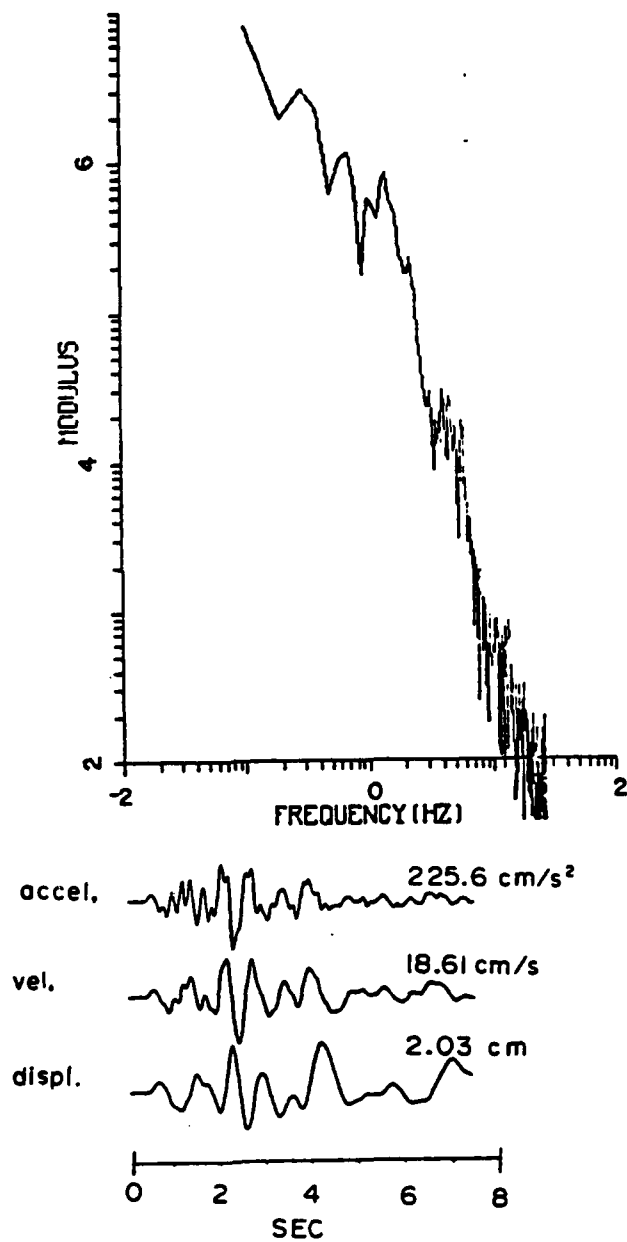


Figure 25

PIPKIN Z 2
SPECTRUM

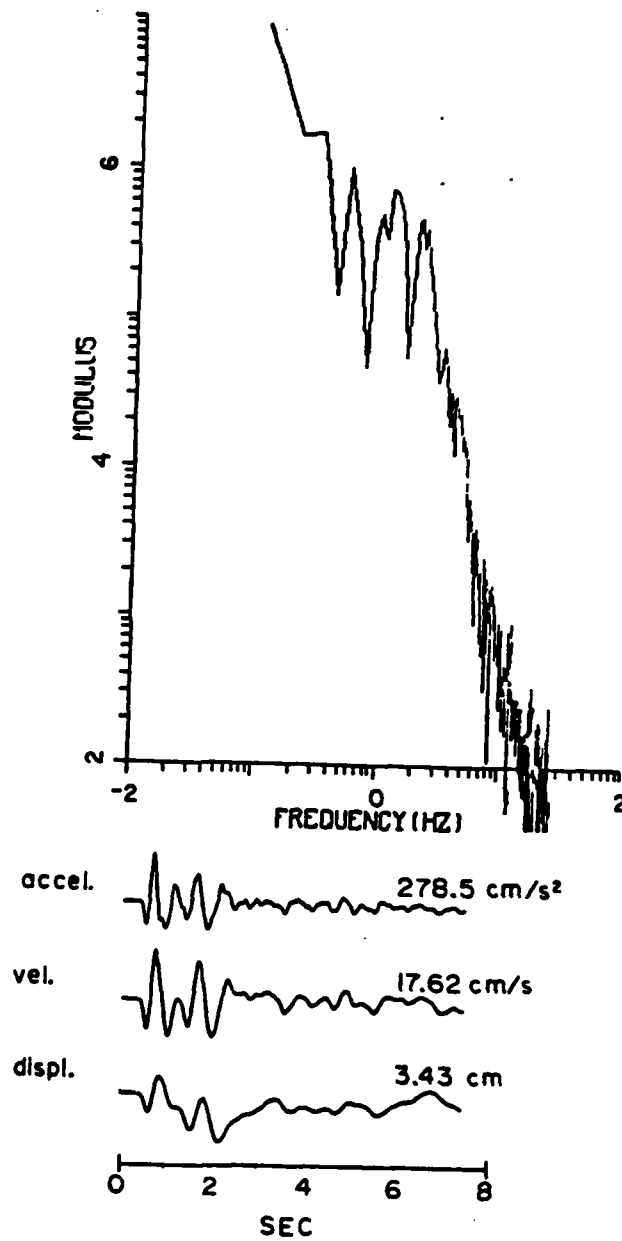
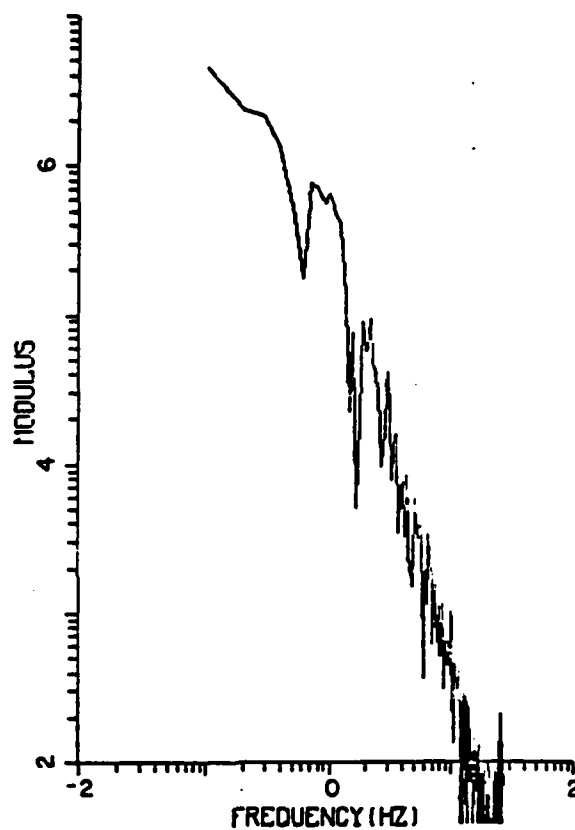


Figure 26

PIPKIN R3
SPECTRUM



accel.  90.33 cm/s²

vel.  8.49 cm/s

displ.  2.88 cm

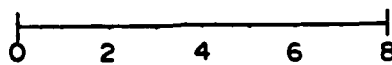

0 2 4 6 8
SEC

Figure 27

PIPKIN T3 SPECTRUM

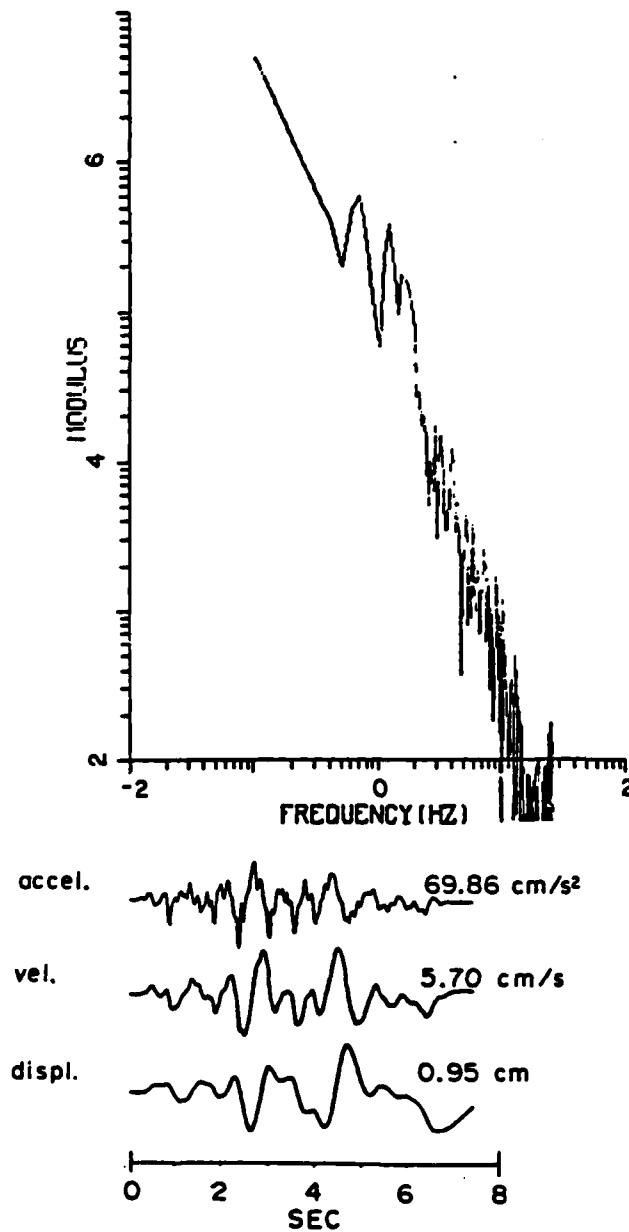


Figure 28

PIPKIN R4 SPECTRUM

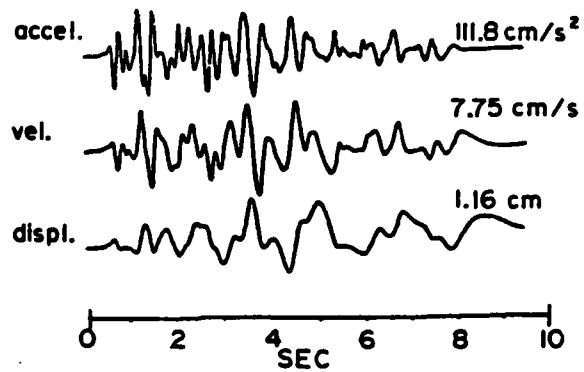
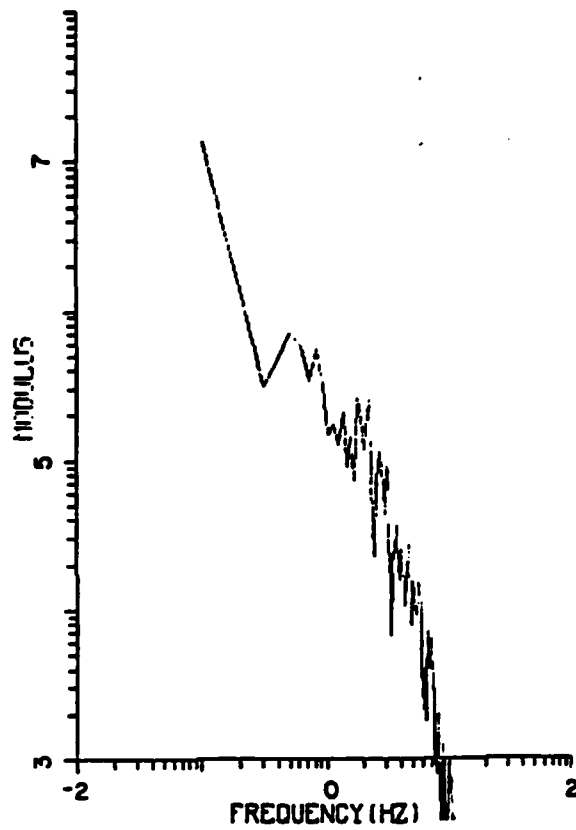


Figure 29

PIPKIN T4 SPECTRUM

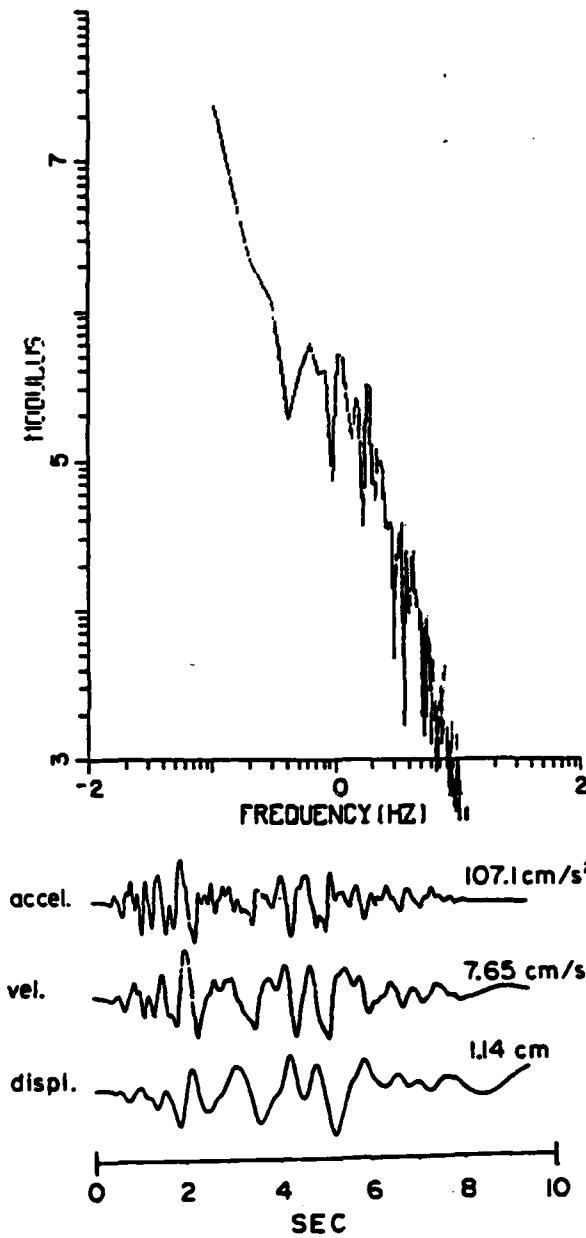


Figure 30

PIPKIN R5 SPECTRUM

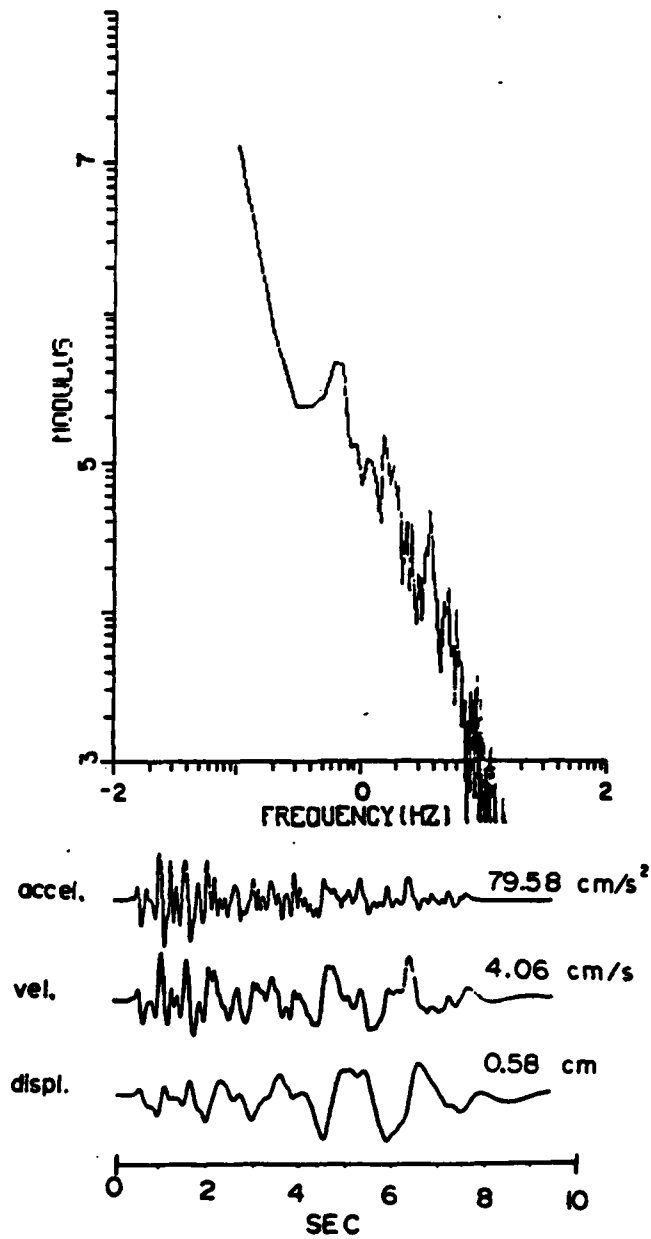


Figure 31

PIPKIN T5 SPECTRUM

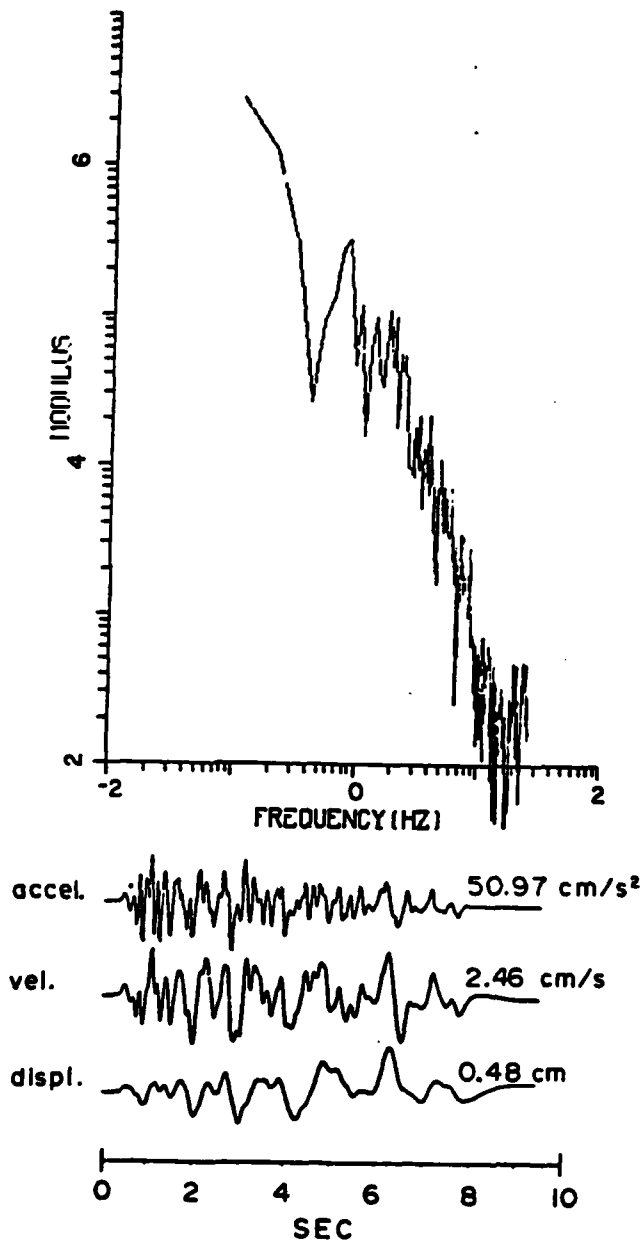


Figure 32

PIPKIN Z5 SPECTRUM

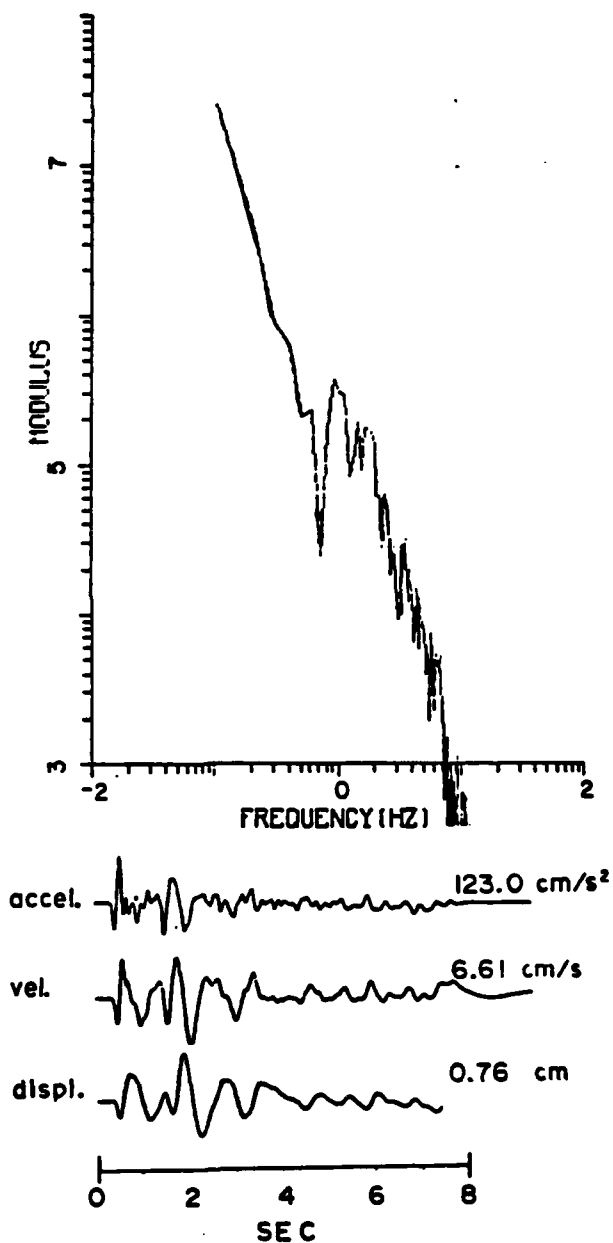


Figure 33

PIPKIN Z6 SPECTRUM

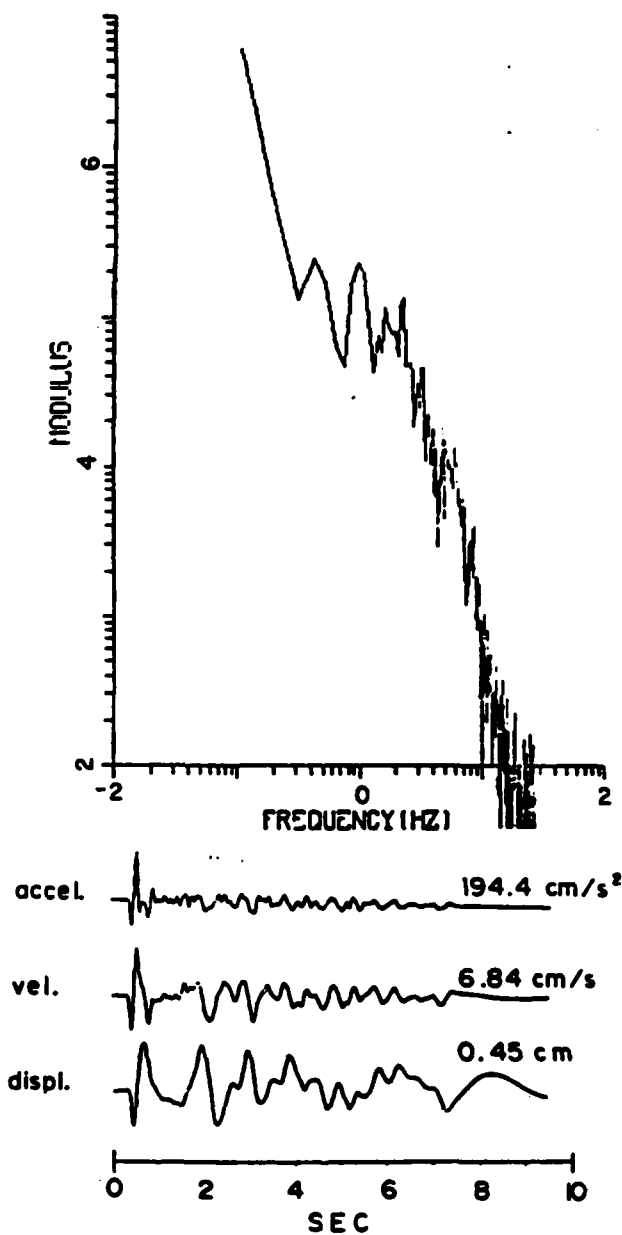


Figure 34

FARM CORRECTED OBSERVATIONS

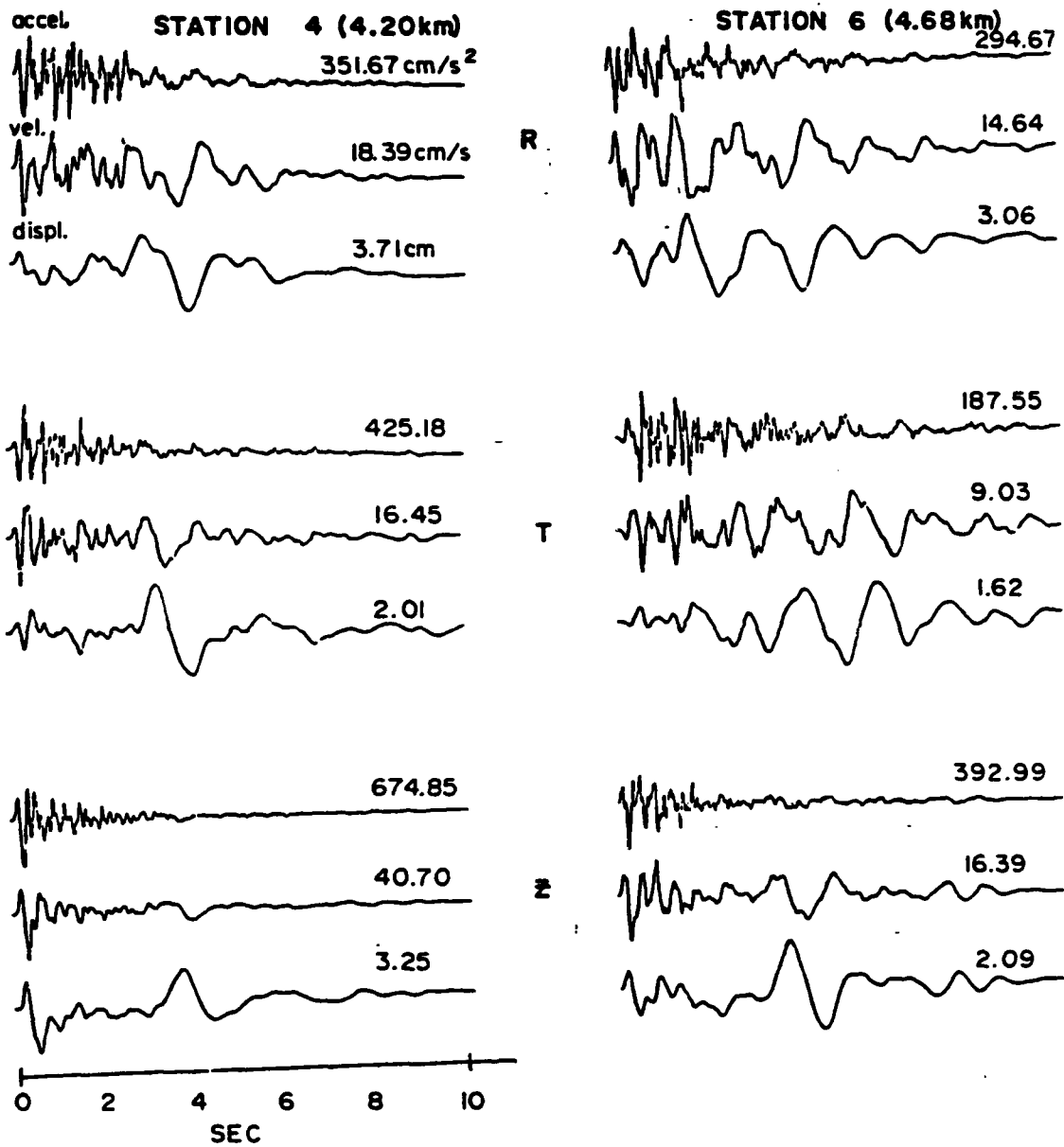


Figure 35

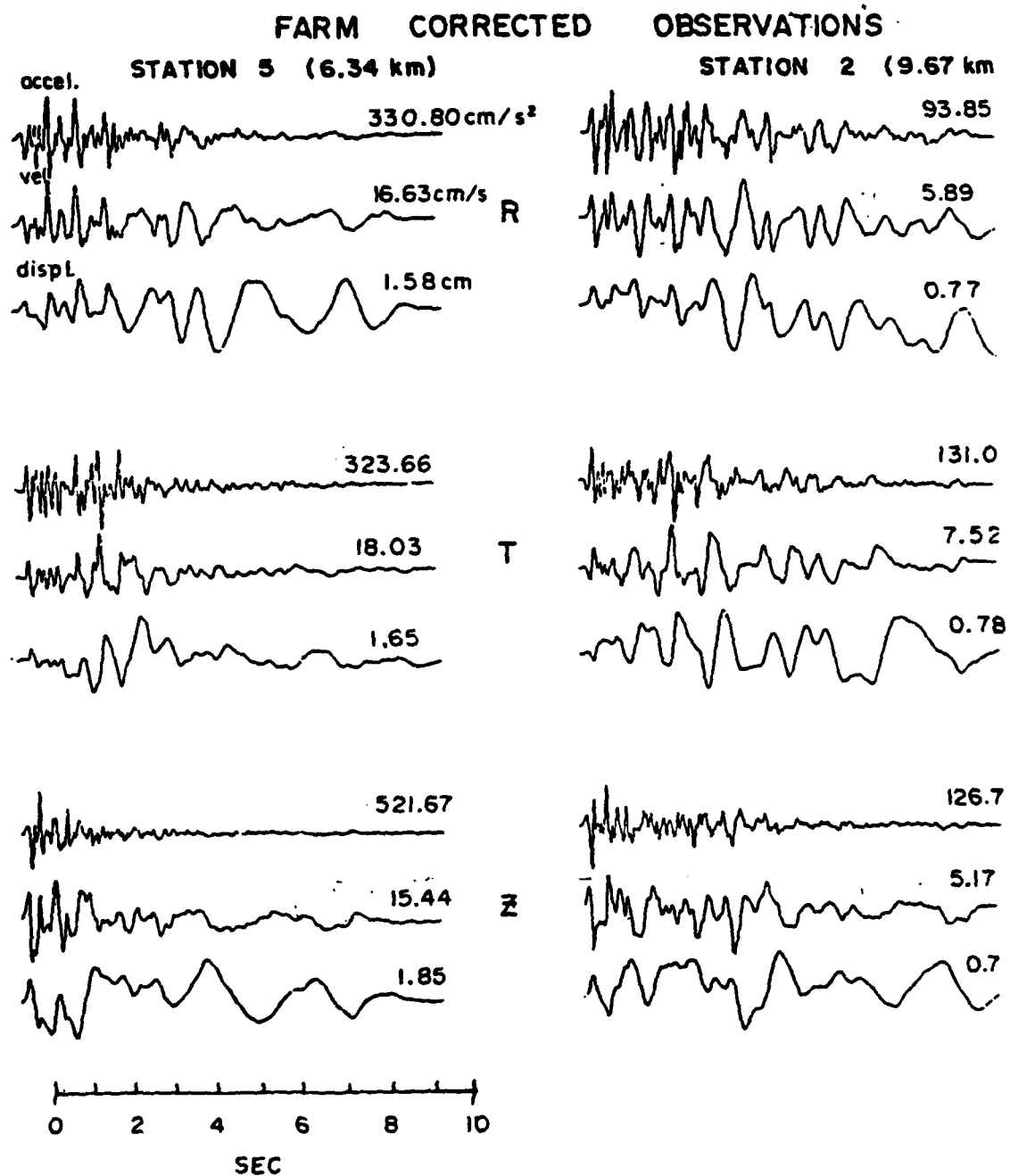


Figure 36

FARM R 4

SPECTRUM

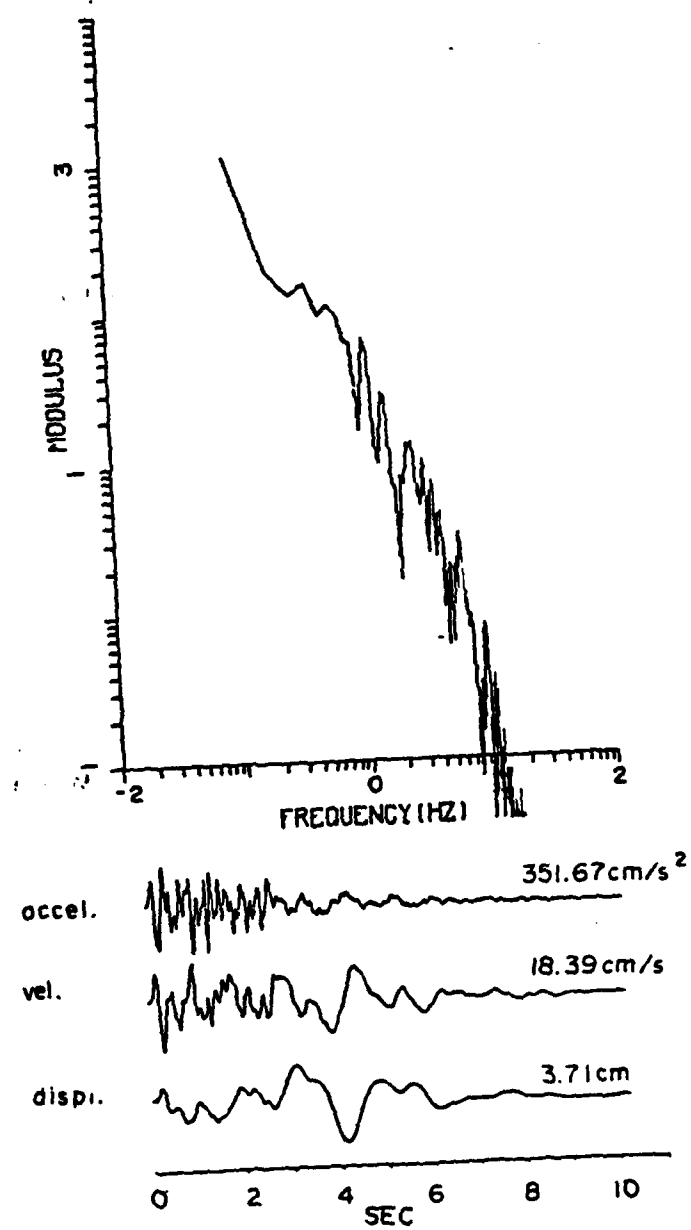


Figure 37

FARM T 4
SPECTRUM

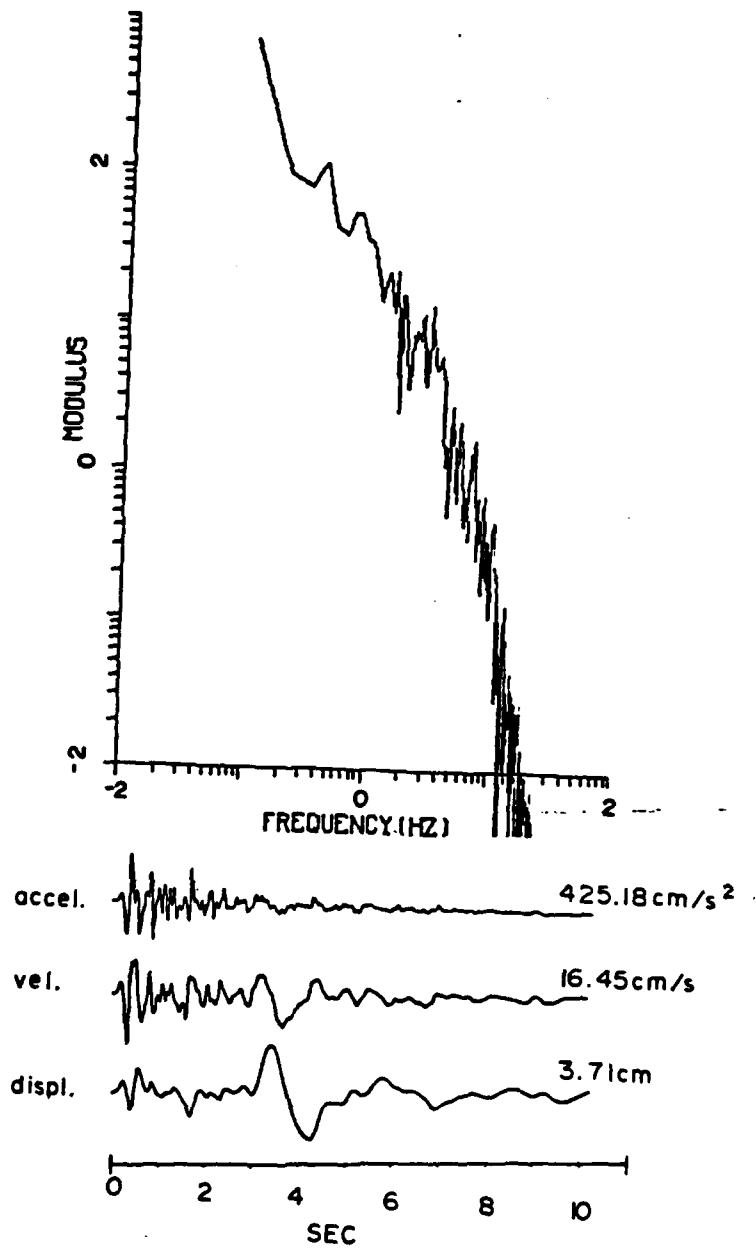


Figure 38

FARM Z4
SPECTRUM

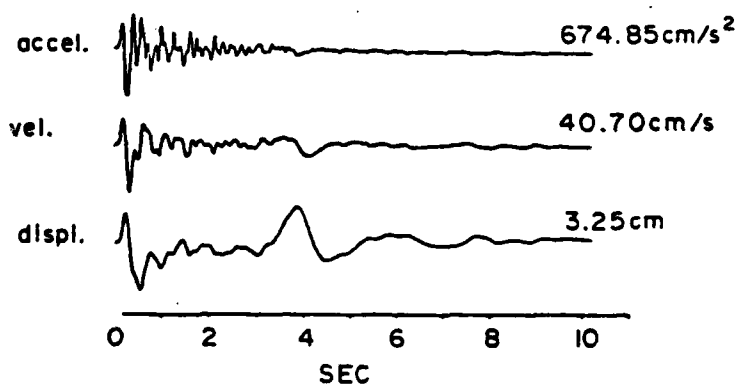
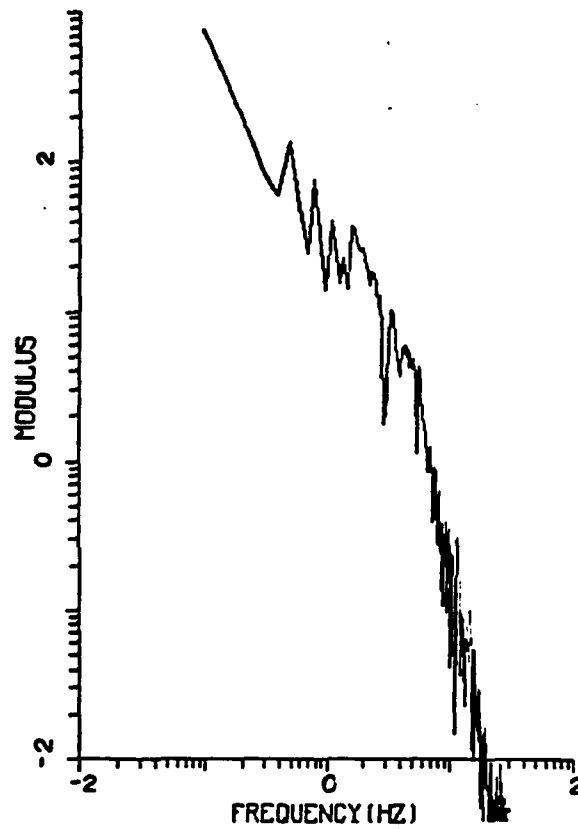


Figure 39

FARM R6 SPECTRUM

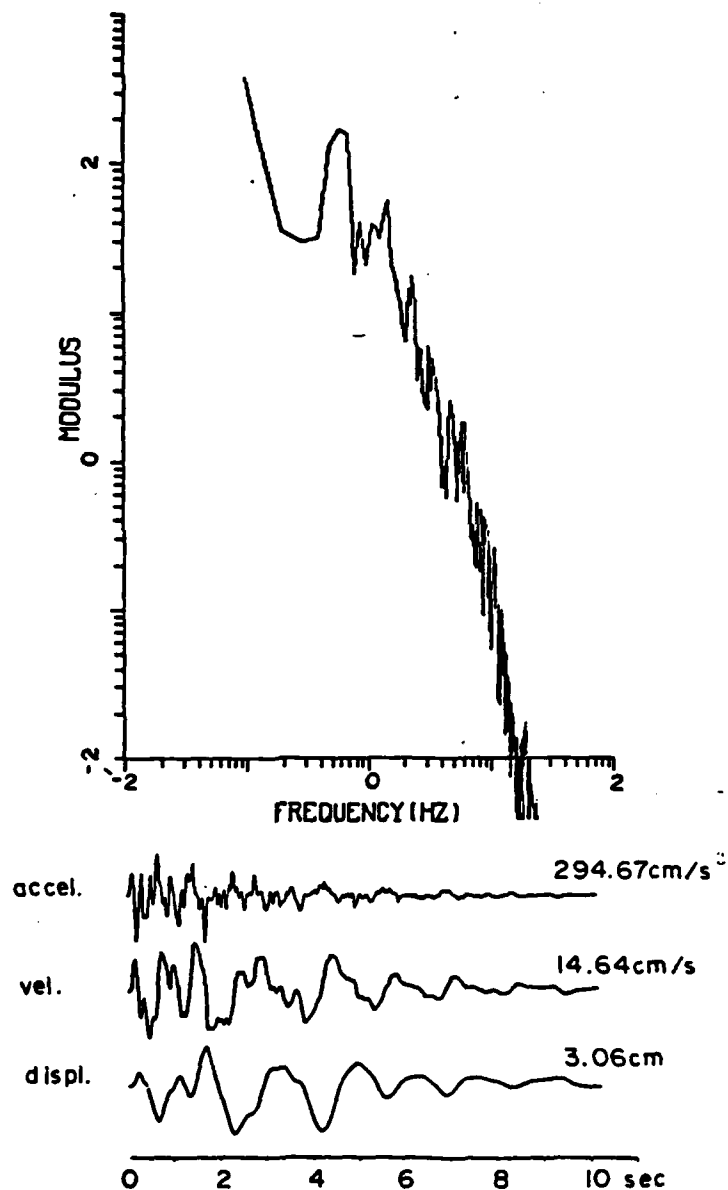


Figure 40

FARM T6
SPECTRUM

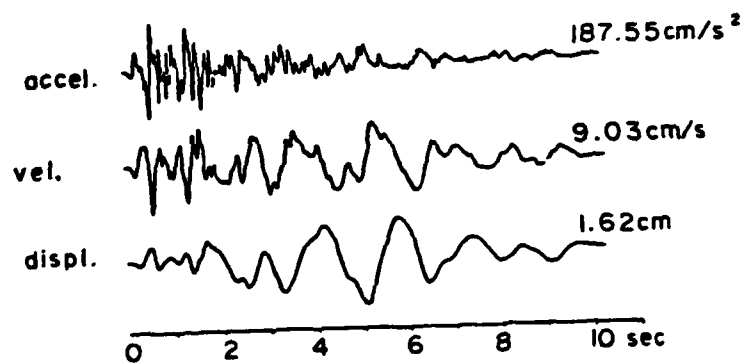
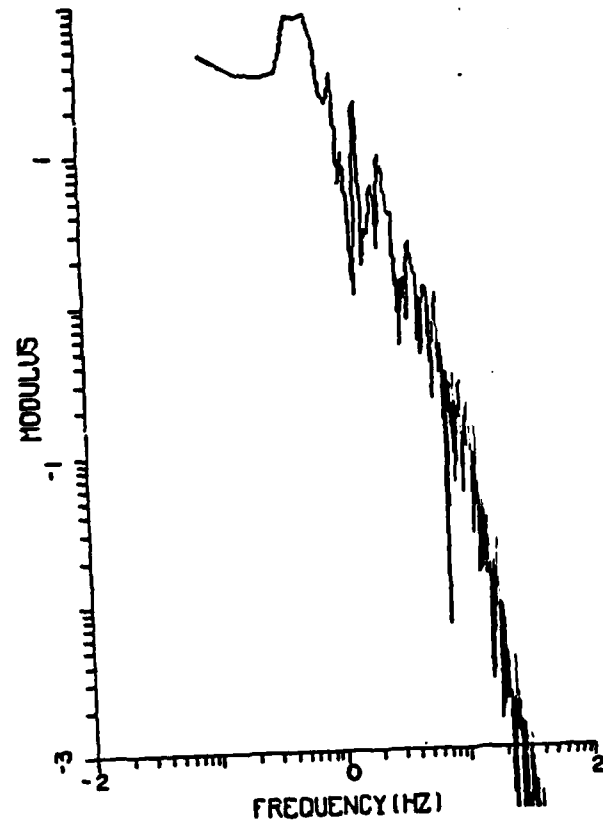


Figure 41

FARM Z6
SPECTRUM

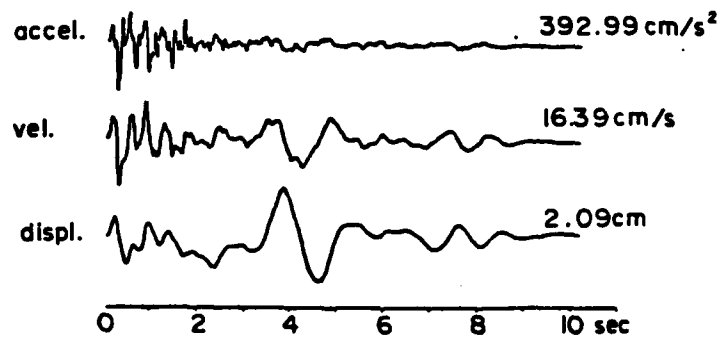
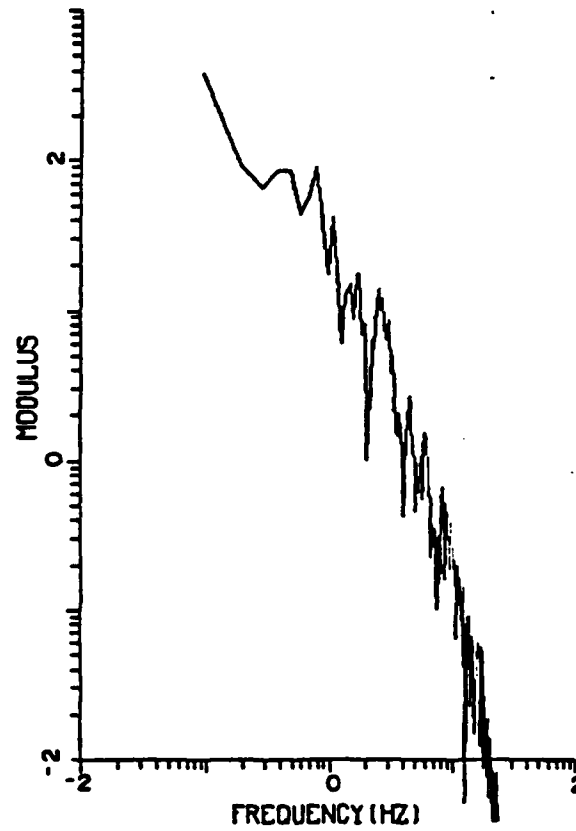


Figure 42

FARM R5 SPECTRUM

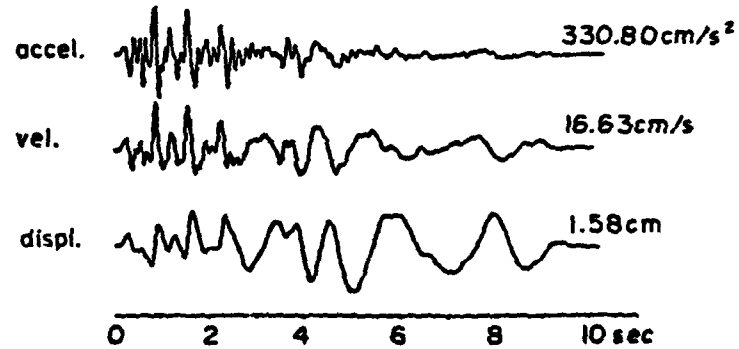
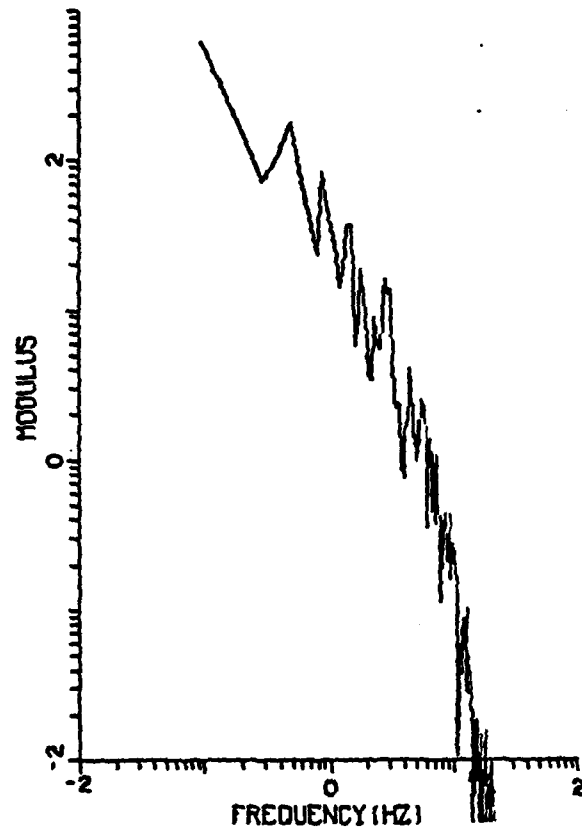


Figure 43

FARM T5 SPECTRUM

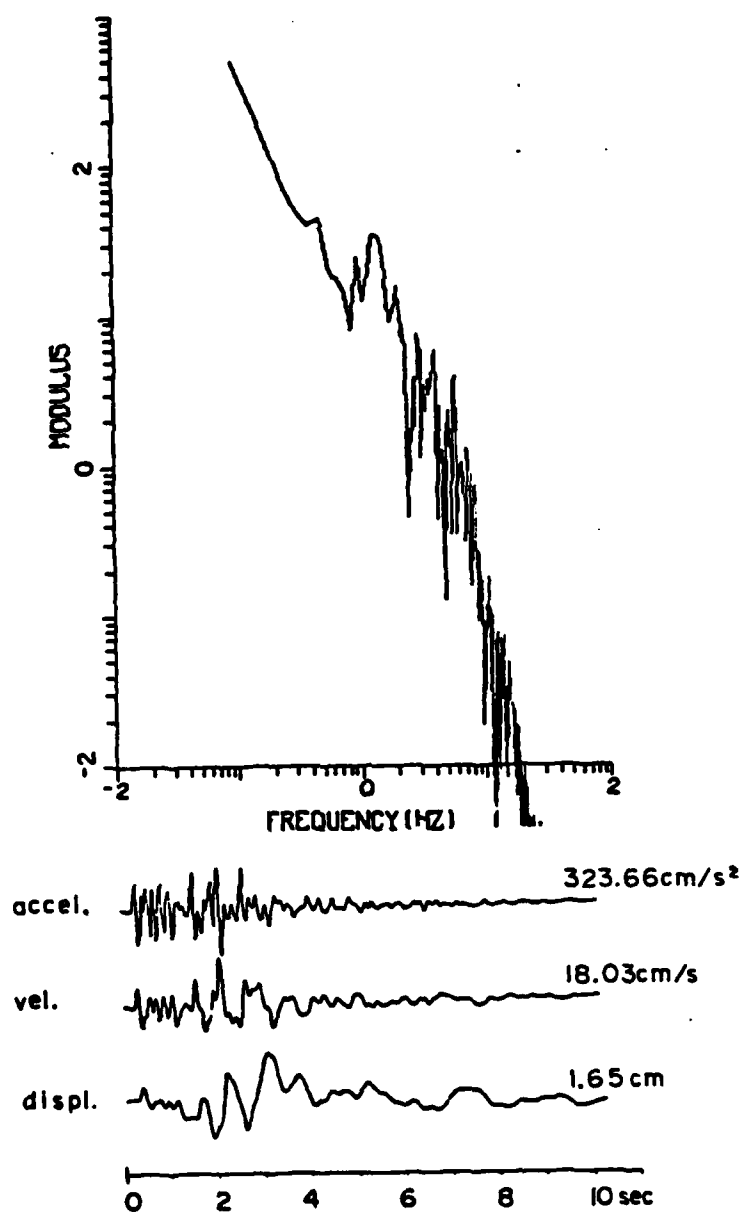


Figure 44

FARM 25
SPECTRUM

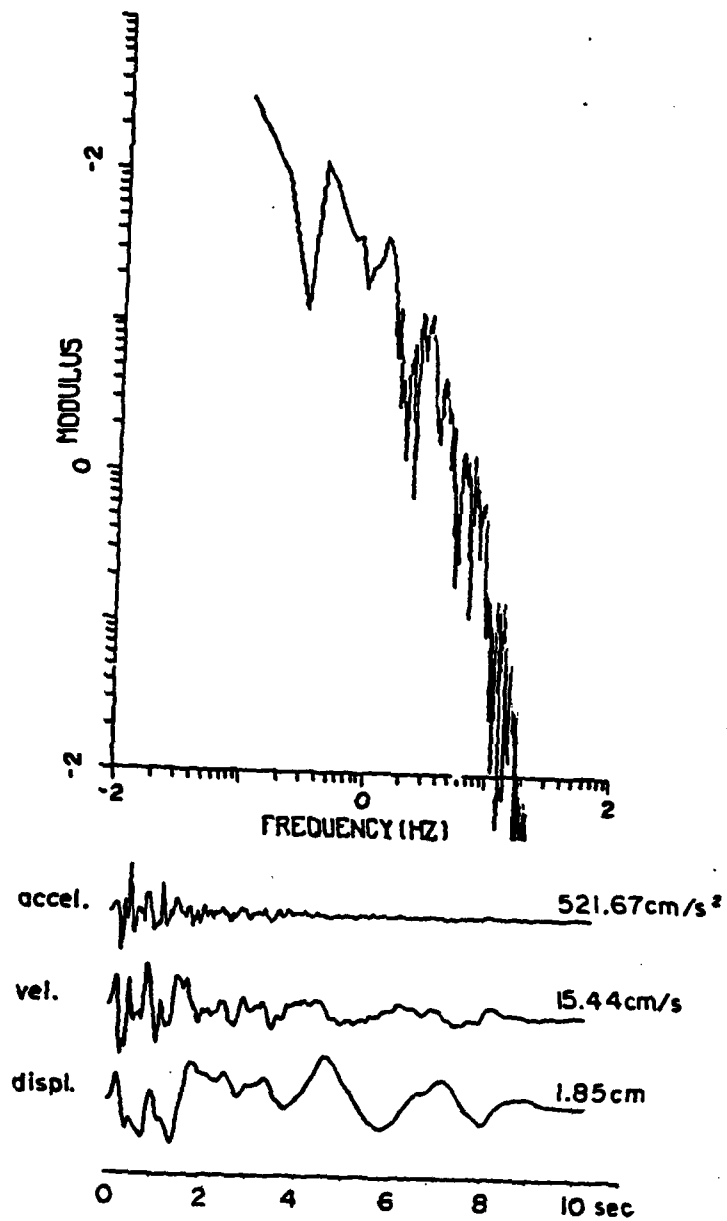


Figure 45

FARM R2
SPECTRUM

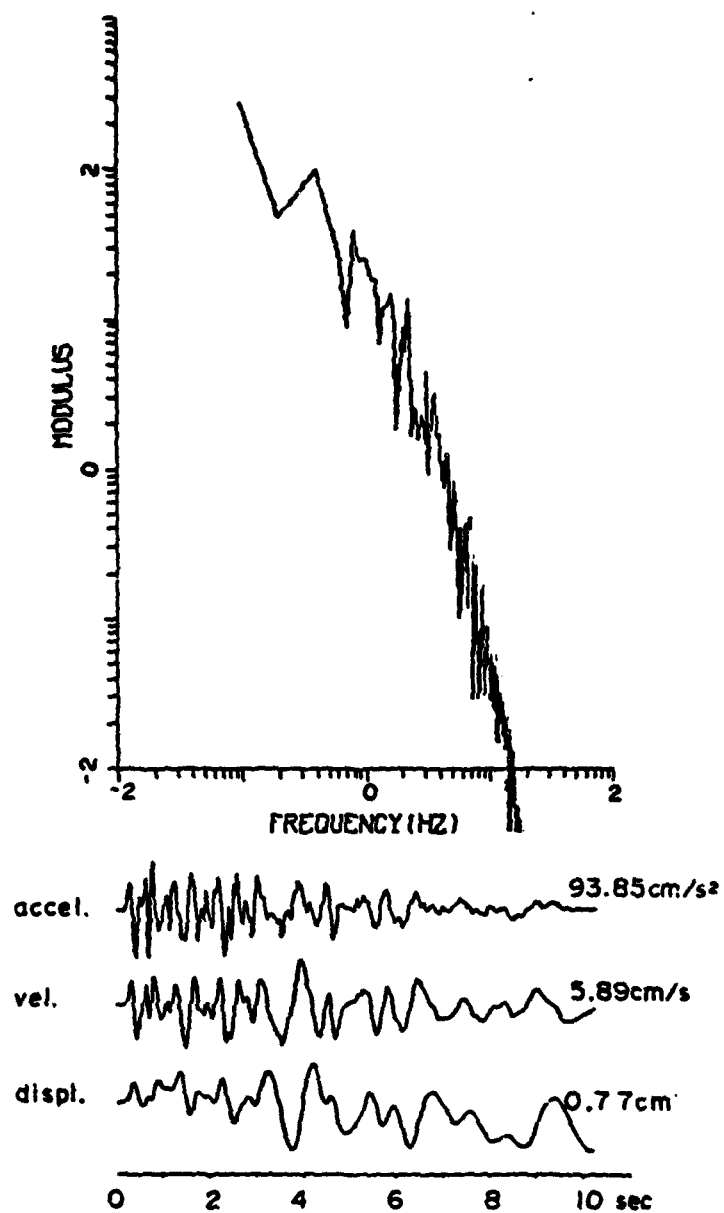


Figure 46

FARM T2
SPECTRUM

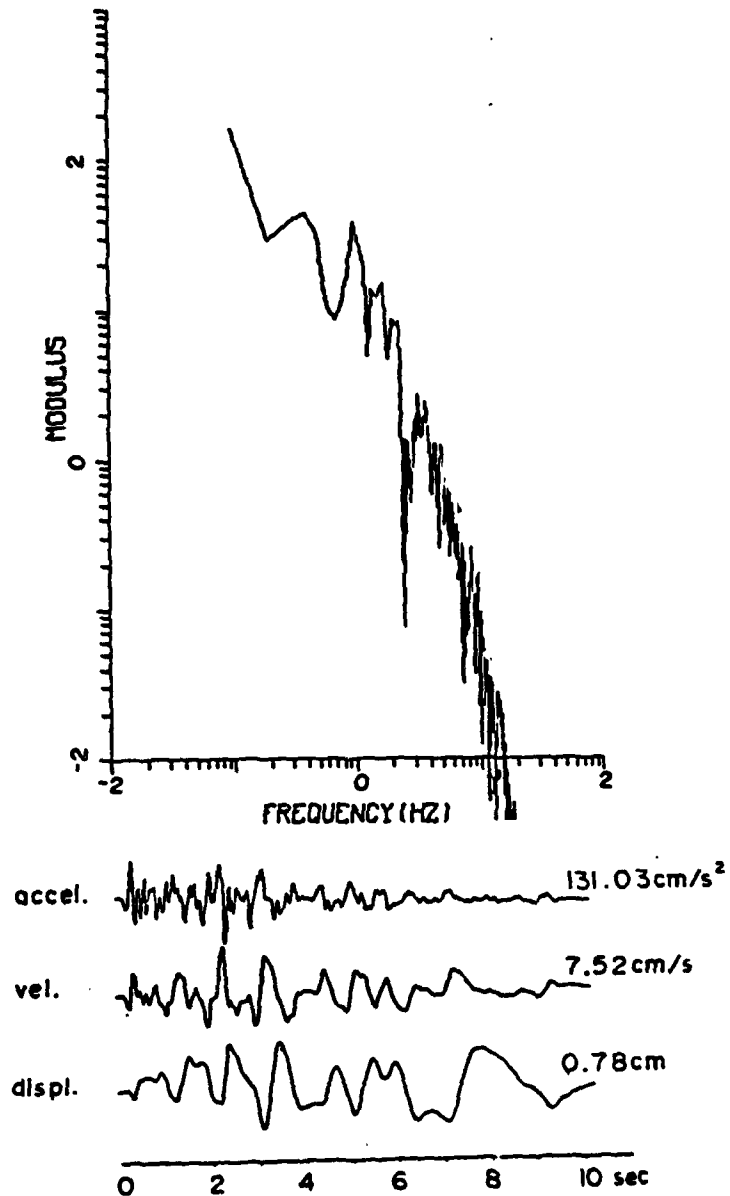


Figure 47

FARM 22
SPECTRUM

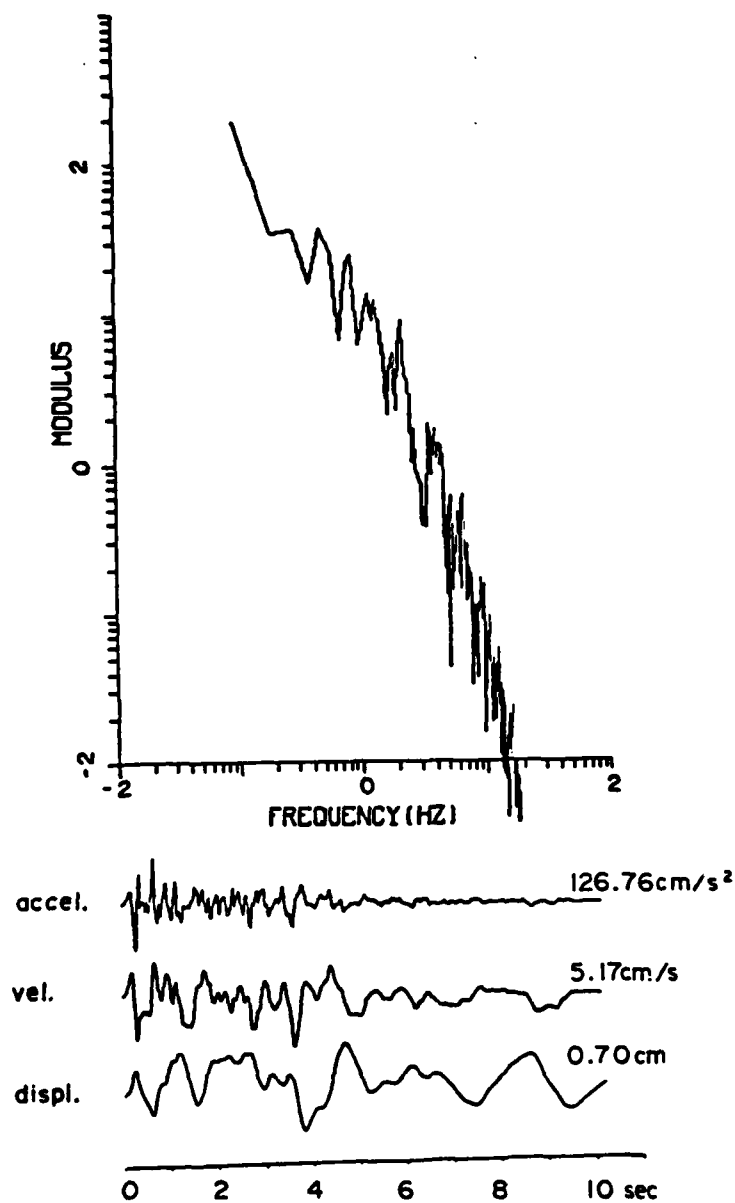


Figure 48

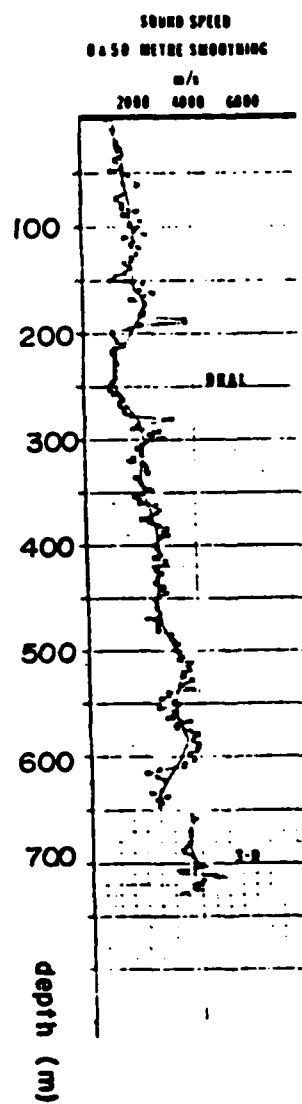


Figure 49

NTS MODEL

	α (km/s)	ρ (gm/cc)	β -news (km/s)	β -olds (km/s)	
H=0.65km	2.70	2.60	1.56	0.80	*PIPKIN *FARM
H=0.80km	3.40	2.70	1.73	1.20	*HANDLEY
H=1.05km	3.80	2.80	2.15	1.8	
HALF-SPACE	4.40	2.82	2.50	2.50	

Figure 50

PIPKIN TRAVEL TIME CURVE

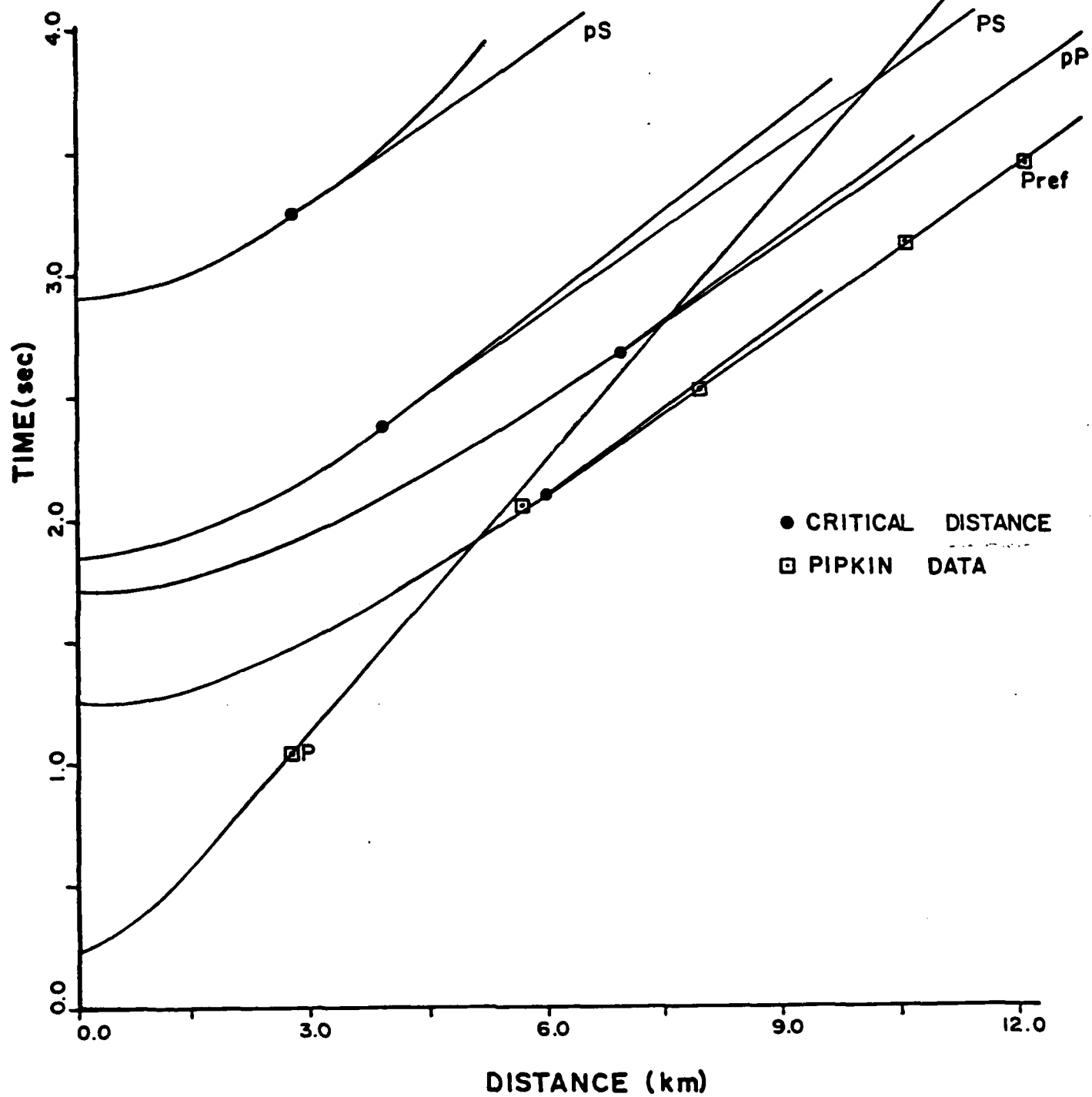


Figure 51

FARM TRAVEL TIME CURVE

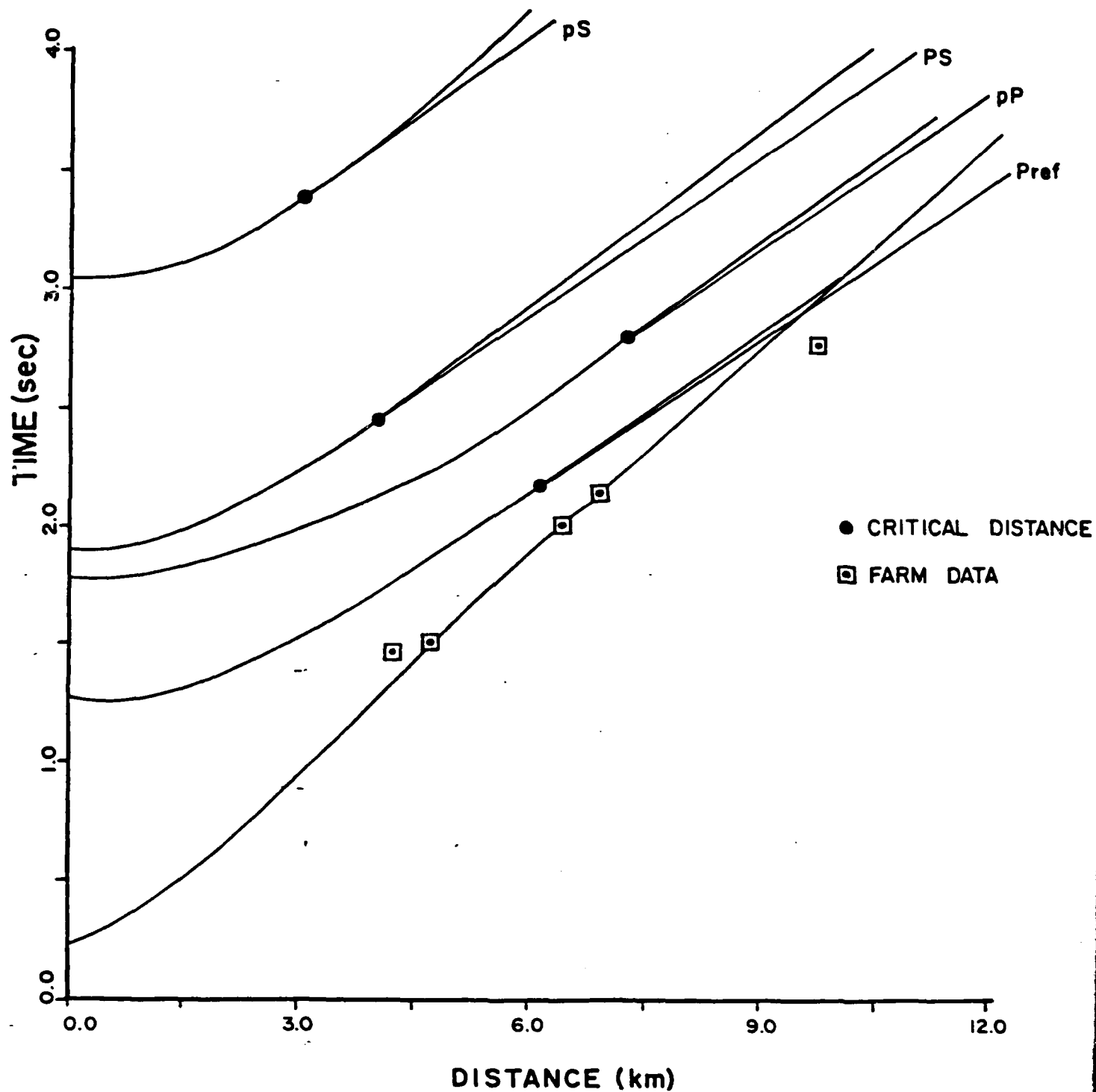


Figure 52

FARM NEWS 31

R-EX

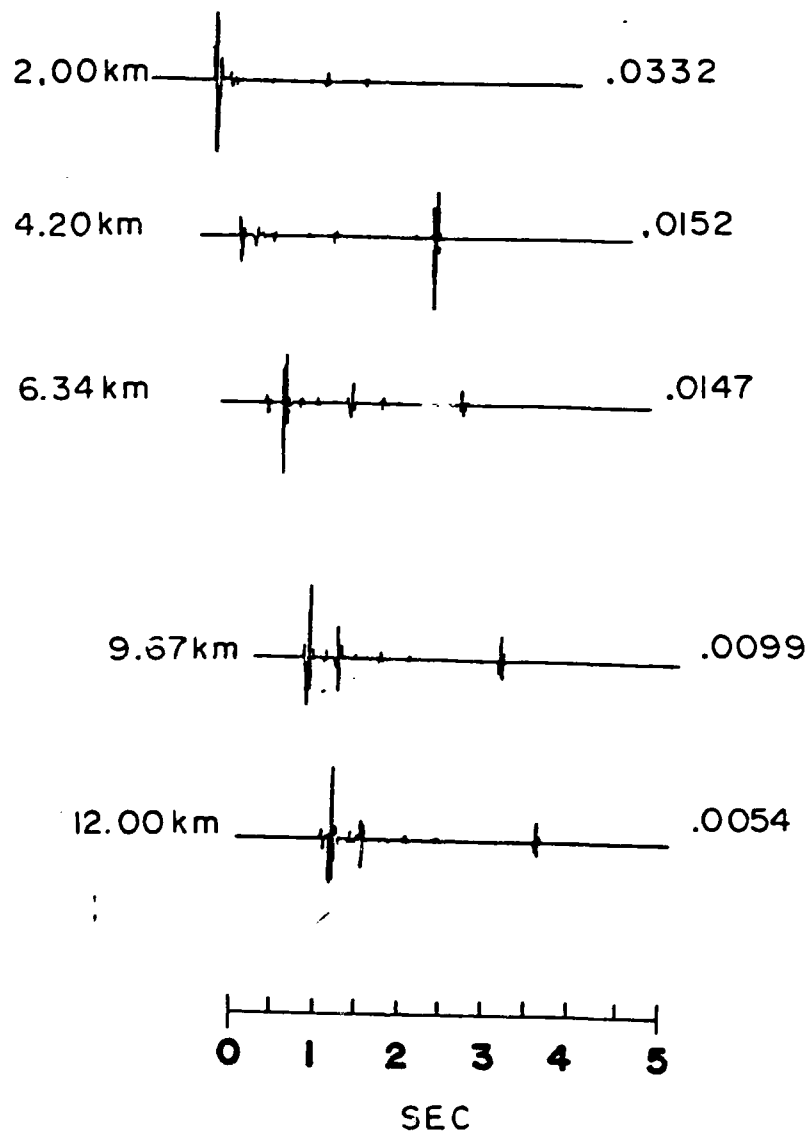


Figure 53

FARM NEWS 31
Z-EX

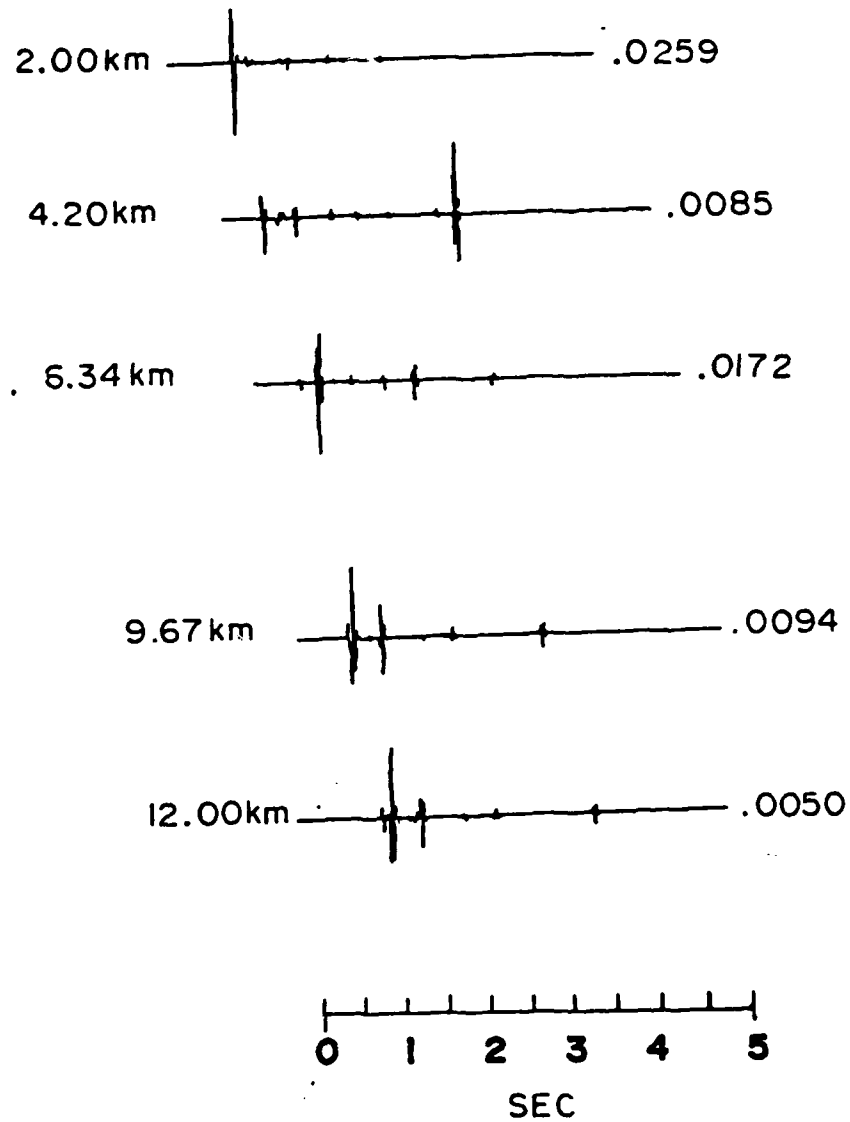
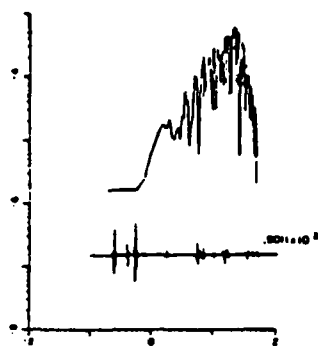
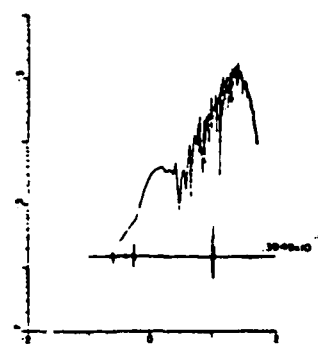


Figure 54

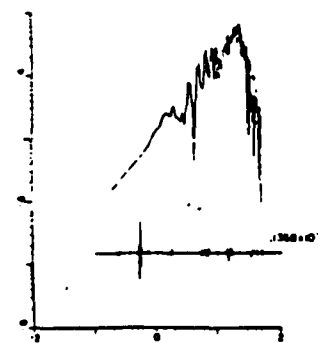
FARM SS-R



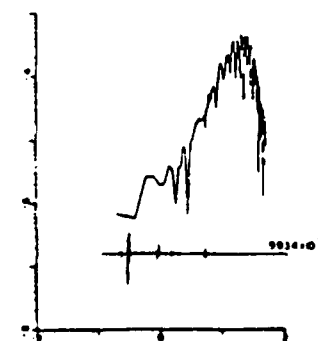
FARM DS-R



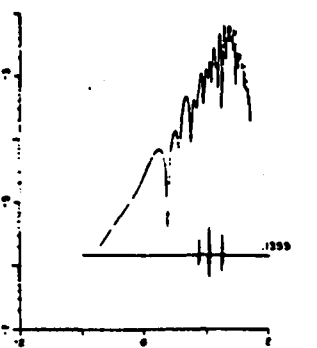
FARM CLVD-R



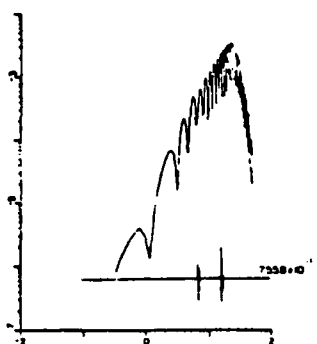
FARM EX-R



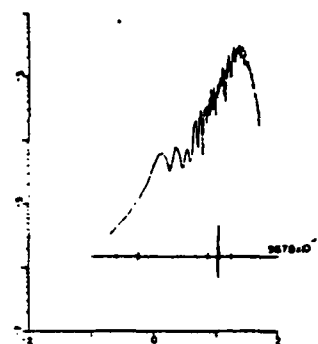
FARM SS-E



FARM DS-E



FARM CLVD-E



FARM EX-E

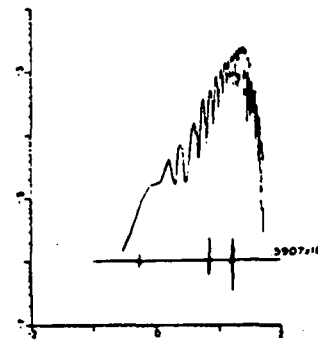
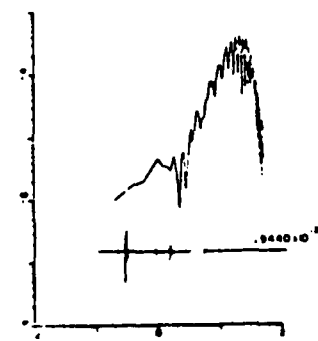


Figure 55



FARM NEWS 67 R-EX

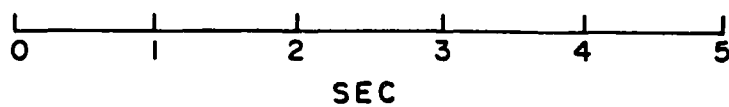
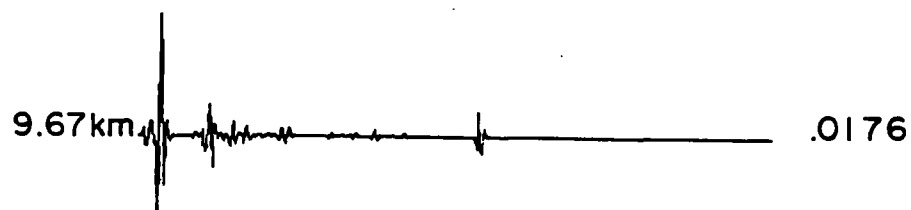
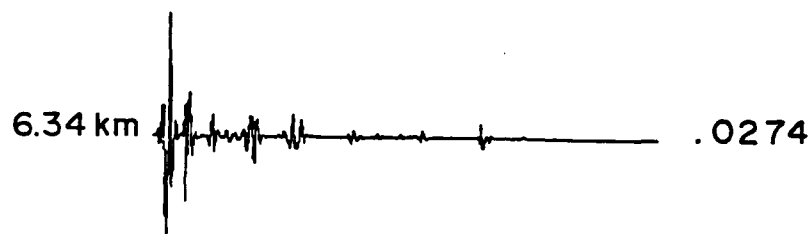


Figure 56

FARM NEWS 67 Z - EX

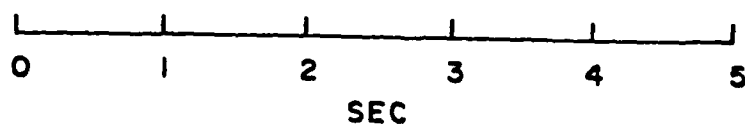
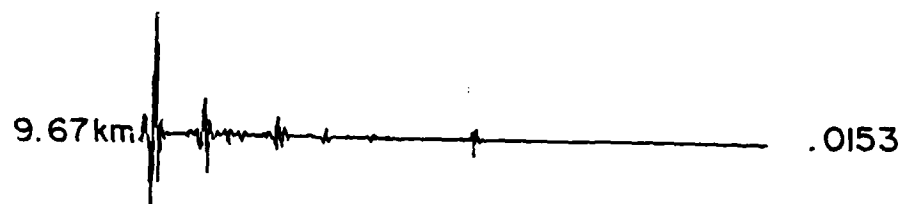
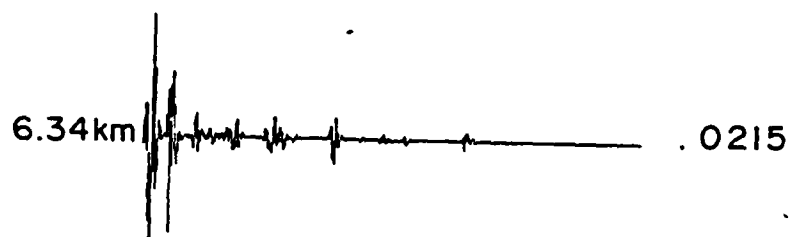


Figure 57

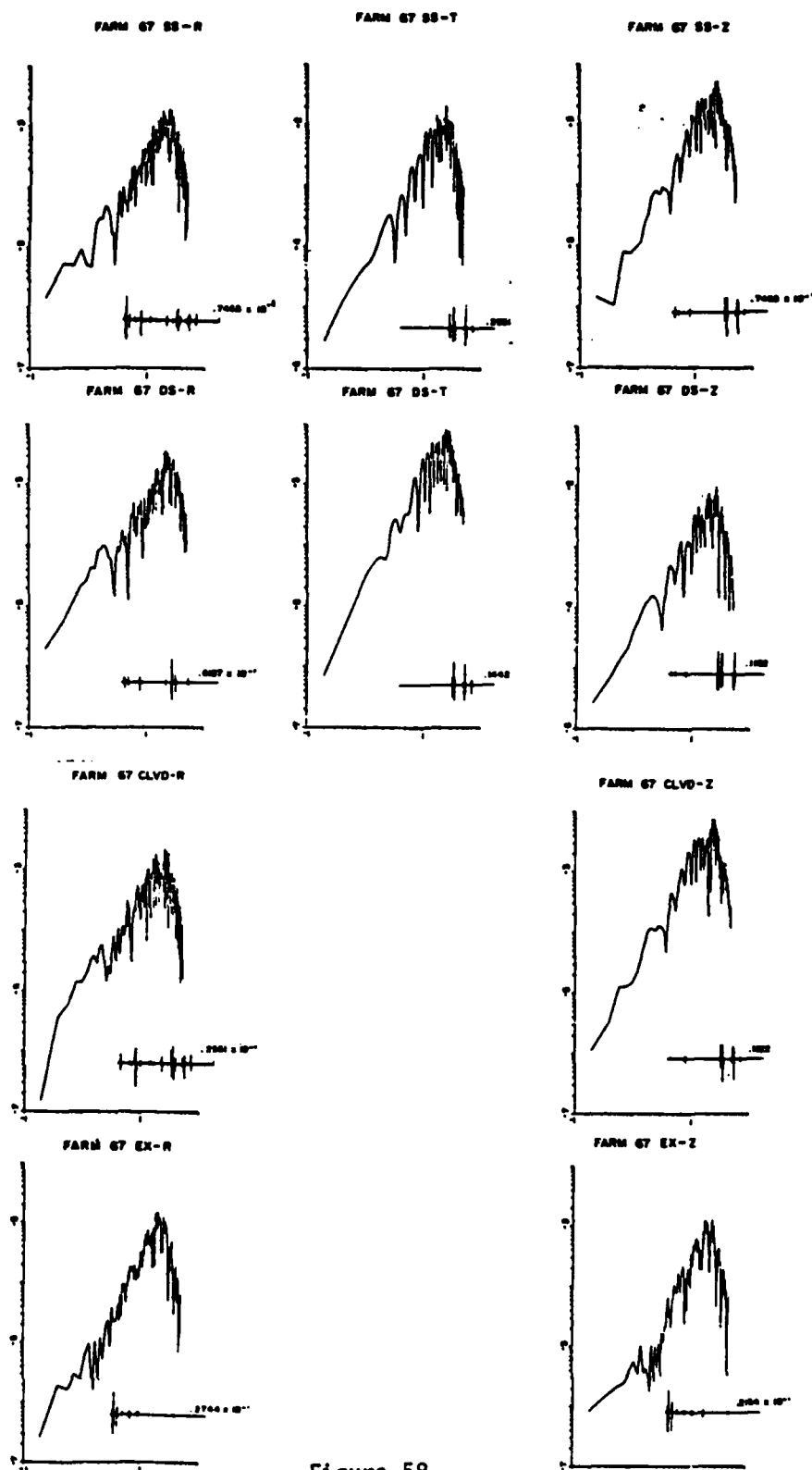


Figure 58

FARM OLDS R-EX

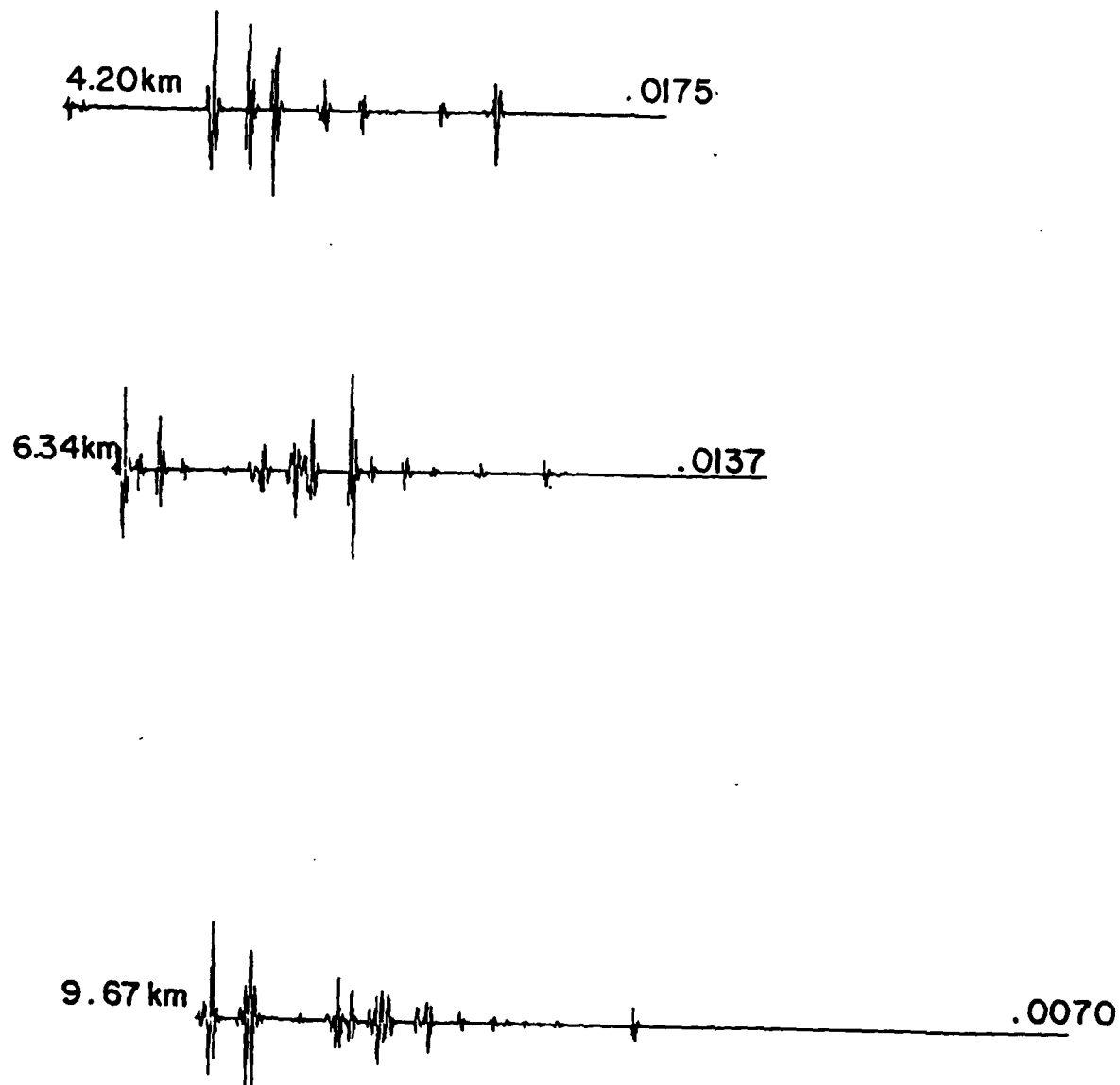


Figure 59

FARM OLDS Z-EX

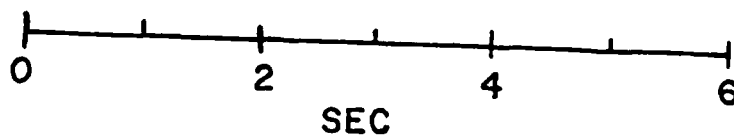
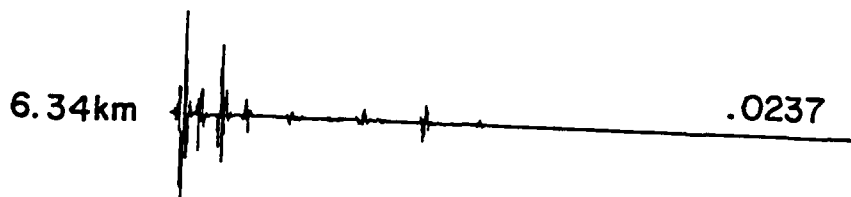


Figure 60

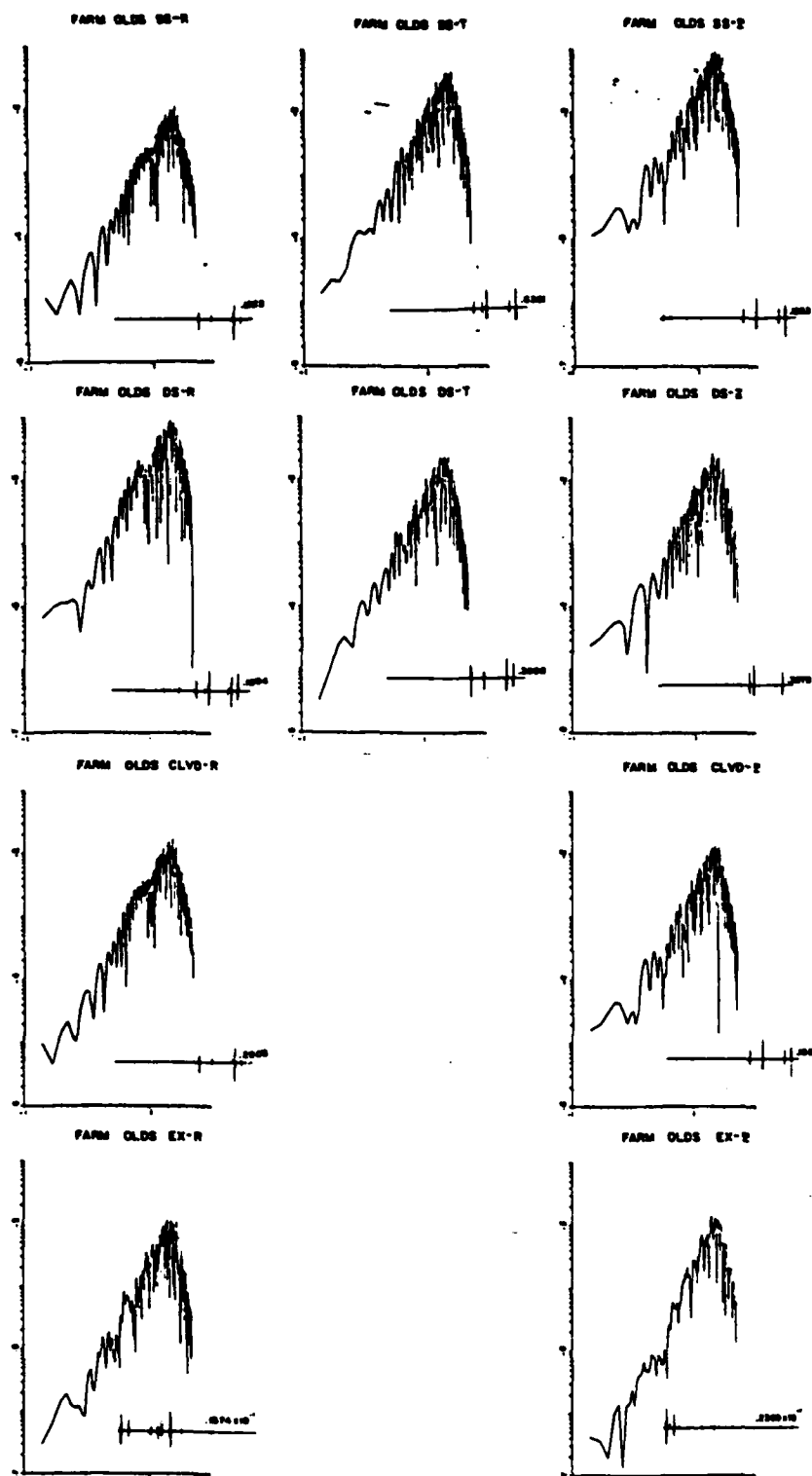


Figure 61

FARM HS R-EX

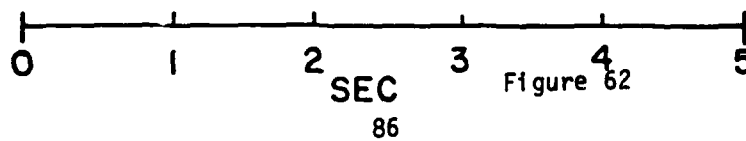
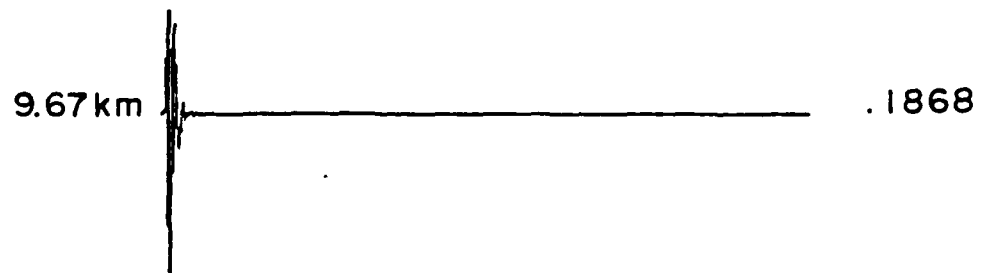
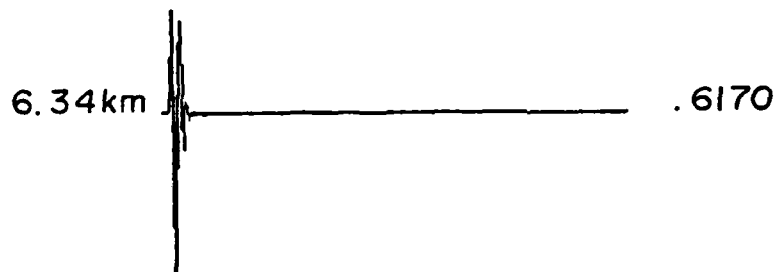
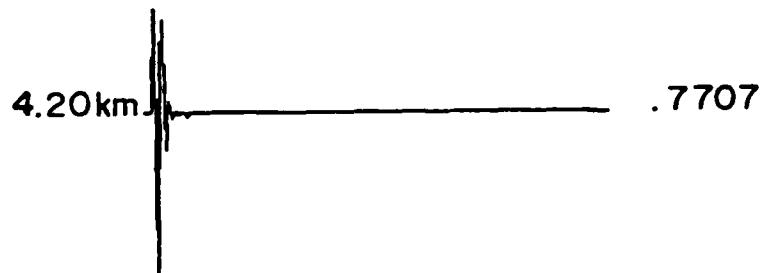
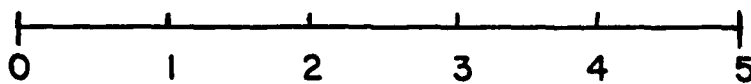
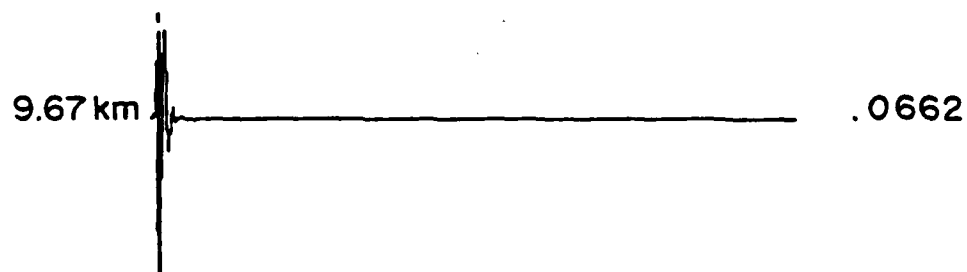
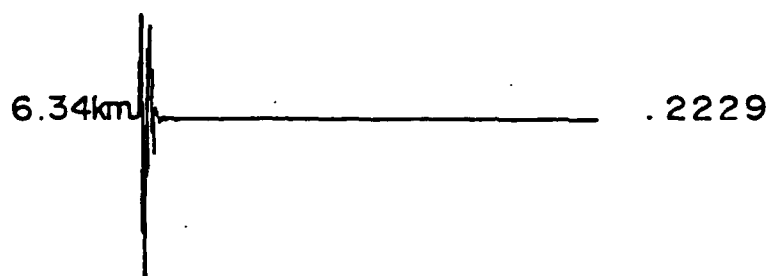
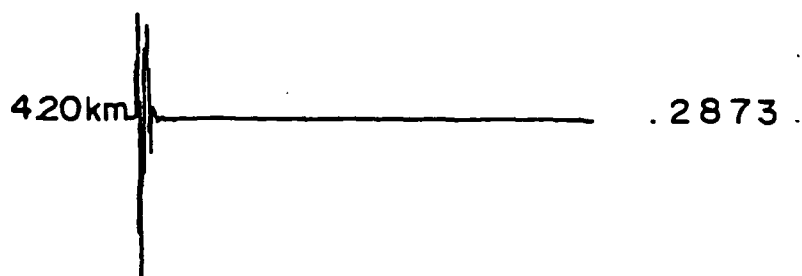


Figure 62

R

FARM HS Z-EX



SEC

Figure 63

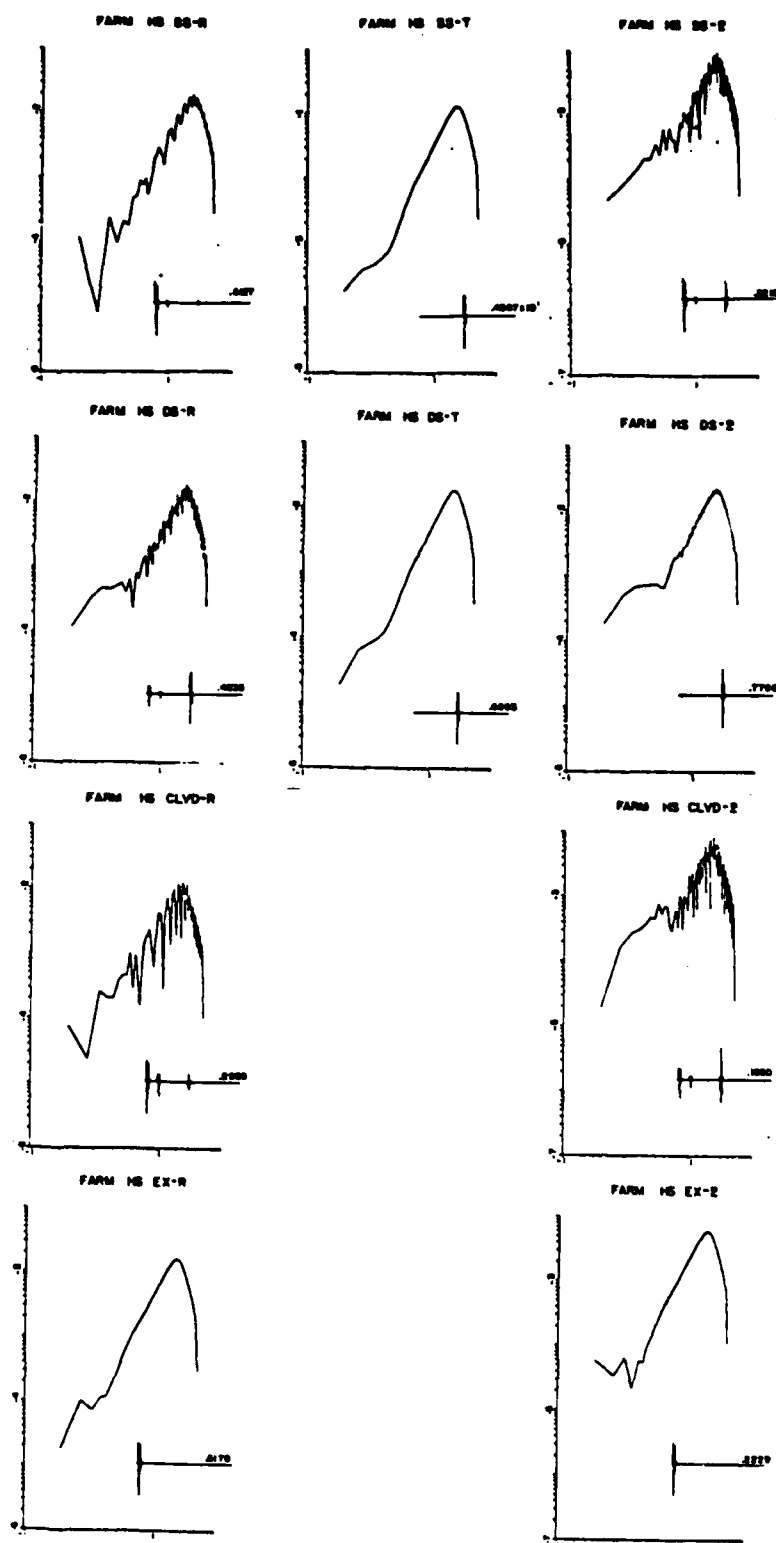


Figure 64

N

Q

PIP KIN

1.37

FARM

0.61

HAND.

0.34

0.46

540

0.34

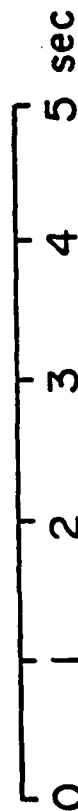
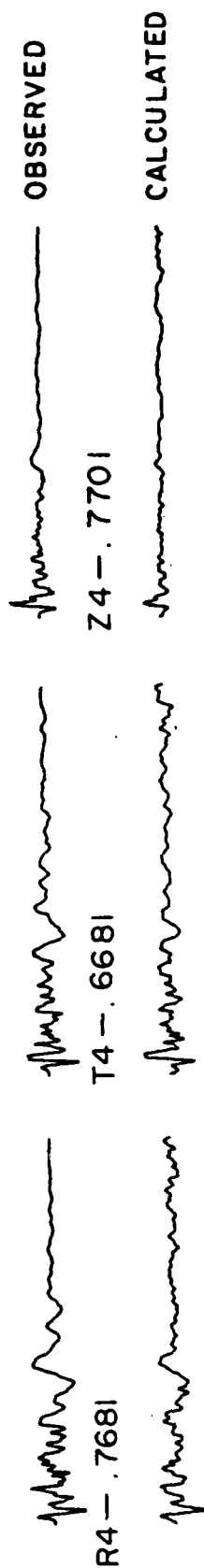


Figure 65

FARM FITS F-31 NEWS



90

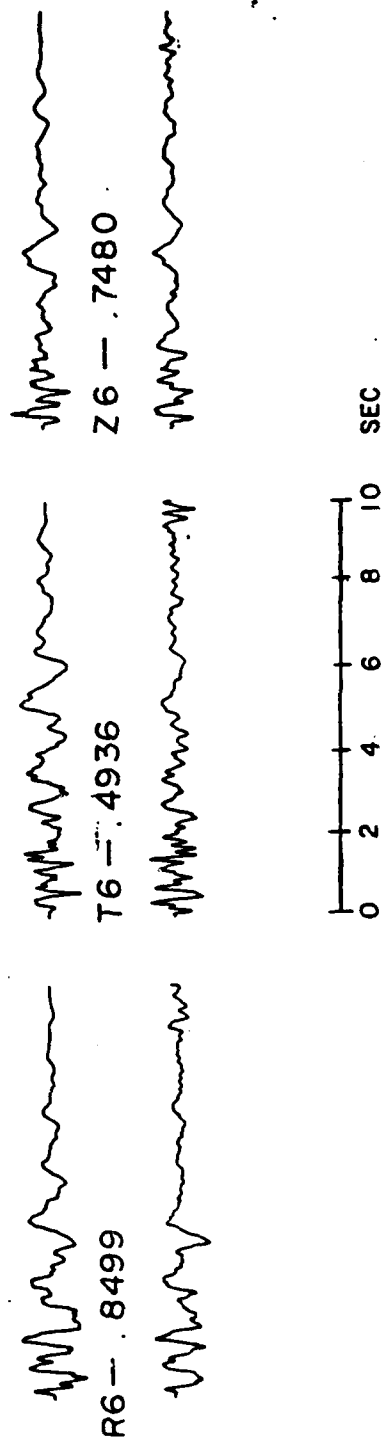


Figure 66

AD-A119 286

AIR FORCE WEAPONS LAB KIRTLAND AFB NM
EXPLOSION AND EARTHQUAKE SOURCE DISCRIMINATION.(U)
MAY 82 B W STUMP, R E. REINKE

F/G 18/3

AFOSR-PO-82-00004

UNCLASSIFIED

AFOSR-TR-82-0733

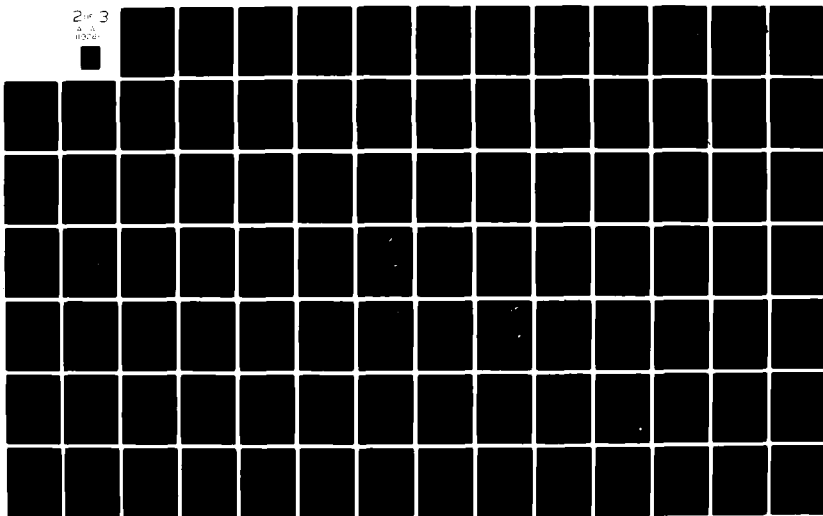
NL

2 of 3




3-1

W376

■



FARM FITS F31- NEWS








 R5 - .8075 T5 - .8680 Z5 - .8290 OBSERVED





 R5 - .8075 T5 - .8680 Z5 - .8290 CALCULATED

 R2 - .6117 T2 - .7161 Z2 - .6028





 R2 - .6117 T2 - .7161 Z2 - .6028



Figure 67

FARM MOMENT TENSORS F31 - NEWS

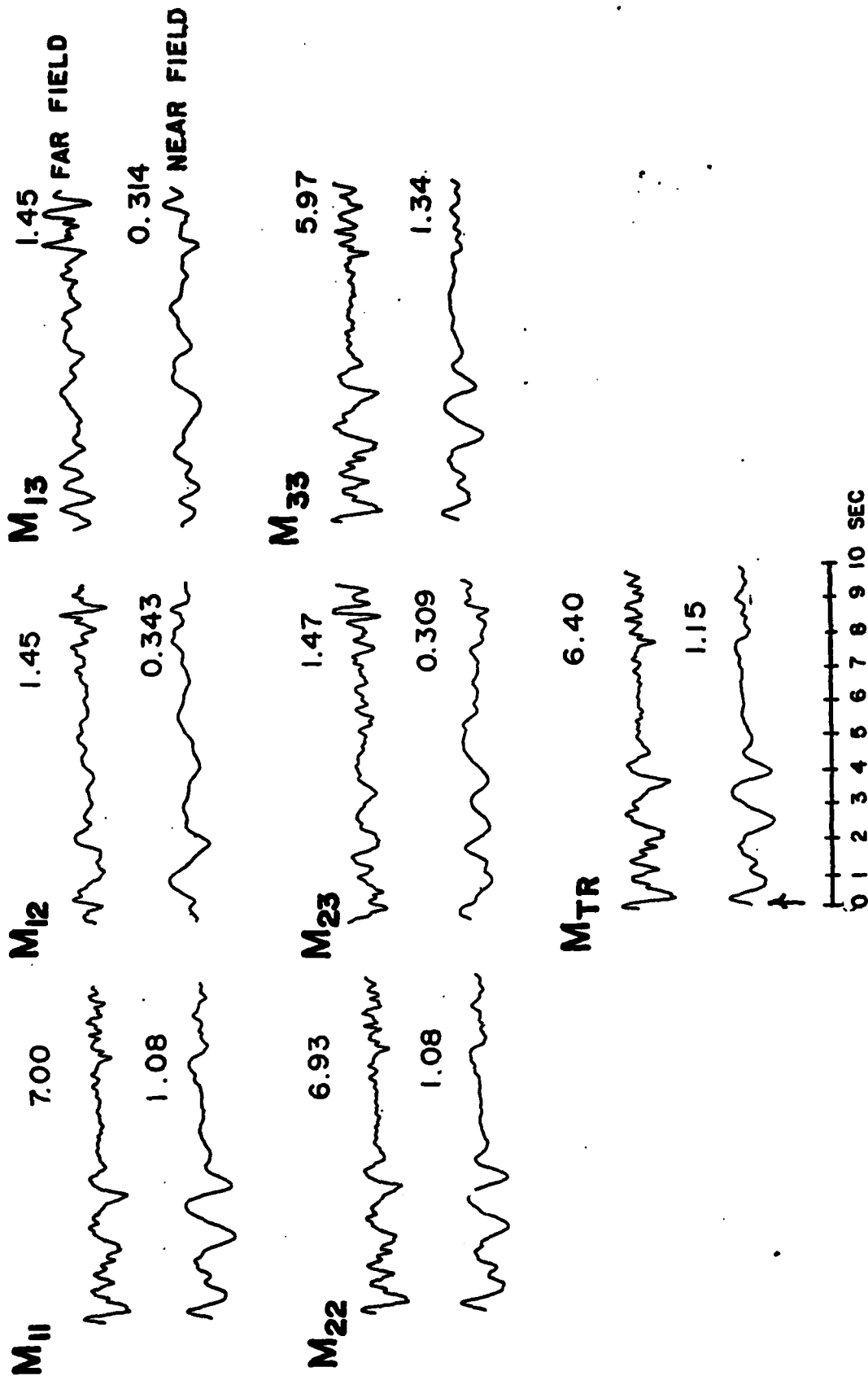
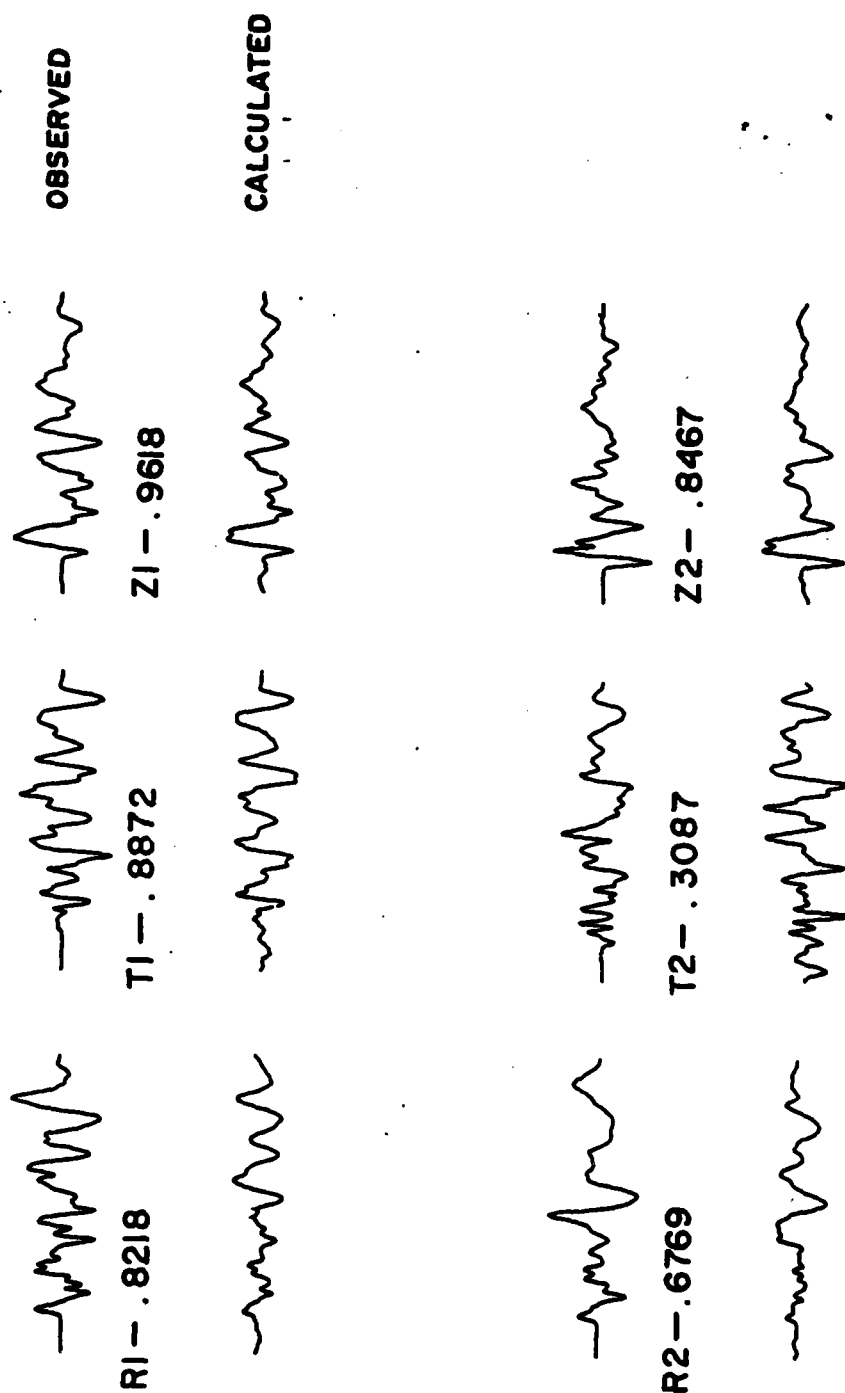


Figure 68

HANDLEY FITS H31 - NEWS



6 1 2 3 4 5 SEC

Figure 69

HANDLEY FITS H31 - NEWS

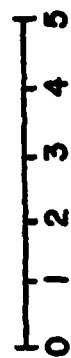
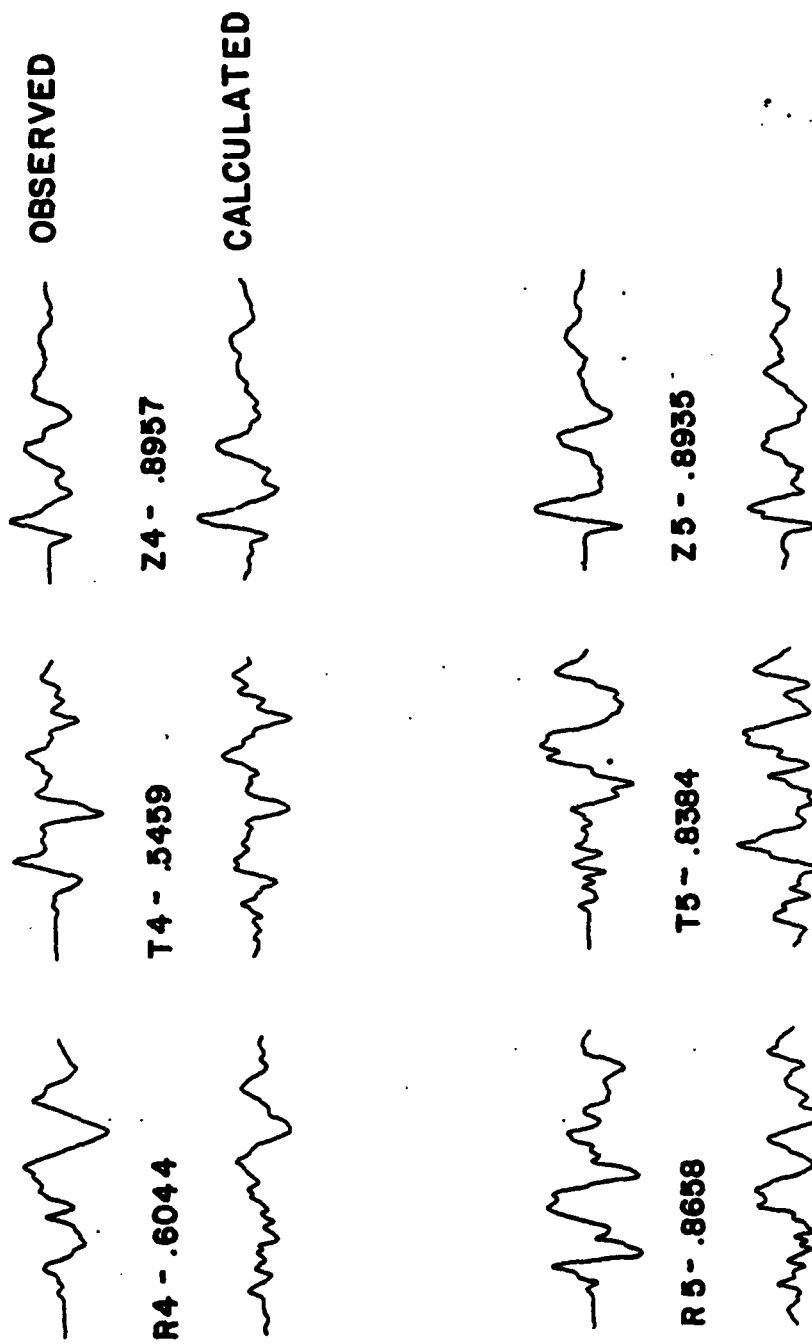
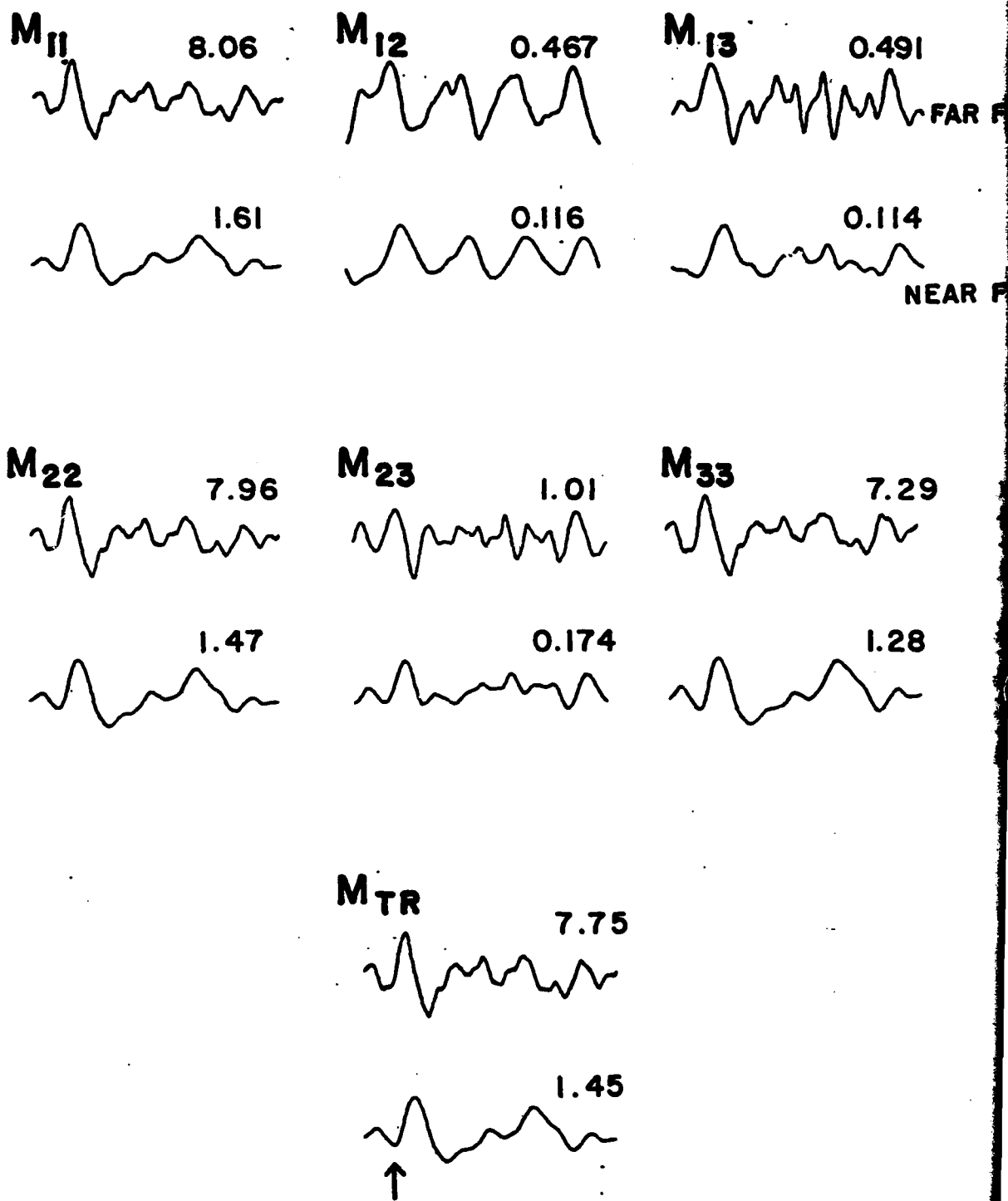


Figure 70

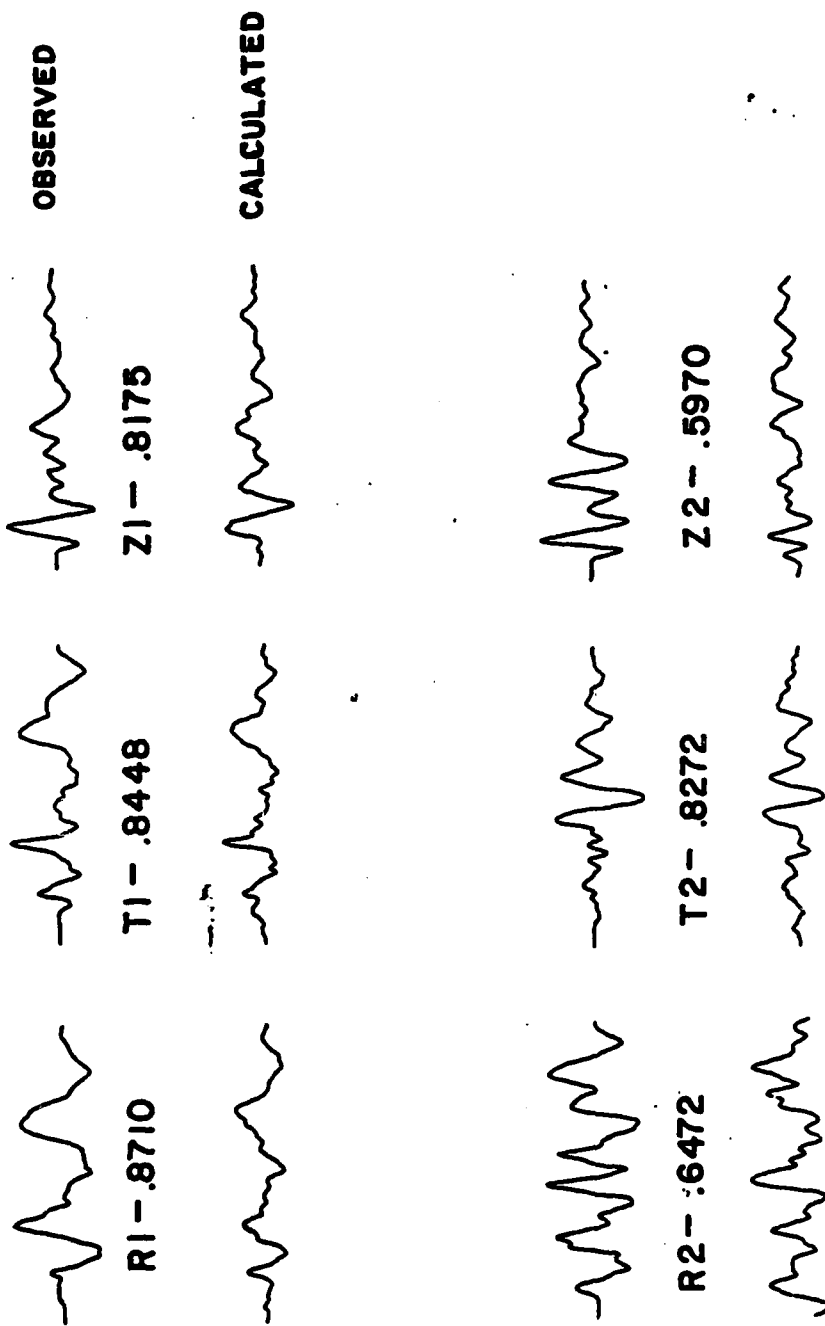
HANDLEY MOMENT TENSORS H31 - NEWS



0 1 2 3 4 5 sec
95

Figure 71

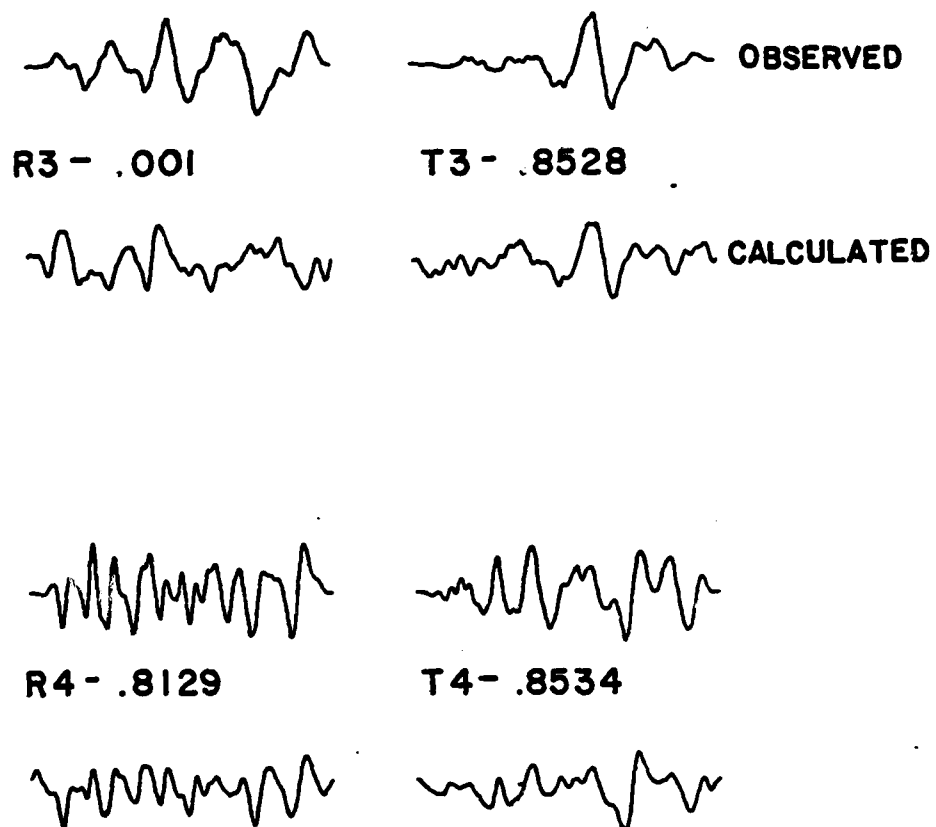
PIPKIN FITS P31 - NEWS



0 1 2 3 4 5

Figure 72

PIPKIN FITS P31 - NEWS



0 1 2 3 4 5 sec

Figure 73

PIPKIN FITS P31-NEWS

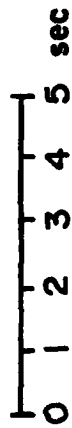
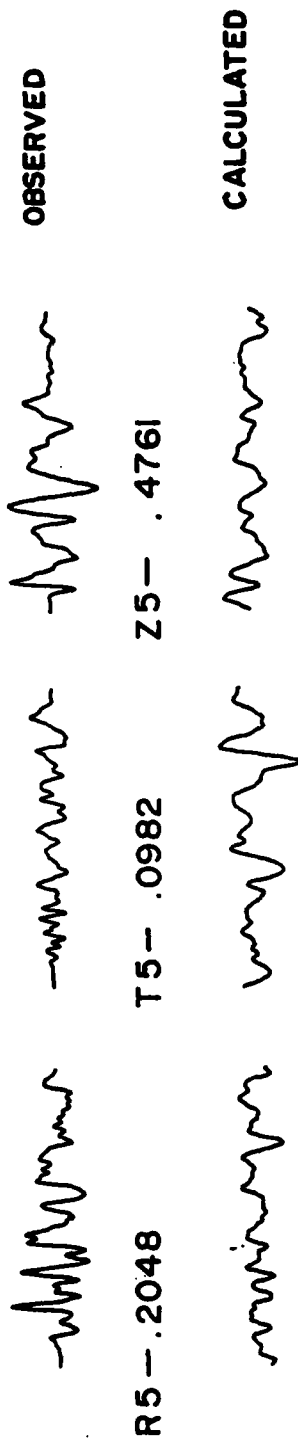


Figure 74

PIPKIN MOMENT TENSORS

P31 - NEWS

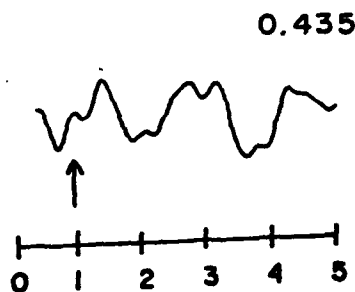
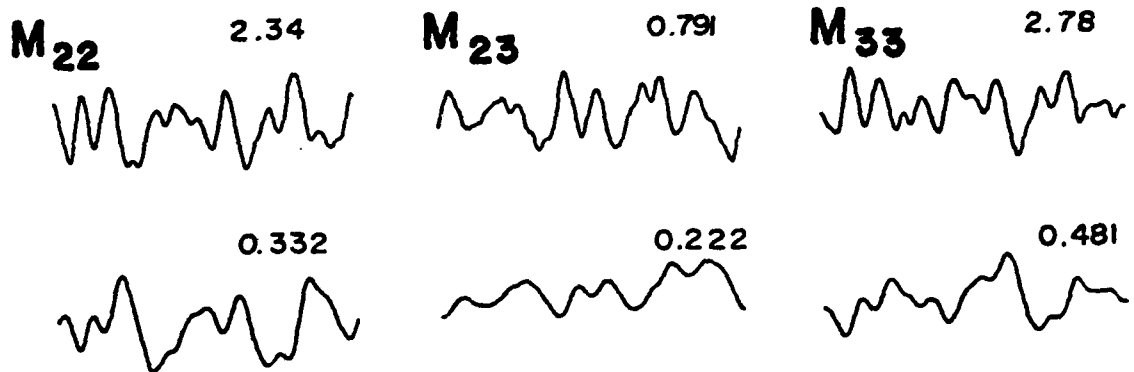
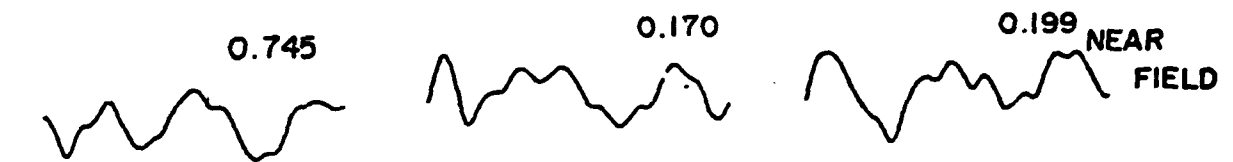
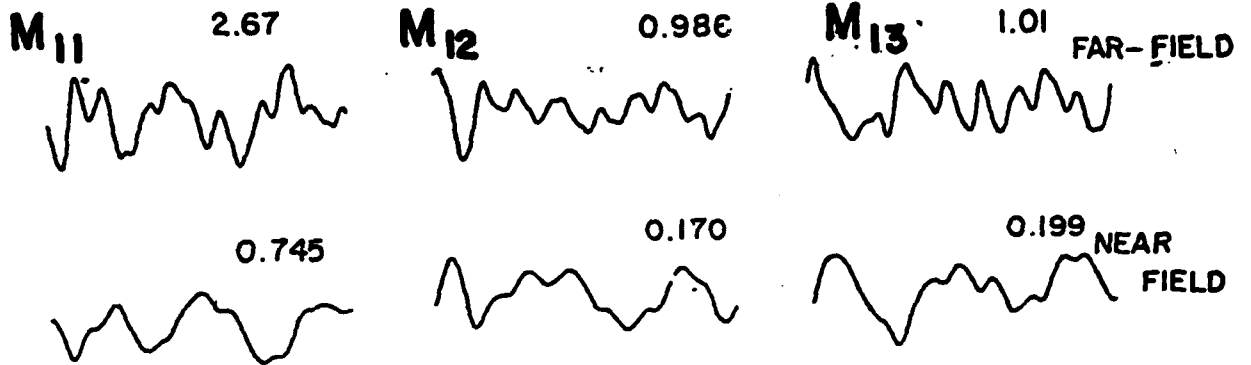


Figure 75

M_{TR} SOURCE FUNCTIONS

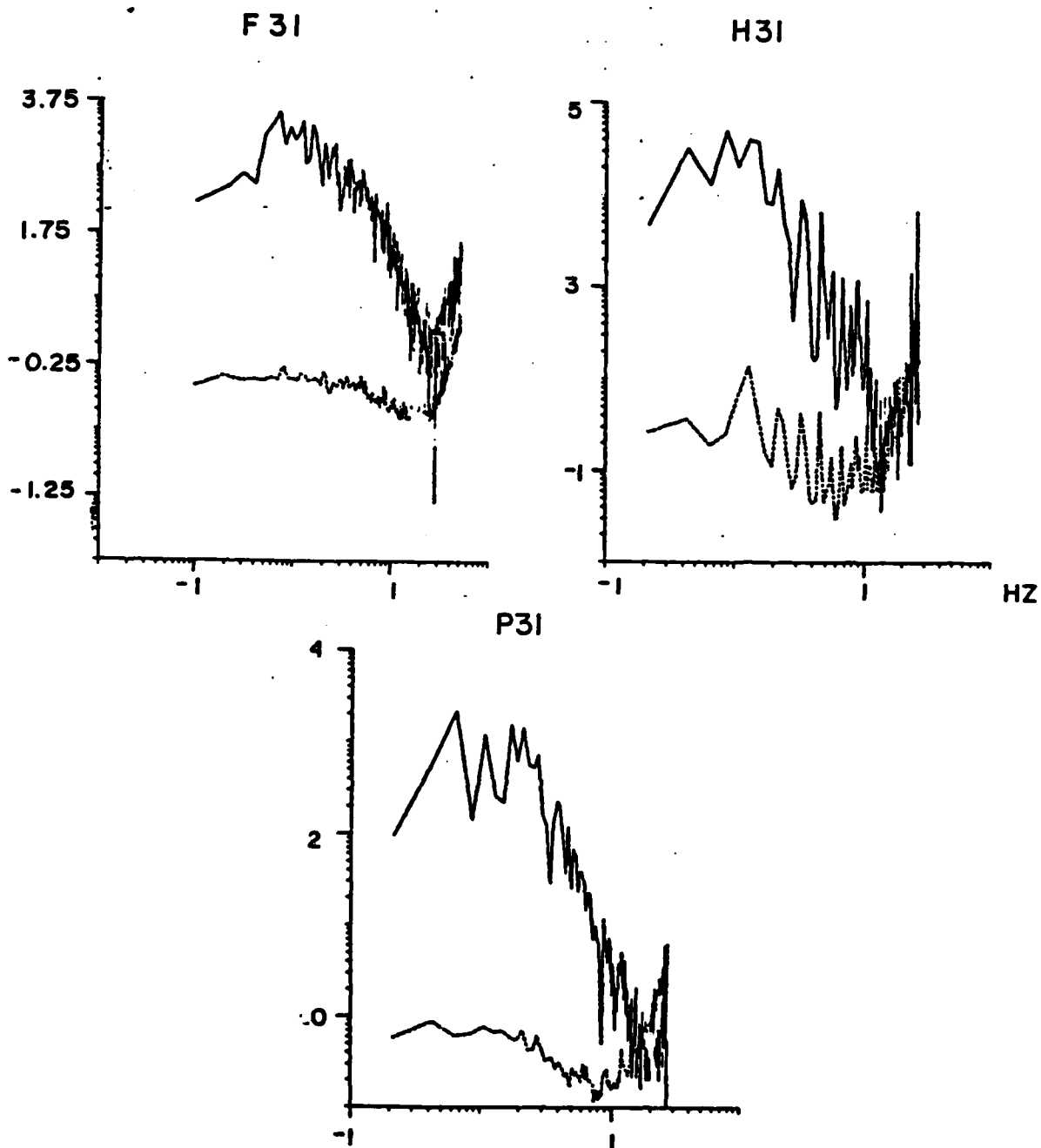


Figure 76

ISOTROPIC SOURCES

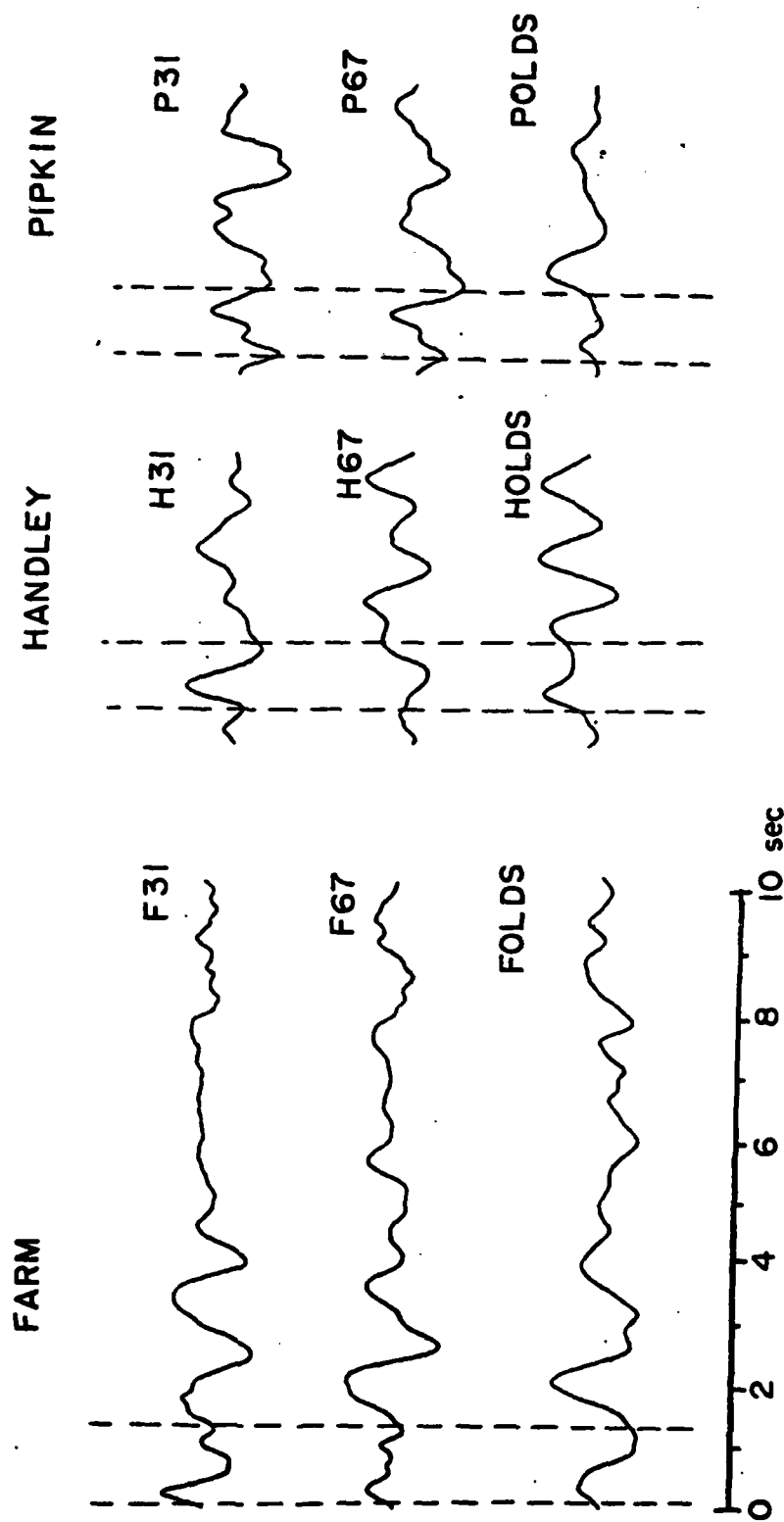
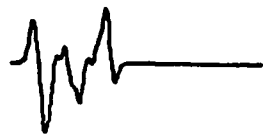
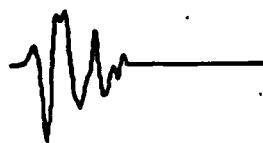


Figure 77

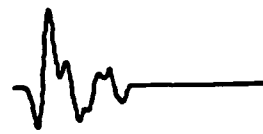
FARM FITS
F67 - P WAVES



R4 - .8924



T4 - .4686



Z4 - .8681



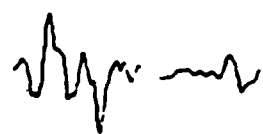
R6 - .9849



T6 - .3400



Z6 - .9129



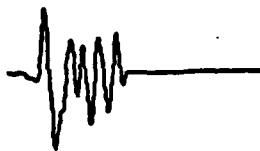
0 1 2 3 sec

Figure 78

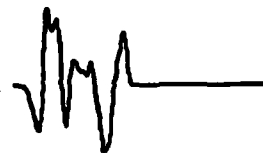
FARM FITS F67 - P WAVES



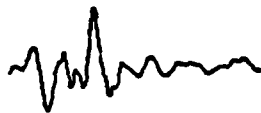
R5 - .9192



T5 - .0434



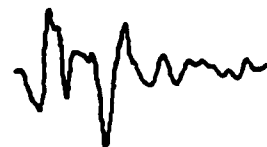
Z5 - .9457



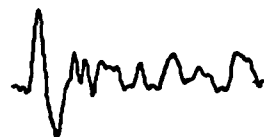
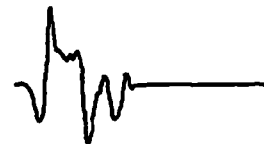
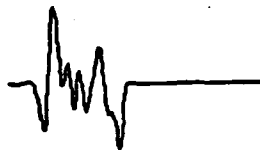
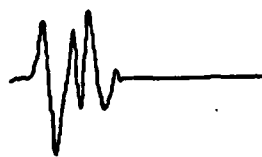
RZ - .4846



TZ - .0641



ZZ - .6563



0 1 2 3 sec

Figure 79

FARM MOMENT TENSOR

F67 - NEWS P WAVES

NEAR - FIELD

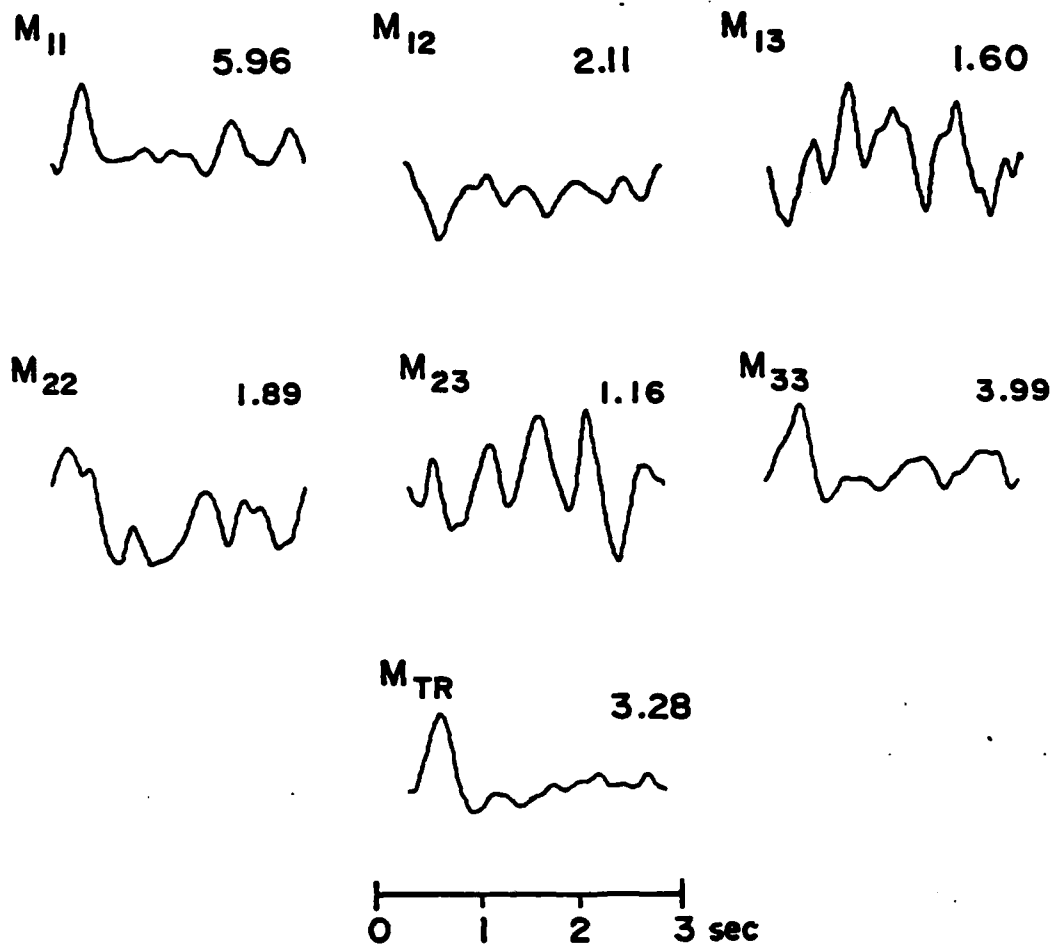


Figure 80

ISOTROPIC SOURCE: FARM P WAVES

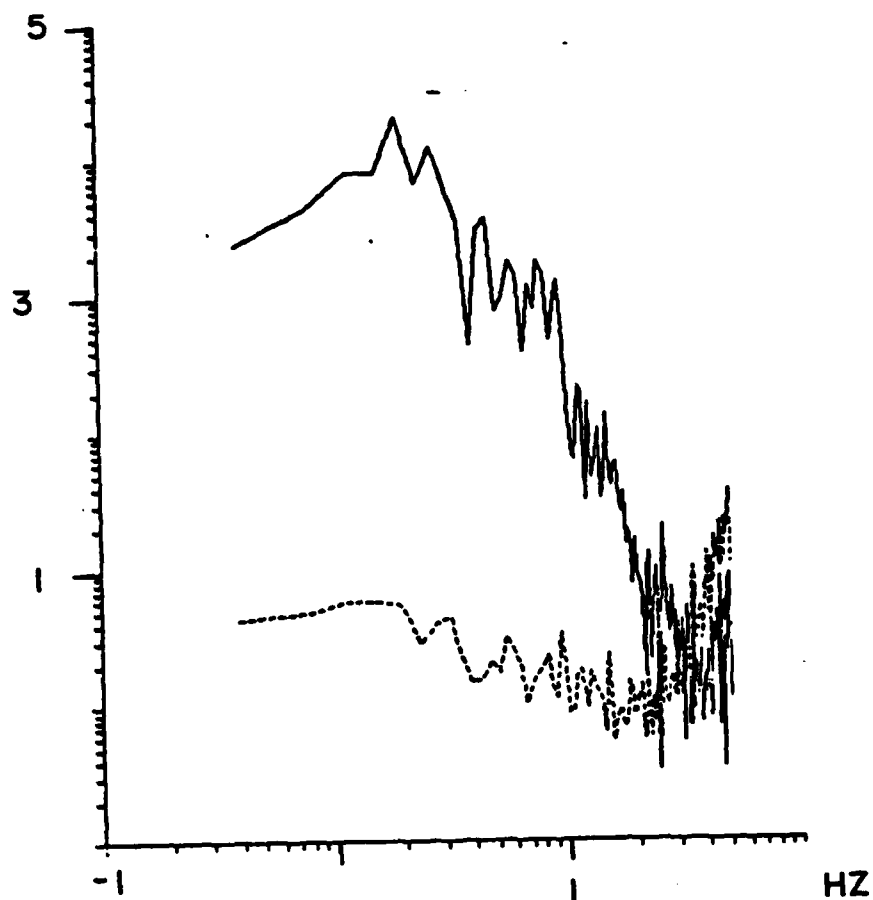


Figure 81

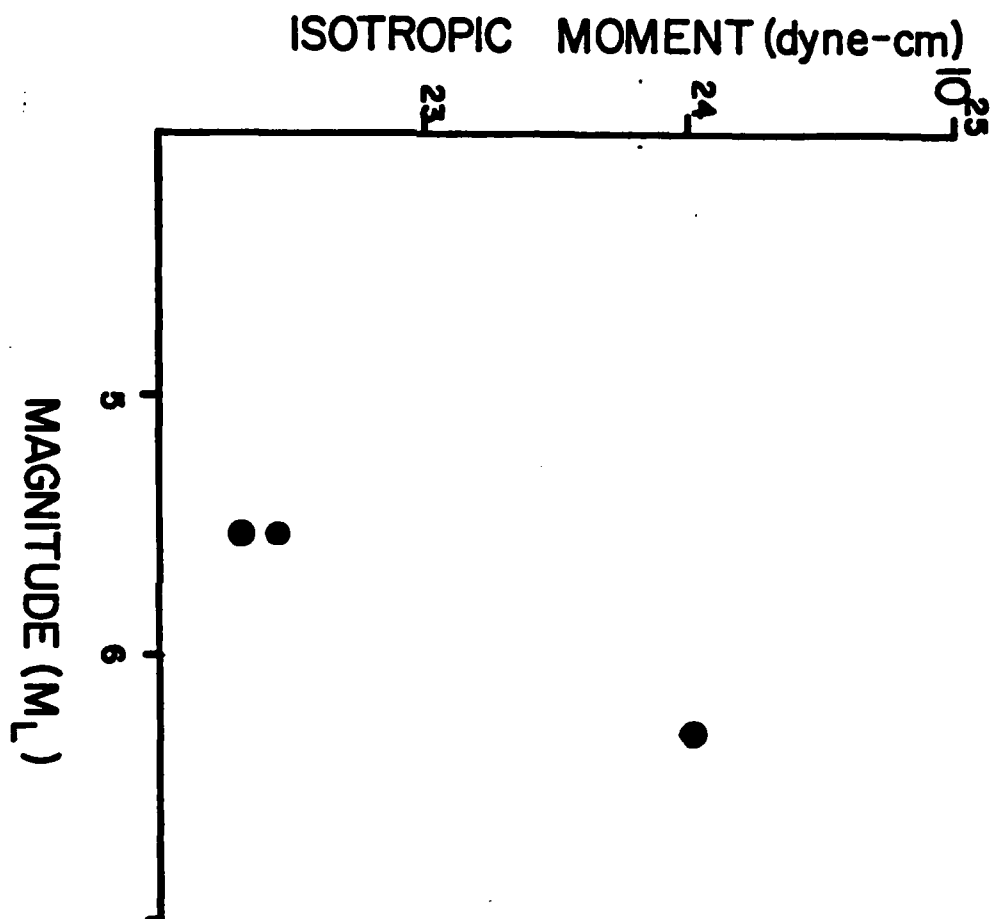


Figure 82

SOURCE CHARACTERIZATION
OF
BERMED SURFACE BURSTS

BRIAN W. STUMP
AFWL/NTES
Kirtland AFB, New Mexico 87117

ABSTRACT

A source characterization of bermed surface bursts utilizing a vertical and horizontal point source has been developed. This representation is formulated so that with analytic propagation path models and observational data inverse techniques can be applied and the source estimated. The inverse procedure is applied to the Pre-HYBRID GUST I-04, 05, and 06 data sets (13.6 kg for 04, 13.6 kg for 05, and 39 kg for 06 of sand bermed C-4). The method is able to model the observational data explaining the $R^{-1.6}$ decay of the radial velocity as nearfield body waves and the $R^{-.5}$ decay of the vertical velocity as Rayleigh waves. The radial source function is a factor of 2 larger than the vertical for all tests, indicating the dominance of the radial force in cratering. Source rise time correlates well with the time the sand berm contains the explosive products while pulse width may be driven by nonlinear processes, such as spall. The sources appear to cube root yield scale. Stresses predicted using the determined source functions indicate large vertical tensile stresses can develop from the Rayleigh wave.

INTRODUCTION

In an investigation of energy coupling from surface explosions, the Air Force Weapons Laboratory has detonated a number of single- and multiple-burst bermed explosions. The surface tangent explosives were covered with berms of sand to eliminate the airblast portion of loading, leaving only the energy directly coupled into the ground at the crater. Airblast measurements made during these tests indicate the berming procedure was successful.

It is this data set that shall be explored to help delineate the seismic source characterization that is appropriate for the cratering process. Much work has been done in characterizing contained explosions, attempting to separate source and propagation path effects (Haskell, 1967; McEvilly and Peppin, 1972; Mueller and Murphy, 1971; Werth and Herbst, 1963; Hadley and Helmberger, 1981; Stump and Johnson, 1977, 1981). Little attention has been paid to the case of surface bursts (Ewing and Press, 1951; Gupta and Kisslinger, 1966). For ground motion prediction purposes, the usual approach to the surface burst problem is to take the data of contained events, correct for the geometric effect of the free surface on the propagation path and then apply the results. No formal consideration is given to the change in source characterization as the explosion approaches the free surface. To first order, the contained explosion can be modeled as a spherical pressure pulse where the bermed surface source is modeled as a point force. Elastic responses for these two sources are quite different--the contained explosion being dominated by P waves, while the point force at the free surface is rich in shear and Rayleigh waves in the near field.

In this paper, observational data from these bermed surface sources are investigated taking into account the difference in source characterization

from contained and bermed surface explosions. Attempts to fit the observational data allows the refinement of the surface source model.

Finally, this study should shed some light on spall mechanisms. Spall, as indicated by -1g dwells on vertical accelerometers followed by impulsive rejoins on the vertical and radial accelerations, were observed on all the bermed surface explosions (Stump and Reinke, 1982). Since the source is at the free surface, the spall or tensile failure of the material cannot be explained in terms of a compressional wave leaving the source, traveling to the free surface, and reflecting as a tensile wave (Eisler and Chilton, 1964). Both the source characterization and the propagation path effects must be well accounted for in order to adequately propose a mechanism for tensile failure.

SOURCE REPRESENTATION

Assuming a source can be represented as either a body force, initial condition, or boundary condition then a general representation can be written as:

$$U_k(x', t') = \int_{-\infty}^{\infty} \int_{V_0} G_{ki}(x', t'; x, t) f_i(x, t) dx^3 dt \quad (1)$$

$U_k(x', t')$ is the ground motion in the k direction at (x', t') , V_0 is the source volume, $G_{ki}(x', t'; x, t)$ is the displacement in the k direction at (x', t') due to a delta function force in the i direction at (x, t) , and f_i is the equivalent body force in the i direction at (x, t) . The summation convention is assumed.

In the case of a contained explosion, assuming the wavelengths of interest are long compared to the characteristic source length, equation (1) becomes:

$$U_k(x', t') = \int_{-\infty}^{\infty} (G_{kij}(x', t'; Q, t) M_{ij}(t)) dt$$

$$M_{ij}(t) = \int_{V_0} x_j f_i(x, t) dx^3 \quad (2)$$

Assuming a buried surface source can be modeled as a vertical and horizontal point force, then the representation becomes:

$$U_k(x', t') = \int_{-\infty}^{\infty} (G_{k1}(x', t'; Q, t) f_1(Q, t) + G_{k3}(x', t'; Q, t) f_3(Q, t)) dt \quad (3)$$

The 1 direction has been chosen radial away from the source and 3 direction is positive down.

Transforming equations (2) and (3) into the frequency domain eliminates the time integral and allows one to write:

$$U = GF \quad (4)$$

U is the observed ground motion, G is the propagation path effect, and F is the source characterization. For the surface source, F consists of two terms,

one for the vertical and one for the horizontal force. In the case of the buried explosion, F consists of six unique terms.

Equation 4 is written for each frequency so that if there are 256 initial time points, then the equation is written 128 times (real and imaginary) for each frequency point. For each frequency, the U matrix is made up of the real and imaginary components of the Fourier transformed ground motion data and is $2n \times 1$ in dimension (where n is the number of individual observations); the G matrix is composed of the real and imaginary parts of the Fourier transformed Green's functions and is $2n \times 4$ in dimension; and the F matrix is 4×1 and consists of the real and imaginary parts of F_1 and F_3 (equation 3).

In the study, U are the observed velocities in the frequency domain from the PHG tests and G the propagation path effects determined analytically for an elastic half-space. The only unknowns are F , the source characterization. Calculating the inverse of the matrix G and multiplying it by U allows one to determine F .

$$F = G^{-1}U \quad (5)$$

The problem is underdetermined when there are less than two seismograms, exact when there are two seismograms, and may be overdetermined when there are more than two observations. The inversions in this study will use a maximum of ten seismograms and a minimum of six.

In solving Equation 4 and writing Equation 5, singular value decomposition of G is used and a generalized inverse is calculated (Lanczos, 1961). G is decomposed as:

$$G = WQV^T \quad (6)$$

Where W is a $2n \times p$ semi-orthogonal matrix consisting of the eigenvectors associated with the nonzero eigenvalues of GG^T , V is the $2 \times p$ semiorthogonal matrix consisting of similar eigenvectors of G^TG , and Q is a $p \times p$ matrix whose

diagonal members are the positive square roots of the largest p nonzero eigenvalues of $G^T G$.

The generalized inverse of G becomes:

$$G^{-1} = VQ^{-1}W^T \quad (7)$$

This formulation always exists, since Q^{-1} can always be calculated with (eigenvalues of $G^T G$)⁻¹ down the matrix diagonal. For the case when p is less than the dimension of $G^T G$, the inverse ignores the eigenvectors associated with the zero eigenvalues and thus may not give a unique solution to the problem. The inverse is unable to resolve the solution in the directions of the eigenvectors associated with the zero eigenvalues. The resolution matrix can be calculated as $G^{-1}G = WV^T$. The eigenvalues and eigenvectors of this matrix tell one if the problem is well enough posed to allow the unique recovery of the source characterization.

Once F has been determined using Equation 5, predicted ground motions (acceleration, velocity, displacement) can be estimated by substituting F into Equation 3 with the appropriate Green's functions. The stress tensor can then be calculated as follows:

$$\sigma_{ij}(x',t) = \int_{-\infty}^{\infty} \left\{ \lambda G_{k_1,k}(x',t';Q,t) \delta_{ij} + \mu (G_{i,j}(x',t';Q,t) + G_{j,i}(x',t';Q,t)) \right\} \quad (8) \\ f_1(Q,t) + \left\{ \lambda G_{k_3,k}(x',t';Q,t) \delta_{ij} + \mu (G_{i,j}(x',t';Q,t) + G_{j,i}(x',t';Q,t)) \right\} f_3(Q,t) \right] dt$$

It should be emphasized that once F has been determined from Equation 5 the stresses and motions can be predicted anywhere in the material using Equations 8 and 3.

GREEN'S FUNCTIONS

The propagation path effects in this study are modeled, as an elastic half-space. The motivation for this choice is threefold: (1) The radial and vertical velocity waveforms from all of the explosions show relatively simple waveforms with the radial component of motion dominated by body waves and the vertical component primarily surface waves (Figure 1), (2) the body wave decay rate of $R^{-1.6}$ indicates the strong influence of near-field components of motion, and (3) the half-space Green's functions allow the analytic calculation of the resulting stress tensor. The half-space model is further supported by geophysical work (Stump and Reinke, 1982) and the first arrival time data at the test site. There is a hint in the data of the presence of a layer over a half-space structure. The first arrival time data indicate a possible break over point at about 10 m while the first motion of the vertical motion is up. This motion is small compared to the predominantly radial body waves at these distances. Our philosophy is to accept the simplest propagation and source model that explains the observational data base.

The wave front diagram for a surface source and buried receiver in an elastic half-space is given in Figure 3. The first arrival is primarily a radial P wave. The second arrival is diffracted PS. This wave leaves the source as a P wave traveling along the free surface and then refracts into the material as an S wave to the receiver. Following these arrivals are the shear and Rayleigh waves.

The Green's functions for a surface point force source and a buried receiver are given in Figure 4. In this model, the P wave velocity is 366 m/sec with a Poisson's ratio of 0.10. The seismic velocities were determined from refraction studies in the area (Stump and Reinke 1982). The delta function displacement responses for a radial (f_1), transverse (f_2), and vertical

(f_3) point force source are illustrated. The P, diffracted PS, S, and Rayleigh arrivals are noted. It is the Green's functions due to f_1 and f_3 which will be substituted into G of Equation 4 for determination of F.

The effect of reducing the shear wave velocity while holding the P wave velocity constant is given in Figure 5. These Green's functions are the radial and vertical displacements due to a radial force localized in space and time. As the shear wave velocity increases, the amplitude of the shear and Rayleigh waves increases. At large Poisson's ratio, an additional arrival, the so-called Leaking mode \bar{P} , is seen on the radial motion between the P and S wave. This phenomena was discussed by Gilbert and Knopoff (1961), Gilbert, et al. (1962), and Chapman (1972). For a complete discussion of this arrival in the context of both motion and stress calculations, see Stump (1982). Inversions utilizing Green's functions with Poisson's ratios 0.10 to 0.45 will be accomplished to investigate the trade-off between the source and propagation effects.

DATA ANALYSIS

The focus of the source characterization in this study was a series of bermed explosions. The test series, known as Pre-HYBRID GUST (PHG), contained three bermed sources. These sources, PHGI-04, PHGI-05, and PHGI-06, consisted of 13.6 kg, 13.6 kg, and 39 kg of C-4 explosive under a sand berm. Figure 6 summarizes the explosive sources and sand berm size which changed with experiment.

The three sources were instrumented with radial and vertical accelerometers in the 3 to 36 m range. The data was recorded analog on high speed FM tapes. These records were then digitized at 2,000 samples per second with an antialias filter at 400 hz (5 Pole Butterworth filter). Figure 7 illustrates a sample spectra (solid line) and noise estimate (dotted line) for the radial gage at 6.55 m from PHGI-06. Good signal to noise ratios were found out to 400 hz. Both the acceleration and integrated velocity records are given. In the inversions, the velocity data is used with a correction for a ramp. This record is characteristic of data quality for all experiments.

1. PHGI-06

The first data set to which the inversion scheme was applied was PHGI-06. This experiment was the biggest of the three studied and consisted of 39 kg of the explosive C-4. Vertical and radial data at the 6.55, 8.50, 10.85, 14.60, and 18.35-meter ranges (1.50 m depth) were used. The instrumental array and data characteristics are summarized in Figure 8. Prior to the inversion and after antialias filtering, the velocity data was decimated to 1,000 samples per second.

All ten components of data were used in the inversion to determine the two equivalent body forces f_1 and f_3 . Both the data and the half-space Green's functions were Fourier transformed prior to substitution into Equation 4. The

U matrix for each frequency became 20×1 , while the G matrix was 20×4 . Since 256 msec of data was analyzed, the 20×4 G matrix was inverted 128 times.

After f_1 and f_3 were determined using Equation 5, F and G were substituted back into Equation 4 to yield a predicted U for comparison to the observational data. The similarity of the observed U to the calculated U is a measure of the adequacy of the source model and inversion. A summary of peak velocity amplitudes in the observed and calculated waveforms is given in Figure 9. The radial data and fits decay as $R^{-1.6}$, while the verticals decay as $R^{-0.5}$. The vertical data are particularly well matched, while errors as large as a factor of two can be seen in the radials. Taking the data set as a whole, both the radial and vertical peaks are well fit.

Now focusing on the entire wave train, the observational and predicted waveforms from the inversions are illustrated in Figures 10, 11, and 12. In each plot, the observed and calculated waveforms are plotted to the same scales. The absolute scale for each plot may change from gage to gage with the peak velocity for each gage indicated in plots. A total of 256 msec of data were fit and plotted. The sign convention for the data is positive radial away and vertical down. The fits of the observational waveforms are well explained by the source model. The mean correlation coefficient between the observed and calculated velocities is 0.84. The radial components of velocity are dominated by the near field body wave yielding the $R^{-1.6}$ spatial decay. The vertical component of velocity is explained by the Rayleigh wave arrival giving $R^{-0.5}$ decay. The most glaring deficiency in the fits is the inability to model the small initial upward pulse on the vertical component of motion.

As Figure 9 illustrates, the radial component of velocity is largest at distances less than 7 m with the vertical component larger at greater distances. There is some hint at a change in decay rate for the radial motion at approximately 18 m. At this distance, the Rayleigh wave on the radial component is approaching the same size as the body wave. One can hypothesize that at ranges greater than 18 m the Rayleigh wave will dominate the radial motion, and spatial decay will be close to $R^{-.5}$.

The source time functions and their integrals for the radial (f_1) and vertical (f_3) point forces determined from the PHGI-06 inversions are given in Figure 13. As indicated by the relative source strengths, the radial force is a factor of two greater than the vertical. The net impulse of the sources is down and away from ground zero. There is some problem with causality in the smaller vertical time function.

In the time domain, the source rise time is 18 msec with a pulse width of 70 msec. Ake (1980) in an analysis of the PHGI-06 films determined the time to venting of the berm to be 17 msec. Figure 15 illustrates the berm growth as a function of time with the explosive by products breaking out of the berm at 17 msec. It appears that the source rise time is controlled by the time that the sand berm contains the explosion.

The corresponding source spectra are given in Figure 14. The factor of two difference in source strength between f_1 and f_3 can be seen in the spectra. The corner between 10 and 20 hz is representative of the pulse width observed in the data. The high frequency roll-off of the source indicates a slope of between 2 and 3.

The least known parameter in the inversion scheme is the shear wave velocity of the test bed. In the initial inversions, a Poisson's ratio of 0.10

was assumed. To investigate the stability of the inversion procedure and the effect of varying the shear wave velocity, two additional runs were made with Poisson's ratios of 0.25 and 0.40. The effect of varying Poisson's ratio on the Green's functions was shown in Figure 5. Not only does the P to Rayleigh wave amplitude decrease as Poisson's ratio increases, but the characteristic frequency of the whole waveform also decreases. The relative sizes of f_1 and f_3 for the inversions using the three sets of Green's functions are given in Figure 16. The two to one ratio of f_1 to f_3 remains the same for all inversions. The relative source strength changed by a factor of three when Poisson's ratio changed from 0.10 to 0.25. This change was only a 20 percent variation in shear wave velocity. Source coupling for this characterization is a strong function of Poisson's ratio. The time functions of f_1 and f_3 for the three Poisson's ratios are given in Figures 17 and 18. Since the Green's functions decrease in frequency as Poisson's ratio increases, the resulting source time functions increase in frequency. The effect of the changing Green's functions on the fits to the observational data is summarized for the vertical velocity at 10.85 m in Figure 19. The fits for Poisson's ratio of 0.10 and 0.25 are indistinguishable, while the fit for 0.40 is greatly degraded. Using the fits as a guide to the adequacy of the model, one cannot distinguish between a Poisson's ratio of 0.10 and 0.25. This conclusion leaves a relative error in source coupling of 3. It is felt that the 20 percent change in shear wave velocity encompassed by these models is difficult to resolve through geophysical exploration techniques.

2. PHGI-05

The second data set to which the source characterization scheme was applied was PHGI-05 (Figure 6). This experiment was identical to PHGI-06, except the yield was reduced from 39 kg to 13.6 kg of C-4.

The instrumentation was somewhat more scarce in this test, so only three gage locations were used in the inversion--6.55, 8.50, and 18.35 meters (Figure 20). The data analysis was conducted with Green's functions for a Poisson's ratio of 0.10. This final propagation path model was chosen because of its agreement with geophysical exploration work at the test site and the success of fits to the PHGI-06 data. As the Poisson's ratio tests on the PHGI-06 data show, Poisson's ratio can go as high as 0.25.

Using the same format as in the PHGI-06 analysis, the observed and calculated seismograms are given in Figures 21 and 22. As in the previous results, the fits are quite good.

The source functions and their spectra are in Figures 23 and 24 respectively. The rise time of the source is again 18 msec which compares to Ake's (1980) observation of berm venting at 19.5 msec (Figure 25). The 2.5 msec difference in vent time between PHGI-05 and PHGI-06 is too small to resolve by this procedure. The pulse width of the source is approximately 64 msec, slightly smaller than the 70 msec observed in PHGI-06.

Since the berm size for PHGI-05 and PHGI-06 is similar, one can begin to study the effect of source yield on coupling. Comparison of inversions utilizing Poisson's ratio of 0.10 is made in Figure 26. The dotted line in the figure is that predicted by cube root yield scaling. The limited source strength data fall close to this line.

3. PHGI-04

The final data set analyzed in this study was PHGI-04 (Figure 6). The experiment was identical to PHGI-05, but the berm was reduced in height and width by 20 percent. Again, three gage locations at 6.55, 8.5 and 18.35 meters were used in the inversion (radial and vertical velocity at each location). As in the PHGI-05 inversion, the Green's functions were for a

Poisson's ratio of 0.10.

The observed and calculated seismograms are given in Figures 27 and 28. As in the other tests, the fits are good. The source time functions and their spectra are given in Figures 29 and 30 respectively. From the films, Figure 31, the time to venting was 12.5 msec (Ake, 1980). This time compares to 11-12 msec rise time on the source function. As in the previous inversions, the f_1 to f_3 ratio remained approximately 2.

STRESS PREDICTIONS

Using the sources determined from the observations, one can predict the stress tensor by plugging $f_1(t)$ and $f_3(t)$ into Equation 8. One can then predict the stresses anywhere within the test bed (Stump, 1981).

Using the source from PHGI-06 inversions, the stress tensor at a distance of 10.85 m and a depth of 1.37 m were predicted (Figure 32). In these plots, down is compression and up is tension. The σ_{11} stress is the largest with a compressive pulse controlled by the body wave arrival (the 1 direction is radial away from the source). A tensile hoop stress can be seen on the σ_{22} component. The σ_{33} component yields a large tensile stress in the vertical direction as a result of the Rayleigh wave. This tensile stress may be a mechanism leading to spall from surface explosions. The stress tensor is decomposed into its deviatoric and isotropic components in Figure 33.

Similar stress calculations were done at a variety of distances and depths from the source. A summary of the maximum vertical tensile stress from these calculations is given in Figures 19 and 20. The decay of the stress with range from the source for a depth of 1.50 m is given in Figure 34. In Figure 35, the stresses are found to increase with depth for the 10.85 m range. This apparent increase of stress with depth is a result of the zero stress boundary condition at the free surface. Since the tensile stress is a result of Rayleigh waves, the σ_{33} term will decay with depth. None of the calculations shown were deep enough to eliminate the free surface effect (at 4 m, one is only 1/5 of a wavelength from the free surface).

CONCLUSIONS

The waveforms from the PHG single-burst bermed explosions can be interpreted as being dominated by nearfield body waves, $R^{-1.6}$, on the radial components and surface waves, R^{-5} , on the vertical velocity components. Using this interpretation and a vertical and horizontal point source model, one is able to fit the data with an average correlation coefficient on PHGI-06 of 0.84.

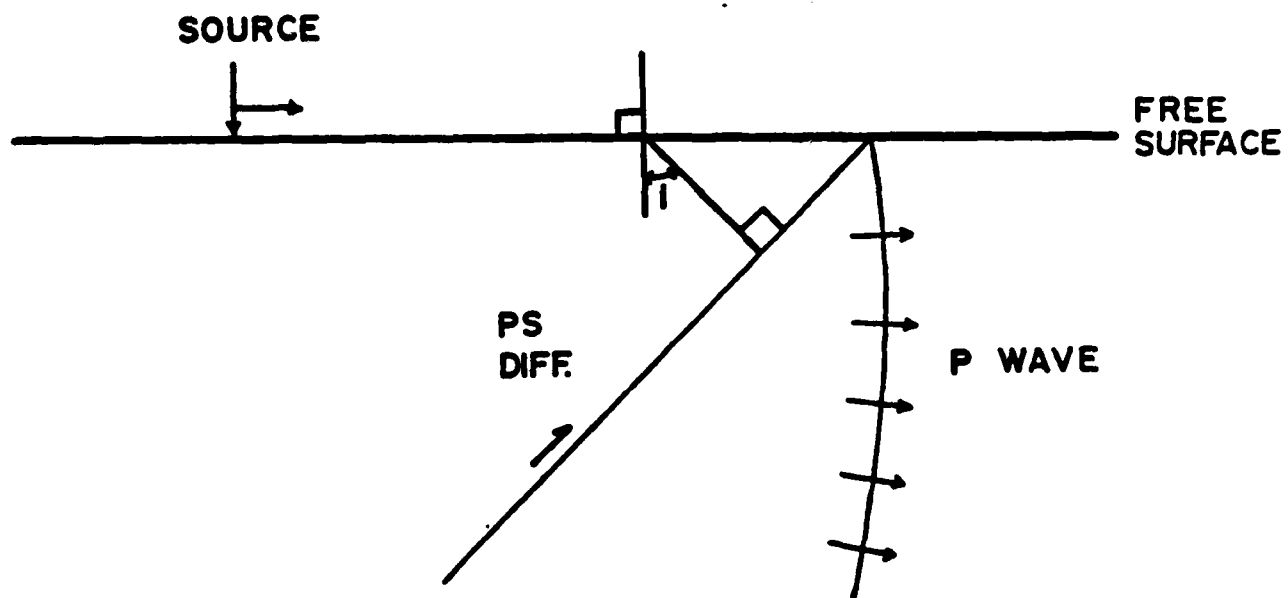
These source inversions indicate the source coupling is sensitive to Poisson's ratio. A 20 percent change in shear wave velocity (Poisson's ratio 0.10 to 0.25) resulted in a factor of 3 change in coupling. This variation in shear properties is what we expect in the variability of our shear properties from geophysical exploration. We, therefore, conclude that the factor of 3 error in coupling estimate is a lower bound for these sources.

A visual comparison of the source time functions from the three bermed experiments indicates great similarities (Figures 36 and 37). PHGI-06 and PHGI-05 have nearly identical time functions, although their relative strengths indicate the decrease in absolute yield from 39 kg to 13.6 kg (PHGI-06 to PHGI-05). The smaller bermed explosion, PHGI-04, shows a higher frequency source than the two previous. In all cases, the rise time of the source agrees within one millisecond of the time to break out of explosive products from the sand berm. The pulse widths of the sources are much longer in duration than the rise time and may correlate with other nonlinear processes, such as spall. The ratio of radial to vertical forces of 2 to 1 remained constant for all sources using a variety of Green's functions. It is felt that this ratio represents the dominance of the radial force in cratering. The mathematical representation of these sources has been well correlated with physical phenomenology near the explosion.

Using the source function developed from the observational ground motion data, the predicted stress tensor has been given. The stresses yield tensile components in the vertical direction resulting from the Rayleigh wave arrival. This tensile stress increases with depth over the 0-4 m depth range due to the free surface effect. A mechanism for tensile failure of a material due to surface bursts has been identified.

BIBLIOGRAPHY

- Ake, J.P., 1980. Ground Motion in a Non-Airblast Environment Letter Report, Engineering Research Institute, University of New Mexico.
- Babcock, S., 1980. Pre-HYBRID GUST Phase I Quick Look Report, Engineering Research Institute, University of New Mexico, CERF-AG-26.
- Gupta, I.N. and C. Kisslinger, 1966. Radiation of Body Waves from Near-Surface Explosive Sources, Geophysics 31, 1057
- Hadley, D.M. and D.V. Helmberger, 1981. Seismic Source Functions and Attenuation from Local and Teleseismic Observations of the NTS Event Jorum and Handley, Bull. Seism. Soc. Am. 71.
- Haskell, N.A., 1967. Analytic Approximation for the Elastic Radiation From a Contained Underground Explosion, J. Geophys. Res. 72, 2583-2587.
- McEvilly, T.V. and W.A. Peppin, 1972. Source Characteristics of Earthquakes, Explosions, and After Events, Geophys. J. Roy. Astr. Soc. 31, 67-82.
- Mueller, R.A. and J.R. Murphy, 1971. Seismic Characteristics of Underground Nuclear Detonations: Part I, Seismic Scaling Law of Underground Nuclear Detonations, Bull. Seism. Soc. Am. 61, 1675.
- Press, F. and M. Ewing, 1951. Ground Roll Coupling to Atmospheric Compressional Waves, Geophysics 16, 416-430.
- Stump, B.W. and L.R. Johnson, 1977. The Determination of Source Properties by the Linear Inversion of Seismograms, Bull. Seism. Soc. Am. 67, 1489-1502.
- Stump, B.W. and L.R. Johnson, 1981. The Effect of Green's Functions of the Determination of Source Mechanisms by the Linear Inversion of Seismograms, Identification of Seismic Sources - Earthquake or Underground Explosion, Edited by Dr Eystein Husebye and S. Mykkehveit, D. Reidel Publishing Co., Dordrecht-Holland.
- Stump, B.W., 1982. Stress Waves in a Three-Dimensional Elastic Half-Space: Single and Multiple Surface Sources, in preparation.
- Werth and Herbst, 1963. Comparison of Amplitudes of Seismic Waves from Nuclear Explosions in Four Mediums, J. Geophys. Res. 68, 1463-1475.



$$i = \sin^{-1}(\beta/\alpha)$$

Figure 3

DISPLACEMENTS - $\delta(t)$

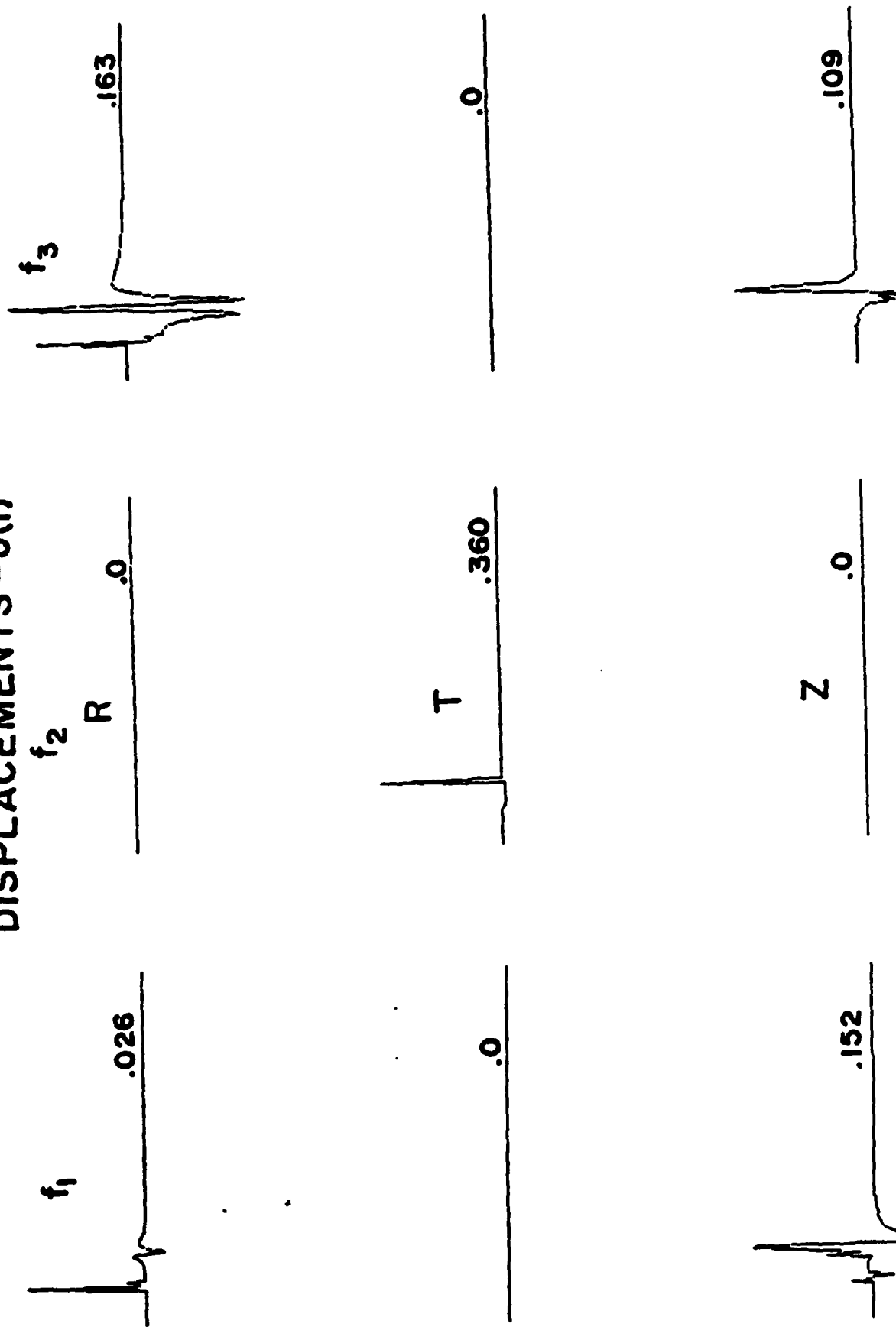


Figure 4

EFFECT OF POISSON'S RATIO - f_1

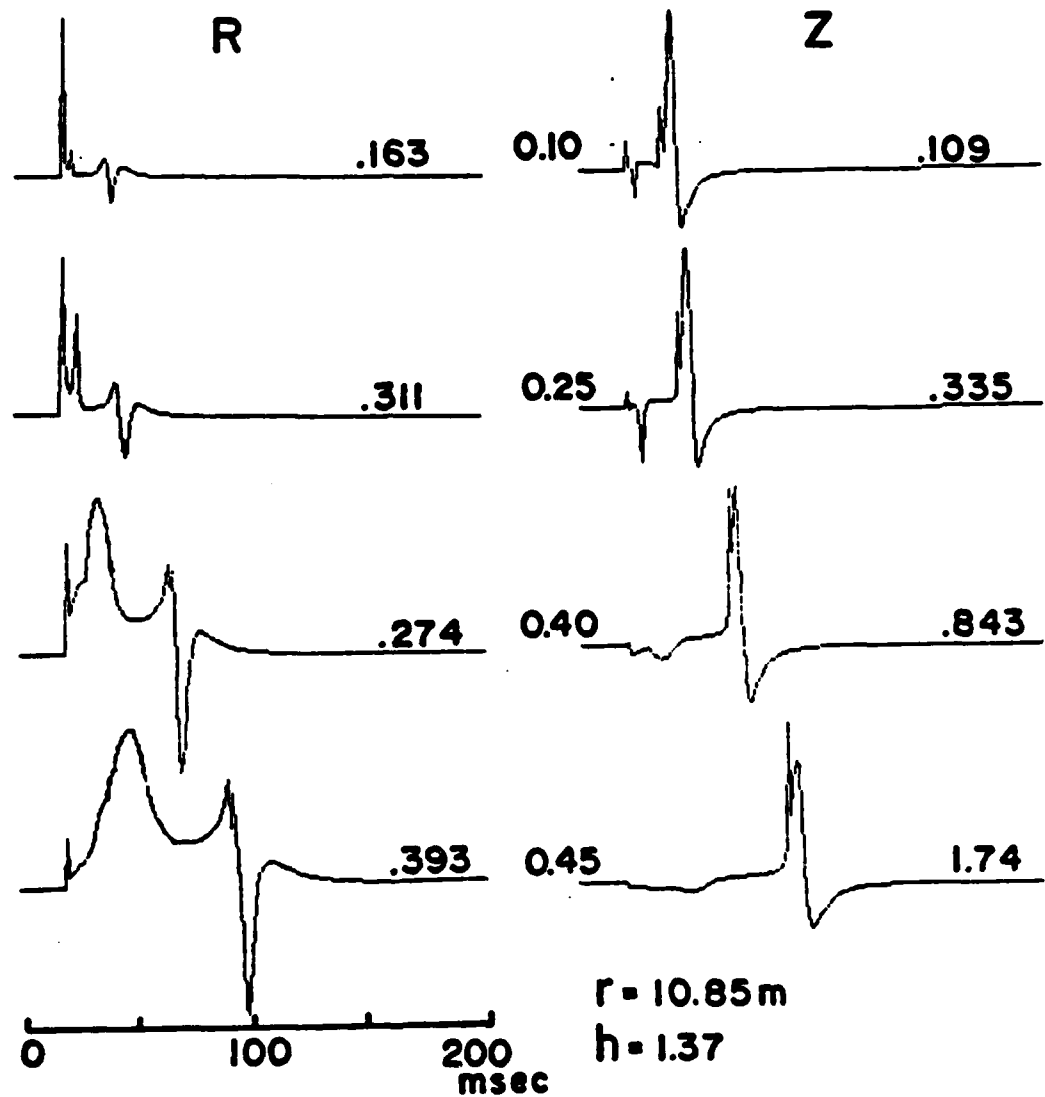


Figure 5

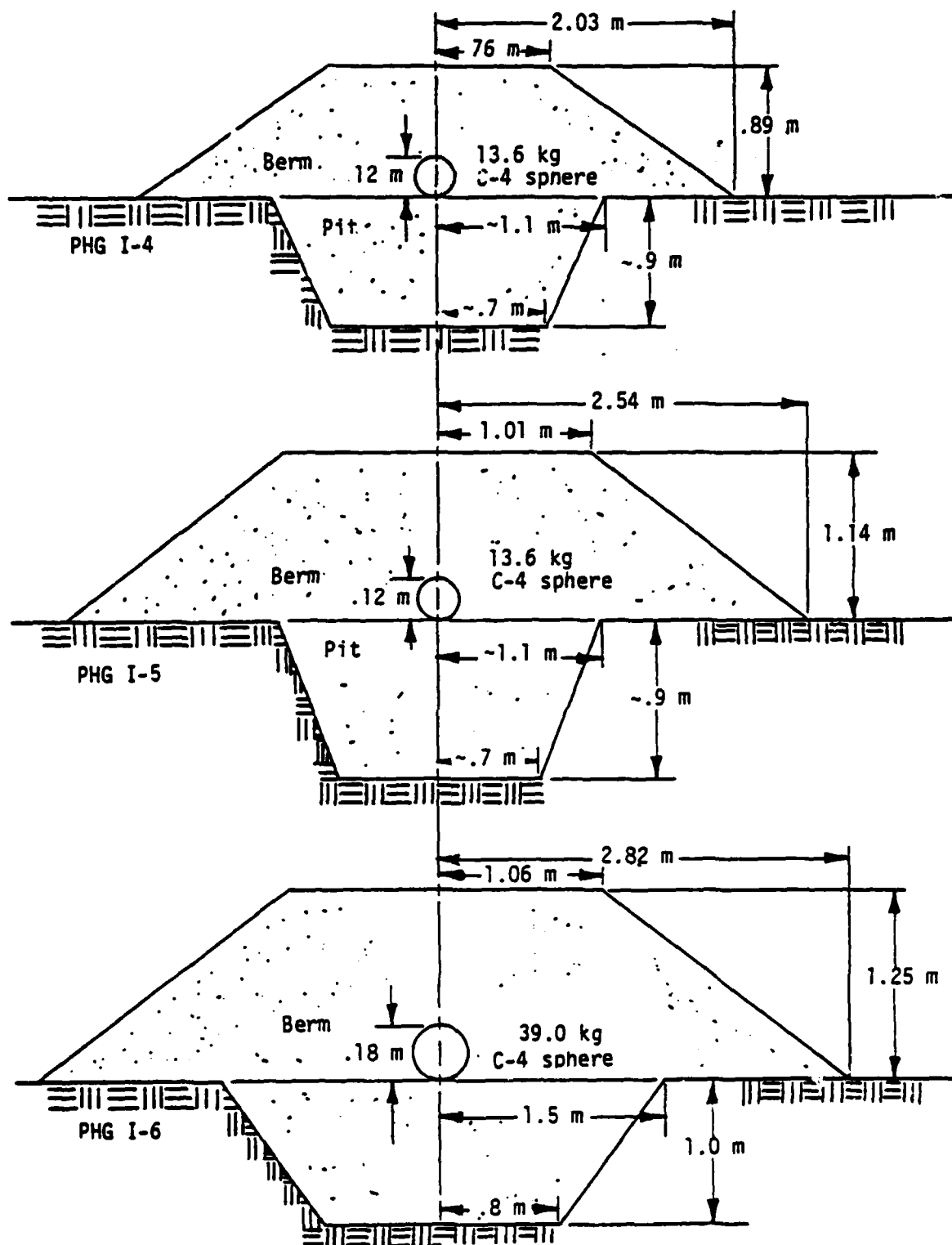
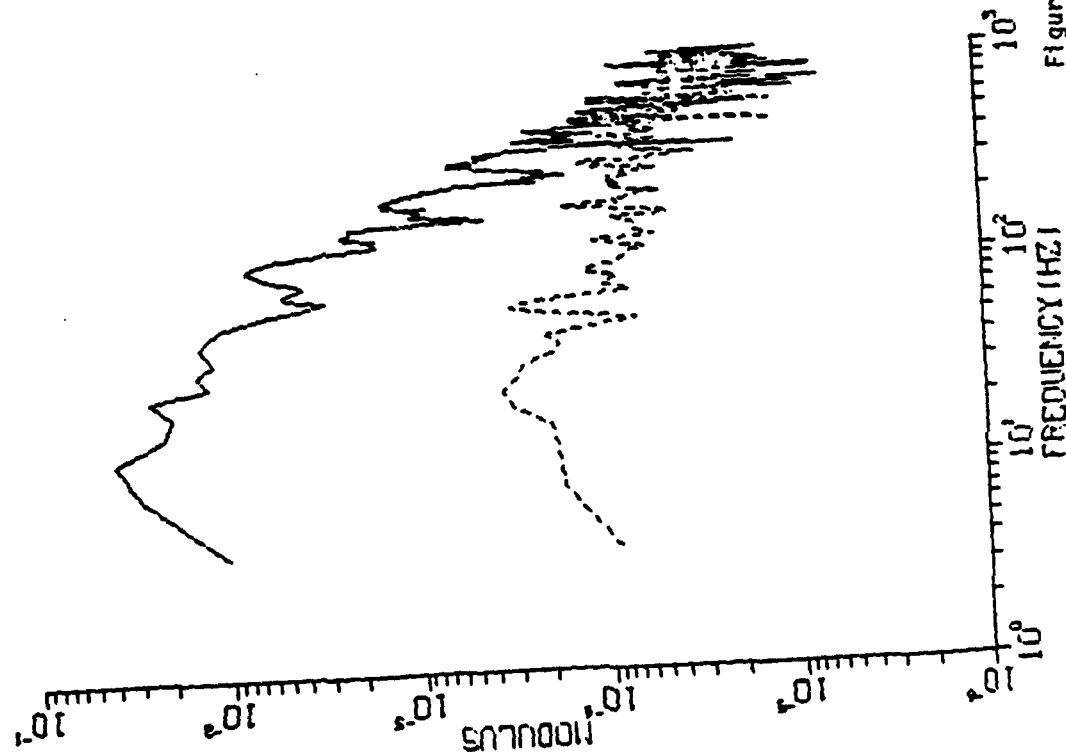


Figure 6

R = 6.55m H = 1.50m horz.

SPECTRUM



TIME SERIES

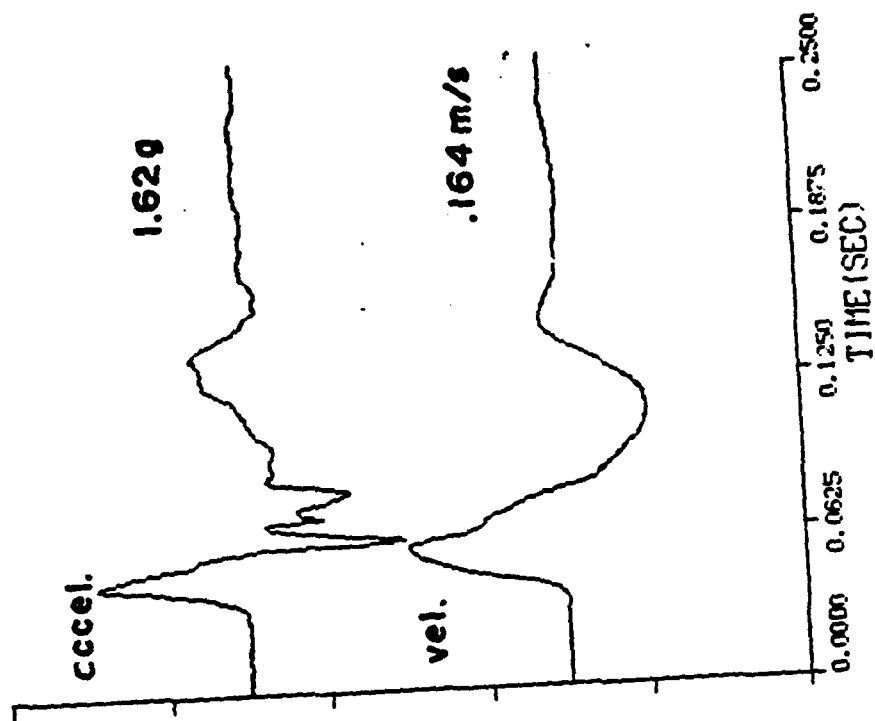
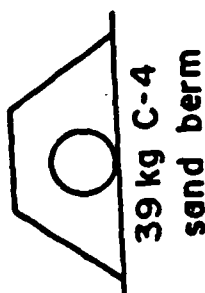


Figure 7

PHG 1 - 06



6.55	8.50	10.85	14.60	18.35 m

DATA - sampled at 2000sps
 - filter, 5pole at 400 hz
 - all accel. data
 - integrated and corrected for
 ramp to yield vel.

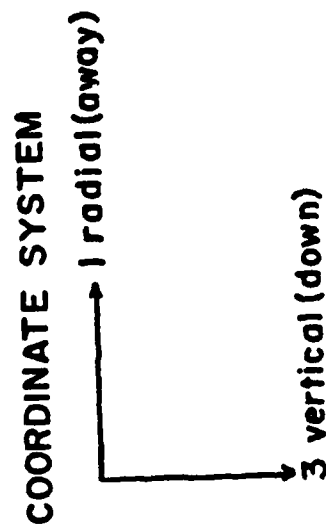


Figure 8

PHG I-06 FITS

poisson's ratio 0.1

depth 1.5m

- peak radial data
- peak radial calculation
- peak vertical data
- peak vertical calculation

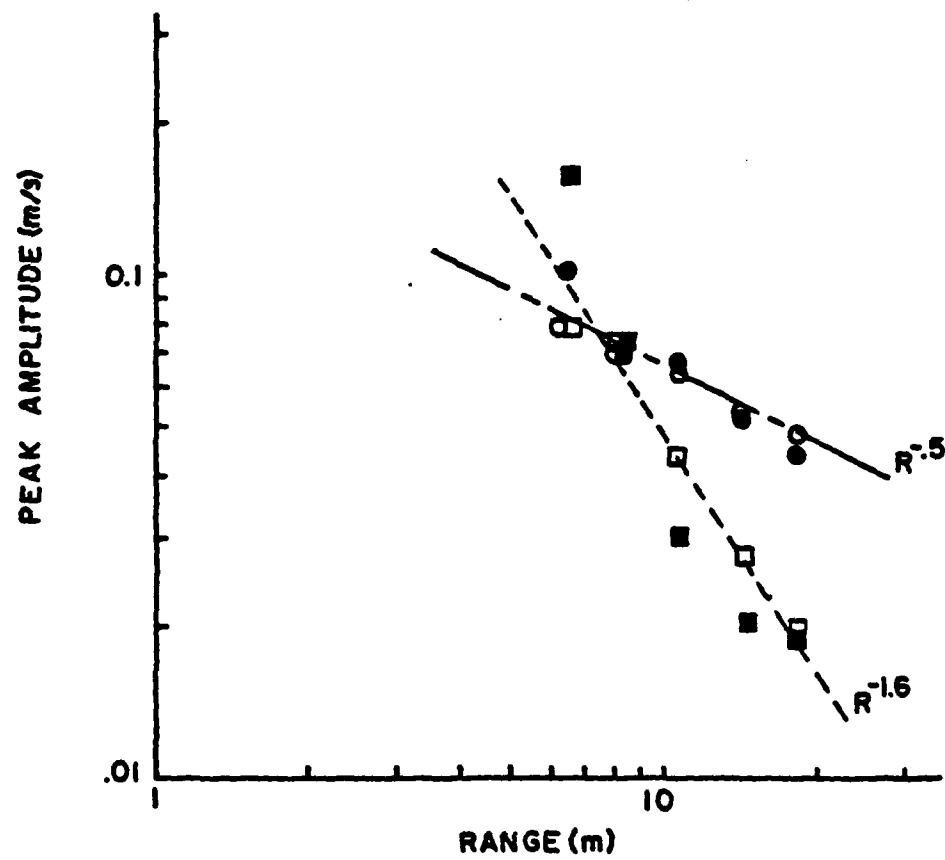


Figure 9

PHG 1-06 FITS
poisson's ratio 0.10
R = 6.55m

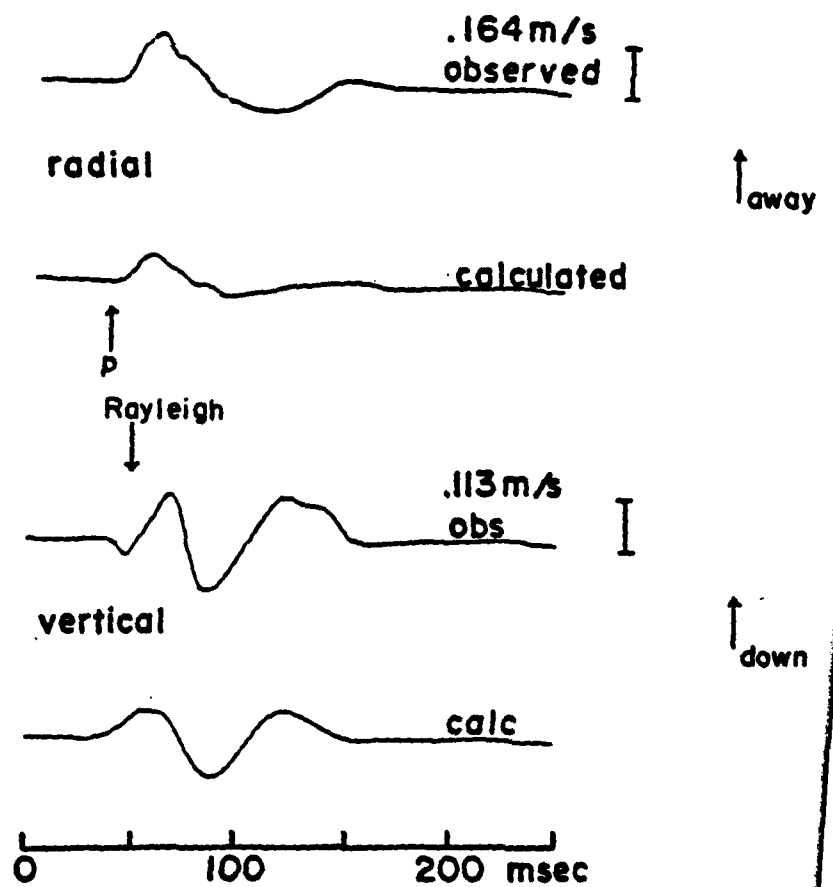


Figure 10

PHG 1-06 FITS
poisson's ratio 0.10

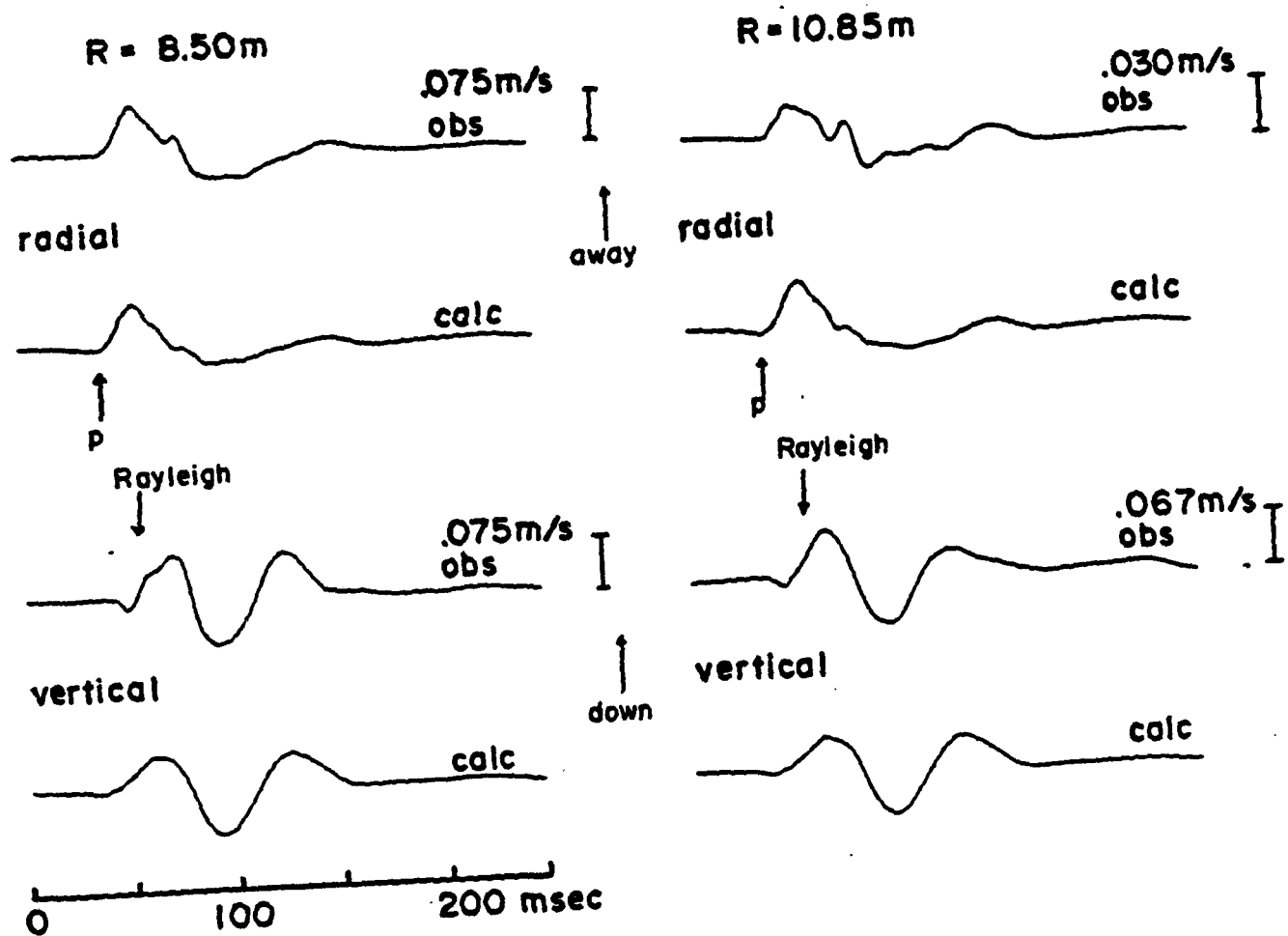


Figure 11

PHG I-06 FITS
poisson's ratio 0.10

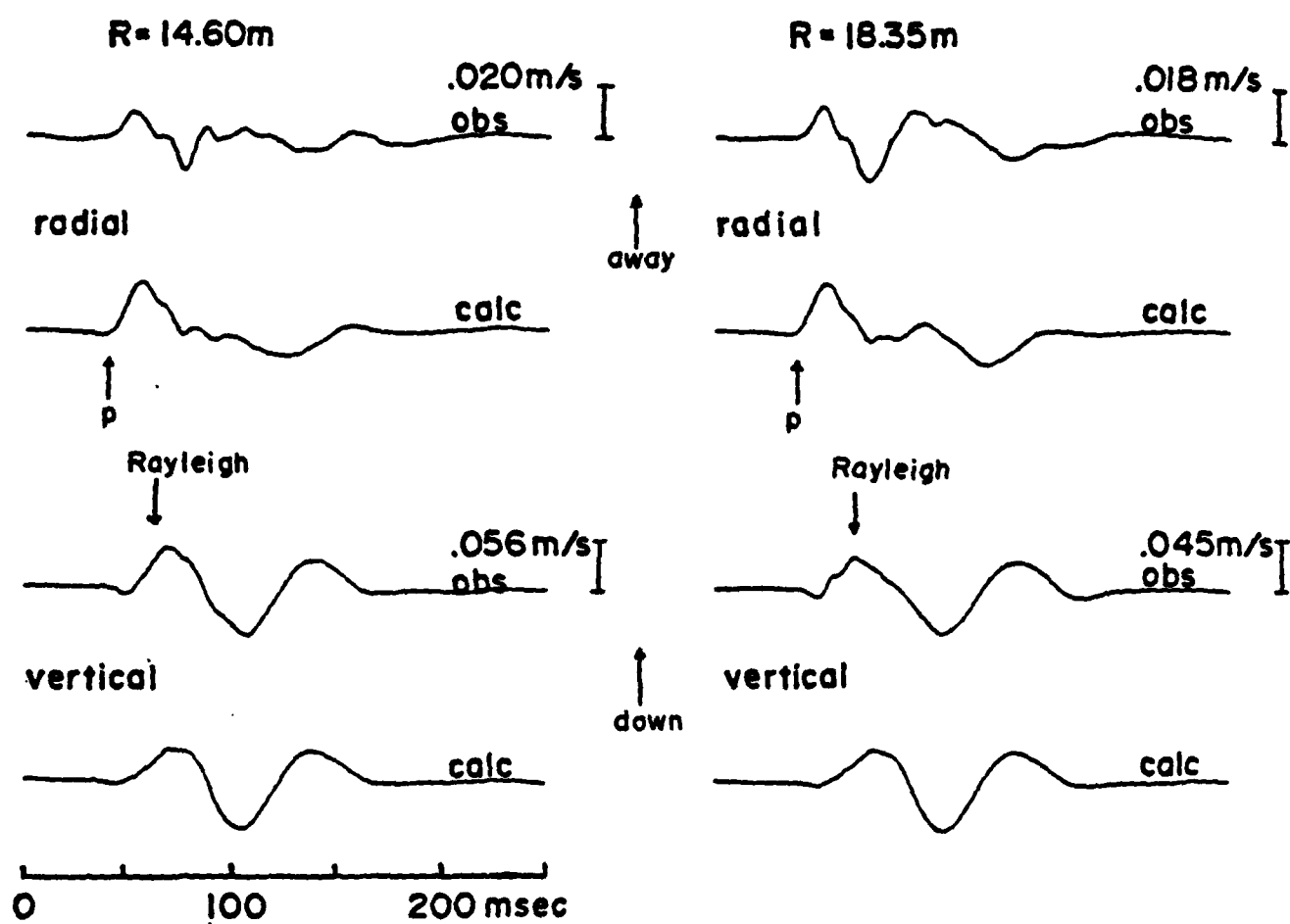


Figure 12

PHG I-06 SOURCE FUNCTIONS
POISSON'S RATIO - 0.1

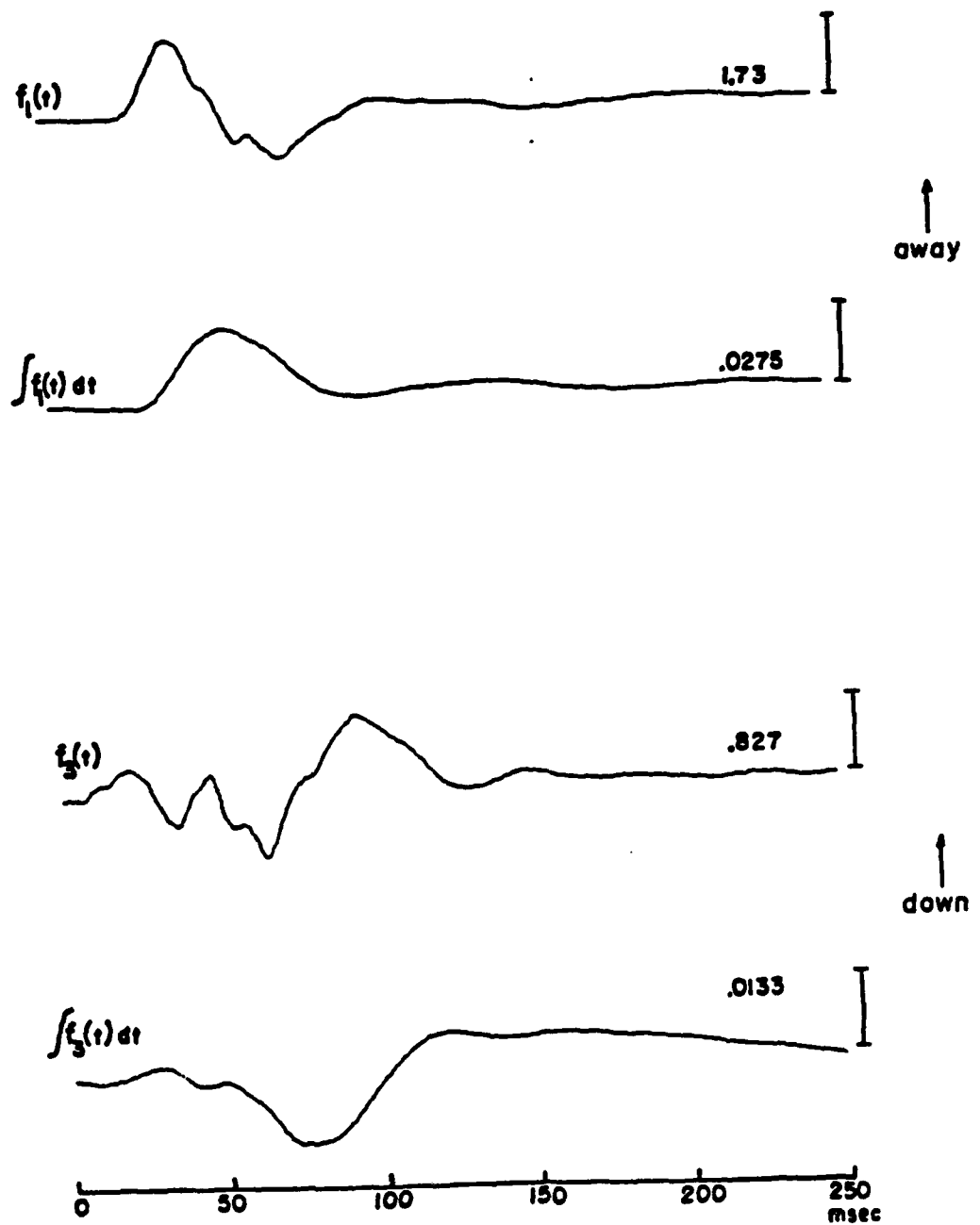


Figure 13

SOURCE SPECTRA
POISSON'S RATIO Q1

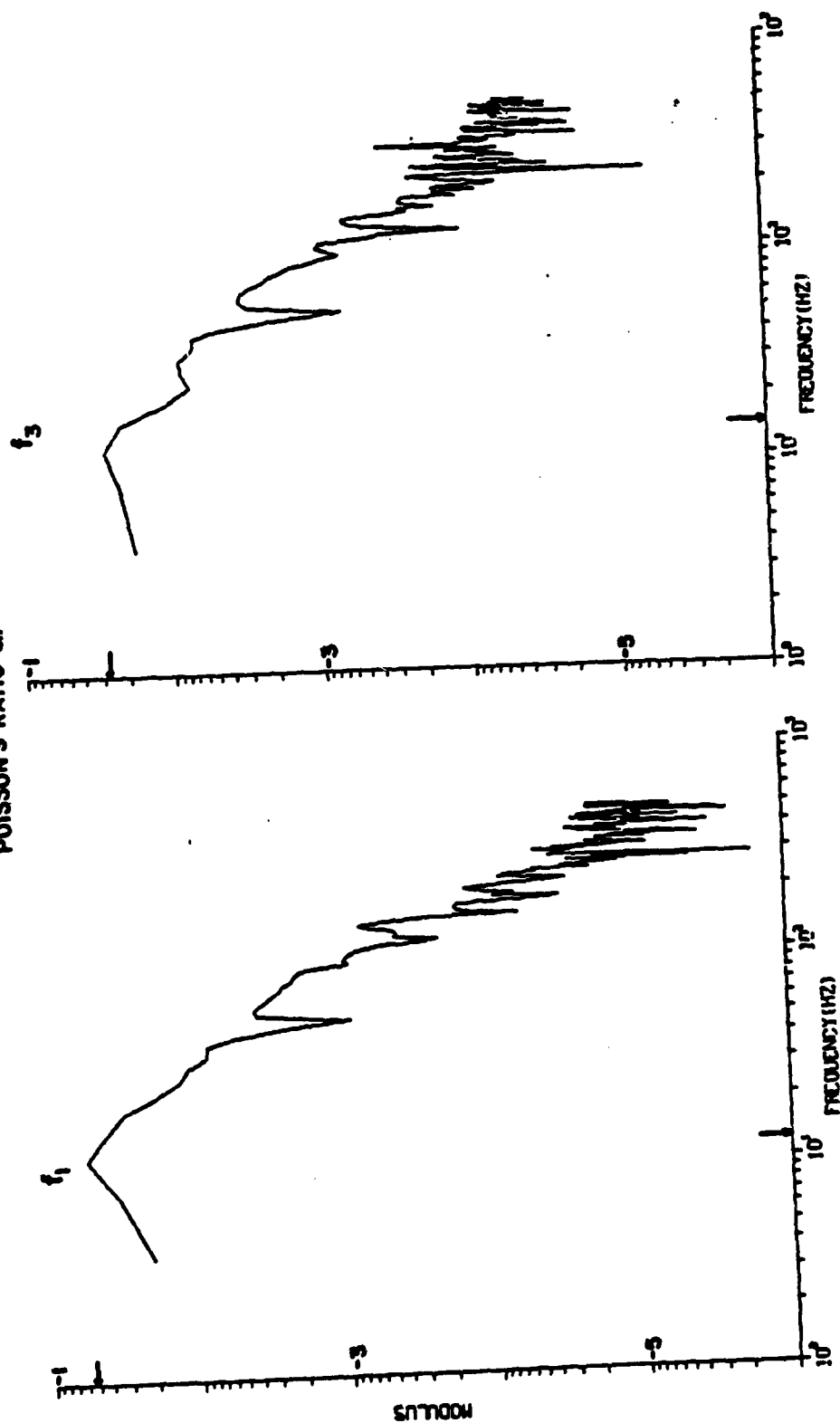


Figure 14

PHG 1-06
Berm Growth

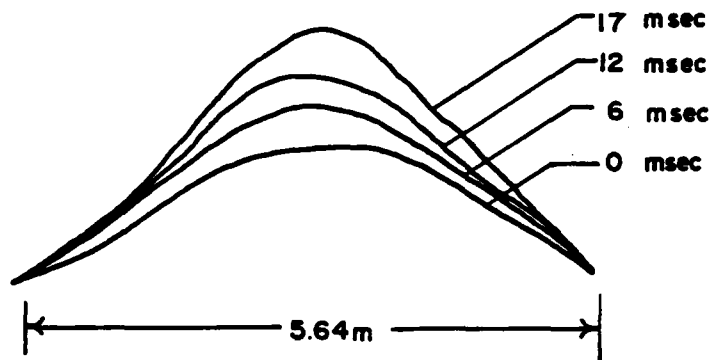


Figure 15

EFFECT OF POISSON'S RATIO ON SOURCE STRENGTH

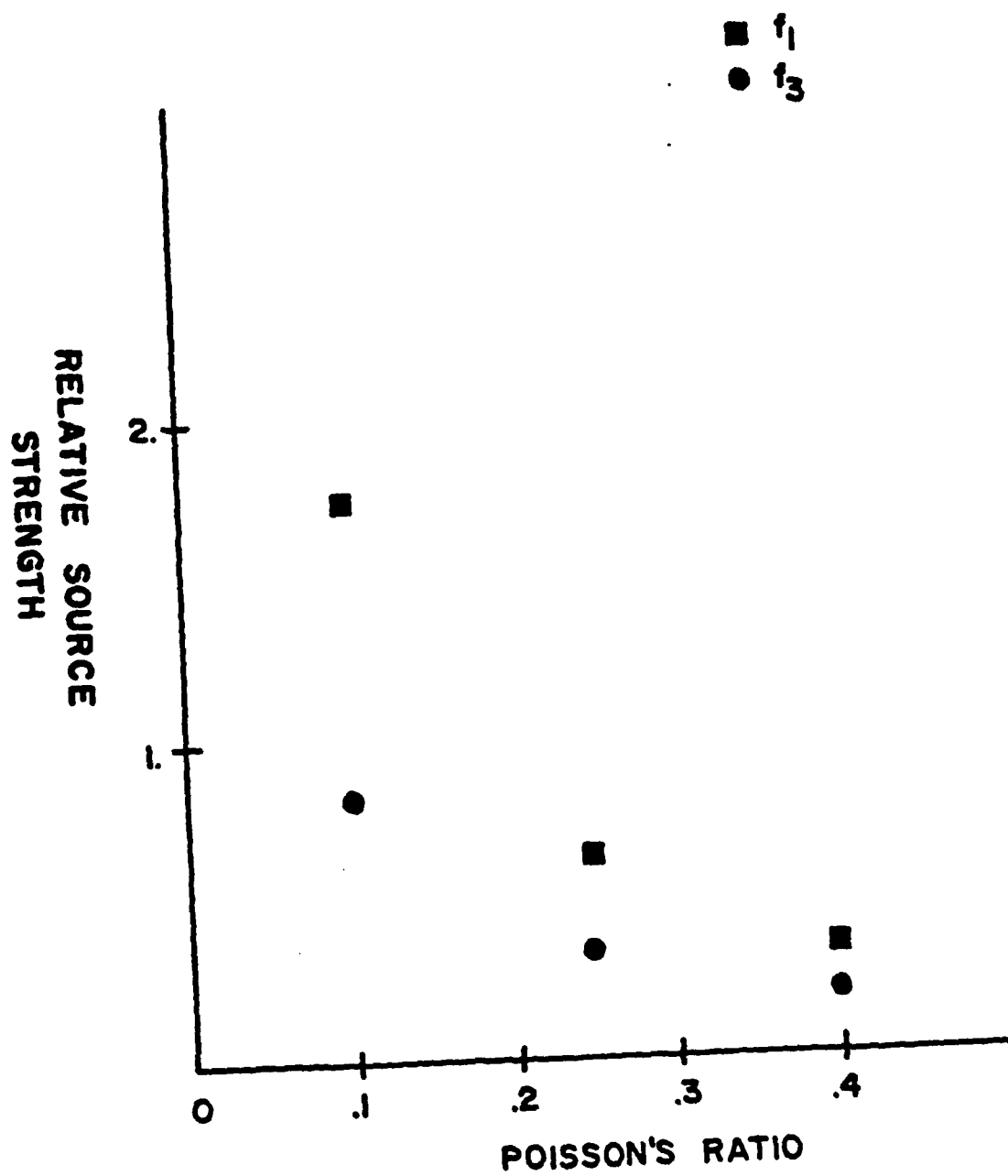


Figure 16

EFFECT OF POISSON'S RATIO ON SOURCE PHG 1-06

f_1

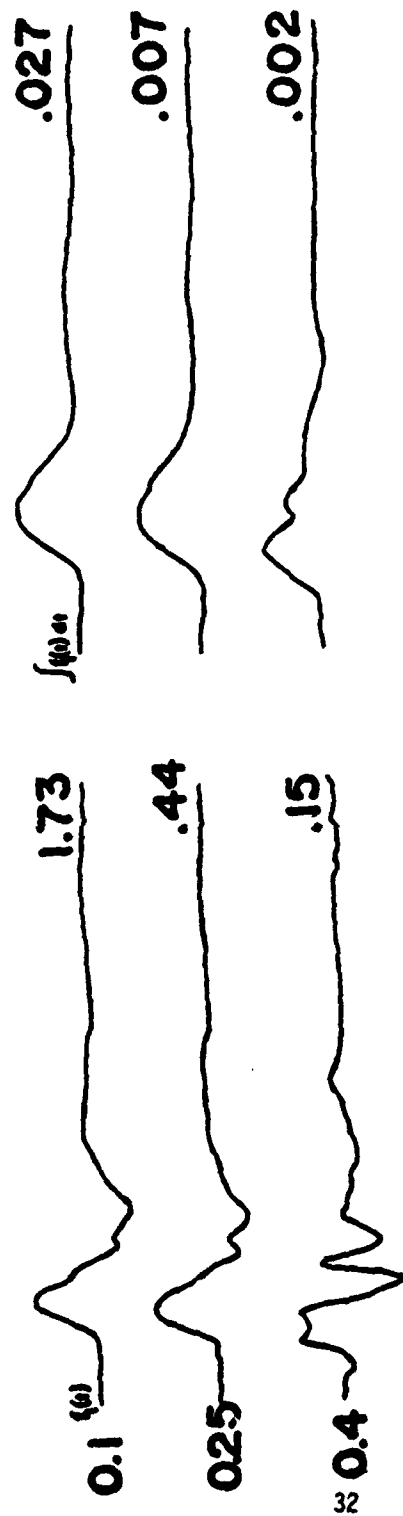


Figure 17

EFFECT OF POISSON'S RATIO ON SOURCE PHG1-06

f_3

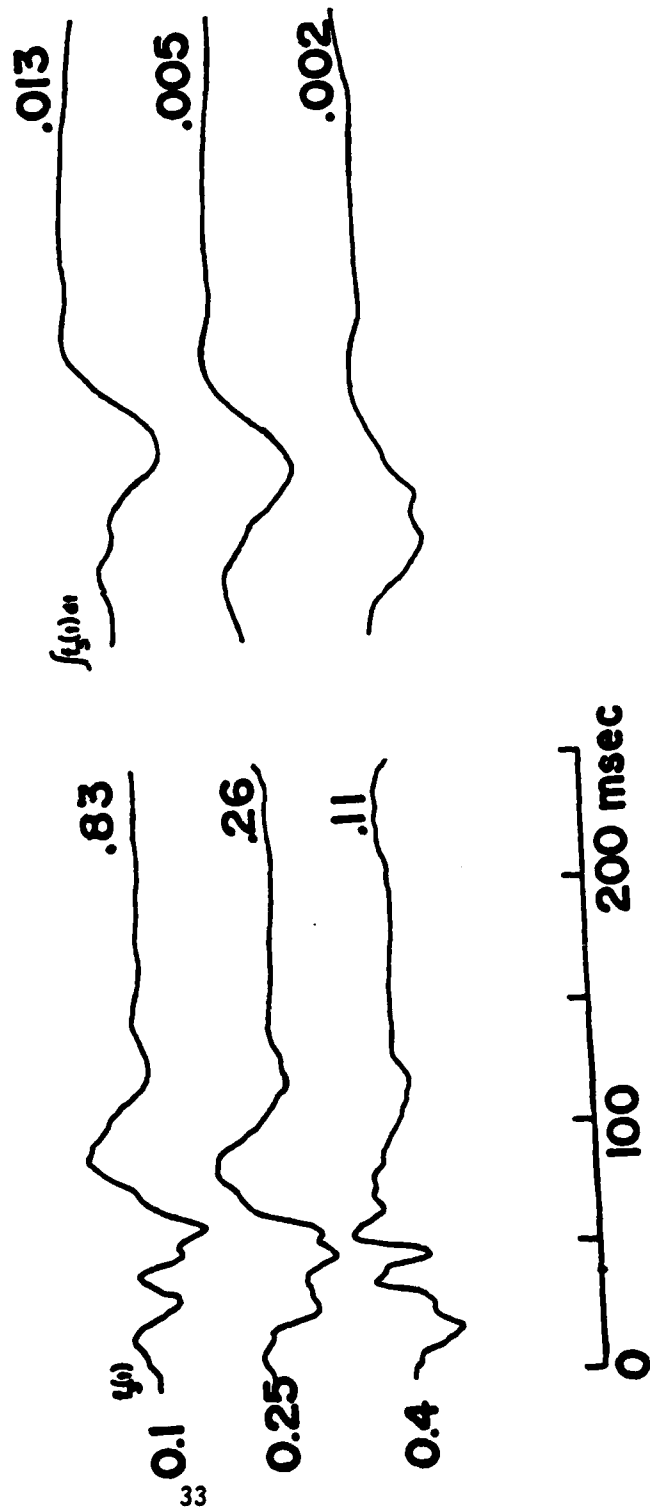


Figure 18

EFFECT OF POISSON'S RATIO ON FITS
PHG I-06, R=10.85m H=1.5m V

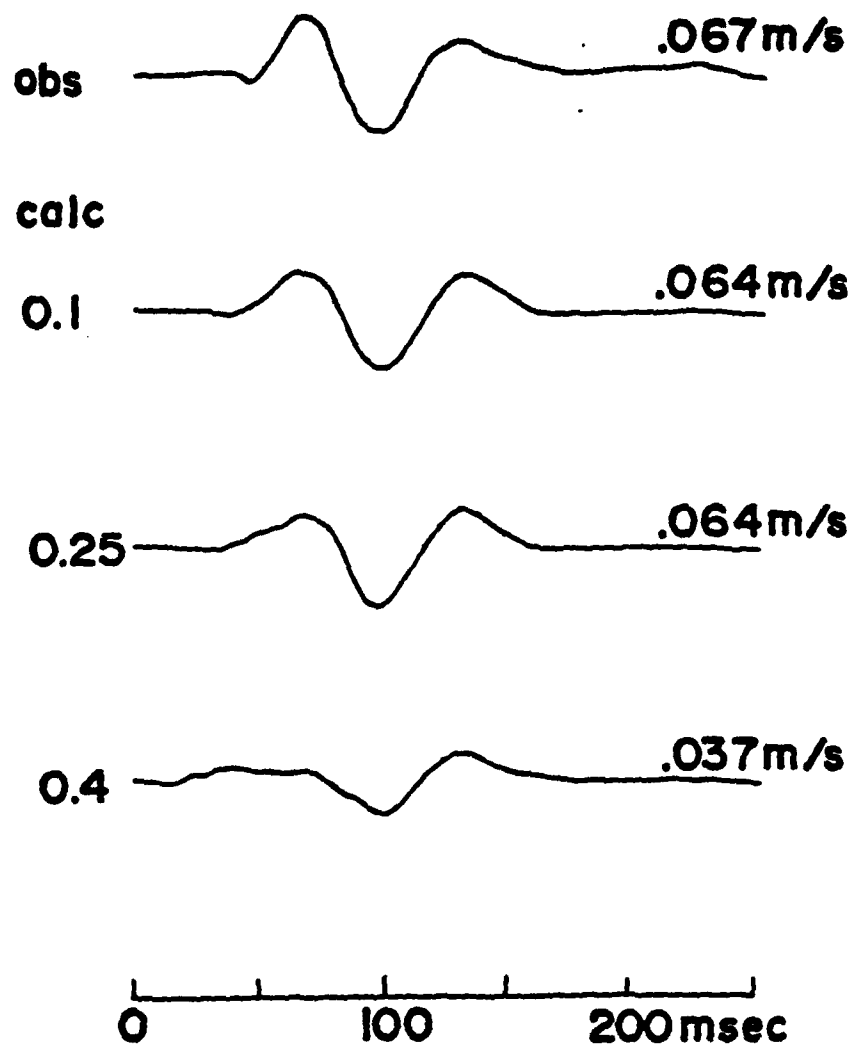
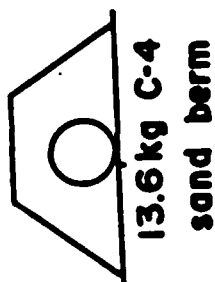
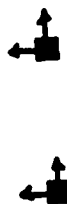


Figure 19

PHG 1-05



6.55 8.5 18.35



- DATA
- sampled at 2000 sps
 - filter, 5 pole at 400 hz
 - accel. data
 - integrated and corrected for ramp to yield vel.

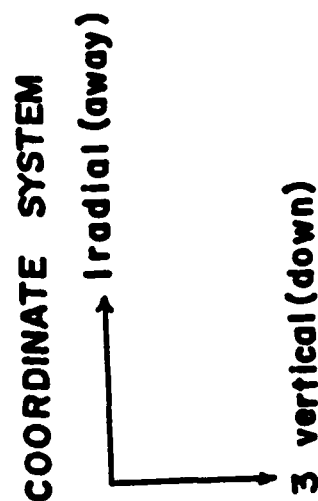


Figure 20

PHG 1-05 FITS
poisson's ratio 0.10
R=6.55m

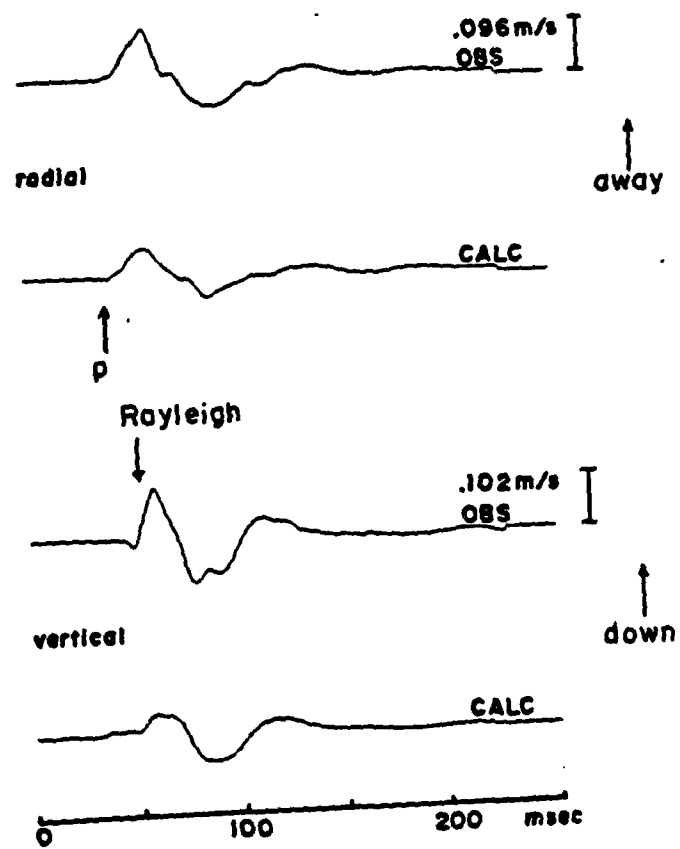


Figure 21

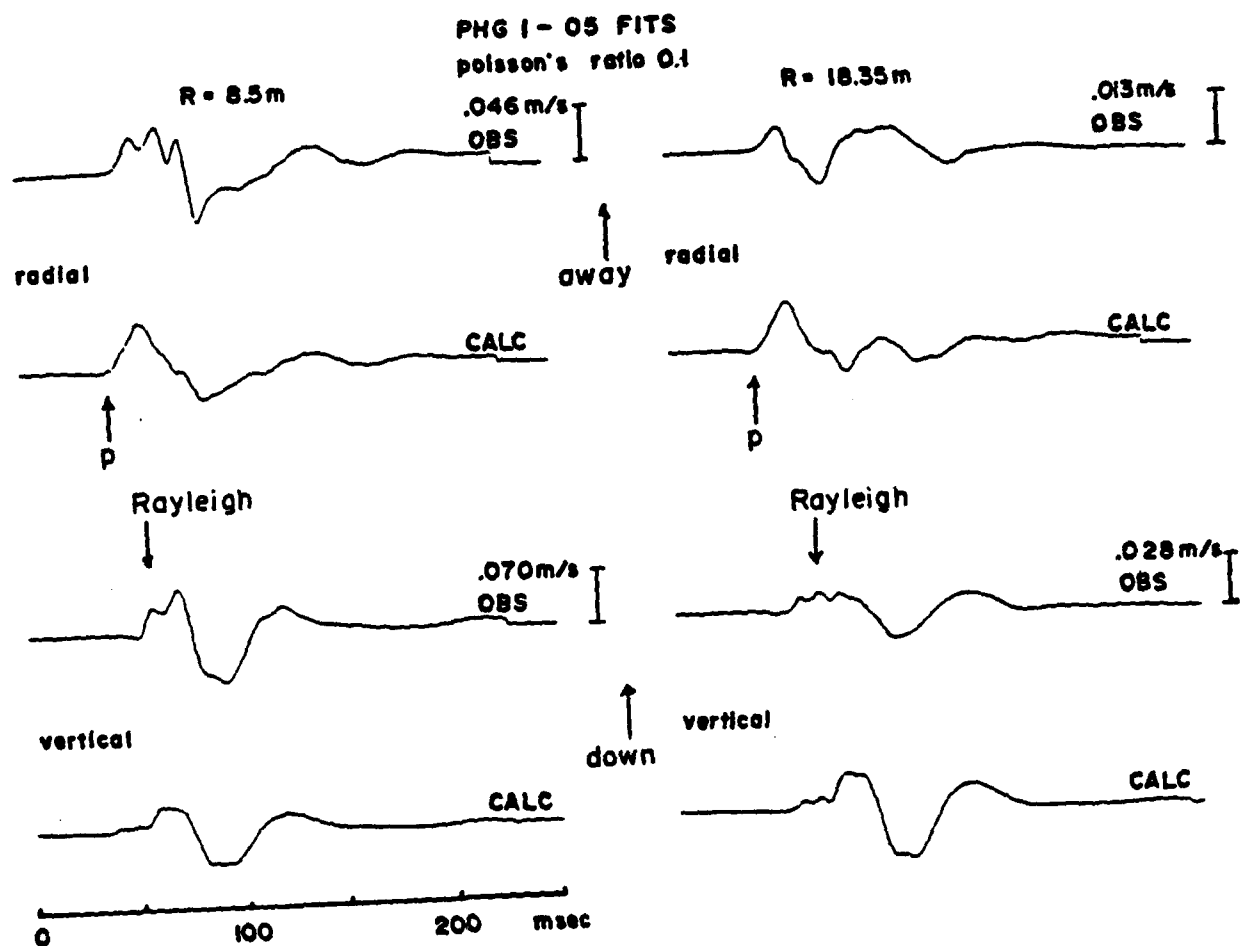


Figure 22

PHG I-05 SOURCE FUNCTIONS

POISSON'S RATIO - 0.1

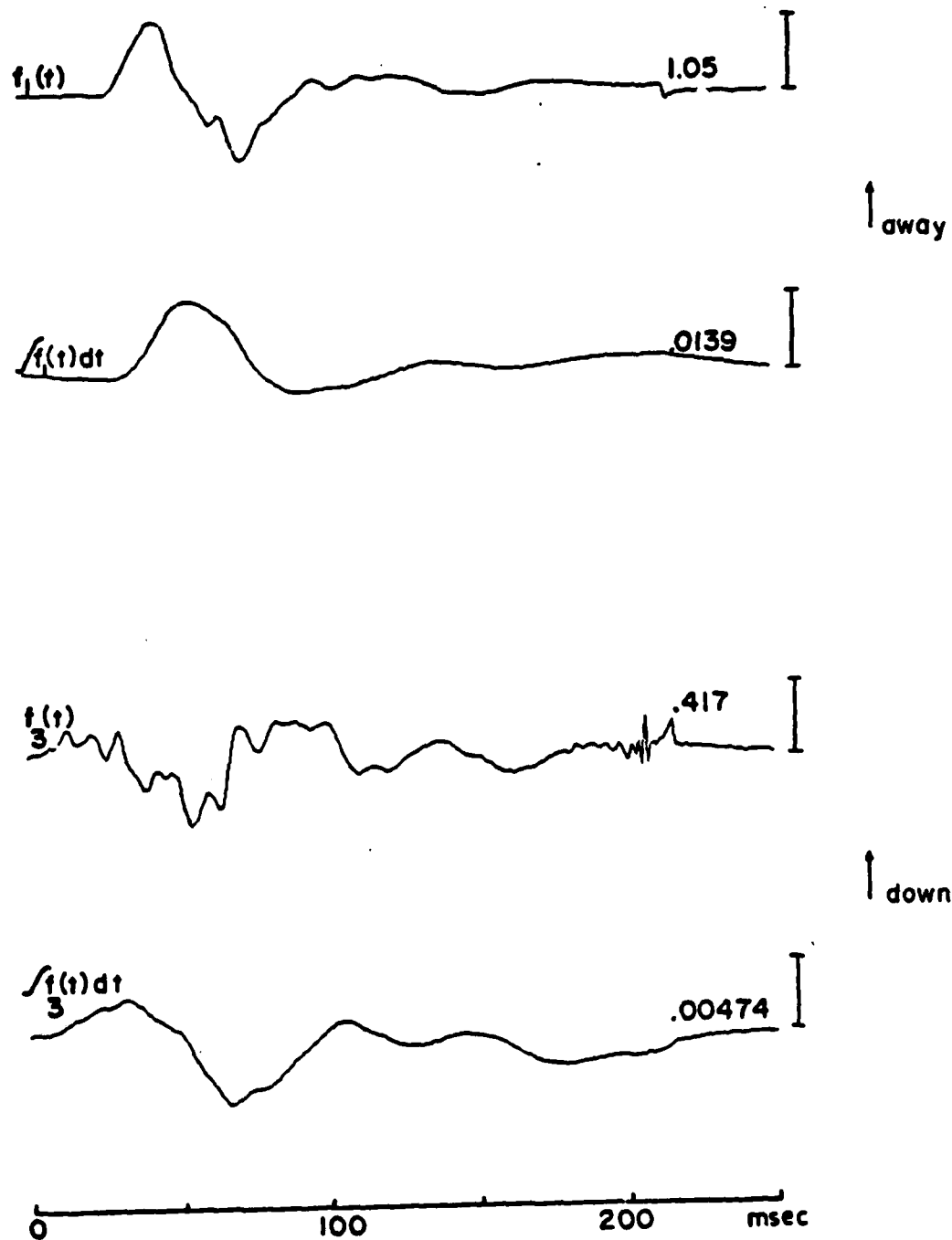


Figure 23

SOURCE SPECTRA
poisson's ratio 0.1

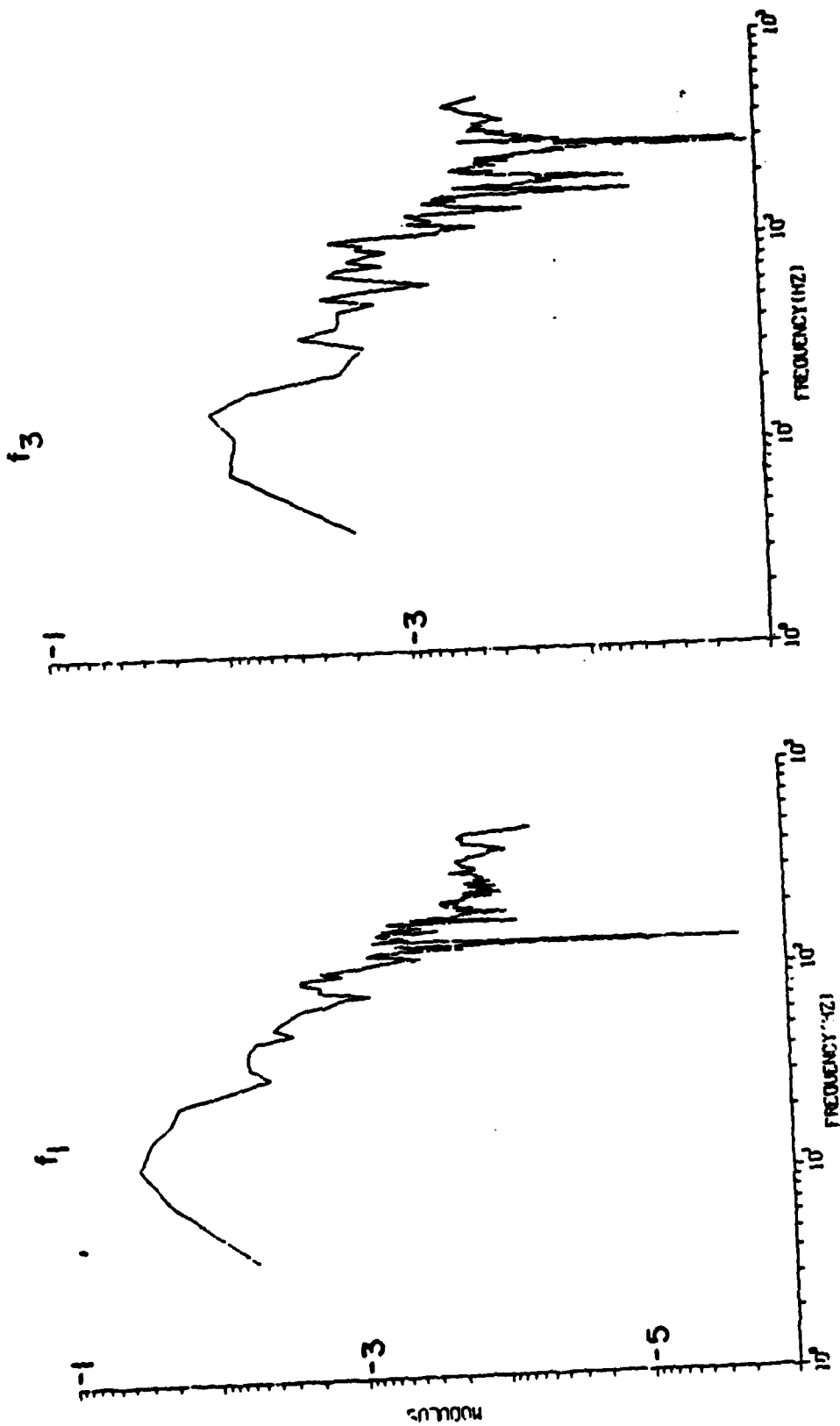


Figure 24

PHG 1 - 05
Berm Growth

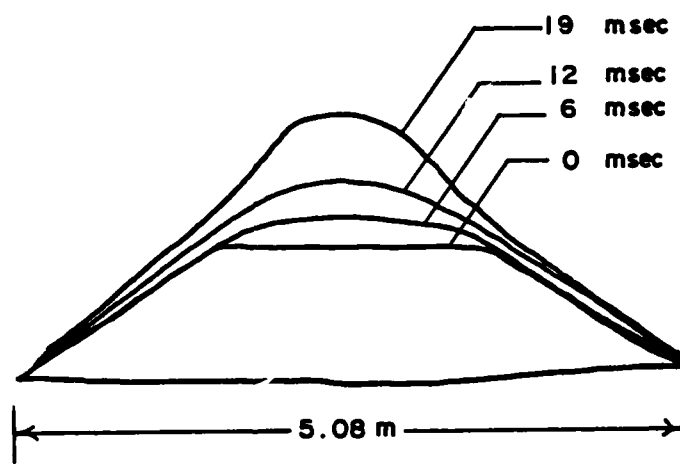


Figure 25

SOURCE SCALING

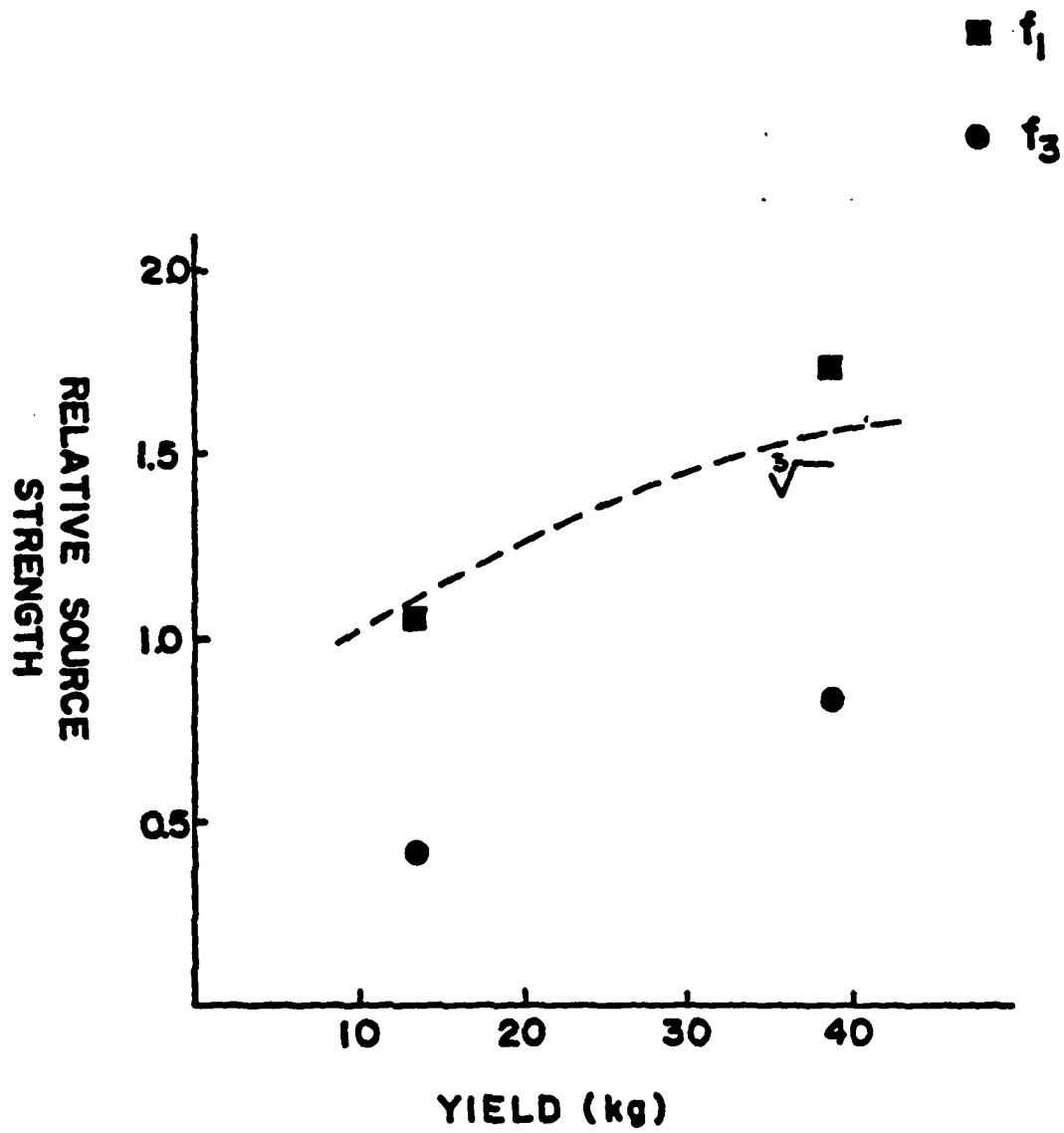


Figure 26

PHG-1-04 FITS
poisson's ratio 0.10
R = 6.55m



0 100 200msec

Figure 27

PHG1-04 FITS
poisson's ratio 0.10

R = 8.5m



radial



calc

R = 18.35m



radial



calc

obs



vertical



calc

obs



vertical



calc



Figure 28

PHG 1-04 SOURCE FUNCTIONS
poisson's ratio 0.1

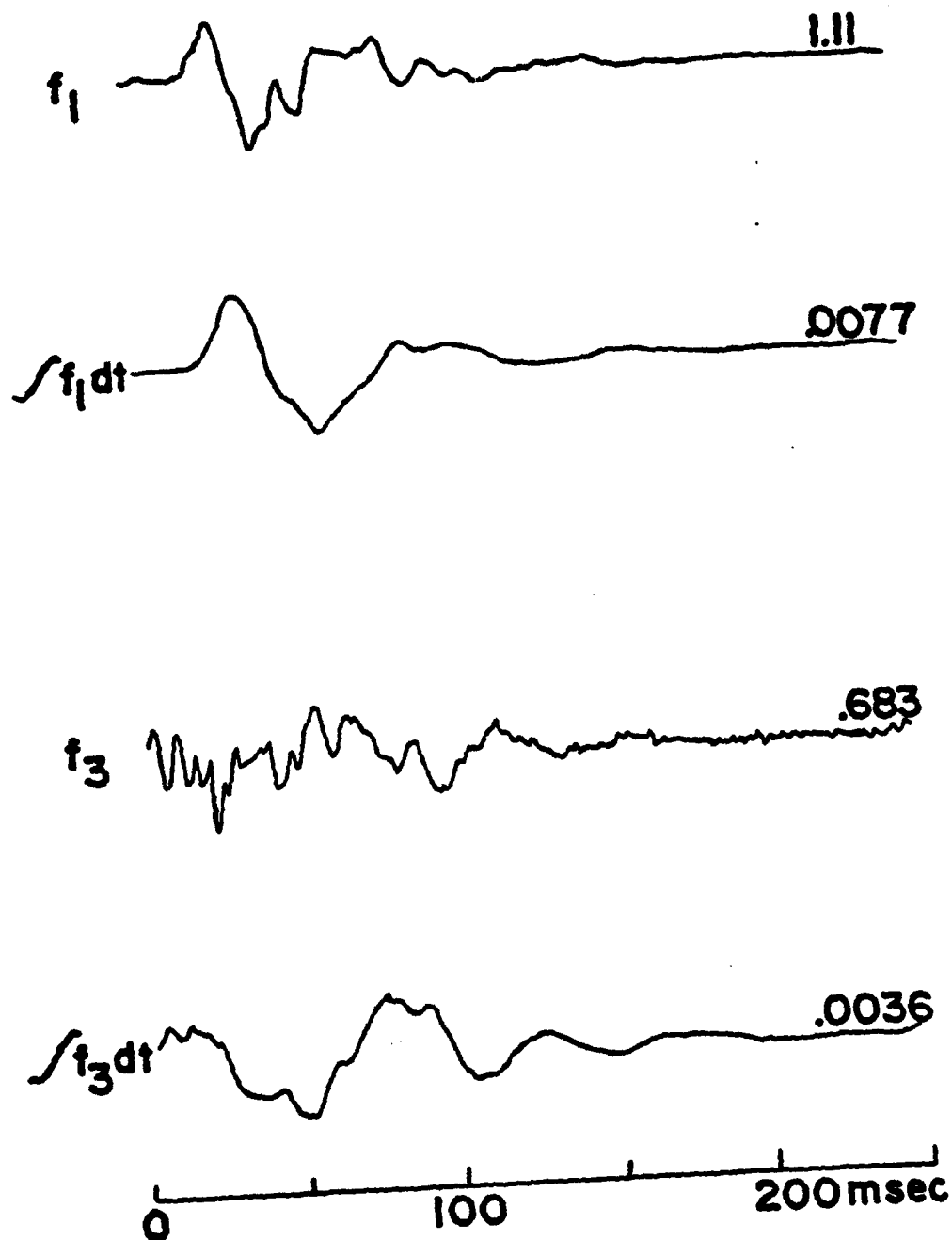
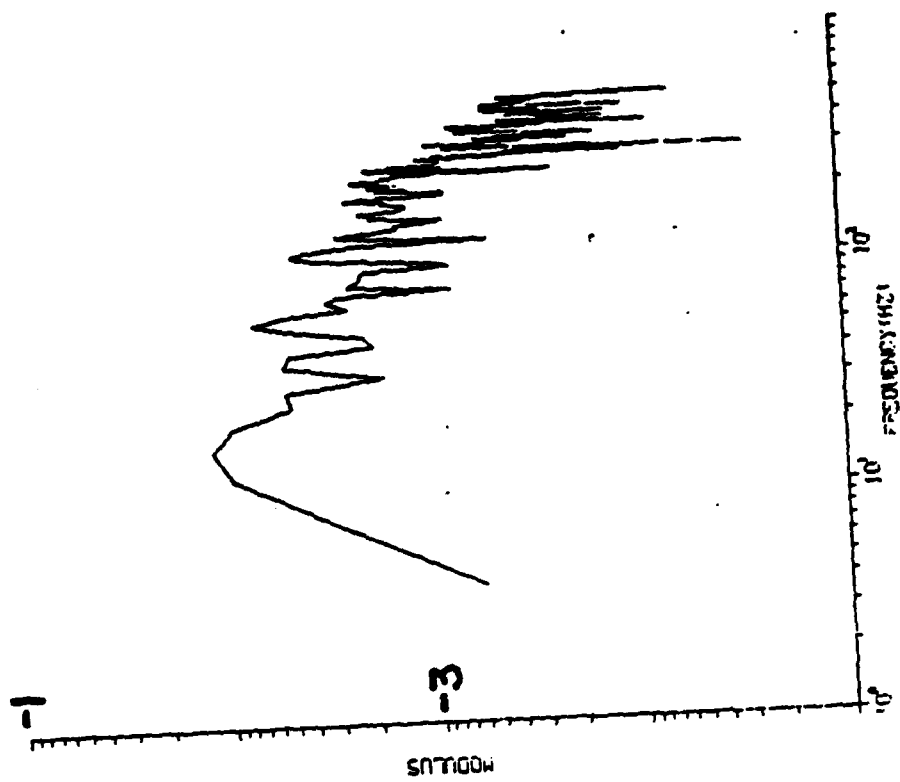


Figure 29

SOURCE SPECTRA PHG1-04

f_3
SPECTRUM



f_1
SPECTRUM

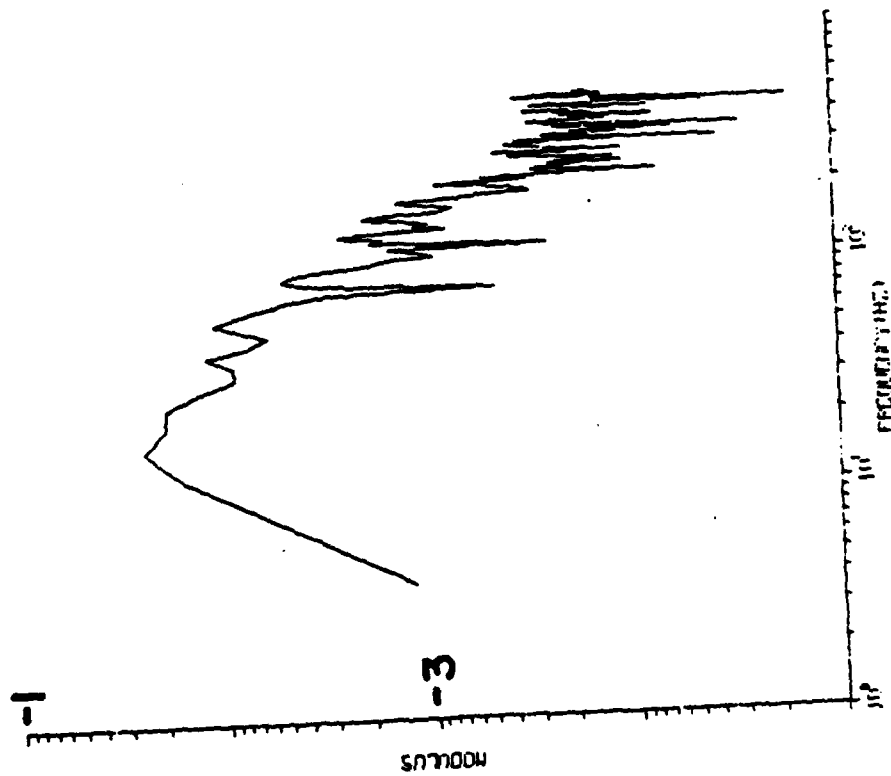


Figure 30

PHG I - 04
Berm Growth

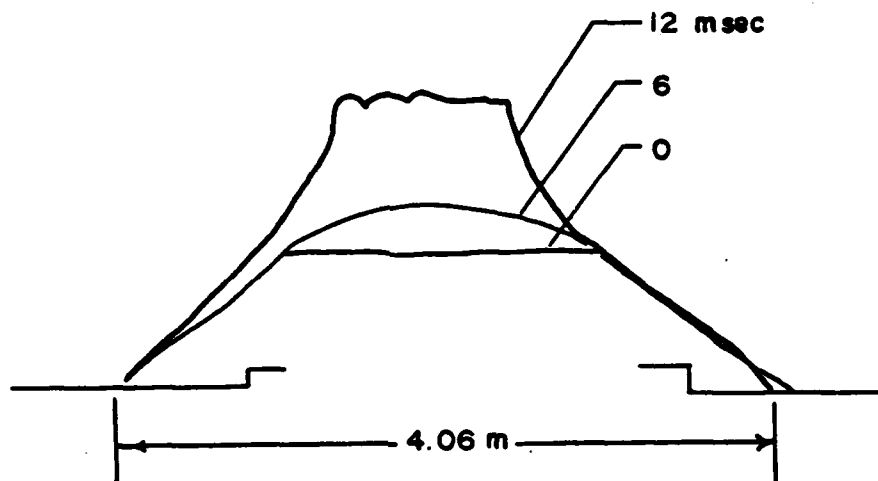


Figure 31

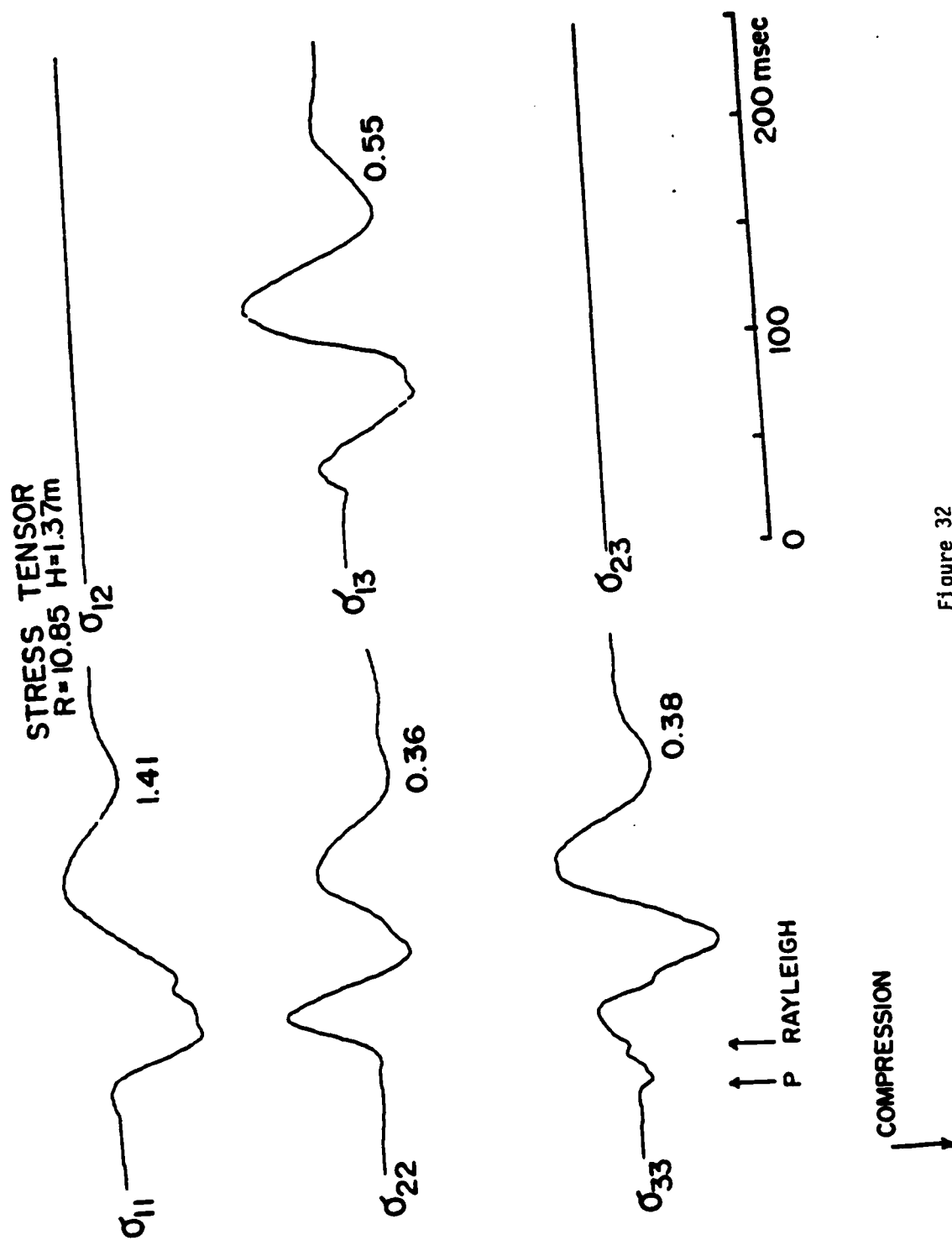
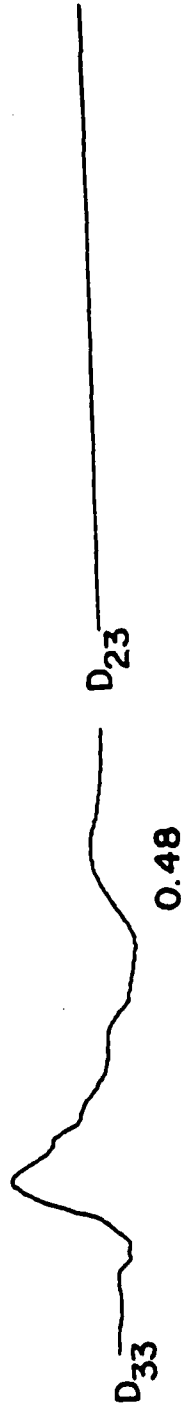
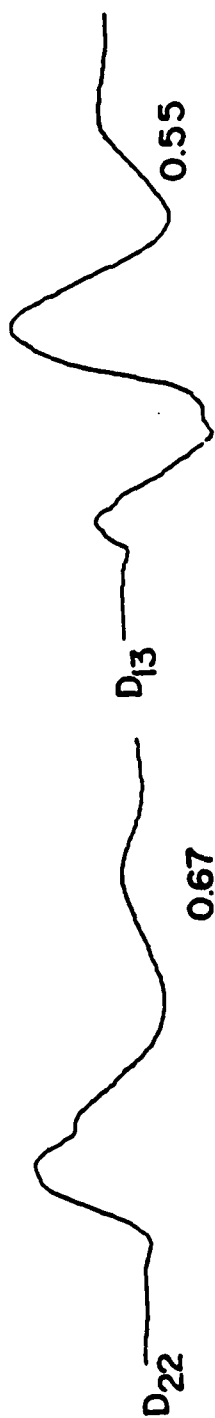
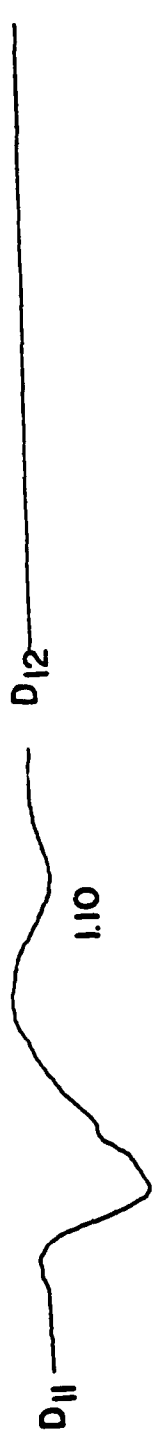


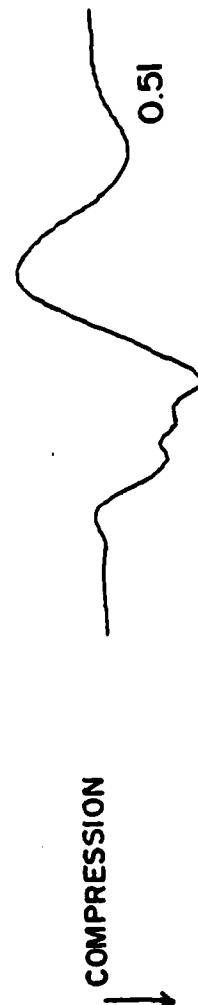
Figure 32

DEVIATORIC STRESS



↑ ↑ P RAYLEIGH

ISOTROPIC



↓ COMPRESSION



Figure 33

PHG 1-06 PRED.

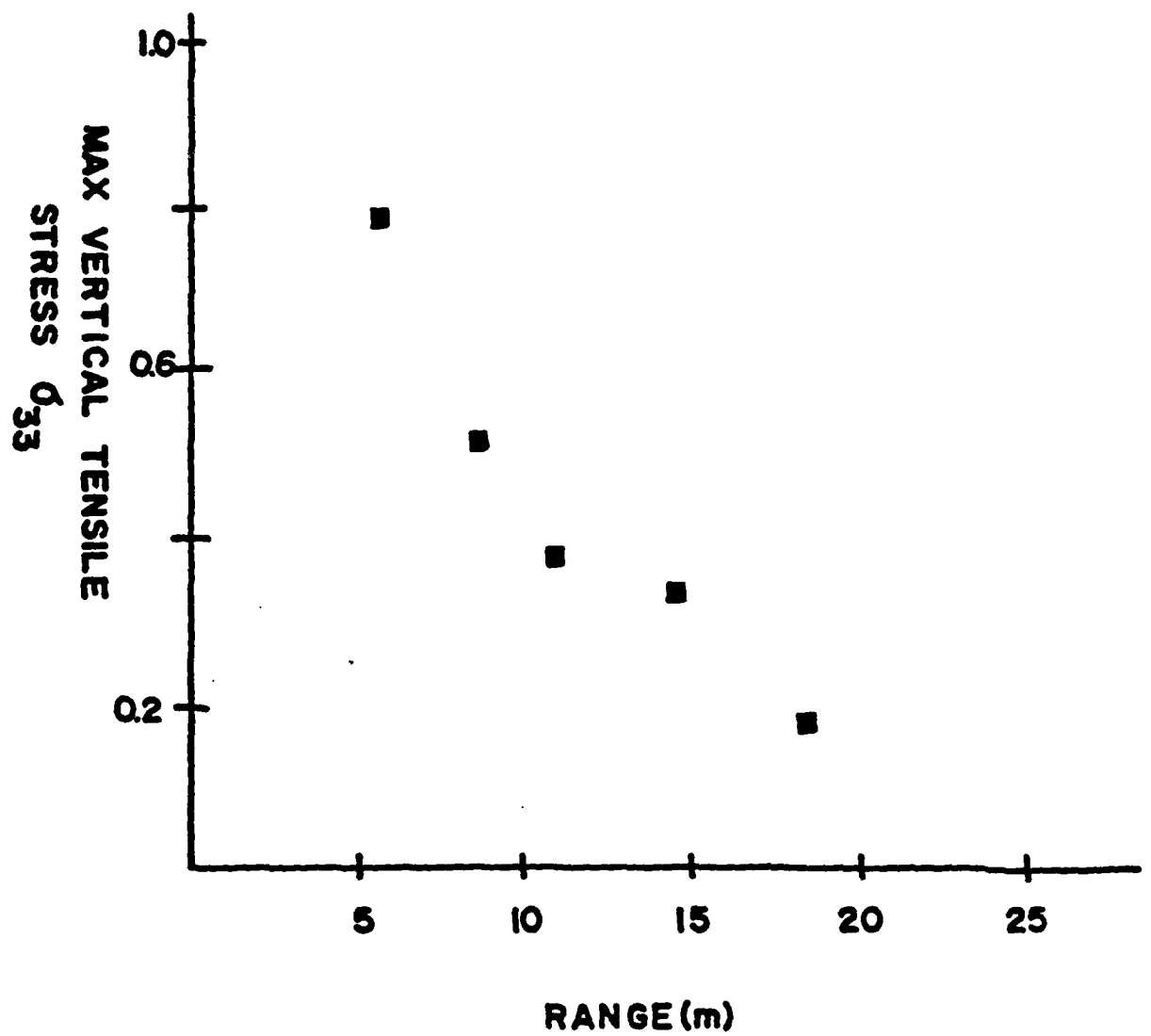


Figure 34

PHG I-06 STRESS PRED.

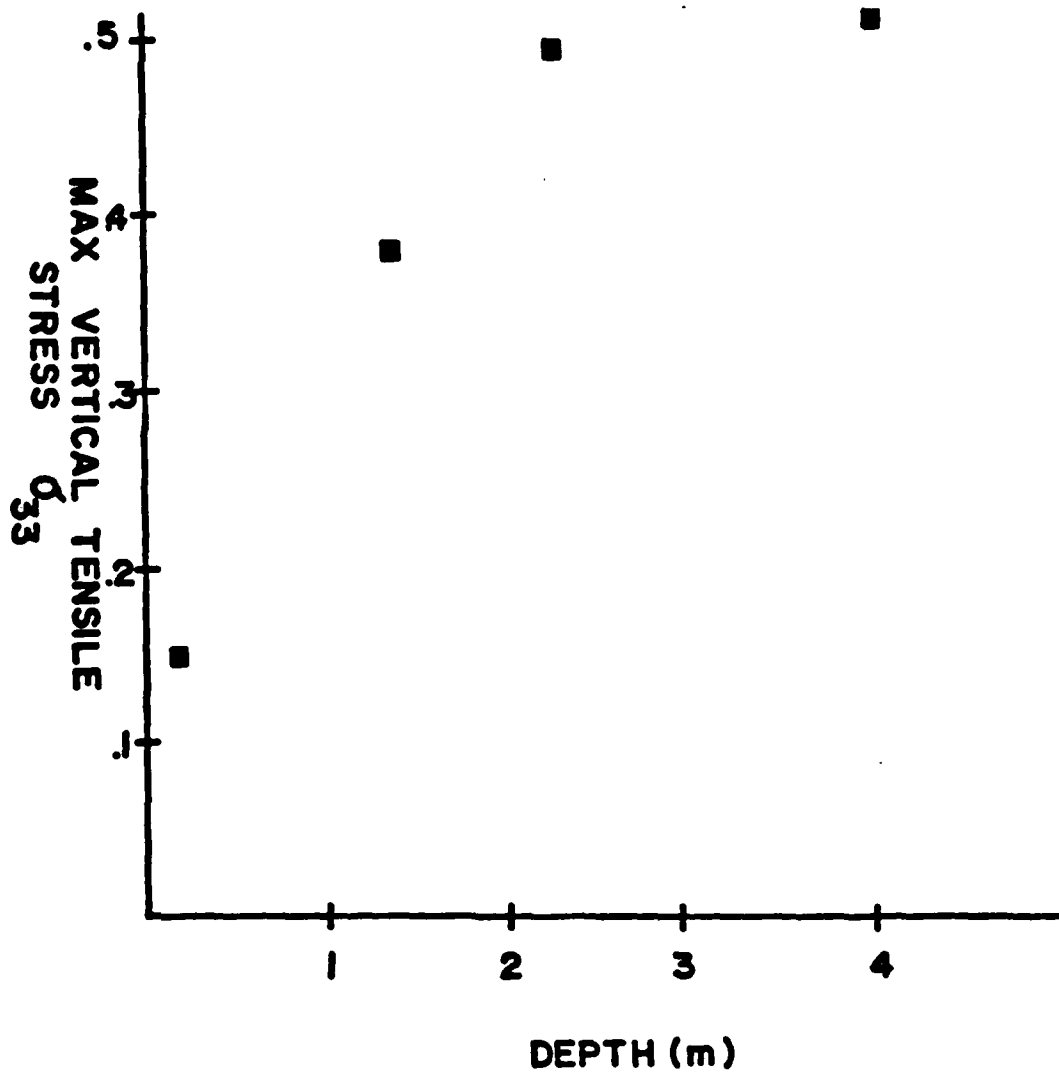


Figure 35

SOURCE SUMMARY PHG 1-04,05,06
poisson's ratio 0.1

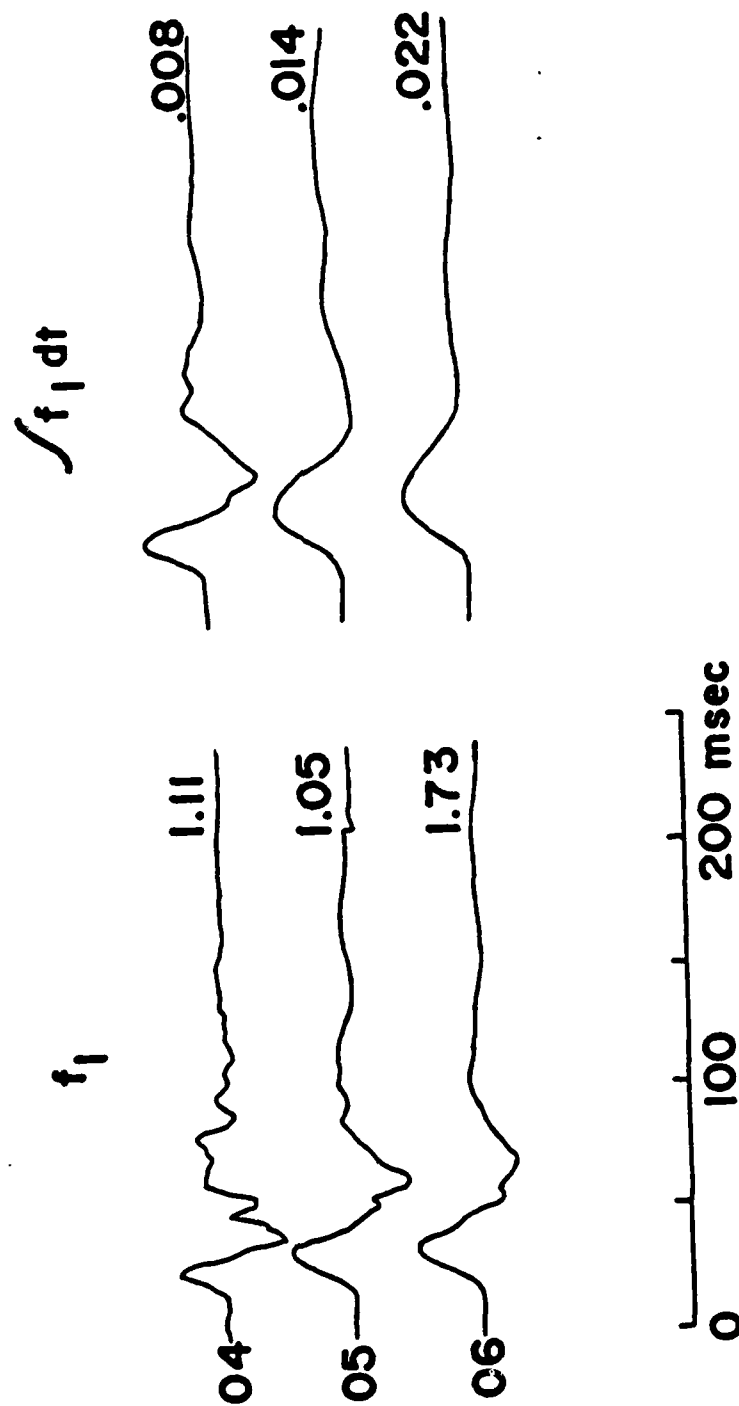


Figure 36

SOURCE SUMMARY PHG I-04.05.06
poisson's ratio 0.1

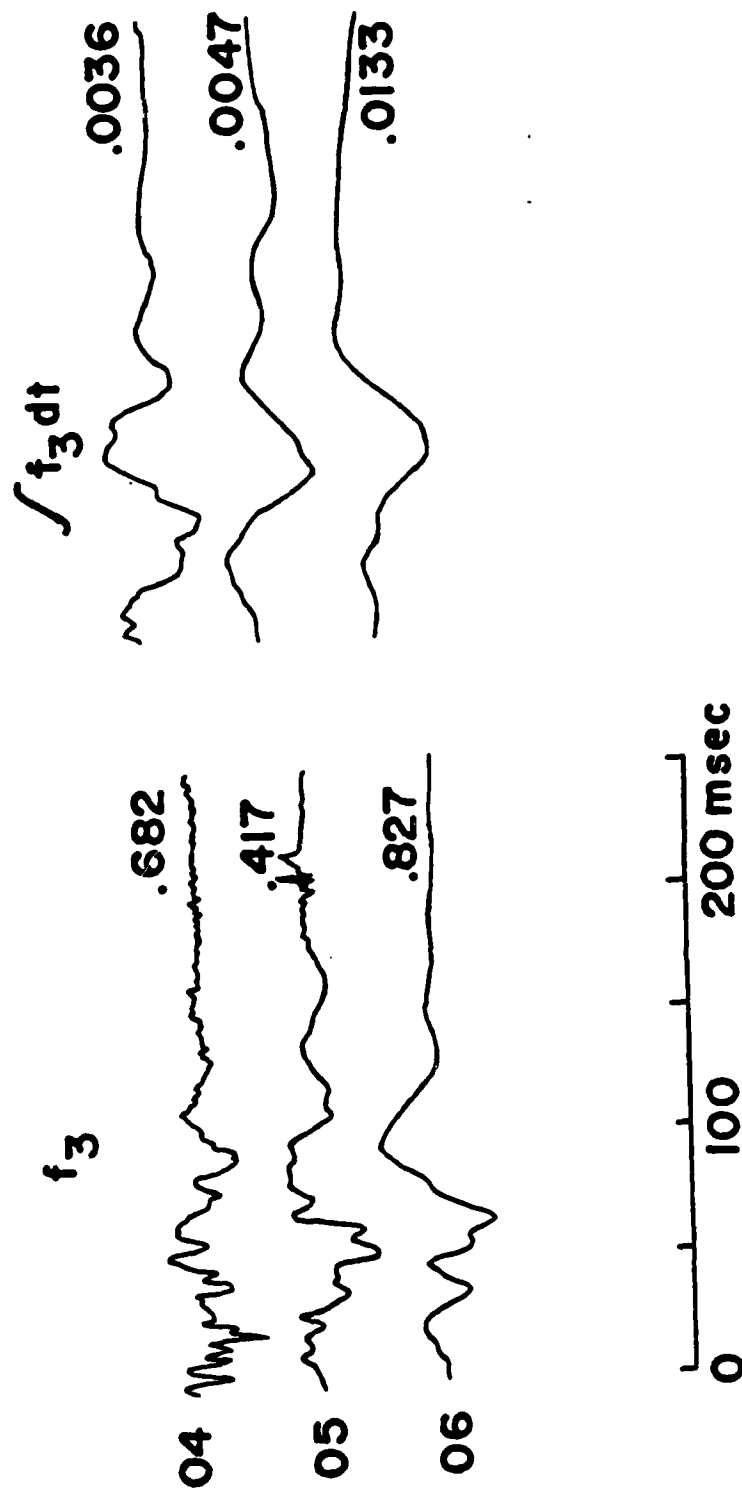


Figure 37

CONTAINED HIGH-EXPLOSIVE

ALLUVIUM TEST

DATA REPORT

BRIAN W. STUMP

ROBERT E. REINKE

AFWL/NTES

KIRTLAND AFB, NEW MEXICO 87117

INTRODUCTION

During August of 1981, the Air Force Weapons Laboratory, in conjunction with personnel from the University of California at Berkeley, instrumented and detonated a chemical explosion of 253 pounds buried at a contained depth of 11.5 meters. The explosive used was a TNT sphere 20 $\frac{1}{2}$ inches in diameter. The test was fired in alluvium.

The purpose of this test was fourfold: (1) We wished to conduct a highly instrumented contained explosive shot in a relatively simple, known geology. Such an experiment would allow a careful characterization of the explosive source from a seismic point of view. (2) The fully contained test, in conjunction with a variety of depth of burst tests (already completed) at the same test site, would allow one to assess the importance of burial depth on source characterization and relative coupling. (3) The fully contained chemical explosion (HE), in conjunction with similar nuclear explosion (NE) data sets from the Nevada Test Site, would allow one to study the differences of NE and HE sources. In particular, we hoped to study the applicability of various scaling relations trying to develop separate procedures for source and propagation path. (4) Spall or tensile failure of the soil as identified by -lg dwells on vertical accelerometers followed by impulsive rejoins on the vertical and radial accelerations was identified on records from a number of surface and near surface bursts. The mechanism of spall for these tests could not be explained in terms of a compressive wave leaving the source reflecting as a tensile wave at the free surface and then failing the material. In order to tie the surface explosion spall data set to the contained nuclear data, a contained chemical explosion was suggested.

We intend to include no analysis in this report. The purpose of this work is to outline the experiment and present the observed data.

TEST OUTLINE

In order to begin the resolution of the four questions already outlined, a contained 253-pound (TNT) chemical explosive test was designed. The test site was chosen to supplement a series of depth of burst studies already completed. The site was plane layered alluvium, close to the Air Force Weapons Laboratory in Albuquerque, New Mexico.

The instrumentation array for the test consisted of three distinct sets. The first part of the instrumentation was made up of close-in accelerometers mainly distributed along one radial (Figure 1). The primary purpose of these gages was to yield good spatial control on the nonlinear processes close to the source and then transition into the near-field part of the instrumentation which will be used for the seismic characterization of the source. We were particularly interested in the timing and propagation direction of the spall phase, so six 2-component gages were placed at a radius of 1 m from GZ in a vertical array. In order to maintain some azimuthal control close-in to the source, two additional azimuths were instrumented at the 3-meter range (Figure 2). All these gages, which were later digitized, were recorded on analog tape. The FM tape drives are run at a high rate of speed, since the shot time is known and the signals quite short. As a result, good signal to noise ratios are obtainable, assuming good preshot ground motion estimates are made. The data from this test were digitized at 5000 samples per second with a 5-pole butterworth filter at 1250 Hz. A total of 48 gages were fielded.

The so-called near-field array was fielded with the help of Lane Johnson and Tom McEvelly from the University of California at Berkeley. The primary design of this part of the instrumentation was to give a data set which could be used to characterize the explosive test seismically. Simple cube root of yield scaling was used to give array dimensions comparable to the 2-20 km

spacings we have used previously for nuclear shots at NTS. A surface view of the near-field array, along with some of radial close-in gages, is given in Figure 3. The near-field array spanned the 50 to 150-meter range with the largest azimuthal separation of gages being 60° . Each station consisted of a 3-component force balanced accelerometer recorded by the DR-100 digital event recorder. The data were sampled at 200 samples per second with a 5-pole butterworth filter at 50 Hz. Eleven stations were fielded for a total of 33 possible records.

The final instruments were placed at 1.6 km north and west of the shot point. From previous tests, it has been learned that at these distances, fundamental and higher mode surface waves become important. Each station consisted of a 3-component Sprengnether S-6000 velocity gage recorded by a Terra Technology digital event recorder. The data were sampled at 200 samples per second with 5-pole butterworth filters at 70 Hz. Two stations 60 meters apart north and one station west of the shot were fielded for a total of 9 components of motion.

DATA SUMMARY

All the data recorded from this experiment are reproduced in this report. Of the 48 close-in gages, 45 were recorded, two of which clipped--gages 1334 and 1337. Figures 4 through 12 contain the close-in data. The signal quality and signal to noise ratios are good for the data set. Longer time windows are available as the analog tape recorders were run for five minutes following the explosion.

The near-field 3-component accelerometer data in the 50 to 150-meter range are illustrated in Figures 13 through 17. Of the 33 gages fielded, 28 yielded satisfactory data.

Finally, the 3-component far-field velocity data are given in Figures 18 through 20. Nine out of nine gages operated satisfactorily, yielding good quality data.

Out of 90 total gages fielded in this experiment, 82 yielded good quality data for a 91 percent return rate on instrumentation. The signal to noise ratio of all the data is high (50 db or more) and so will warrant careful analysis.

EXPLOSIVE

The spherical charge was 20 $\frac{1}{4}$ " in diameter and was made of TNT. The burn rate of TNT is approximately 20,000 ft/sec giving a detonation time of 42 microseconds. To check this estimate, a number of similar TNT spheres were instrumented with time of arrival crystals which break when the explosive front reaches them. The data from these crystals for a 1000-pound TNT sphere are summarized in Figure 21. Assuming it takes 8.7 microseconds to break the time of arrival crystal (supported by experimental evidence), the burn time for the sphere was 55.8 microseconds with a maximum 2-microsecond variation across the sphere. These numbers yield a burn rate of 24,492 ft/sec and a burn time for our 253-pound TNT sphere of 34.5 microseconds.

GEOLOGY SUMMARY

The geology of the alluvial test site has been extensively studied. Downhole logging, as well as P and S wave refraction surveys, has been conducted (Stump and Reinke, 1982). A summary of some of the P wave refraction data is given in Figures 22 and 23. By using this data, other surveys, geological hole logs, and first arrival time data from explosive shots at the site, the average velocity structure of Figure 24 was arrived at. A simple 3-layer over a half-space structure appears appropriate. The effect of these layers will certainly depend on the wavelength of the energy passing through the structure. Much of the observational waveforms indicate that at some ranges, a simple half-space may adequately model the data.

FUTURE WORK

We feel a high quality data set giving good close-in and near-field coverage of a contained explosive source has been created. With this data set, we intend to characterize the source in the nonlinear regime including fairly sophisticated material models and do an equivalent elastic representation of the source from a seismic point of view. It is hoped that the nonlinear modeling of the source will allow us to understand the physics of the phenomena occurring very close to the explosive and that this physics can be used to explain the equivalent elastic source representation developed from the near-field seismic data.

Comparison of the modeling and source characterization of this scaled chemical explosion to similar work on contained nuclear explosions will allow investigation of chemical and nuclear explosive differences and problems in scaling. We are particularly interested in pursuing the idea of scaling the propagation path and the source separately.

In the long term, it is hoped that a series of these small scaled experiments may be conducted in a variety of geologic materials. This work should allow us to determine the influence material responses have on the seismic source characterization. We hope these experiments could include material asymmetries, such as faults and bedding planes.

AFWL CLOSE-IN STATIONS CHEAT

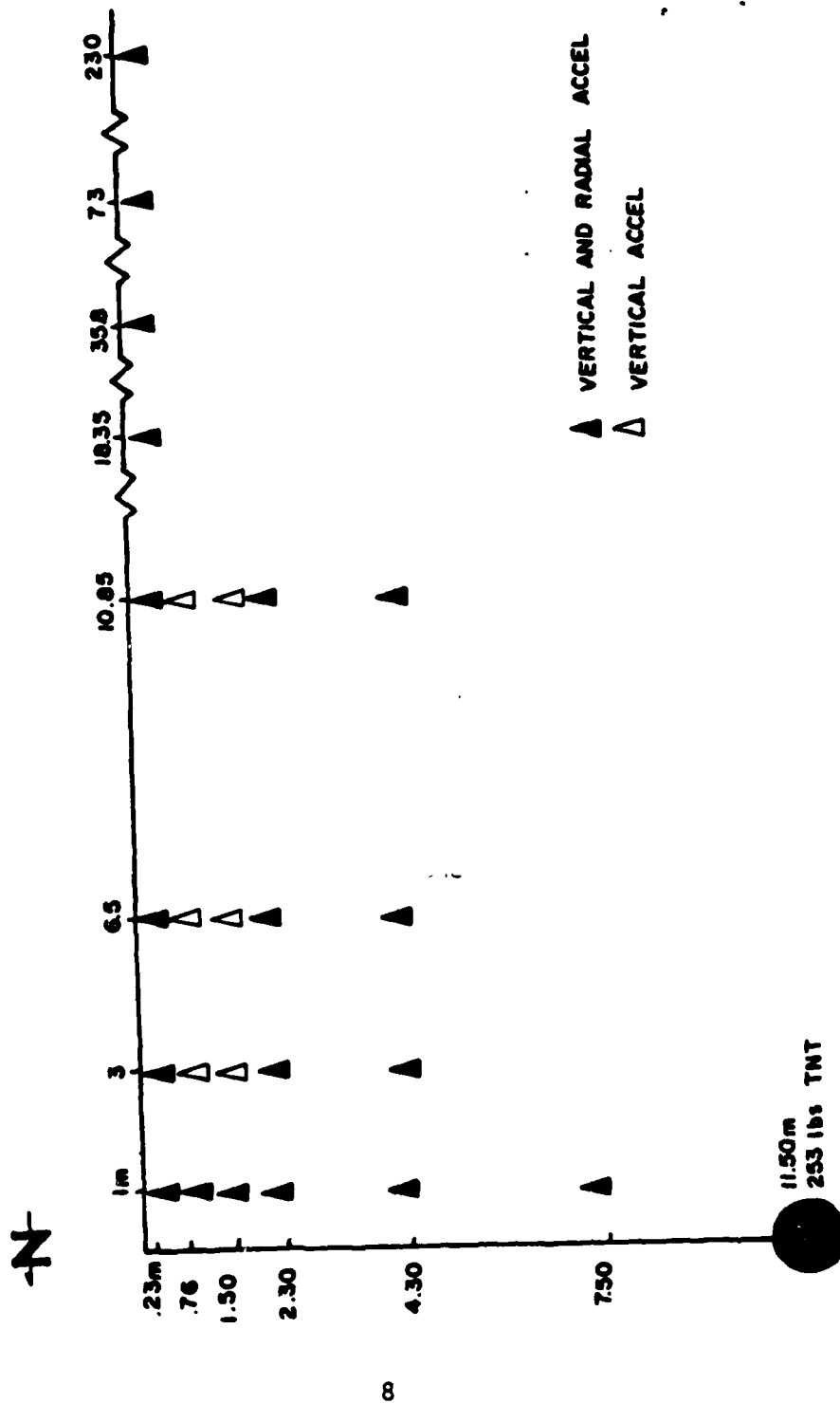


Figure 1

AFWL CLOSE-IN STATION PLANS CHEAT

▲
3 m

▲
3 m

GZ
+

▲
1 m

▲
3 m

▲
6.5 m

▲
10.85 m

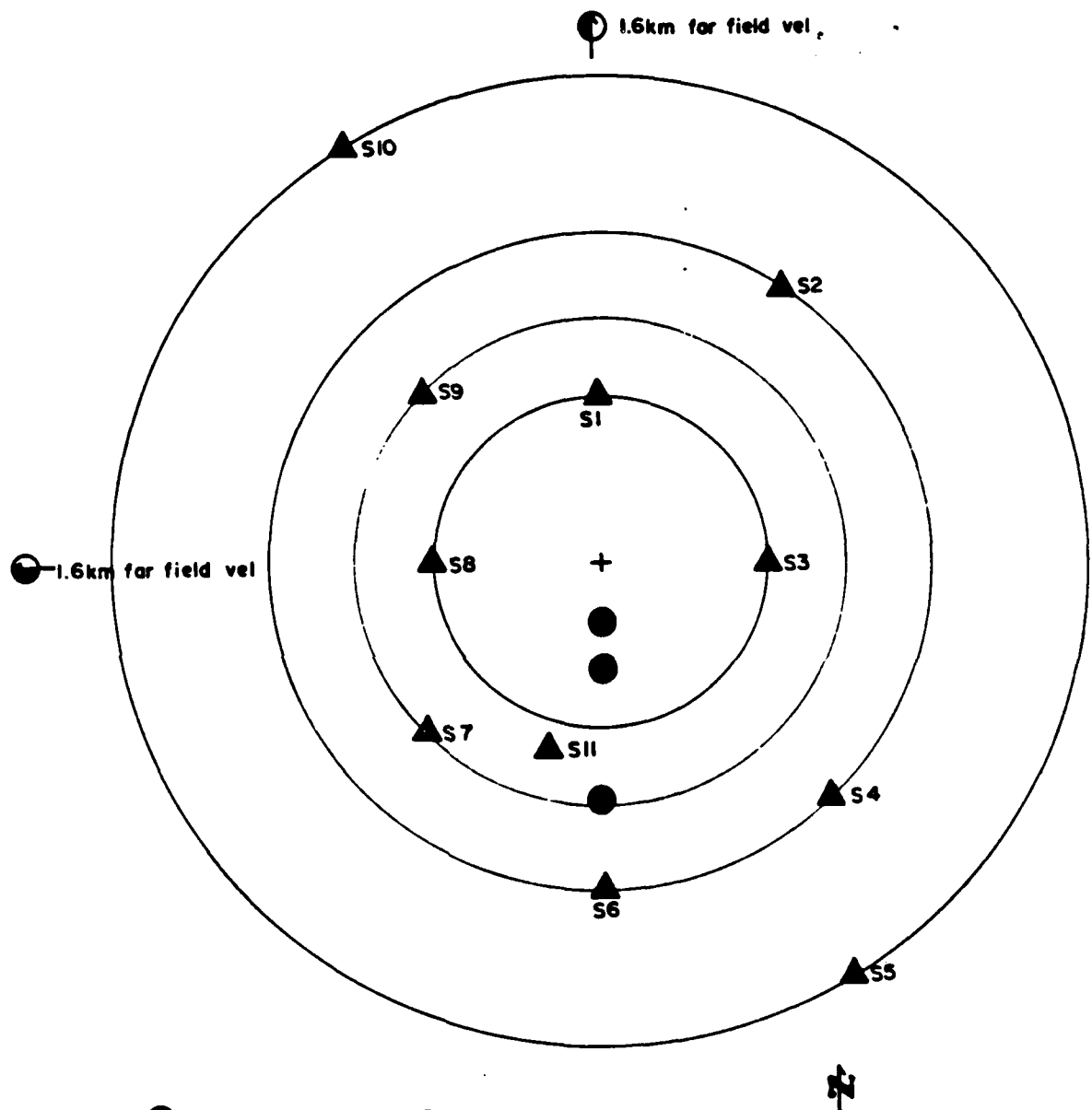
N

1 m

▲
18.35 m

Figure 2

CHEAT DISTANT STATIONS



- AFWL 2 COMP ACCEL
- ▲ UC BERKELEY 3 COMP ACCEL

50 m

Figure 3

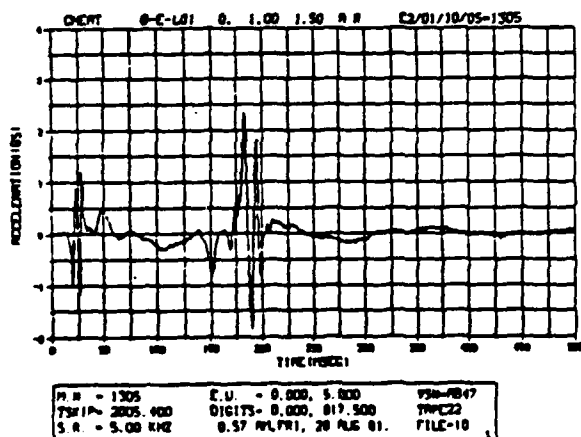
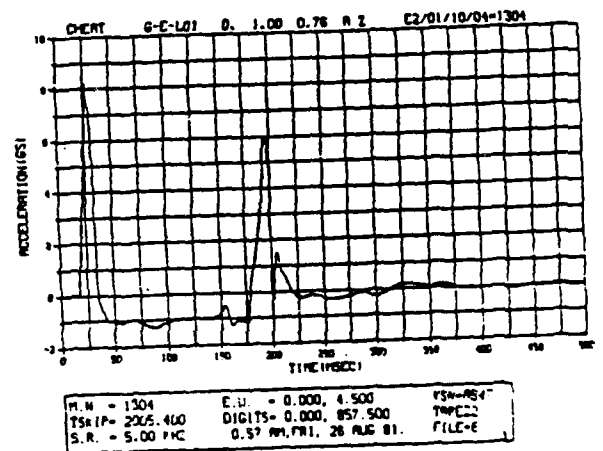
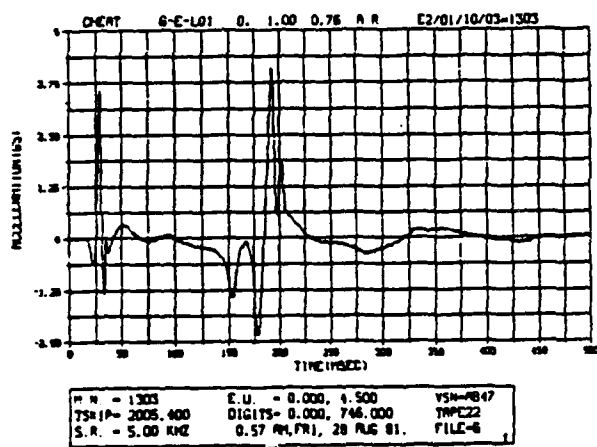
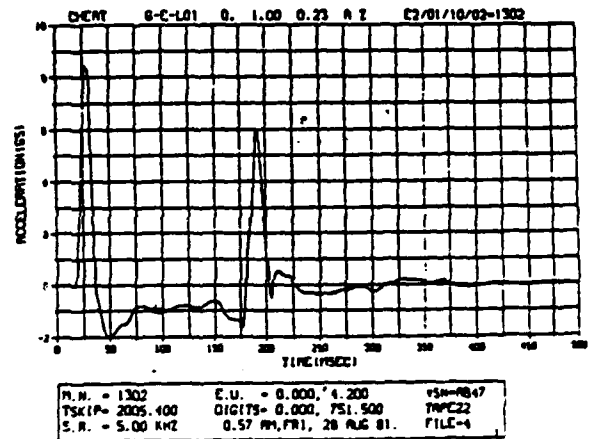
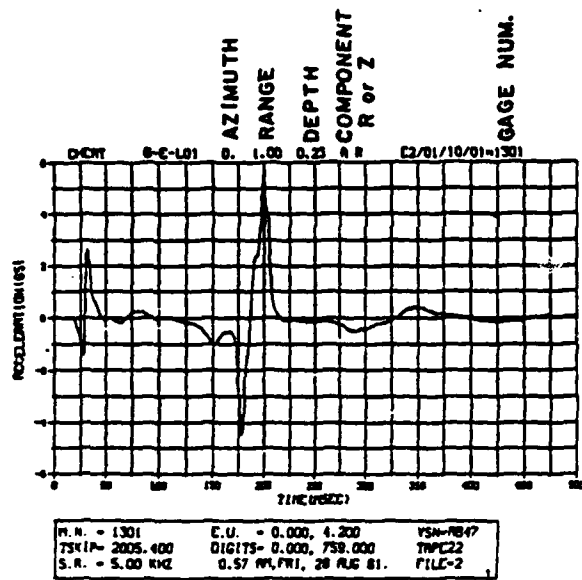
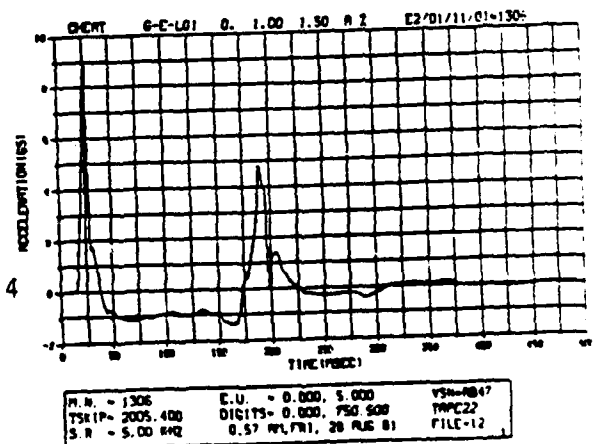


Figure 4



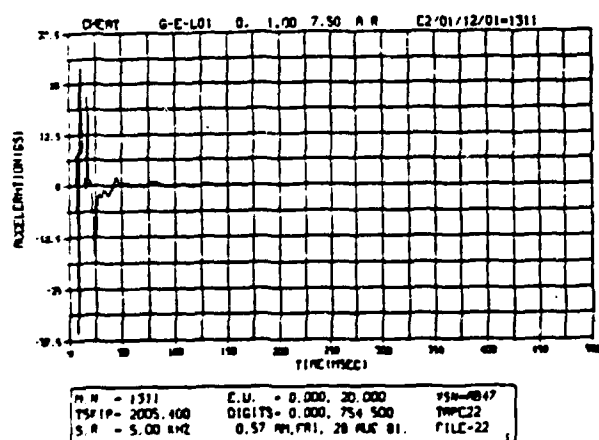
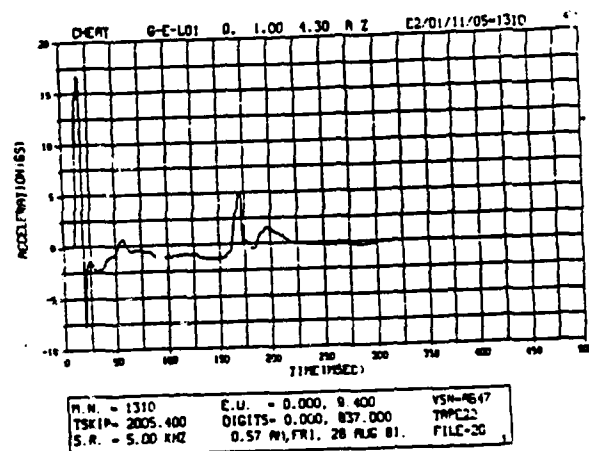
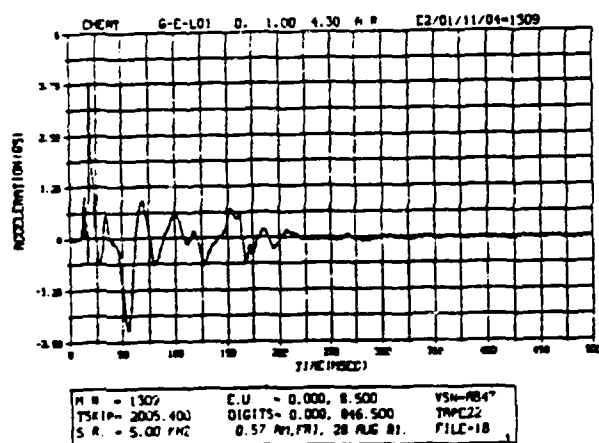
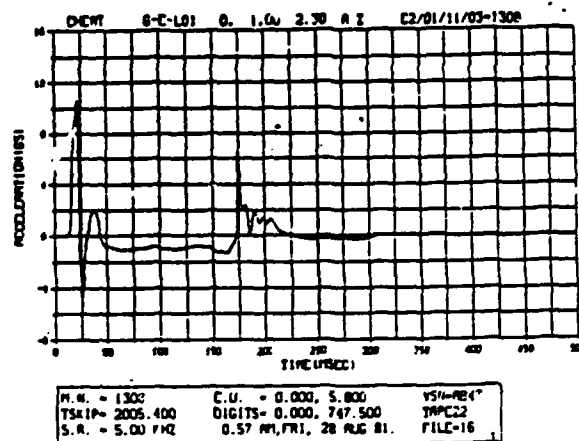
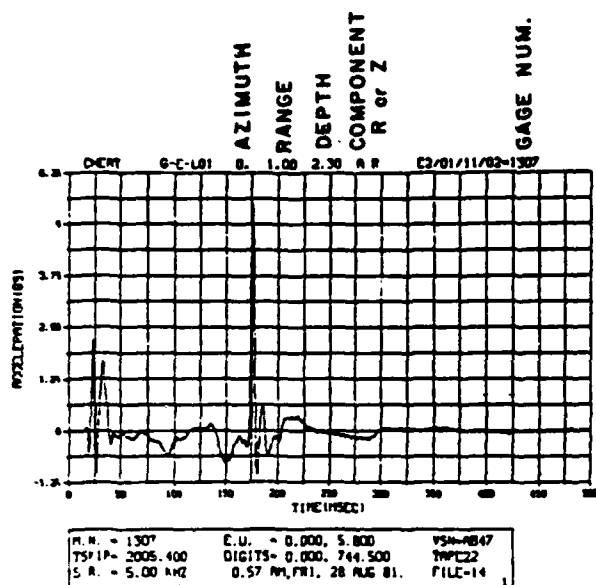
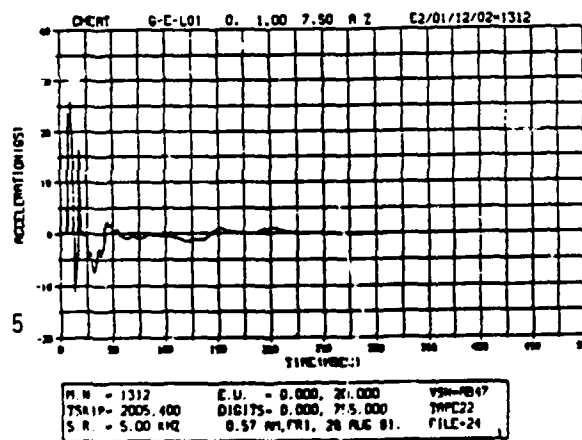


Figure 5



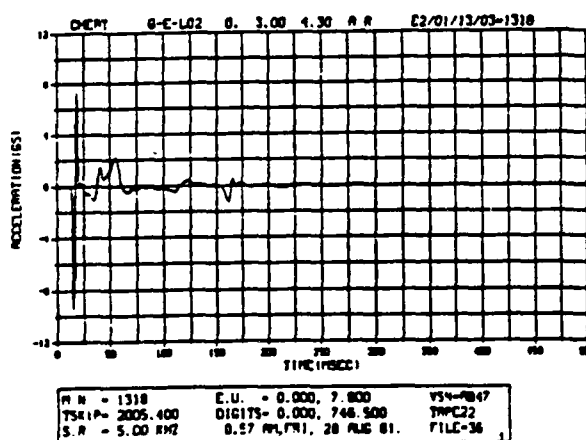
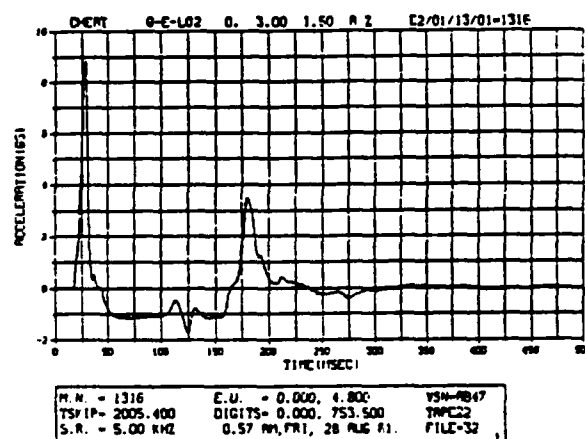
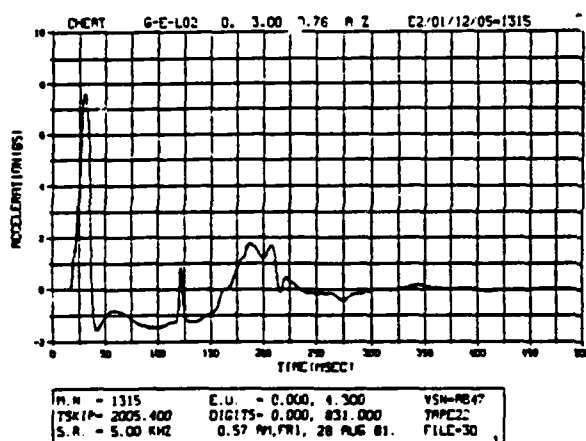
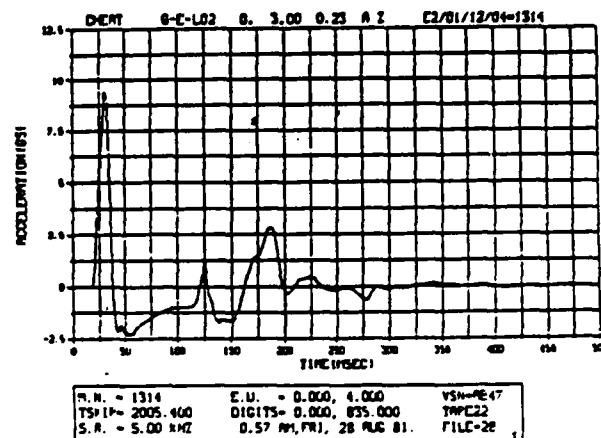
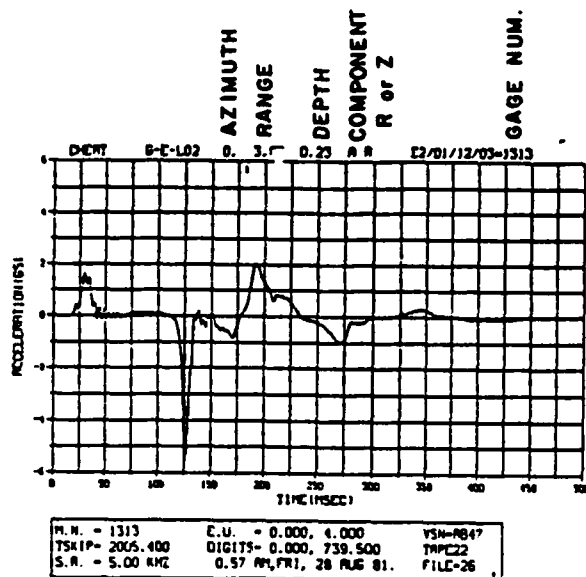
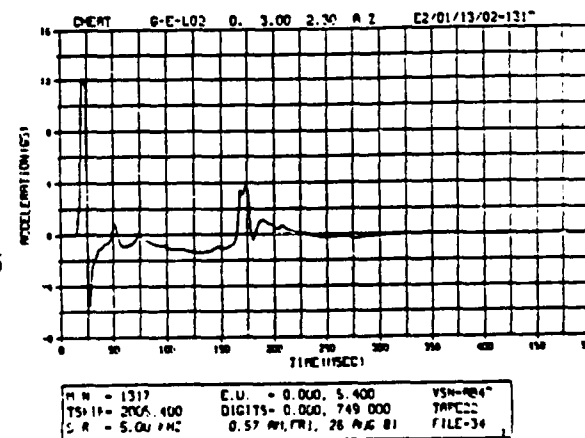


Figure 6



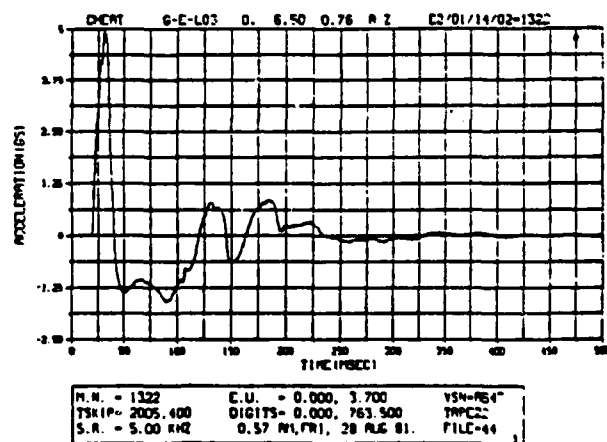
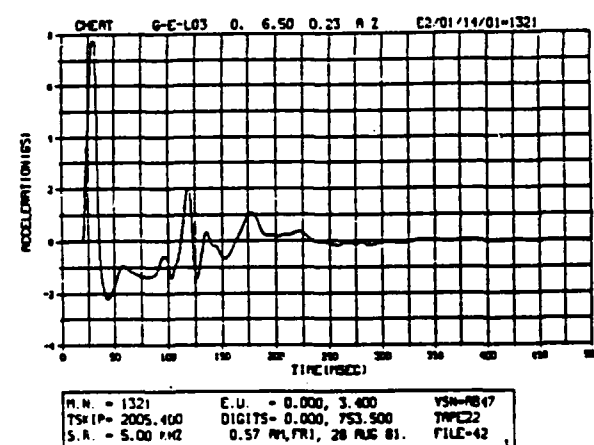
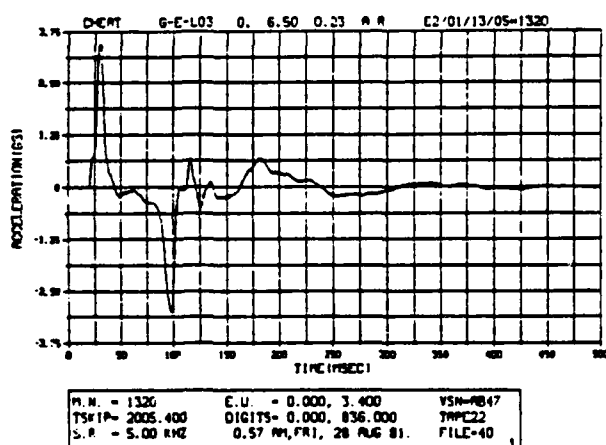
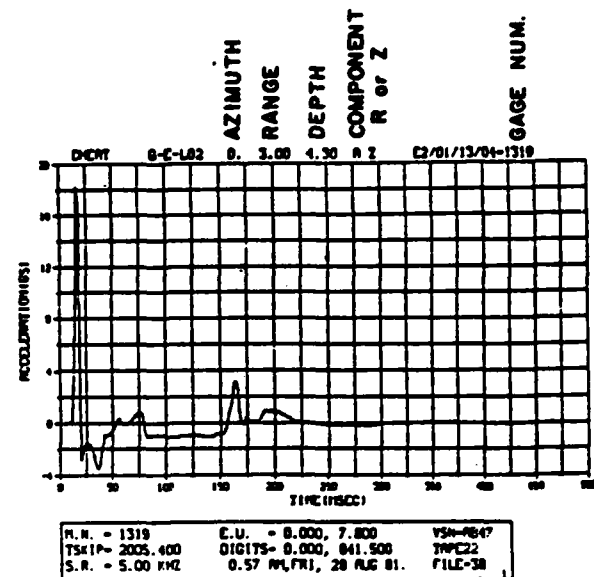


Figure 7

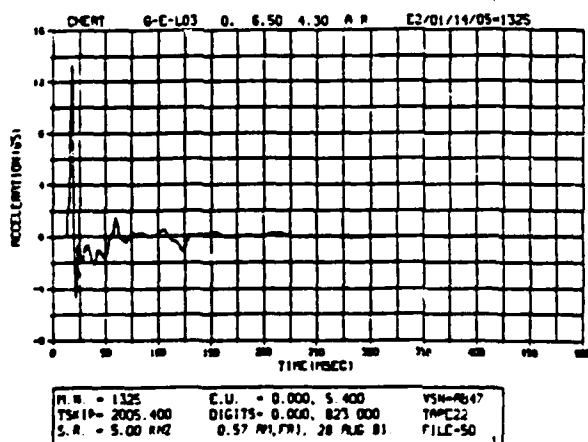
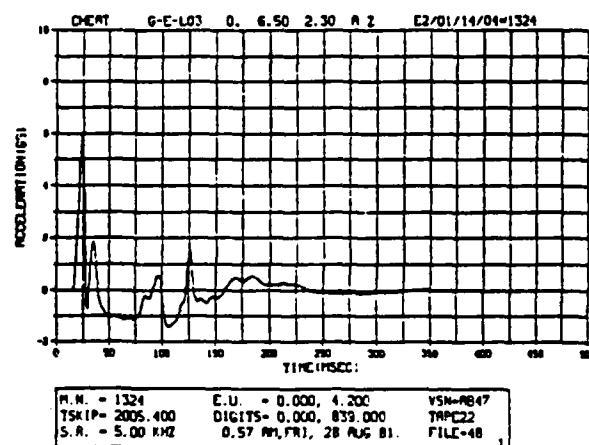
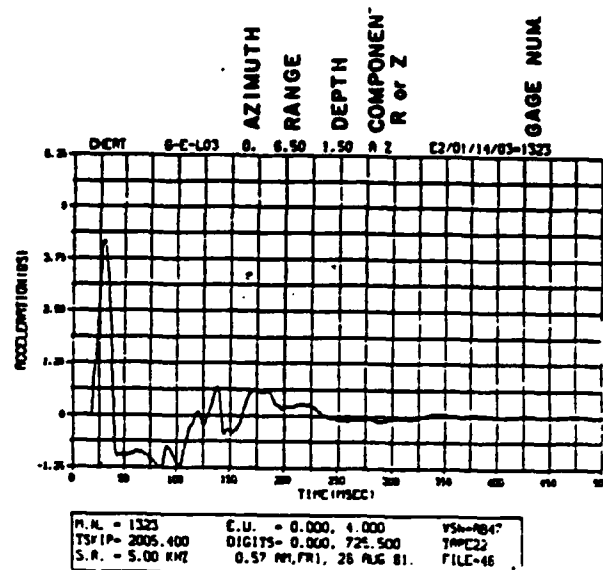
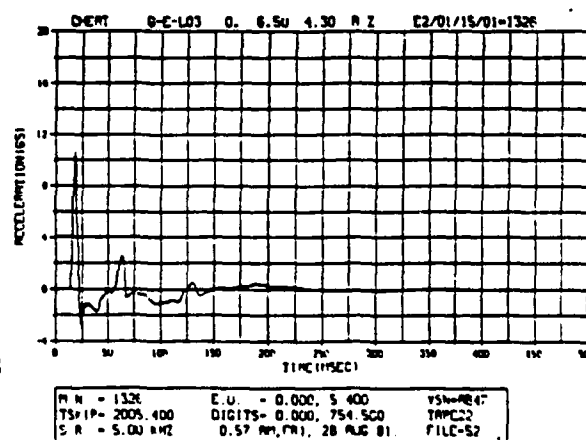


Figure 8



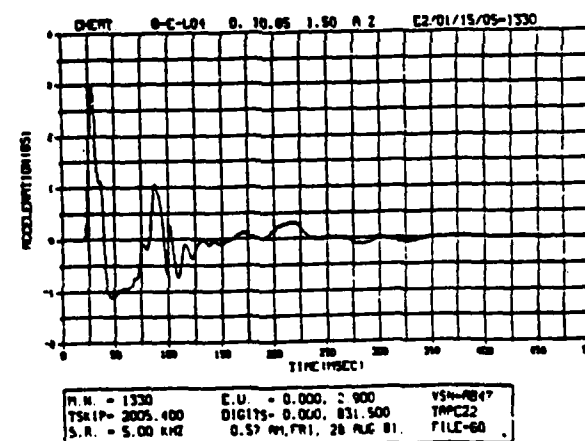
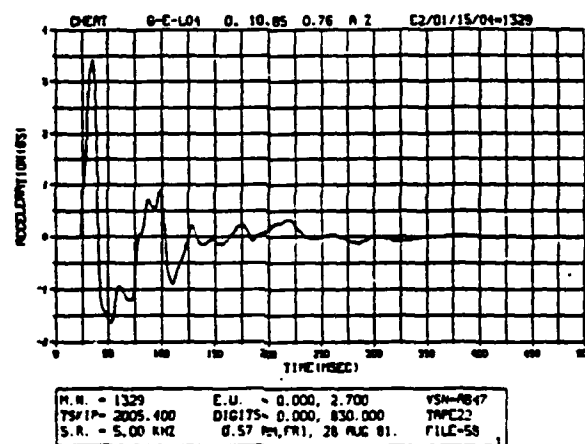
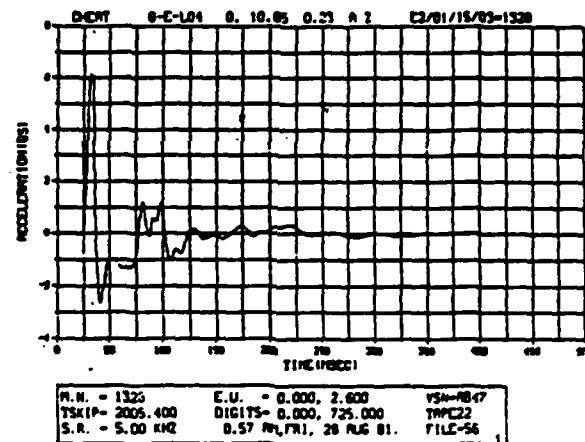
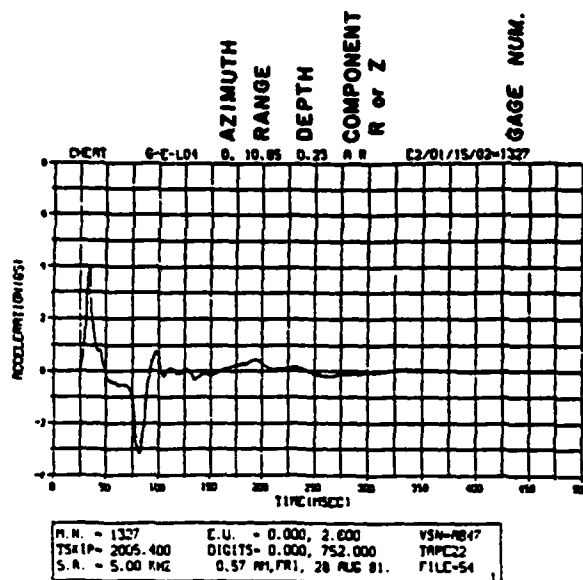


Figure 9

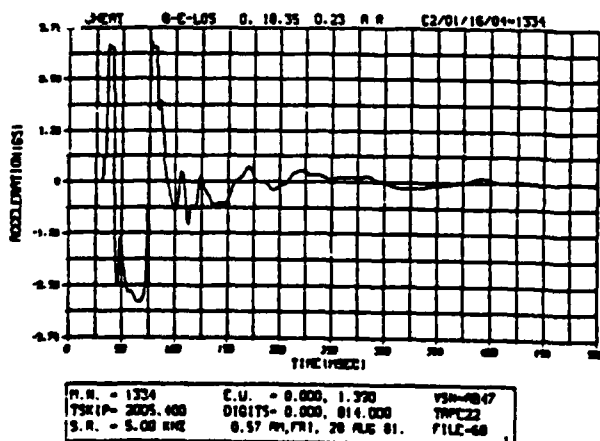
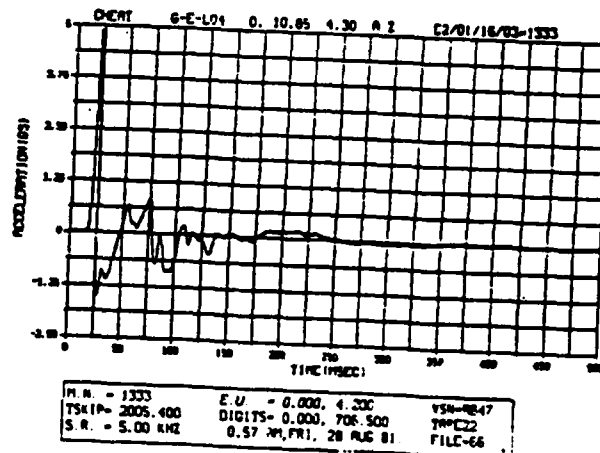
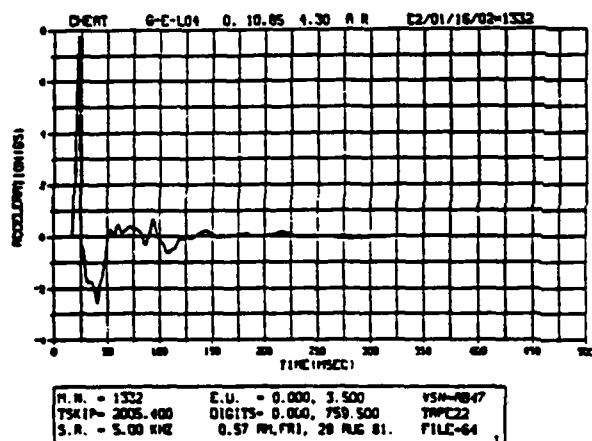
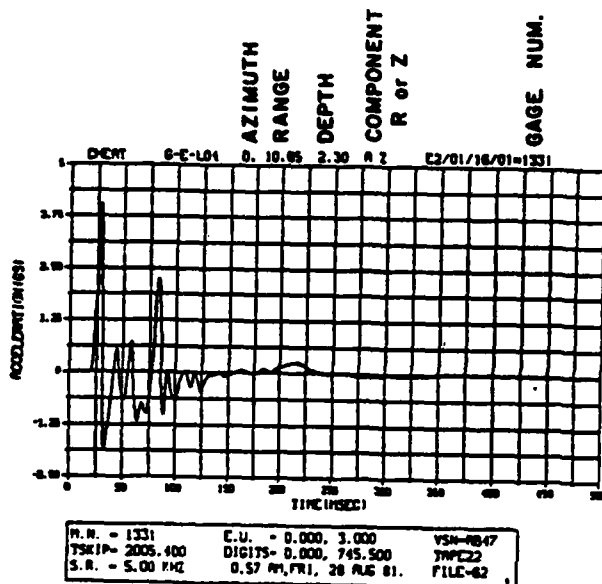
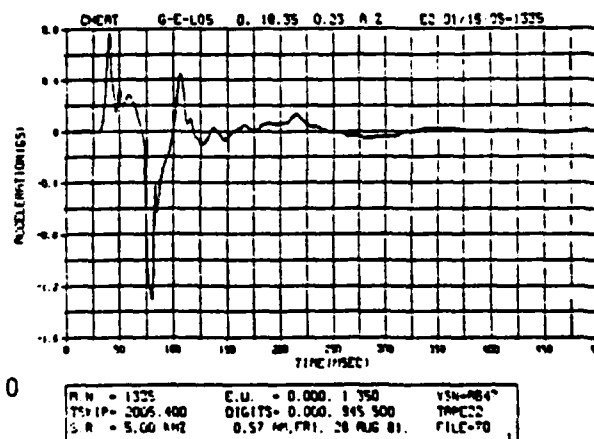


Figure 10



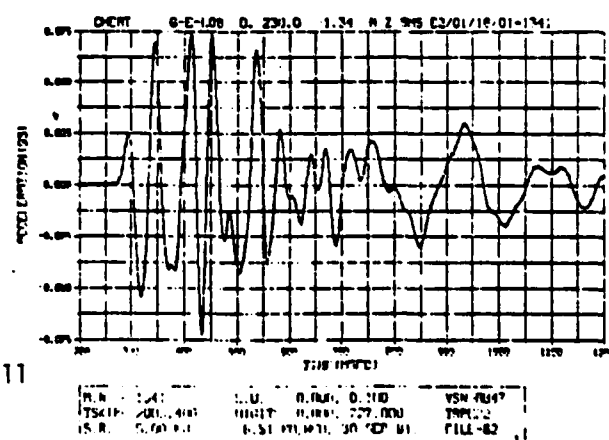
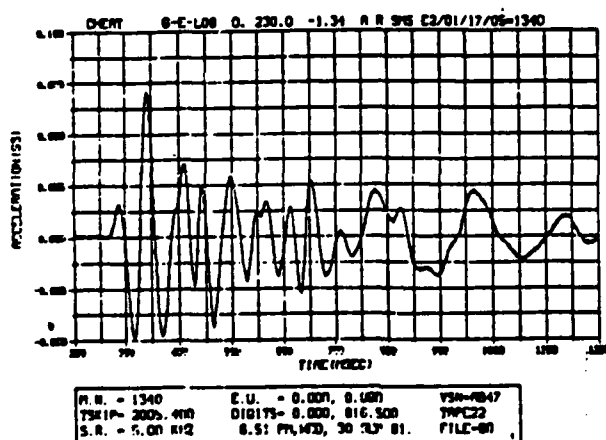
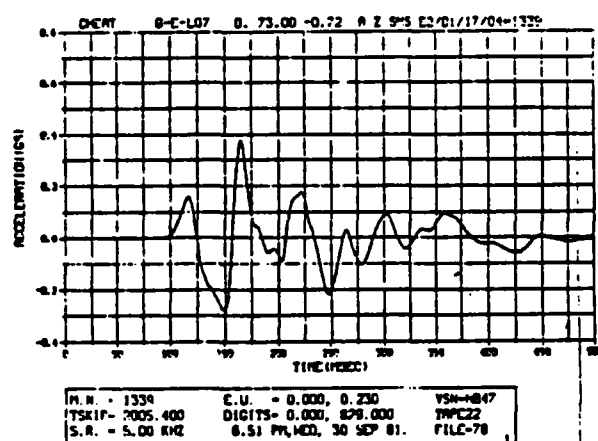
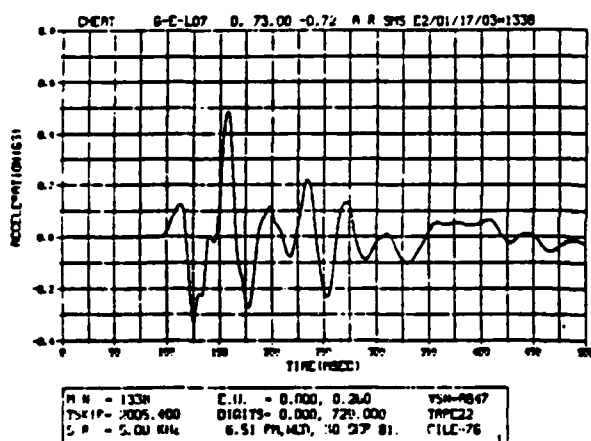
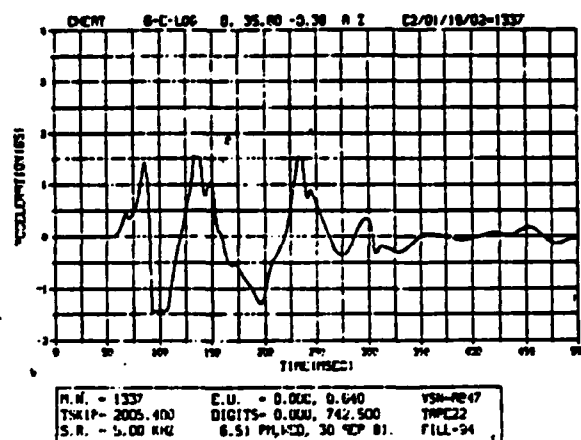
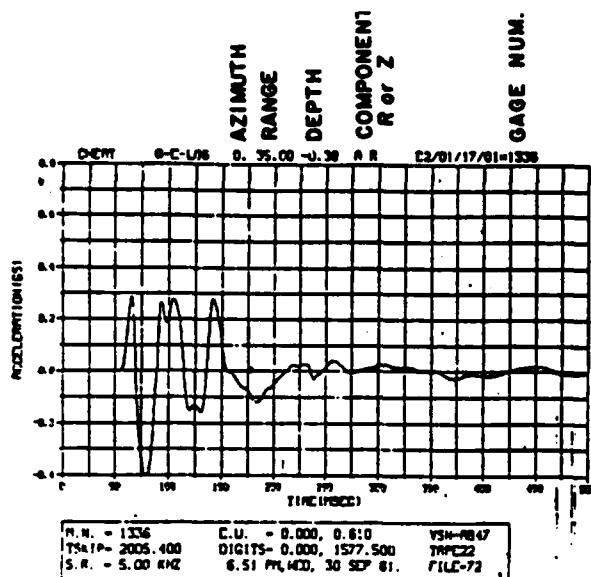


Figure 11

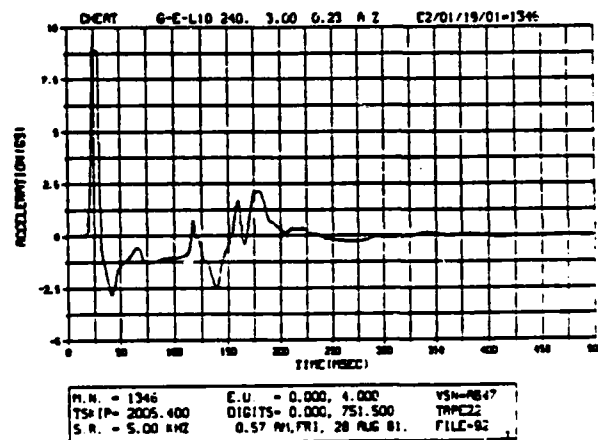
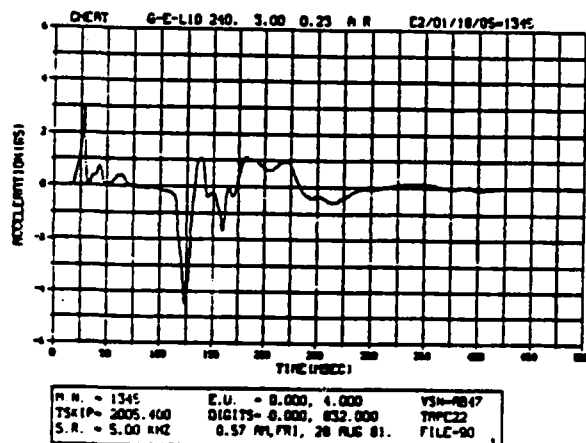
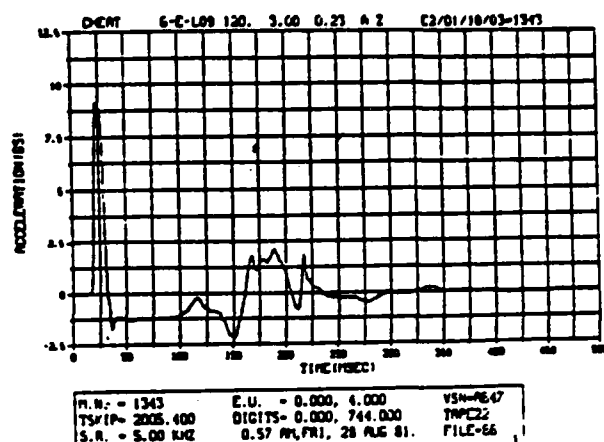
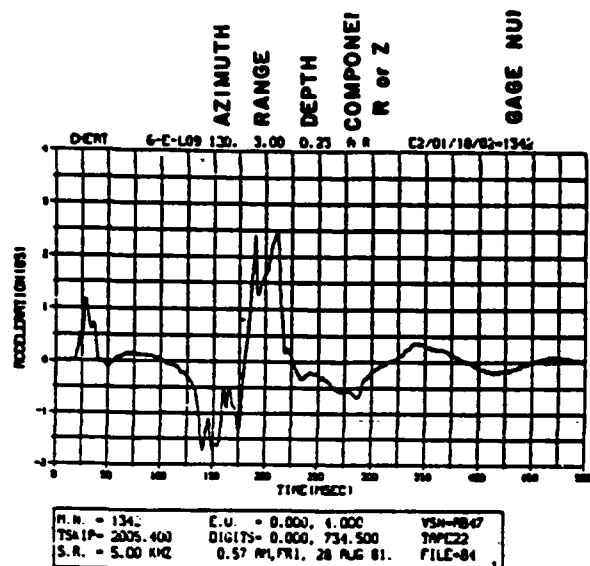


Figure 12

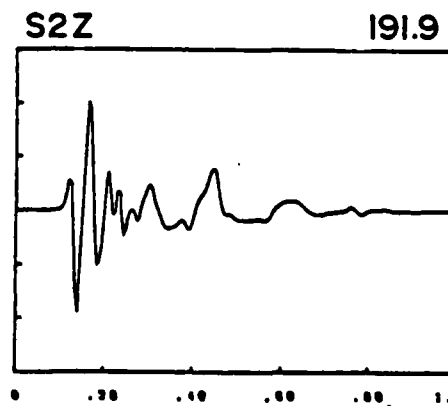
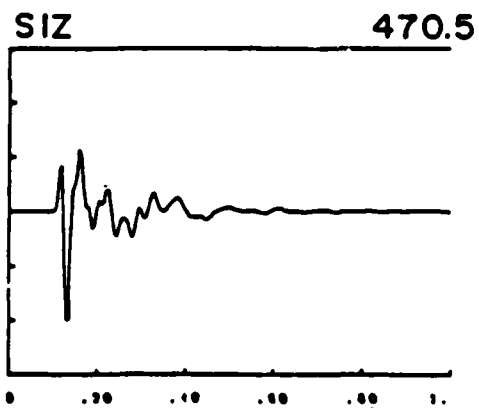
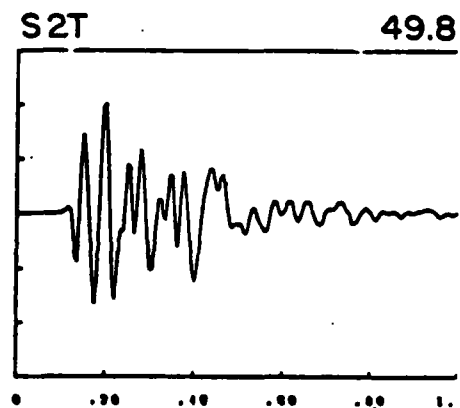
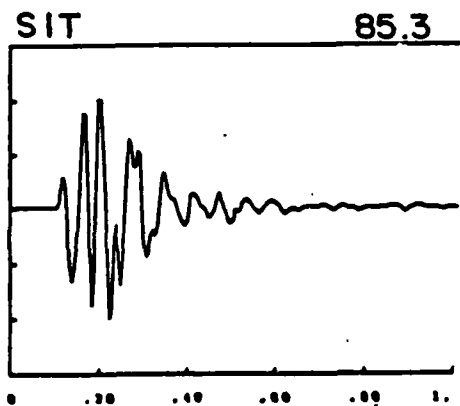
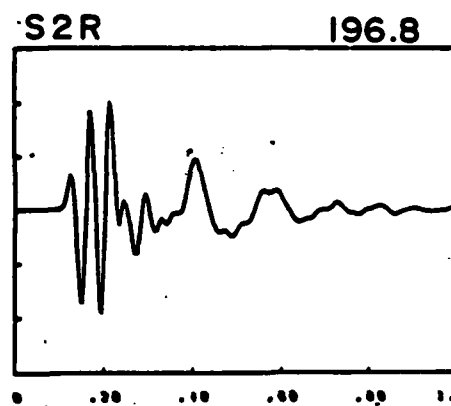
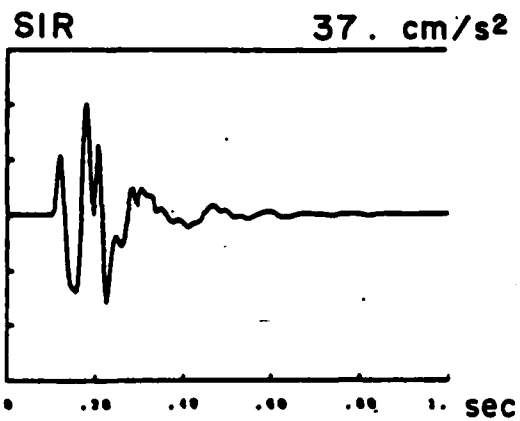


Figure 13

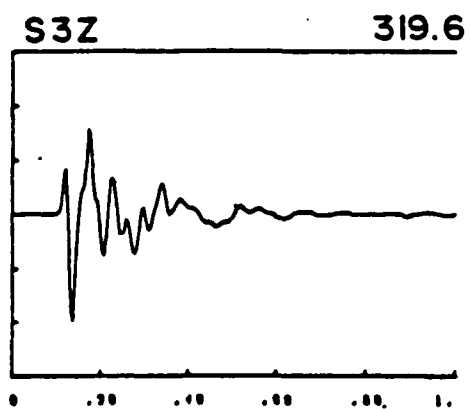
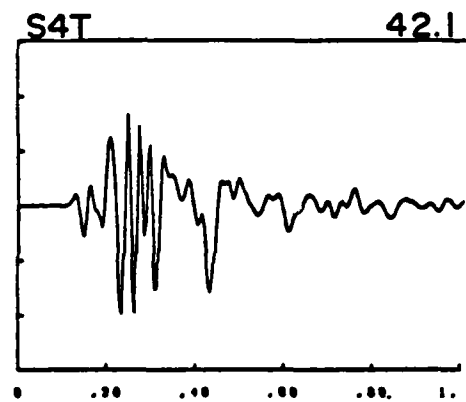
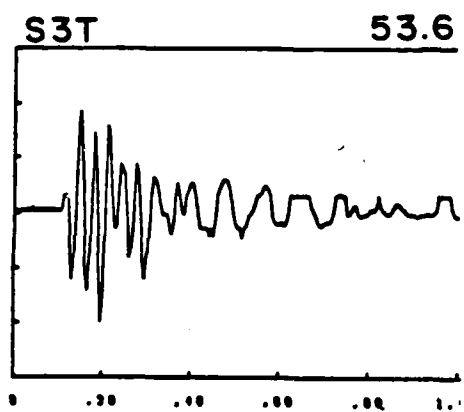
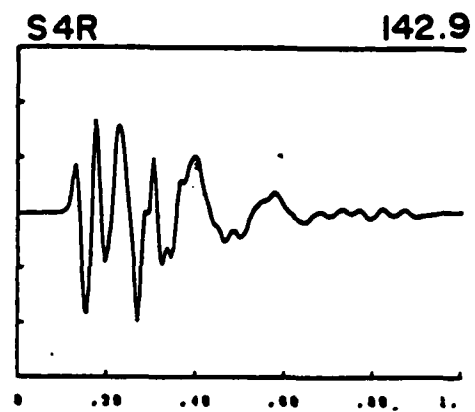
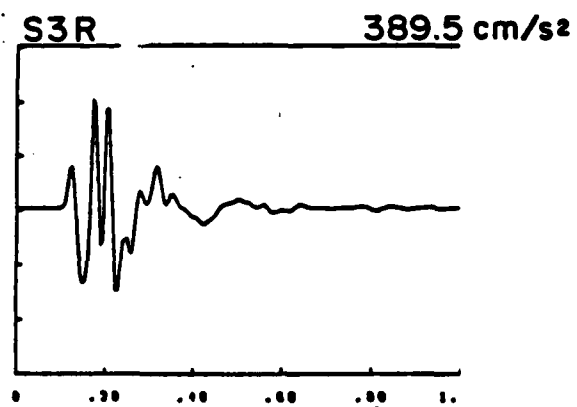


Figure 14

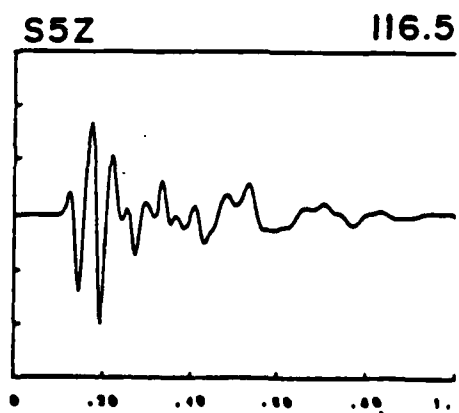
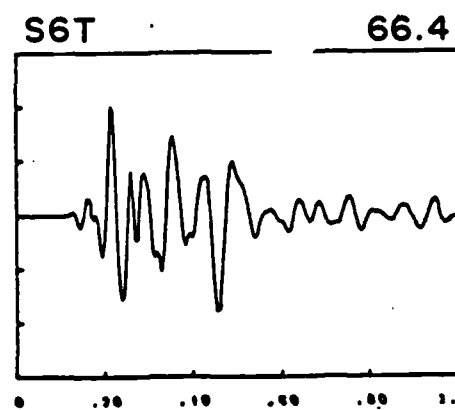
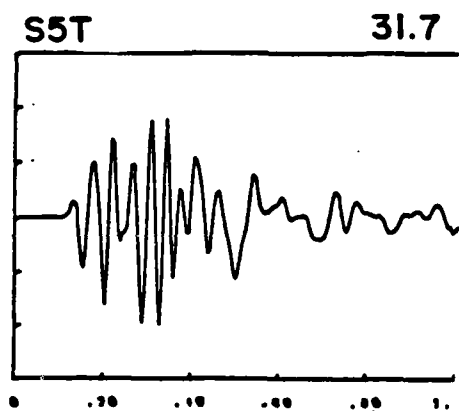
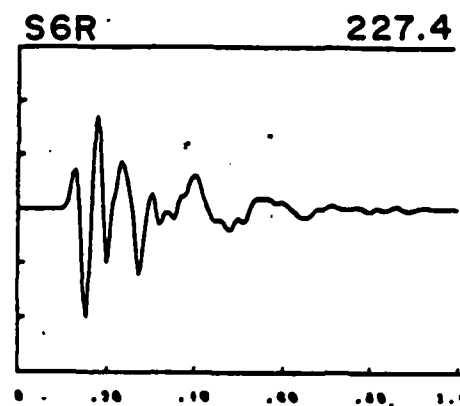
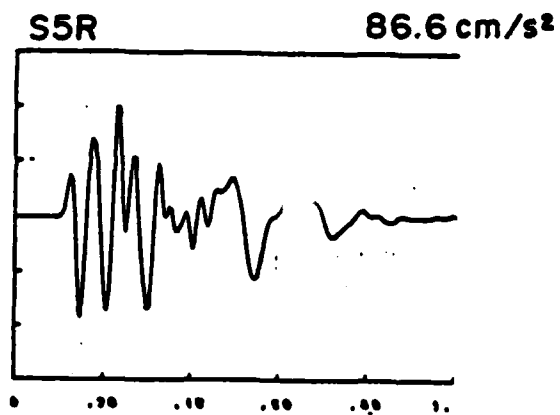
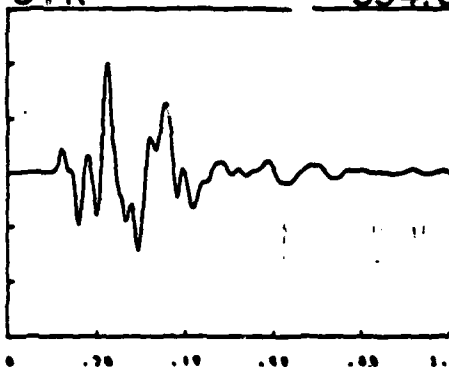
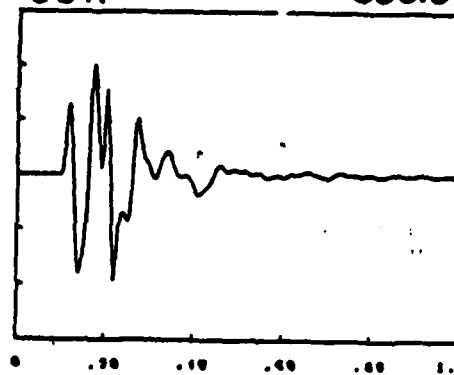


Figure 15

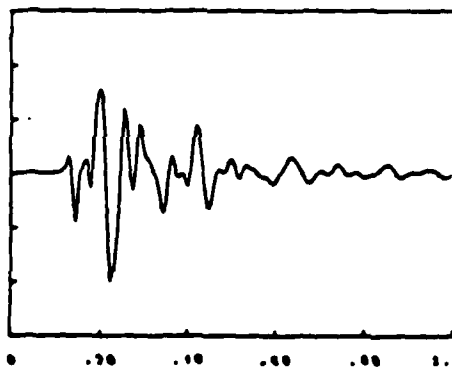
S7R 394.0 cm/s²



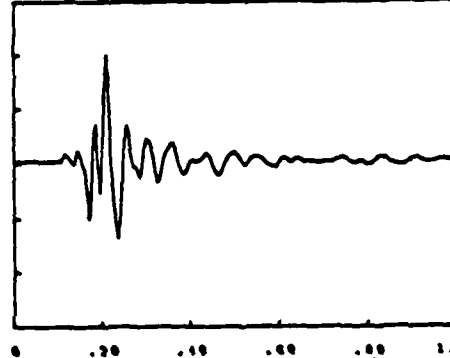
S8R 356.5



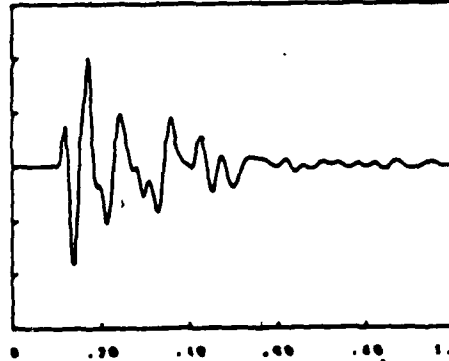
S7T 197.5



S8T 157.1



S7Z 328.7



S8Z 316.6

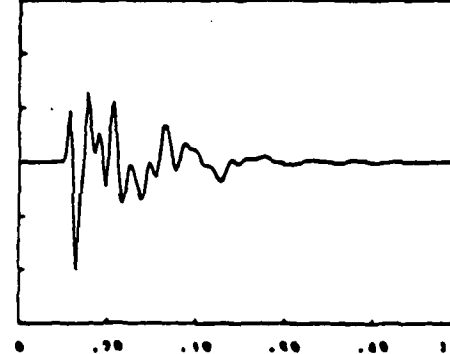
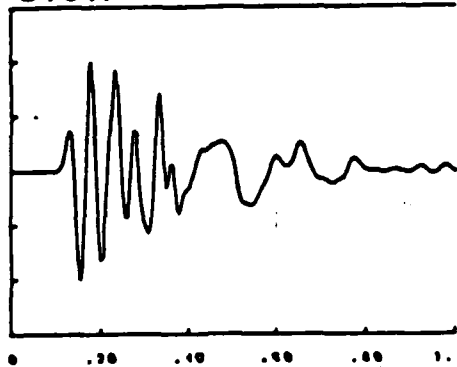
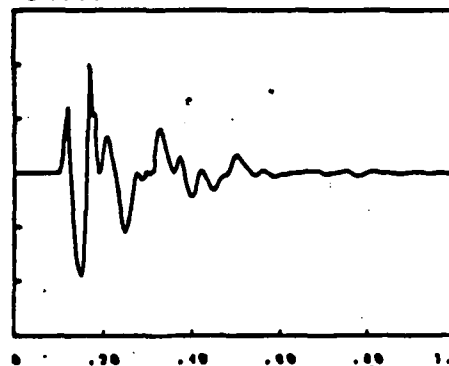


Figure 16

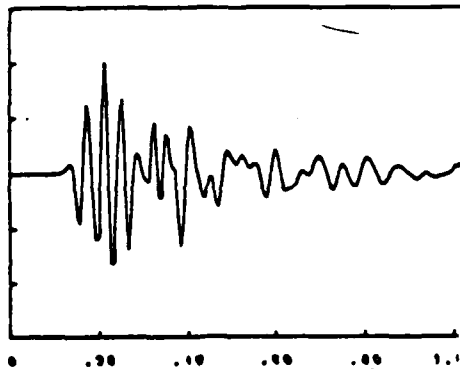
SIOR 95.7 cm/s²



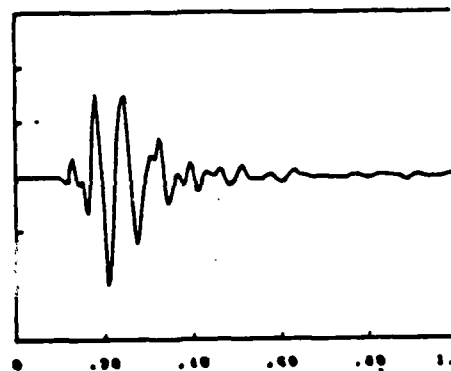
SIIR 322.2



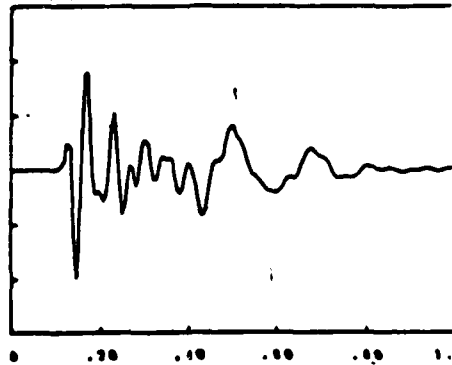
SLOT 31.3



SIIT 177.0



SIOZ 86.1



SIIZ 291.9

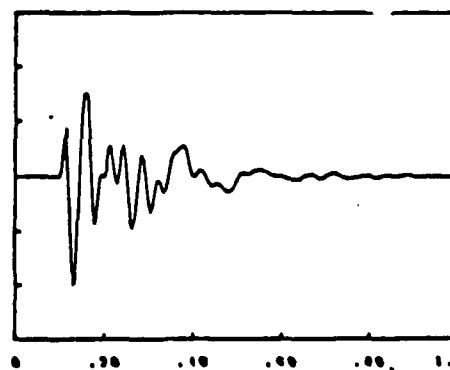


Figure 17

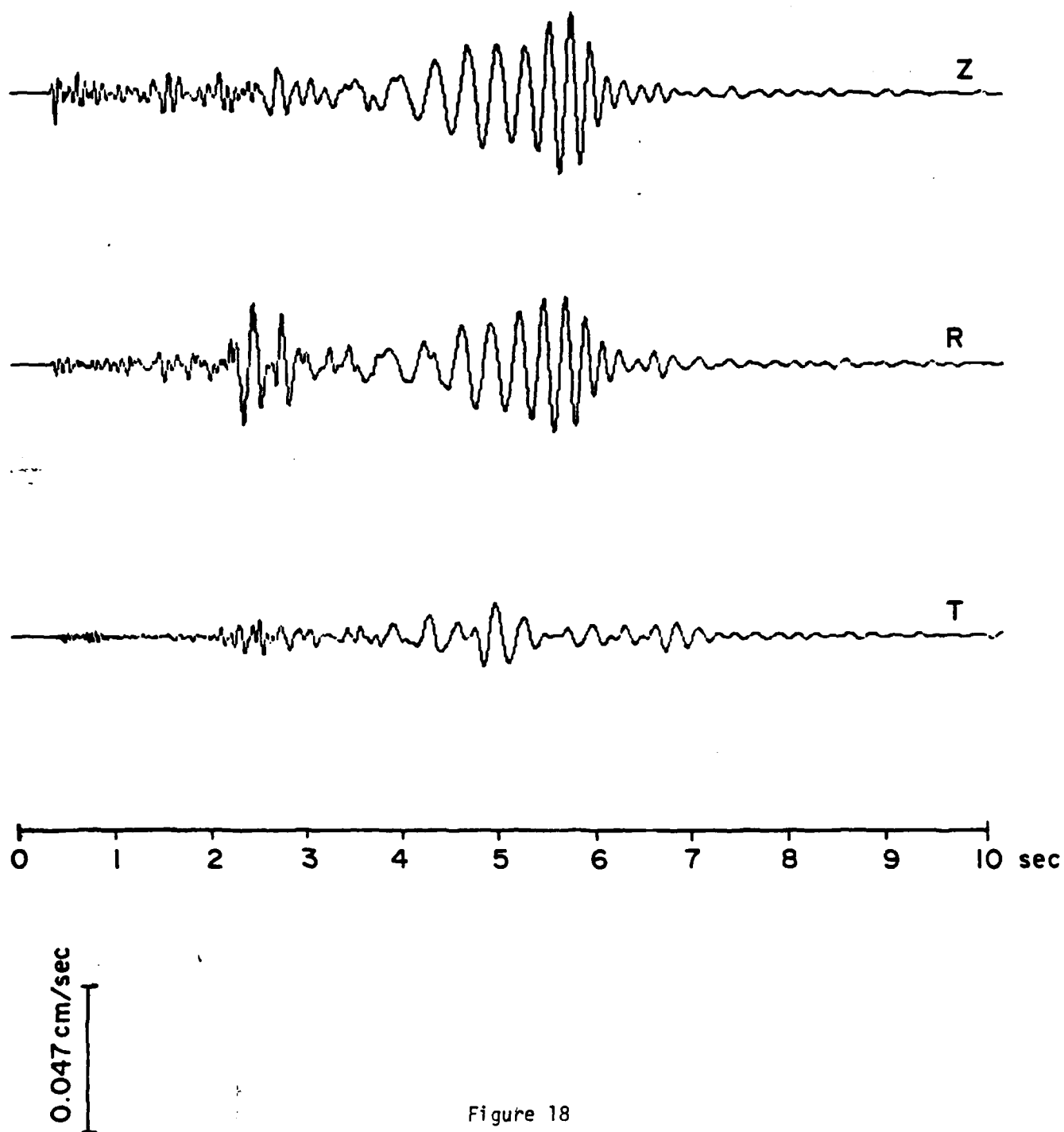


Figure 18

AD-A119 286

AIR FORCE WEAPONS LAB KIRTLAND AFB NM
EXPLOSION AND EARTHQUAKE SOURCE DISCRIMINATION. (U)
MAY 82 B W STUMP, R E REINKE

F/G 18/3

AFOSR-P0-82-00004

UNCLASSIFIED

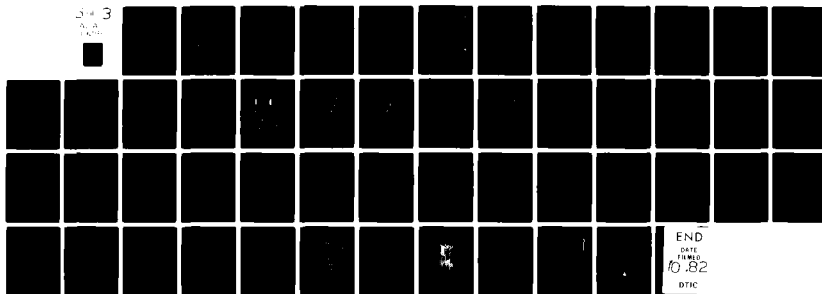
AFOSR-TR-82-0733

NL

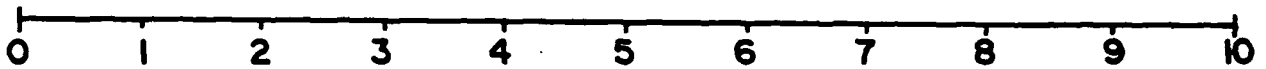
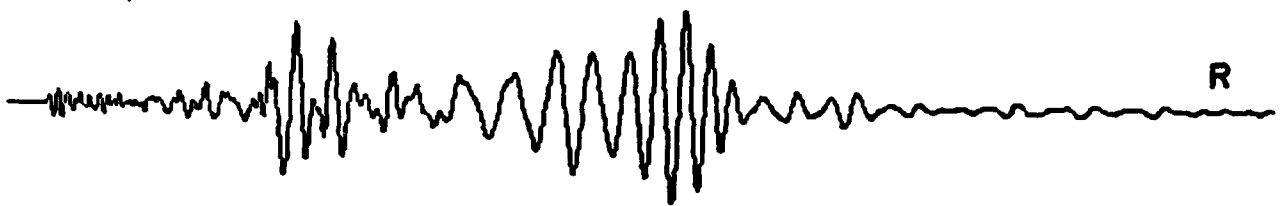
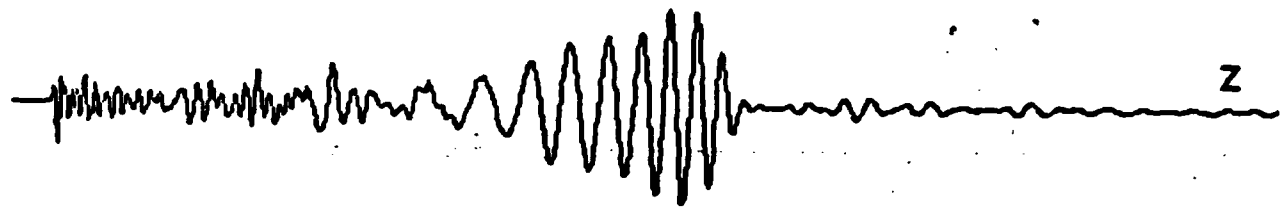
343

343

343



END
DATE
10.82
DTIC



0.047 cm/sec

Figure 19

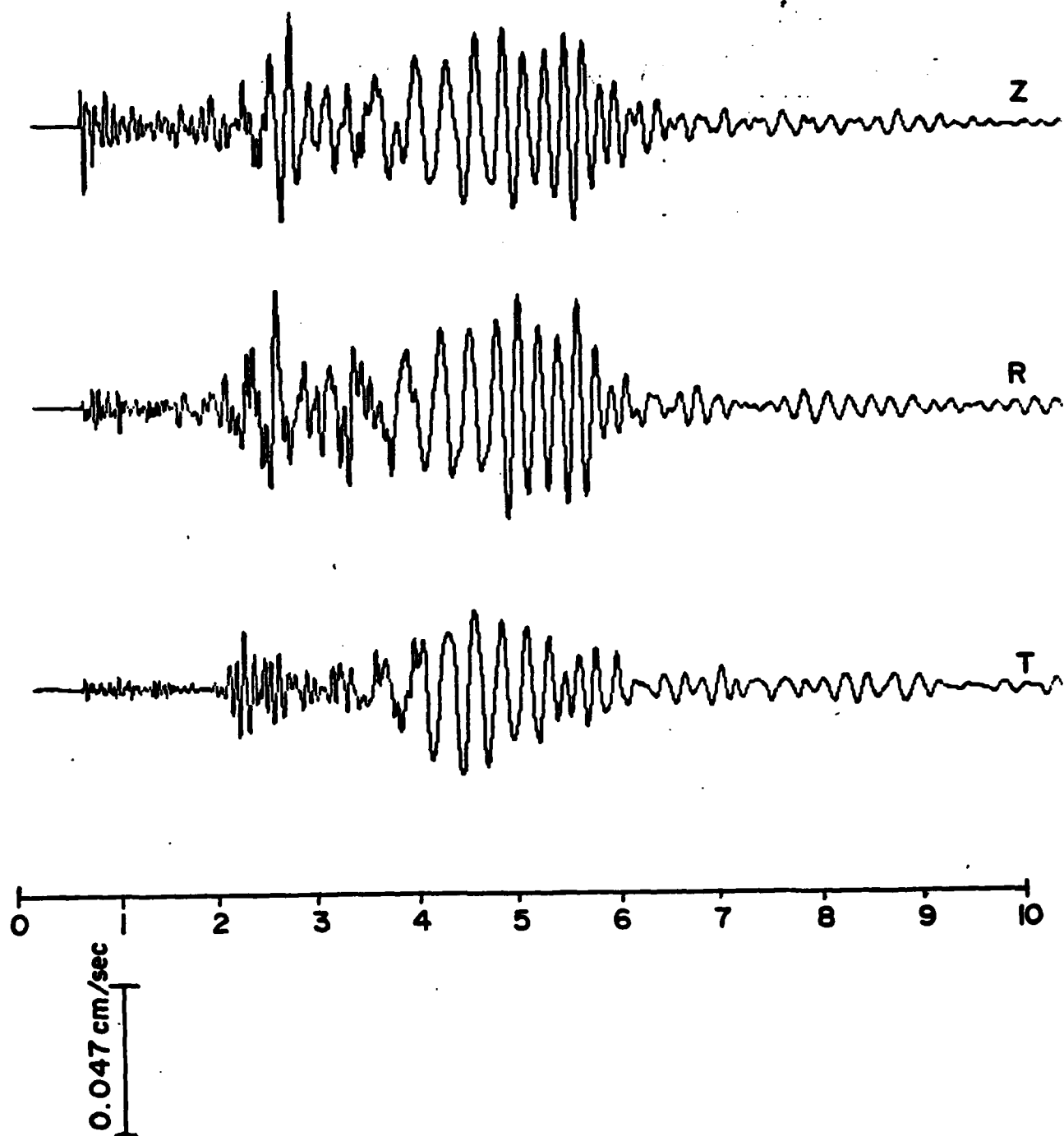


Figure 20

DETONATION TIMES of TNT SPHERE

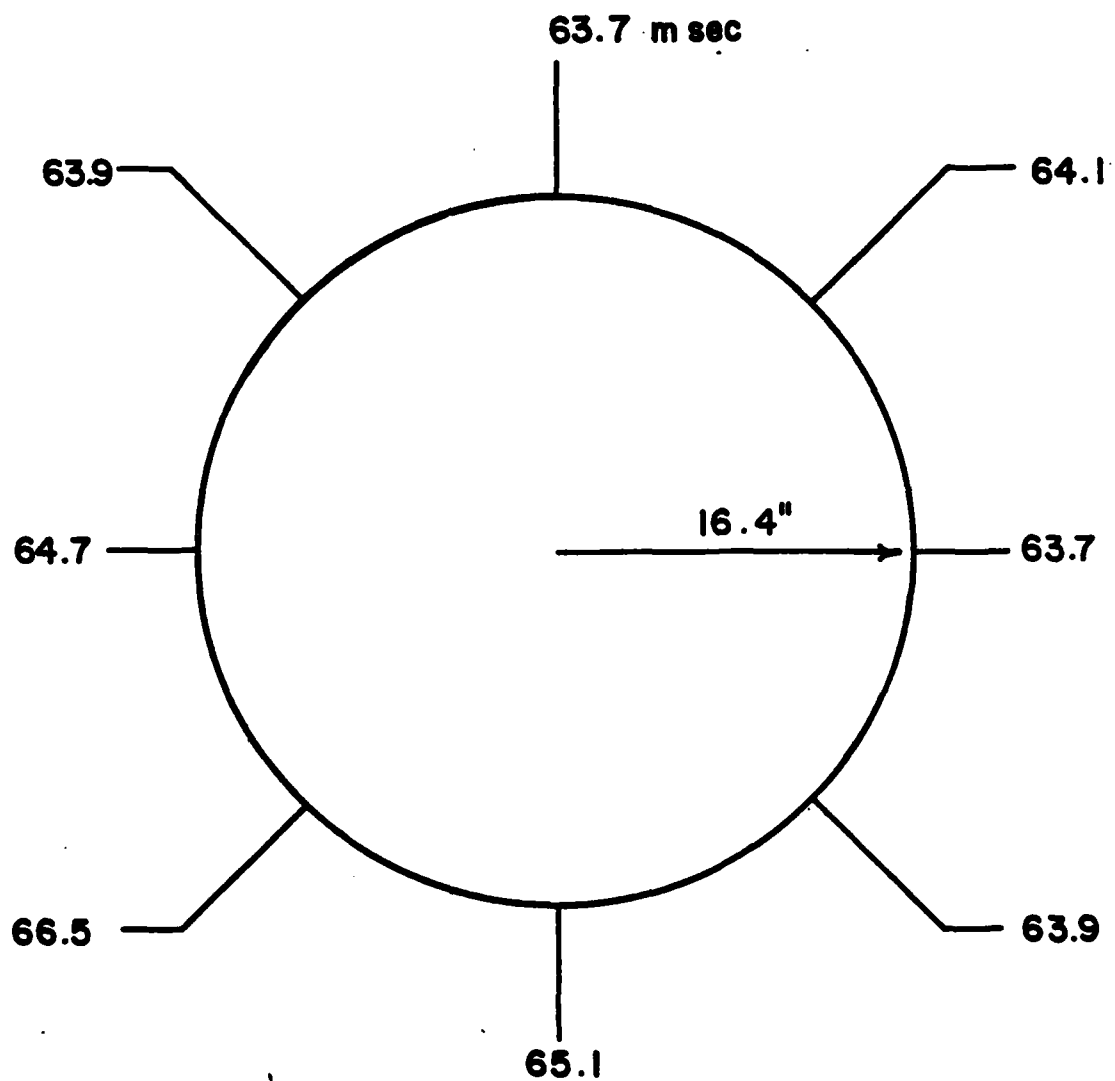


Figure 21

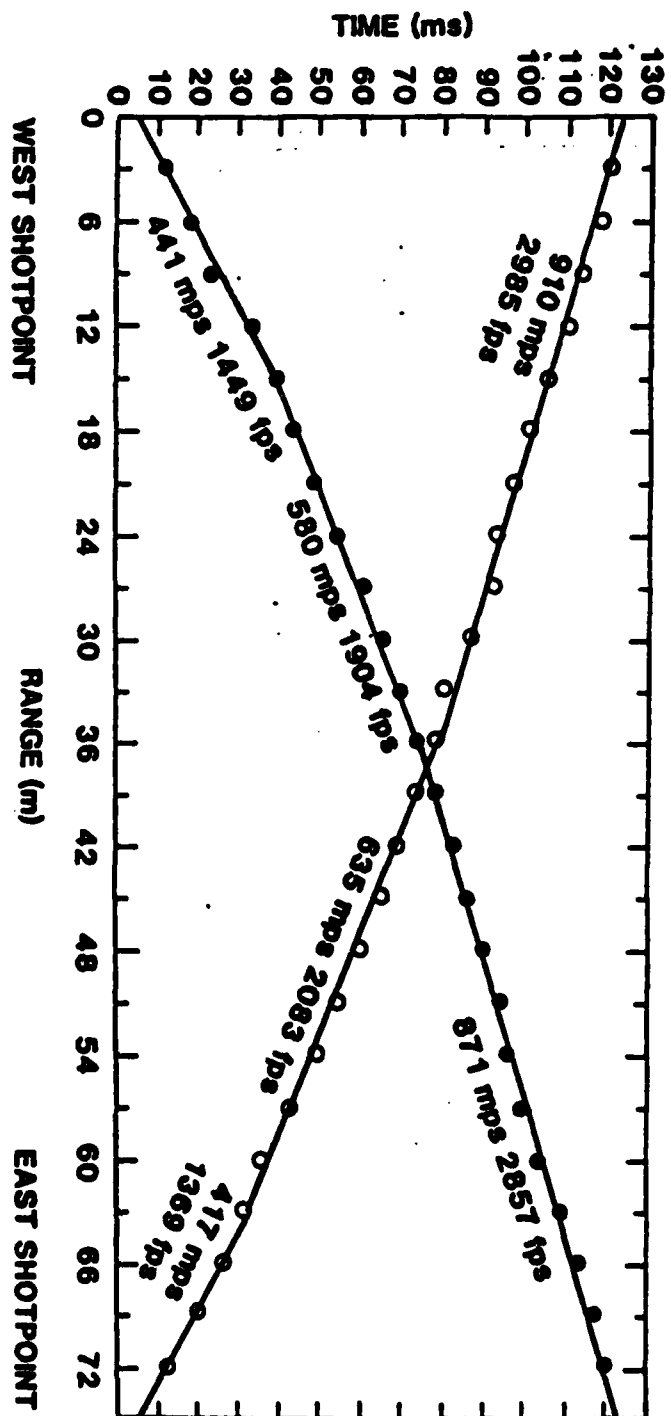


Figure 22

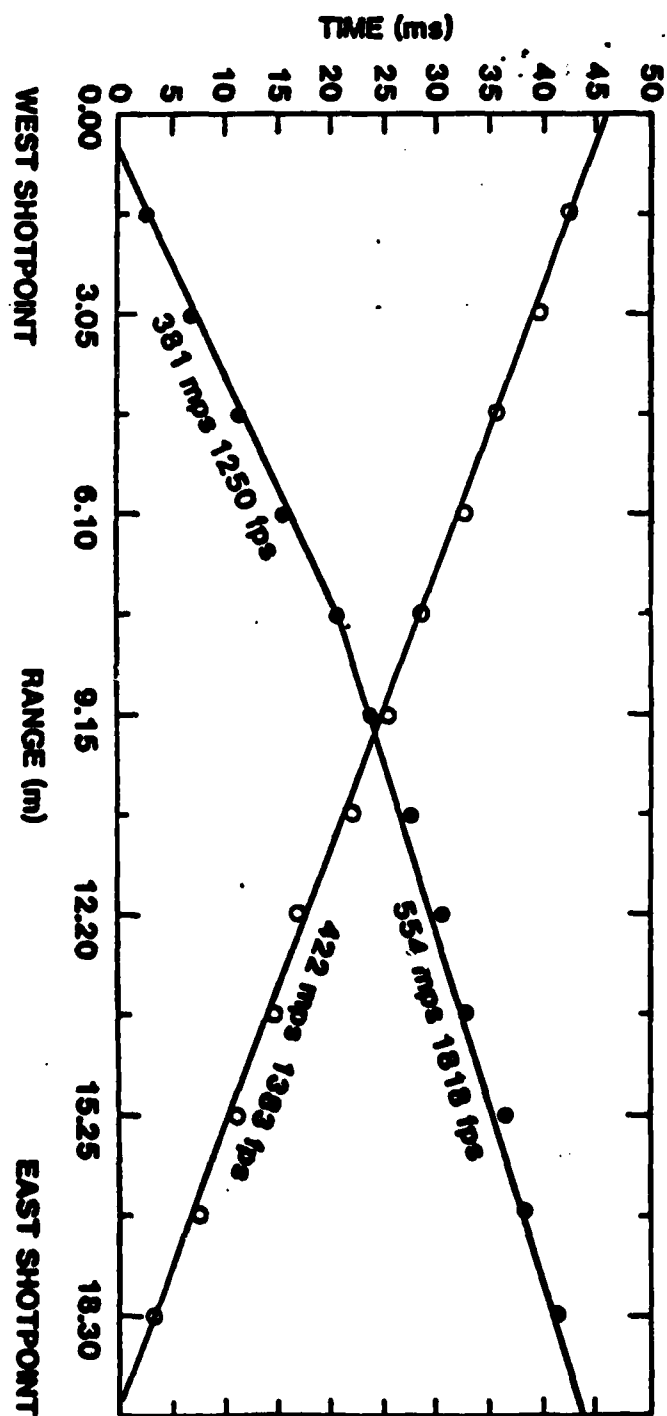
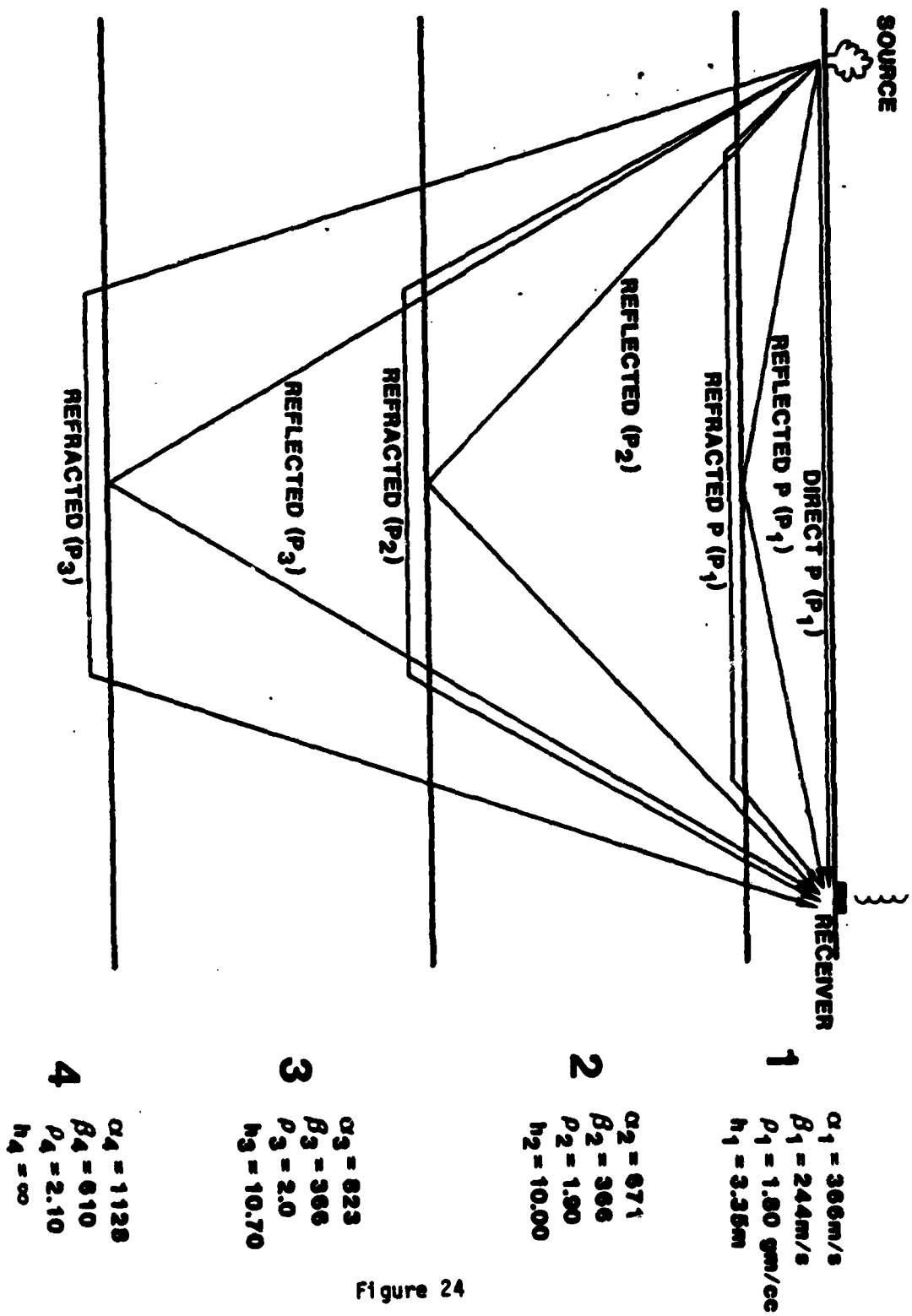


Figure 23



OBSERVED AND COMPUTED SEISMOGRAMS
FROM SMALL YIELD HIGH-EXPLOSIVE EVENTS

ROBERT E. REINKE

BRIAN W. STUMP

Air Force Weapons Laboratory

KENNETH H. OLSEN

Los Alamos National Laboratory

Local (1.6 km range) seismograms have been obtained from seven high-explosive events fired in alluvium at the McCormick Ranch Test Site a few kilometers to the south of Albuquerque, New Mexico. The recorded events ranged in yield from 253 pounds to 16 tons. The explosive configuration varied from above ground and buried single charges to surface bermed and buried distributed charges. This series of shots provided a unique opportunity for studying the effects of source configuration, yield, and geologic structure upon the observed seismograms.

The McCormick Ranch Test Site is situated along the eastern margin of the Rio Grande Valley in Central New Mexico. The site is underlain by fairly deep alluvium. Most of the shots were fired in near-surface playa deposits. An idealized 2-layer over half-space geologic profile is shown in Figure 1. This profile represents a surface layer of dry alluvium over a layer of wet alluvium in turn overlaying a paleozoic half-space. The properties of the first and second layers and the first layer thickness were determined by shallow refraction surveys. Properties of the paleozoic half-space were estimated from the results of a nearby shallow seismic reflection survey.

Figure 2 shows a schematic diagram of the charge configuration for each of the seven recorded events. Three of the shots were single charge depth of burst (DOB) events, 250 pounds buried 2.5 meters, 253 pounds buried 11.6 meters and 2.5 tons fired at a depth of 9.8 meters. A fourth single charge event consisted of 1000 pounds fired surface tangent to the ground surface. One of the distributed charge events was a 0.5 ton HEST (HEST is an acronym for High Explosive Simulation Technique). The HEST charge configuration consists of a uniform layer of explosive spread over the ground surface which in

turn is covered with an earth layer in order to contain the air blast and increase the coupling to the ground. Another of the distributed charge events was a 16-ton DIHEST (DIHEST is an acronym for Direct-Induced High-Explosive Simulation Technique). The DIHEST consisted of 16 tons of explosive buried at a depth of 10 meters in a row of 14 drill holes spaced 2 meters apart. All charges were detonated simultaneously. The third distributed charge event was a combined HEST-DIHEST event made up of a 16-ton buried DIHEST and a 0.5 ton surface HEST. The HEST center was approximately 30 meters distant from the vertical axis of the DIHEST. Both were fired simultaneously.

On all events, stations were placed at a range of 1.6 km to the north and west. On some events, a 2-component linear array was placed at the north stations. The stations were made up of 3-component, 2-Hz natural frequency seismometers recorded on digital cassette tape at a sample rate of 200 samples per second.

Samples of the records from the seven detonations are shown in Figures 3, 4 and 5. All of these records are from the 1.6 km north station. The first four (250 lb 2.5 m DOB, 253 lb 11.6 m DOB, 0.5 ton ST, and 0.5 ton HEST) records in each figure have the same amplitude scale so that direct comparisons may be made among these twelve records. The amplitude scale on the fifth record (2.5 ton 9.8 m) is five times as large as the first four (i.e., an excursion of the trace on record 5 represents a velocity amplitude 5 times that of the same excursion on records 1 through 4). Amplitude scales on the last two records (16-ton DIHEST and 16-ton DIHEST + 0.5 ton HEST) represent motions 25 times greater than the first four records and 5 times greater than record 5.

Examining the first four records in Figures 3, 4, and 5 (the low yield events), the HEST event appears to be the most efficient at coupling energy

into the ground. The surface tangent burst is perhaps the least efficient as far as energy coupling is concerned, with the exception of the prominent air coupled Rayleigh wave appearing at about 4 seconds.

The 11.6 m DOB records show a very nicely dispersed fundamental mode Rayleigh wave train with a rather sharp cutoff at the end indicating the presence of an Airy phase. Almost all of the records contain two groups of surface waves. The first arriving group is likely composed mainly of higher mode propagation with the later arriving packet being associated with fundamental mode propagation. The HEST event records contain a third prominent high-frequency wave group arriving between the lower frequency higher and fundamental mode packets. This arrival is apparently some type of higher mode surface wave as well. Since this particular phase is not distinct on the records from any of the other events, its excitation may be a result of the HEST type of source configuration. In general, the fundamental mode surface wave frequency content appears to vary little from shot to shot. The main changes seem to occur in the higher mode phases.

The body wave frequency content changes relatively little for the four low yield shots. The HEST and the 11.6 m DOB event seem to be somewhat more efficient at exciting the higher frequencies than the 2.5 m DOB and the 0.5 ton ST shots. The larger yield shots, as would be expected, excite body waves possessing a frequency content roughly a factor of two lower than that of the four small yield shots. Unfortunately, the recorders did not trigger early enough to record the body wave portion of the combined HEST-DIHEST event so that we were unable to determine what effect the simultaneous firing of the HEST had on the lower frequency DIHEST body waves.

Given the asymmetric nature of some of the sources, we had hoped to observe differences between the waveforms recorded at the north and west

locations. Figure 6 shows a comparison between the north and west recordings of three of the shots. As seen, there are indeed differences between the two stations for the DIHEST event, which is a strongly asymmetric source, however, the north versus west differences are just as apparent for the buried 253-pound spherical charge. In general, the amplitudes are uniformly higher on the west for all shots suggesting that the observed north versus west differences result from local geologic effects. While source-induced azimuthal variations may be present, they are probably obscured by the local geologic effects.

Rayleigh wave group velocity dispersion curves were computed, using Haskell-Thomson technique, for the 2-layer over half-space model shown in Figure 1. The observed dispersion for the first and second arriving surface wave phases from the DIHEST event, determined using the zero crossing method, was then plotted (solid circles) on the theoretical fundamental and first two higher mode group velocity curves (solid lines) shown in Figure 7. While the observed group velocity values are in the same range overall as the computed values, the observed fundamental mode dispersion is normal while the computed fundamental mode dispersion is inverse (higher frequencies arrive first). Some adjustment to the assumed 2-layer over half-space model is needed to achieve normal dispersion in the frequency range of interest.

A preliminary attempt at modeling some of the observed waveforms has been made using the reflectivity code (Fuchs and Mueller, 1971). The code was written by Rainer Kind and is in operation on the CRAY-1 computer at the Los Alamos National Laboratory. The initial runs were made using the 2-layer over half-space geology shown in Figure 1 and symmetric explosive and vertical point force source functions at a depth of 10 meters. The experimental waveforms we attempted to match for the first run were those from the HEST and

DIHEST events. The frequency of the source function in the reflectivity calculations was set equal to that of the first P wave arrival observed in the records from the corresponding events.

Figure 8 shows a comparison between two of the calculated vertical waveforms and the corresponding observed records. The explosive source function was used for these calculations. Considering the simplicity of both the source function and the geologic model input, the comparisons are quite good. The observed and calculated DIHEST comparison is the best. There are a few subtle differences between observed and calculated waveforms--the calculated fundamental mode Rayleigh wave exhibits inverse dispersion, the observed is normally dispersed (as we saw in the calculated versus observed dispersion comparison), and the relative amplitude of the higher mode is a bit low in the calculation as compared to the recorded waveform--however, the calculations capture the overall character of the observed DIHEST waveform.

The HEST observed and calculated comparison is not as good as the DIHEST comparison which is perhaps to be expected since the HEST is really a number of surface point forces spread over a finite area rather than a buried explosive source. The calculation fails to pick up the intermediate high frequency higher mode surface wave phase and, again, the observed fundamental mode dispersion is normal while the calculated is inversely dispersed suggesting a need for a slight change in either the velocities or thicknesses of the input structure. The calculation does capture the higher frequency nature of the HEST waves quite well. Figures 9 and 10 show a set of computed vertical seismograms from 200 meters to 2 km for these two calculations.

Since the initial modeling phase, a series of calculations using shallow sources and slightly different frequencies has been attempted. Some selected

examples of the results are shown in Figures 11 through 18. Figures 11 and 12 are from a calculation using a 1 meter point force at 12.8 Hz. Figures 13 and 14 are for a 1 meter explosive source at 12.8 Hz. Figures 15 and 16 contain the results of a 17-Hz explosive source at 1 meter, while Figures 17 and 18 are waveforms from a 17-Hz point force at the 1 meter depth. The explosive sources appear somewhat higher frequency than the point forces.

If the time scales were removed from some of these records, they would not be unlike, in overall appearance, seismograms recorded at regional distances from larger events. To determine if the recorded seismograms were in any way scaled versions of those recorded at larger ranges from higher yield shots, a simple wavelength scaling relationship was borrowed from the seismic model laboratory (Goforth, 1976). The scaling relationship used and the resulting full scale profile are shown in Figure 19. For the sake of argument, a factor of 10 change in frequency was assumed between the McCormick Ranch events and a 150 kt event recorded at near regional distances. Using this value and obtaining velocity ratios between the McCormick Ranch half-space and the real earth mantle, an earth to model length ratio of 17.3 was obtained. The profile in Figure 19 is the full scale earth profile modeled by the McCormick Ranch events. The profile is not a very relevant one in terms of any real earth structure, however, it does illustrate the scaling principle involved which applied to other test sites and events might yield more realistic results.

These preliminary results indicate that body and surface wave responses are fairly well modeled using the reflectivity technique at these relatively close-in distances. The different source configurations result in some subtle and some not so subtle differences in the observed waveforms. The similarity in character of these waveforms to those recorded at regional distances from

larger events suggests that it may be possible to study some problems of regional wave propagation by using relatively small HE events. Although the recorded events and geology at McCormick Ranch do not scale to any real earth situation of interest, other sites might well be useful for small scale testing.

REFERENCES

Fuchs, K., G. Mueller (1971). Computation of synthetic seismograms with the reflectivity method and comparison with observations, Geophys. J. Roy. Astr. Soc. 23, pp 417-433.

Goforth, Tom T. (1976). A model study of the effect on the Rayleigh spectrum of lateral heterogeneity in earthquake source regions, Jour Geophy Research, Vol 81, No. 20, pp 3599-3606.

SIMPLIFIED PROFILE

$\alpha = 850 \text{ mps}$ $\beta = 365 \text{ mps}$

$\rho = 1.9 \text{ g/cc}$ $H = 85 \text{ m}$

$\alpha = 2000 \text{ mps}$ $\beta = 675 \text{ mps}$

$\rho = 2.1 \text{ g/cc}$ $H = 830 \text{ m}$

$\alpha = 4500 \text{ mps}$ $\beta = 2600 \text{ mps}$

$\rho = 2.6 \text{ g/cc}$ $H = \infty$

Figure 1

2.5m DOB

11.6m DOB

0.5 ton ST

0.5 ton HEST



250 lb.

253 lb.

9.8m DOB

DIHEST

DIHEST+HEST

0.5 ton



2.5 ton

16 ton

16 ton

Figure 2

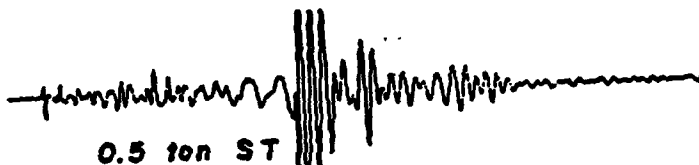
VERTICAL



250 lb 2.5m DOB



253 lb 11.6m DOB



0.5 ton ST



0.5 ton HEST



2.5 ton 9.8m DOB



16 ton DIHEST



16 ton DIHEST + 0.5 ton HEST

10 seconds

Figure 3

RADIAL

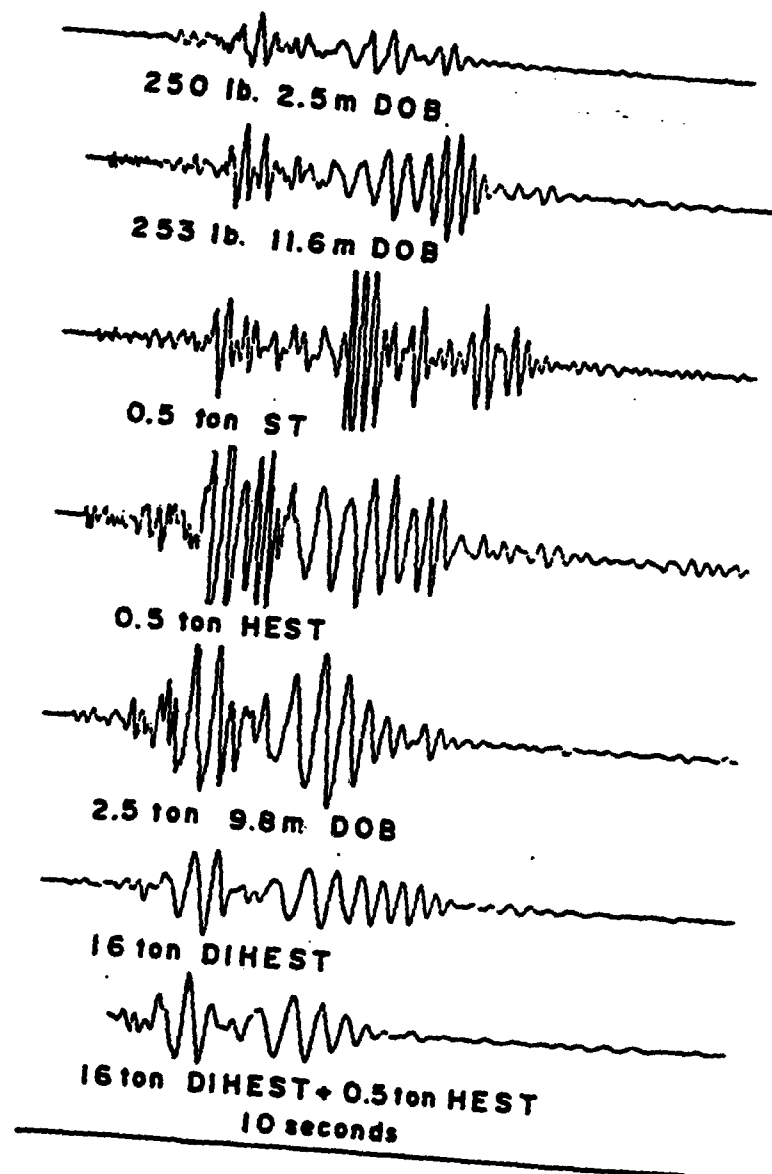


Figure 4

TRANSVERSE

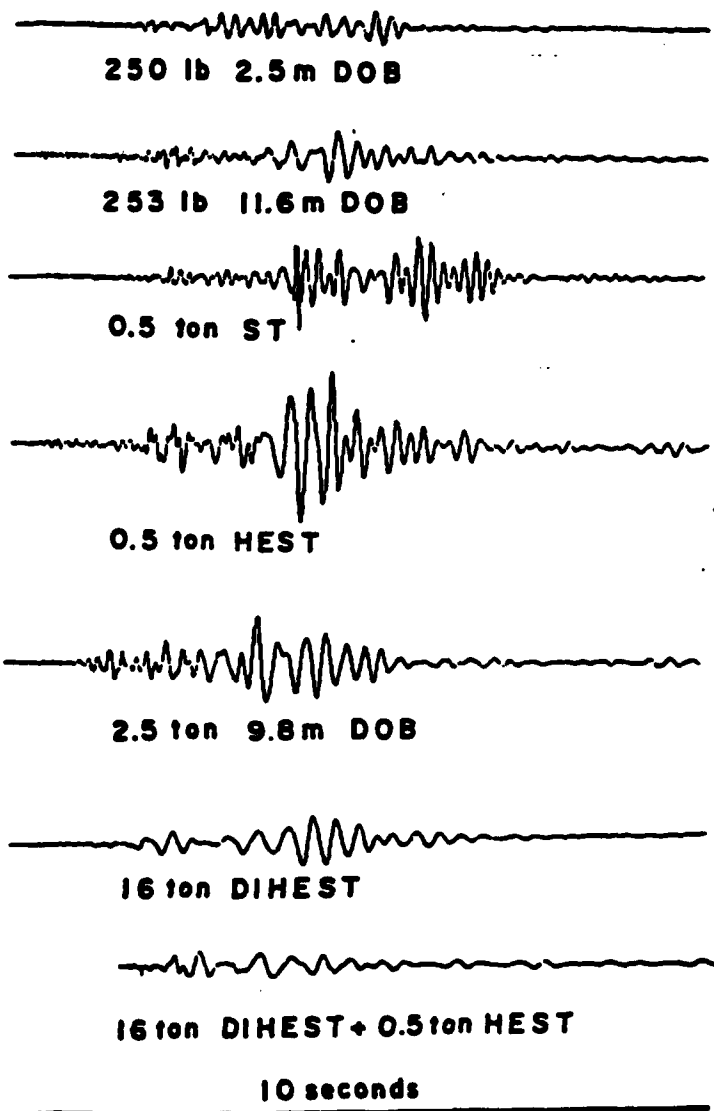
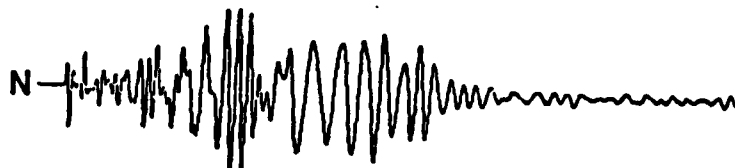


Figure 5



253 lb. 11.6 m. DOB



HEST



DIHEST

Figure 6

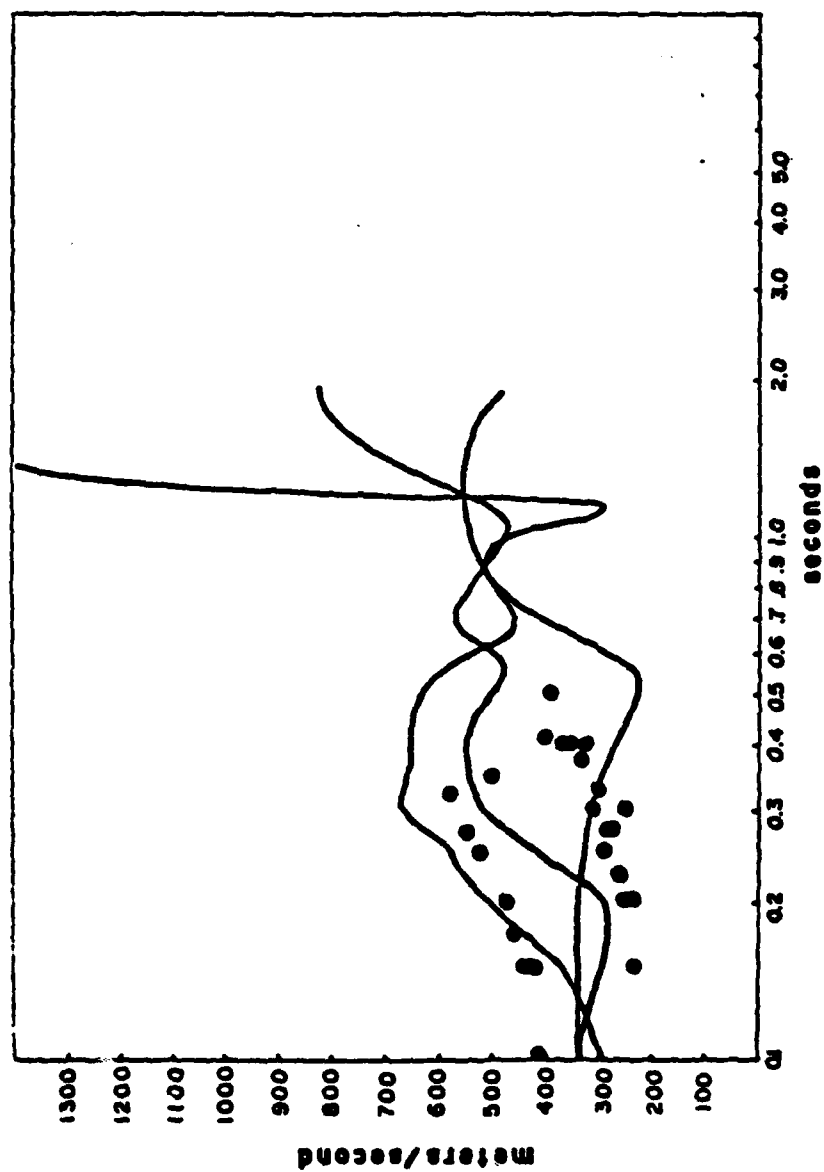
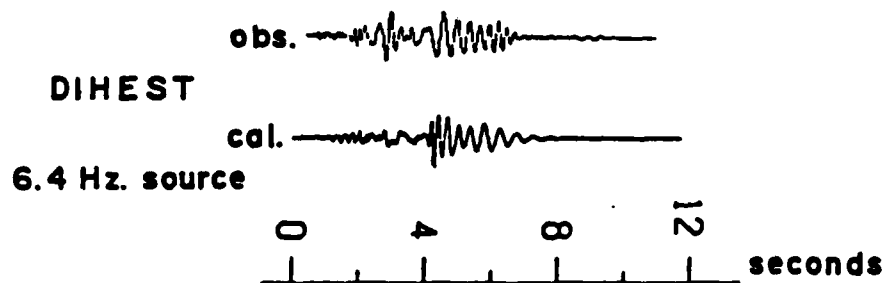
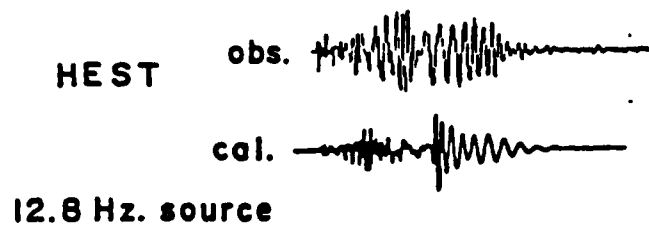


Figure 7



OBSERVED AND CALCULATED VERTICALS
1.6 KM. NORTH

Figure 8

CALCULATED VERTICAL COMPONENT
DIHEST (6.4 Hz. source)

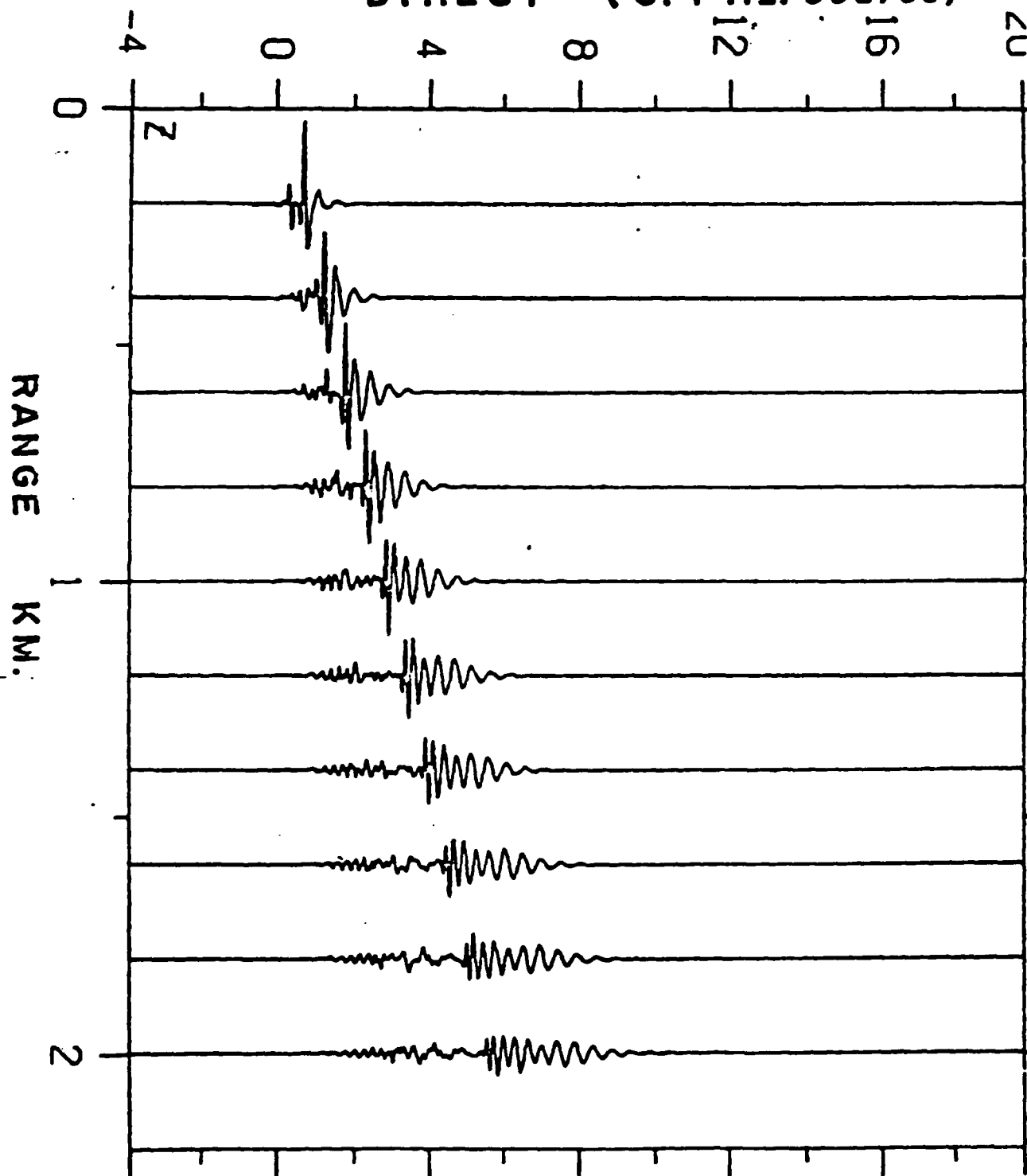


Figure 9

CALCULATED VERTICAL COMPONENT
HEST (12.8 Hz. source)

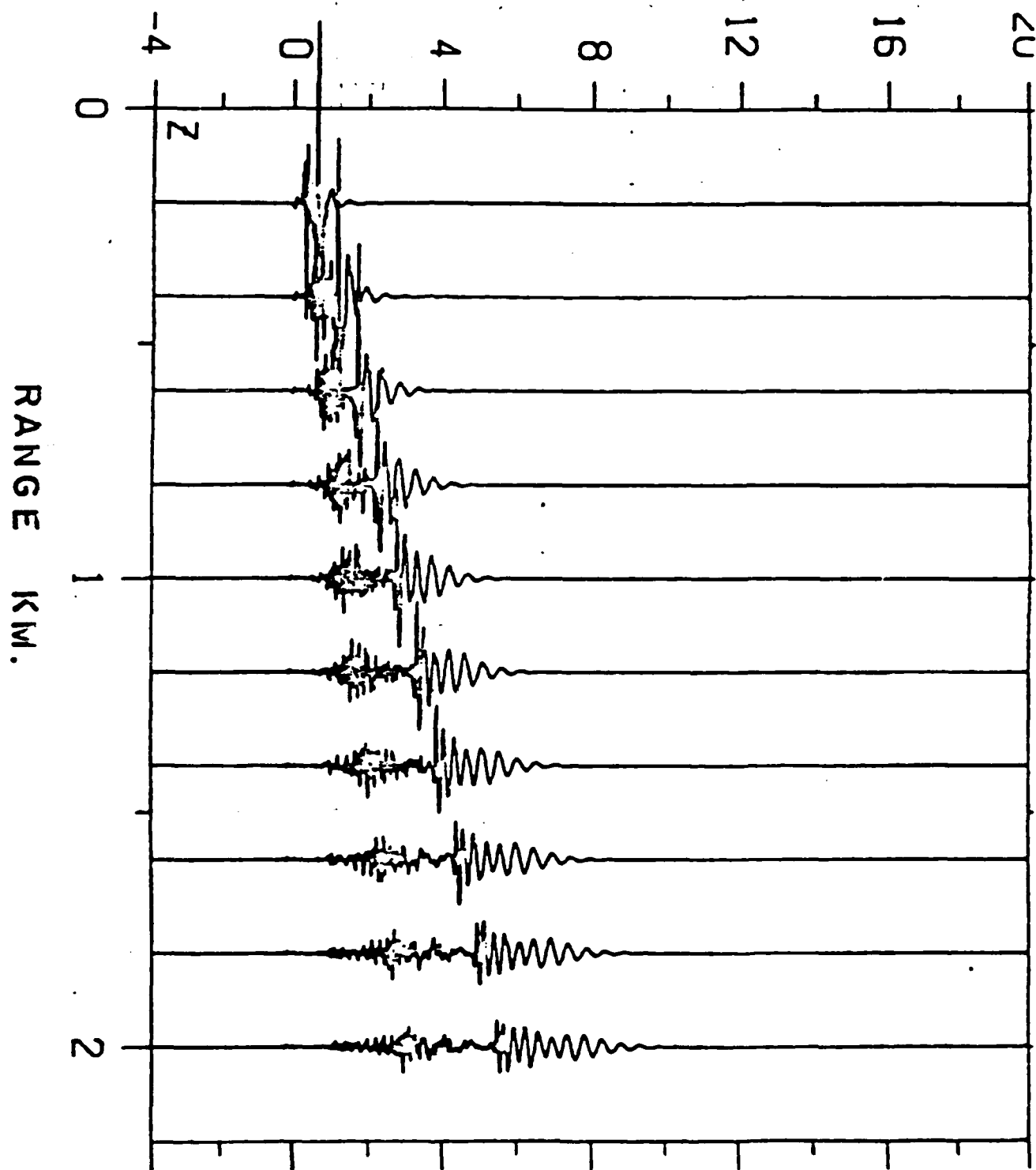


Figure 10

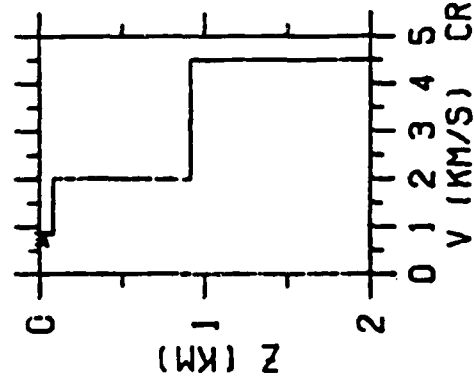
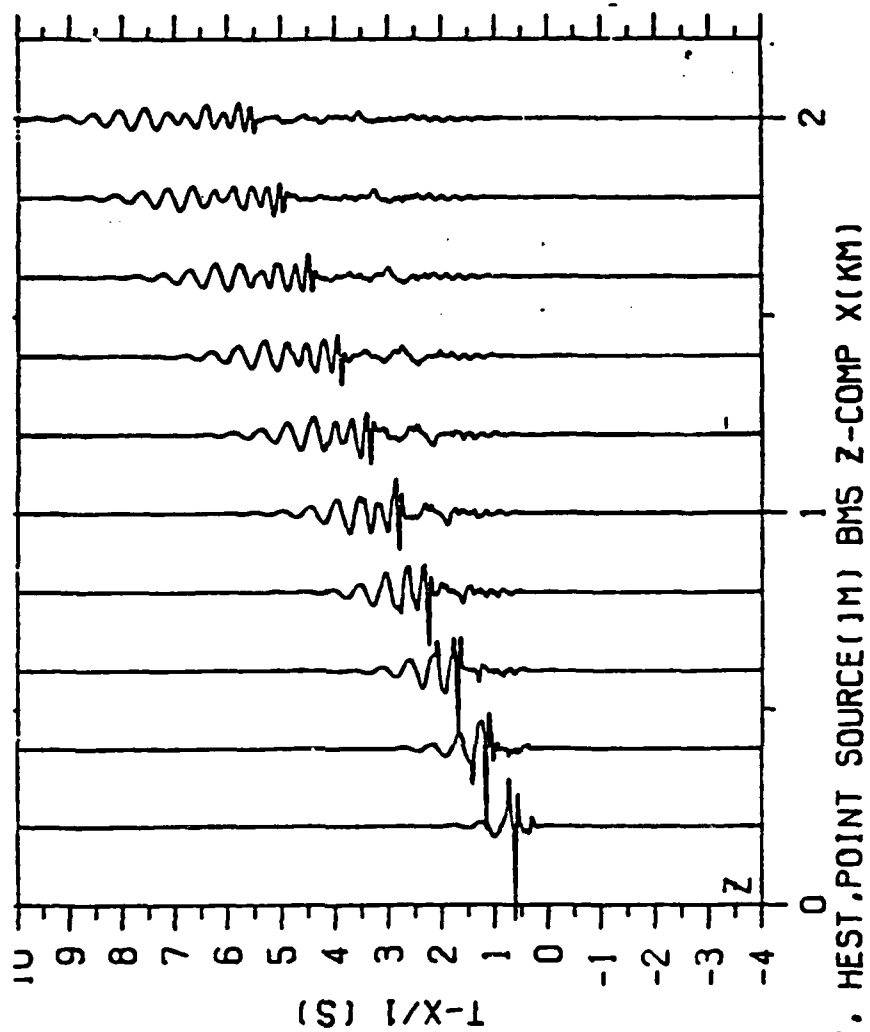


Figure 11

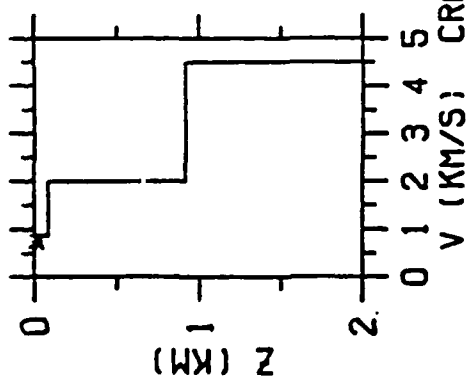
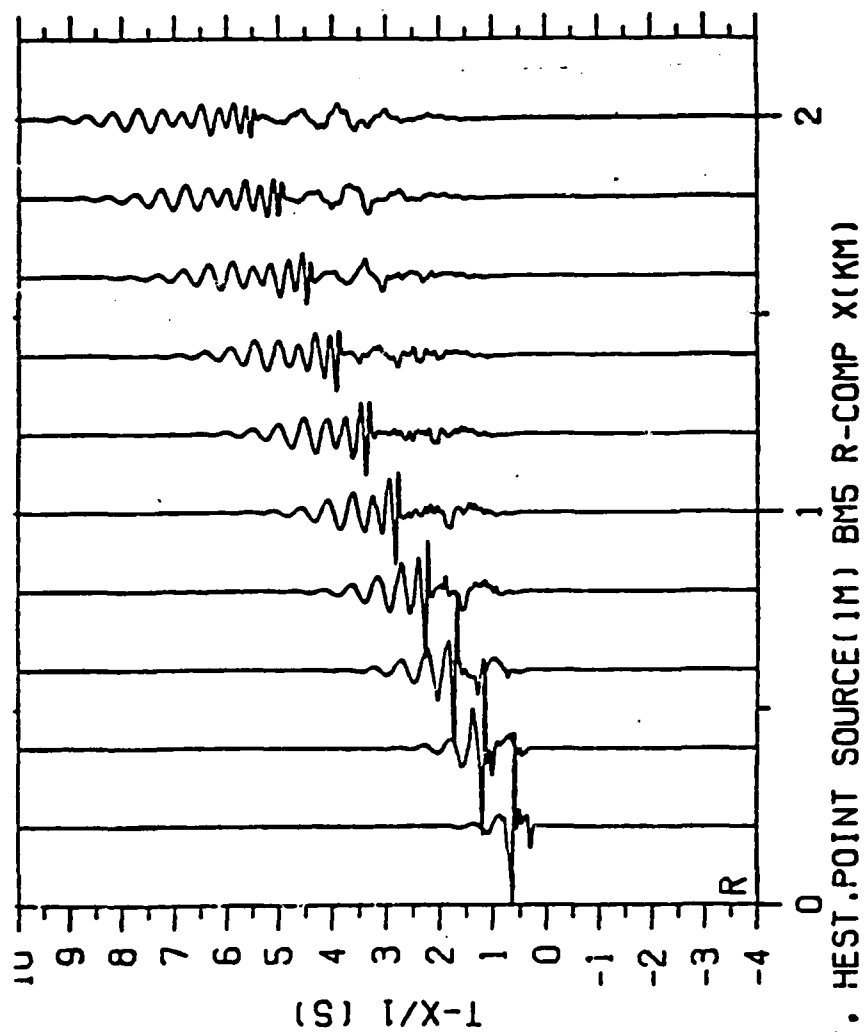


Figure 12

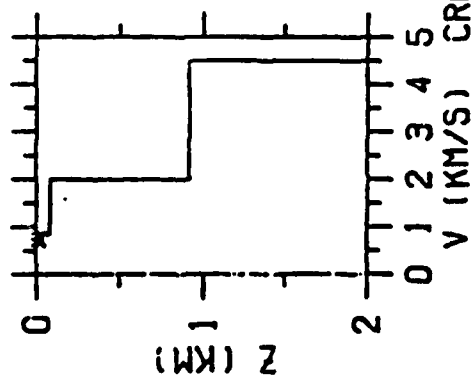
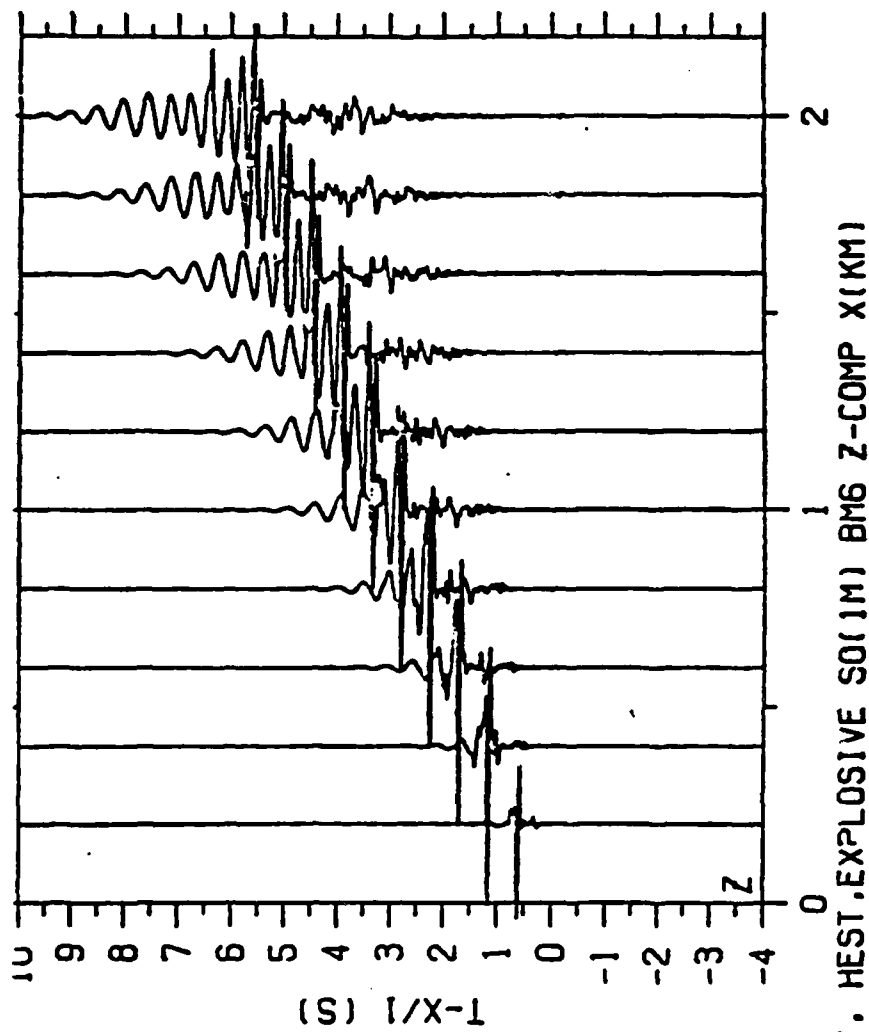


Figure 13

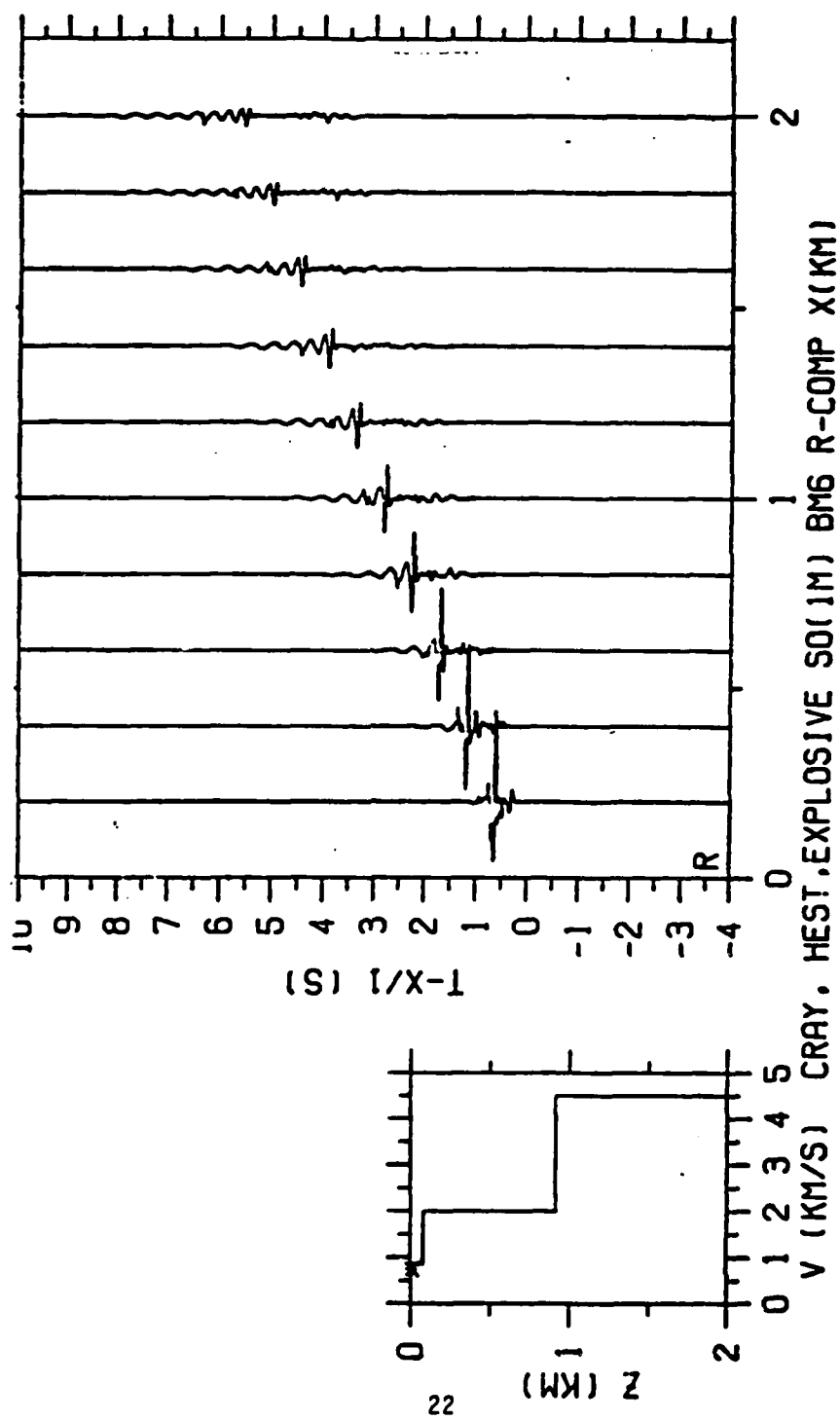


Figure 14

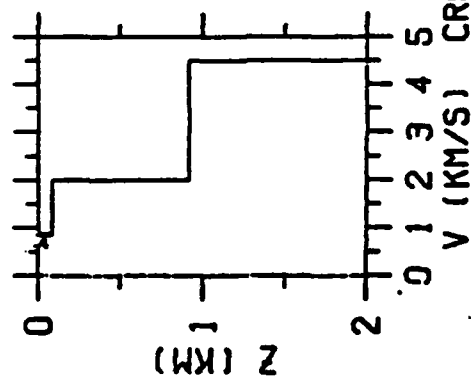
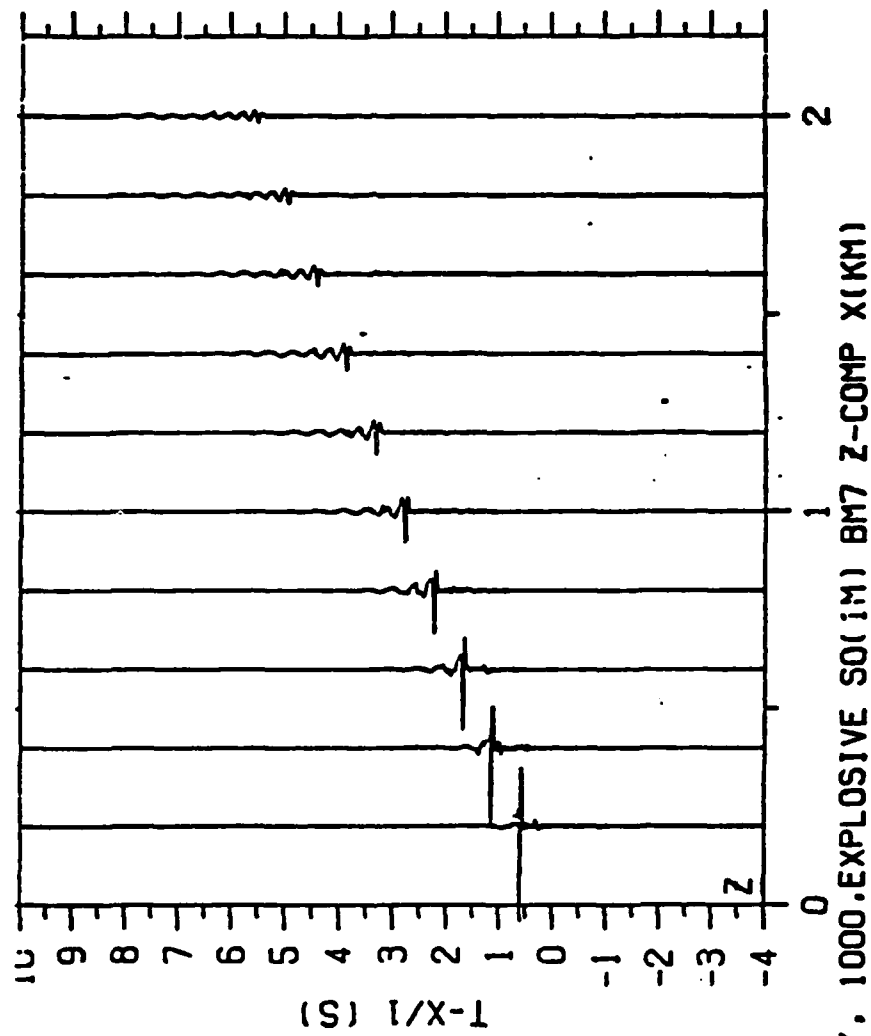


Figure 15

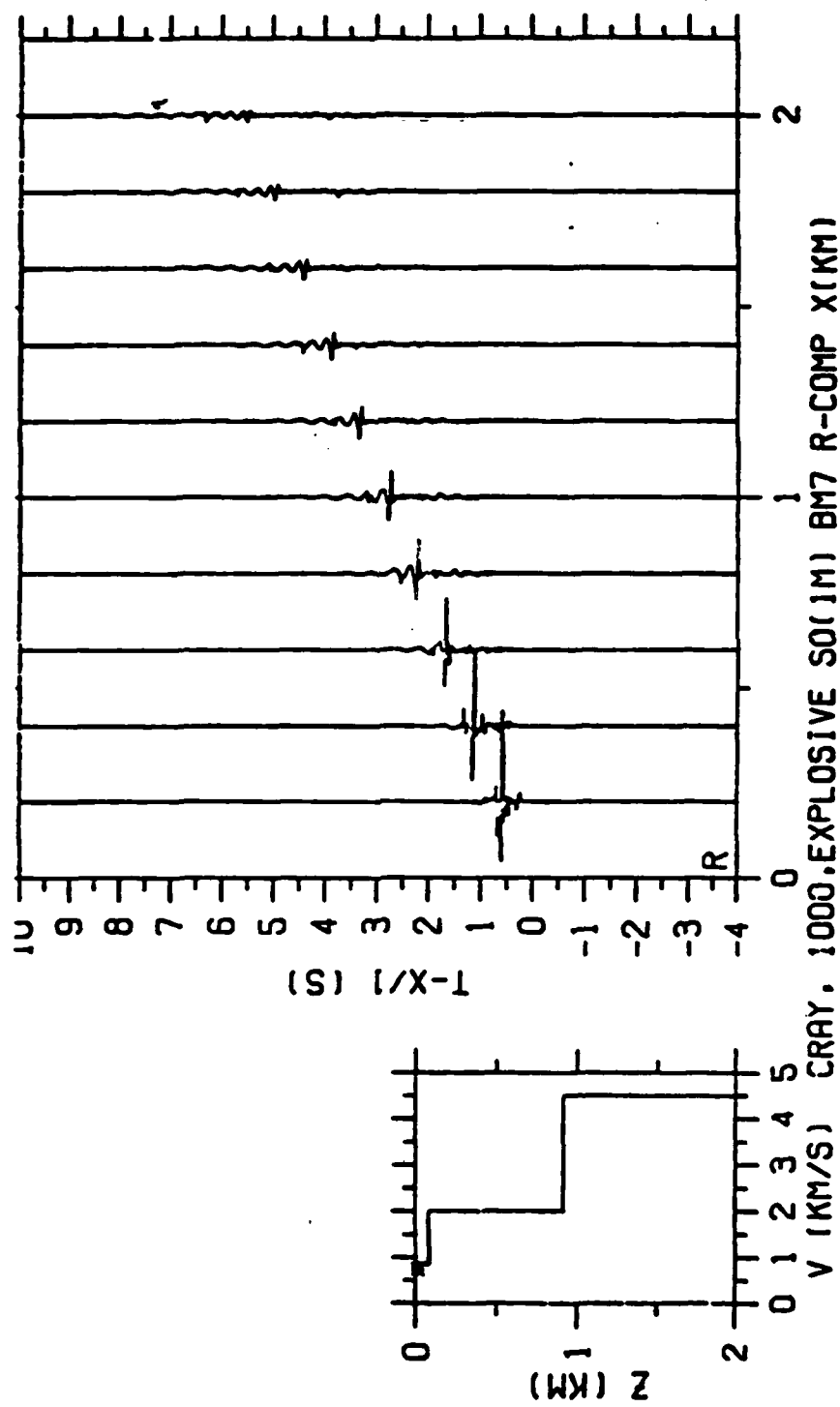


Figure 16

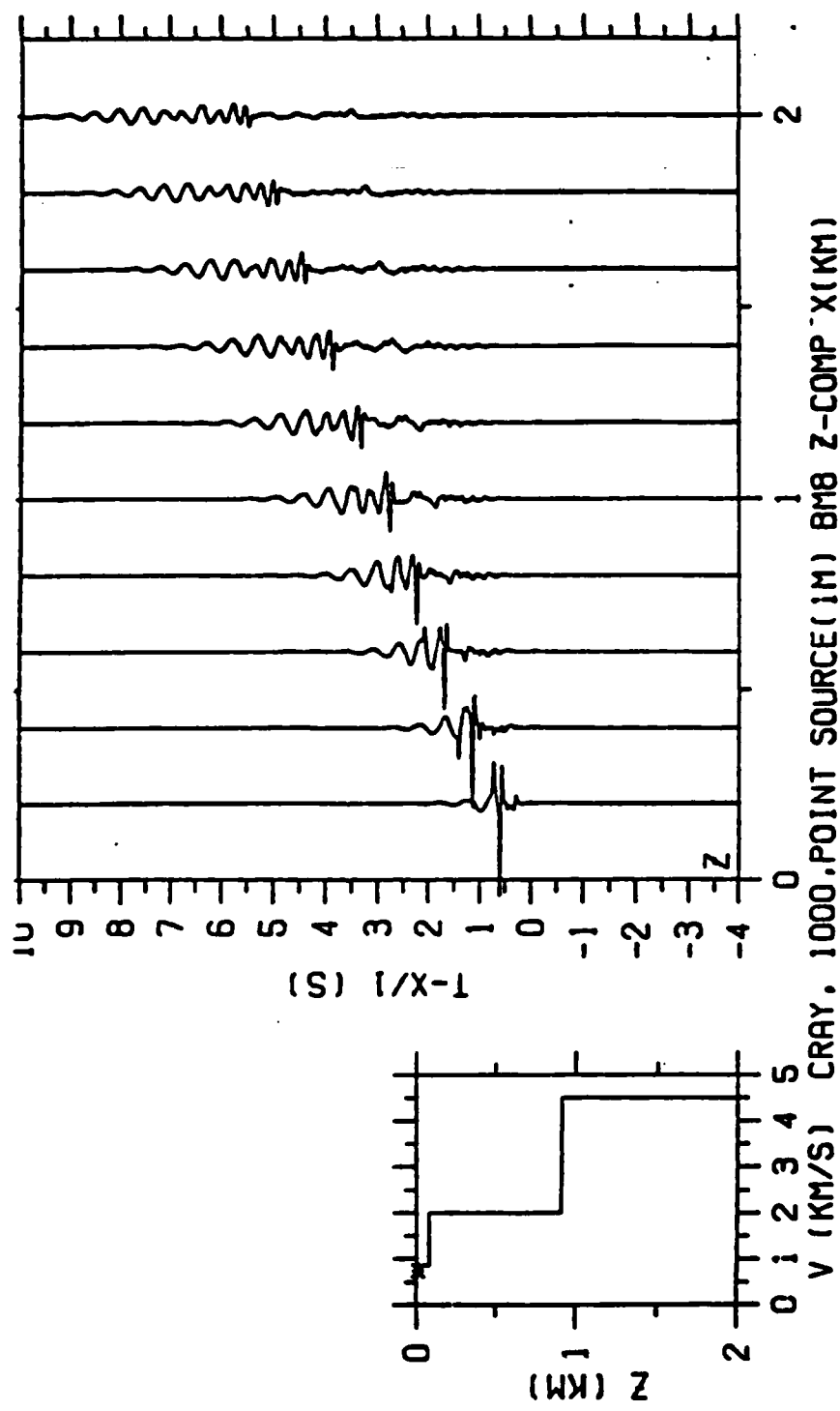
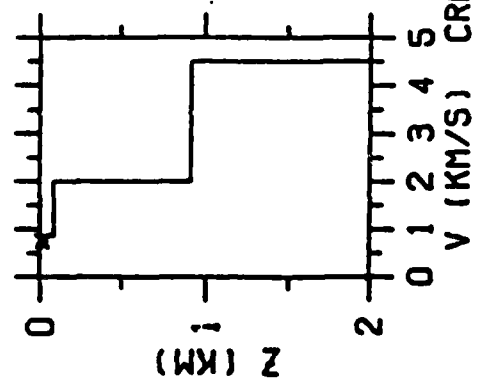
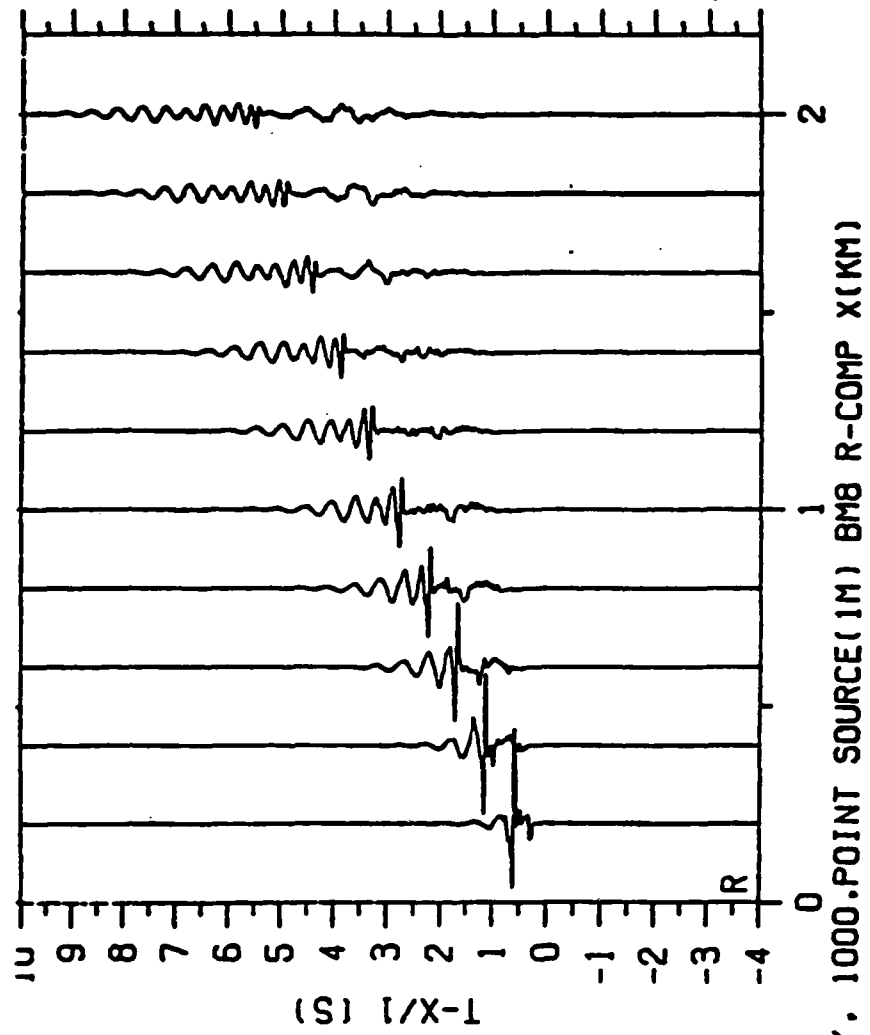


Figure 17



CRAY. 1000.POINT SOURCE(1M) BMB R-COMP X(KM)

Figure 18

3.5 Hz - 0.35 Hz

$L_e = 17.3 \text{ Lm}$

$L_e = \beta_{ne} / \beta_{nm} \cdot T_e / T_m \cdot L_m$

L_e = earth length

L_m = model length

β_{ne} = earth halfspace S vel.

β_{nm} = model halfspace S vel.

T_e = earth period

T_m = model period

Scaled Profile

$a = 1.47 \text{ Km/sec}$ $H = 1.47 \text{ Km}$
 $\beta = 0.63 \text{ Km/sec}$

$a = 3.46 \text{ Km/sec}$ $H = 14.35 \text{ Km}$
 $\beta = 1.17 \text{ Km/sec}$

$a = 7.8 \text{ Km/sec}$ $H = \infty$
 $\beta = 4.5 \text{ Km/sec}$

Figure 19

TRINITY-MILL RACE SEISMIC EXPERIMENT

R.E. Reinke

B.W. Stump

SITE CHARACTERIZATION AND SEISMOLOGY SECTION

AIR FORCE WEAPONS LABORATORY

K.H. Olsen

GEOPHYSICS DIVISION

LOS ALAMOS NATIONAL LABORATORY

ABSTRACT

The proximity of the MILL RACE test site to the Trinity site where the first atomic bomb was detonated in July of 1945 offered a unique opportunity to compare the unusual appearing seismic waves recorded on the Trinity event with those excited by MILL RACE. Two of the Leet seismographs used to record the 1945 Trinity event were obtained and fielded on MILL RACE alongside modern digital instrumentation in an effort to verify the Trinity seismograms. Due to failure of the Leet instruments, the experiment was only partially successful.

TABLE OF CONTENTS

	<u>Page</u>
1.0 INTRODUCTION	3
2.0 DESIGN OF THE EXPERIMENT	4
2.1 The Leet Seismographs	6
2.2 Modern Instrumentation used and Instrument Locations	6
3.0 RESULTS	8
4.0 CONCLUSIONS	

LIST OF ILLUSTRATIONS

<u>Figure</u>	<u>Page</u>
1. Seismic Station Map for MILL RACE	10
2. Leet's Trinity Seismogram	11
3. Drawing of Leet Seismograph	12
4. Seismograms from North Digital Recorder	13
5. Seismograms from West Digital Recorder	14
6. Seismogram from 7.5 km North of DICE THROW	15

1.0 INTRODUCTION

The MILL RACE Event was sited in the eastern margin of the Jornada del Muerto Valley, roughly six kilometers south of Trinity site, where the first atomic bomb was detonated in 1945 (Figure 1). Several measurements were made of the strong seismic motions excited by the Trinity Event. Five Leet 3-component strong motion mechanical seismographs recorded the Trinity motions at five different ranges and azimuths (Reference 1). The seismogram from one of these stations (8.2 km north of Trinity) was discussed by Leet in a 1946 paper (Reference 2) and has been the subject of some controversy since Leet gave the name "Hydrodynamic Wave" to one unusual appearing section of the seismogram because the particle motion was prograde and elliptical, resembling that of a water wave (Figure 2). In a 1962 paper (Reference 3), Leet suggested that the "Hydrodynamic Wave" emanated only from explosions and might be useful in discriminating between the seismic waves produced by nuclear explosions and those resulting from naturally occurring earthquakes.

The DICE THROW Event, fired a few kilometers west of Trinity in 1976, was recorded by a fairly extensive array of close-in seismic stations utilizing modern analog and digital instrumentation. Some of the seismograms (Figure 6) recorded from this array closely resembled Leet's 1945 Trinity record (References 4 and 6). Reference 4 attempted to explain Leet's "Hydrodynamic Wave" and the similar appearing waves observed on the DICE THROW Event as higher mode Rayleigh surface waves. The availability of the original Leet instruments for the MILL RACE Event offered a unique opportunity to once again record the "Hydrodynamic Wave" on the original Trinity instrumentation. By placing modern digital instruments alongside the Leet seismographs, it was hoped that the Trinity seismograms could be verified.

2.0 DESIGN OF THE EXPERIMENT

2.1 The Leet Seismographs.

The Leet instruments were designed and constructed primarily for the registration of vibrations from dynamite blasts, traffic, machinery, and general industrial sources. The instruments have roughly a magnification factor of 25 for frequencies above 3 Hz. The seismograph is optical and mechanical in operation in that mirrors are attached to each of the three inertia elements. Light from a single filament galvanometer lamp is reflected from the mirror and onto a moving strip of photographic paper after being reflected several more times in order to lengthen the optical path and, hence, increase the magnification (Figure 3, Reference 5).

A total of five Leet 3-component strong motion seismographs were set out to record the strong motion seismic waves resulting from the Trinity Test. In addition to the one at 8.2 km north, they were also placed in the neighboring towns of San Antonio, Carrizozo and Tularosa and at Elephant Butte Lake (Reference 1). Two of these original instruments were found to be in the archives of the Los Alamos National Laboratory (LANL). LANL archive personnel were kind enough to grant permission to field the Leet instruments on the MILL RACE Event.

The Leet instruments were found to be in fairly good condition after some 36 years in storage, with the exception of some missing parts. Missing from one instrument were several gears from the camera drive train and the camera itself. The other instrument was complete and in operating condition. Using the complete instrument as a model, LANL technicians were able to fabricate the camera and drive train sections missing from the second instrument.

The instruments were then bench tested, whereupon, it was discovered that the film moved past the camera slit at a speed of only about two inches per minute

rather than the average speed of about four inches per second mentioned by Leet in Reference 5 and roughly the apparent film speed of the instrument which produced the record from Trinity (References 1 and 2). Apparently, the two archive instruments were used at the more distant ranges on Trinity where a longer recording time was needed, and resolution of the higher frequencies was not so important. To remedy the problem, the LANL geophysics division procured two higher RPM motors which were installed by AFWL/NTESC technicians, bringing the average film speed to near four inches per second.

Several additional problems were encountered during the fielding of the Leet instruments. The seismographs were designed to operate on 110 volt, 60 cycle A.C. power which was not available at the desired station location. This necessitated the use of two 24-volt D.C. to 110-volt A.C. inverters to provide the required power. Since safety requirements associated with the MILL RACE Drone experiment prohibited the manning of the Leet seismograph station, a way was needed to turn the Leet instruments on shortly before shot time. Initially, it was decided to use timers to apply the 24-volt power supply to the inverters approximately 30 seconds before shot time. This plan was ruled out when it was learned that, because of the drone experiments, shot time would not be known in advance to within two or three minutes.

The lack of advance knowledge of the shot time made it necessary to find a way to turn on the Leet instruments remotely from the observation point. To accomplish this, AFWL/NTESC modified a radio-controlled firing system normally used for firing explosive charges while conducting seismic refraction surveys. The system was modified so that, rather than detonating a charge, 24-volt power was switched on to the inverters, which in-turn supplied 110-volt A.C. power to the Leet instruments.

2.2 Modern Instrumentation Used and Instrument Locations.

Two station locations were selected for the MILL RACE Event (Figure 1). One was approximately 8 km slightly west of north of MILL RACE; the other was approximately 8 km west-northwest of the MILL RACE Test Bed. The northern location was approximately along the same radial from Trinity as was the Leet seismograph station on the Trinity Event. It was of course much nearer Trinity than the original 1945 station, but was at approximately the same range (8 km) from MILL RACE as the original station was from Trinity.

Both Leet seismographs were placed at the north station. Two modern digital event recorders were placed alongside the Leet instruments for comparison purposes. These instruments record digital data directly onto magnetic tape cassettes. They are equipped with event triggers so that recording will occur when the amplifiers see a signal--if the definition of what constitutes a signal is set correctly by the user. A 3-component 2 Hz natural frequency seismometer was connected to one digital recorder. Three 1 Hz vertical seismometers supplied the input for the other three channel digital recorder. These three vertical seismometers were set out in a linear array with 100-meter spacing--that is, the three seismometers were set out on a single radial in increasing distance away from the MILL RACE GZ. The purpose of this array was to obtain closely spaced waveforms so that a phase velocity dispersion curve could be obtained for the "Hydrodynamic Wave" and other portions of the surface wave train.

3.0 RESULTS

Out of 15 total channels (if film records of light traces can be properly referred to as channels), only six recorded successfully. The remote control system did successfully turn on the Leet instruments; however, neither instrument produced a seismogram of the event. The film in one Leet camera slipped off the

take-up reel. The film in the other Leet instrument did run; however, no traces were visible after the film was developed. Each camera is equipped with a slit and spring loaded cover for the slit which does not open until the instrument trap door is closed and locked (Figure 3). Locking the trap door also engages the clutch for the camera drive. The camera door was one of the last things checked the morning of the shot. This was checked by pulling up on the door handle to ensure that the door was indeed locked. In this instrument, there was evidently some play or misalignment in the system which allowed the door over the camera slit to close just enough to block the light beams. This situation had not occurred in pre-event tests of the instrument, evidently, because the trap door was not pulled up to check for the camera drive engagement.

Only two of the three digital recorders operated successfully. Seismograms from these (the west and north 3-component stations) are shown in Figures 4 and 5. The recorder connected to the three vertical seismometers did not trigger and begin recording until arrival of the airblast. The average value of all three channels is used to activate the record trigger. In this case, the three vertical seismometers were placed at increasing distances from the blast so that the separation between the seismometers was, in general, on the order of one-quarter to one-half the wavelength of the incoming ground motions, resulting in destructive interference and explaining why the recorder did not trigger.

Examination of the two 3-component records obtained from the north and west stations reveals that amplitudes are somewhat lower than those observed at similar ranges on the DICE THROW Event. In addition, the amplitudes observed at the west MILL RACE Station were roughly a factor of two higher than those at the north station. Neither of the records bears a strong resemblance to the Trinity or DICE THROW records (Figures 2 and 6). This suggests that the geologic structure

underlying the travel path between the MILL RACE GZ and the north station, especially, is shallower (the alluvial thickness is less) and perhaps less uniform than the Trinity or DICE THROW GZ to recording station travel paths.

4.0 CONCLUSIONS

This experiment was only a limited success. Due to freakish equipment failures, the two Leet instruments originally used on the Trinity Event did not produce seismograms of the MILL RACE Event. Two out of three of the modern instruments did record successfully. The digital record at the north station, however, bears little similarity to the Leet seismogram of the Trinity Event or to seismograms of the DICE THROW Event which are similar to the Trinity Seismogram. This suggests that the geologic structure associated with the path from MILL RACE to the north station is somewhat different from that along the path from Trinity to the Leet seismograph station. If future large high-explosive shots are to be fired in the Trinity-MILL RACE area, the Leet instruments should again be fielded; however, the station location should be, probably, placed on an azimuth 10 or 20 degrees west of the MILL RACE radial in order to move into a more favorable geologic structure for reproducing the "Hydrodynamic Wave."

REFERENCES

1. Leet, L. Don, July 16th Nuclear Explosion: Ground Vibrations, Los Alamos Laboratory Report LA-438, 15 November, 1945.
2. Leet, L. Don, Earth Motion From the Atomic Bomb Blast, American Scientist, Vol 34, No. 2, April 1946.
3. Leet, L. Don, The Detection of Underground Explosions, Scientific American, Vol 206, No. 6, June 1962.
4. Reinke, R.E. and Eugene Herrin, Surface Wave Propagation in the Tularosa and Jornada del Muerto Basins, South Central New Mexico, Final Technical Report to the Air Force Office of Scientific Research, Contract Number: AFOSR-76-2890, Southern Methodist University, December 1977.
5. Leet, L. Don, A Three-Component Portable Seismograph for the Measurement of Vibrations, Transactions, American Geophysical Union, Vol 26, Part 1, August 1945.
6. Turpening, R.M. and A.R. Liskow, Seismic Measurements for the Pre-DICE THROW II-I (TNT Shot), Pre-DICE THROW II-2 (ANFO Shot) and DICE THROW Events, Final Technical Report, Air Force Office of Scientific Research Contract, No. F44620-76-C-0077, December 1978.

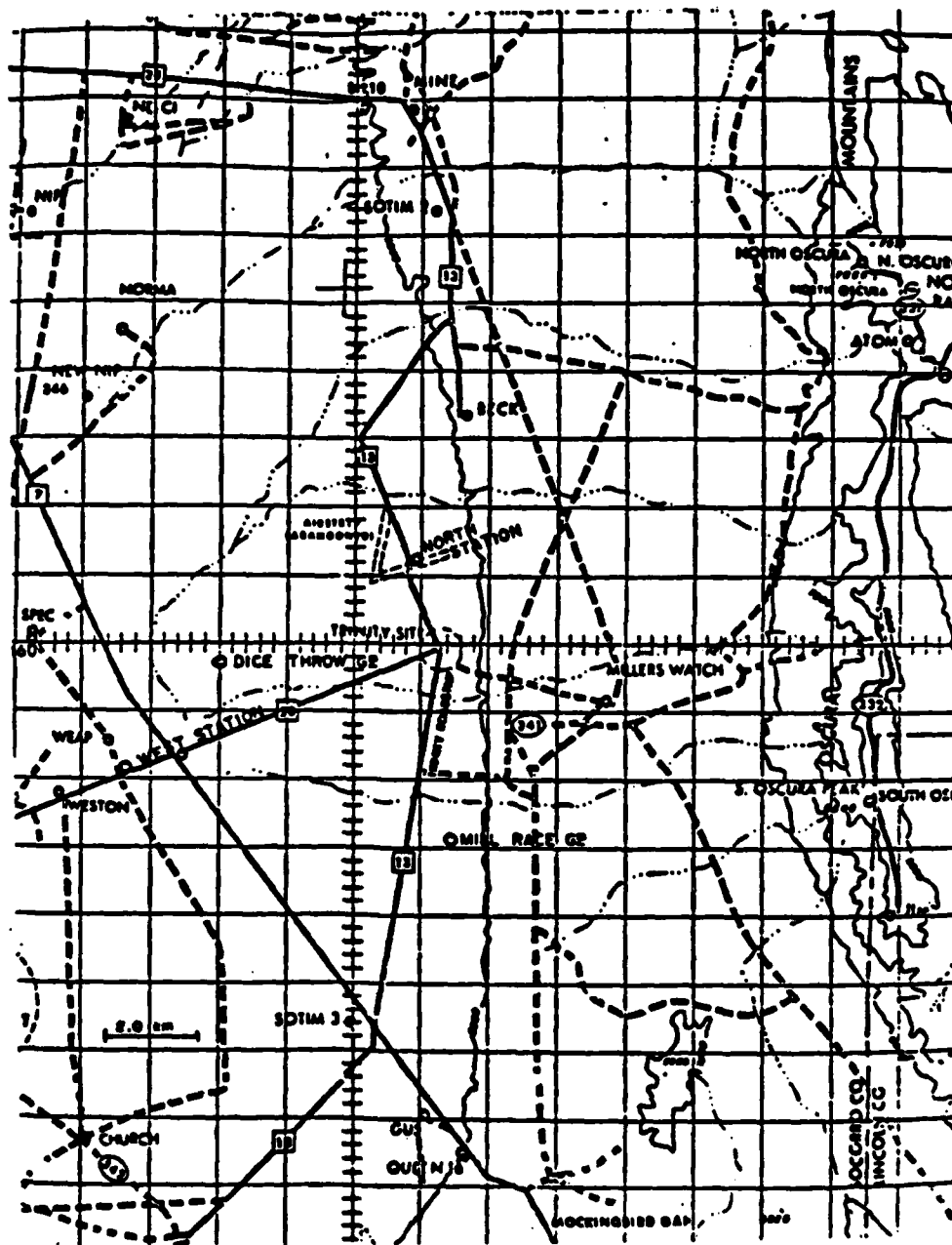
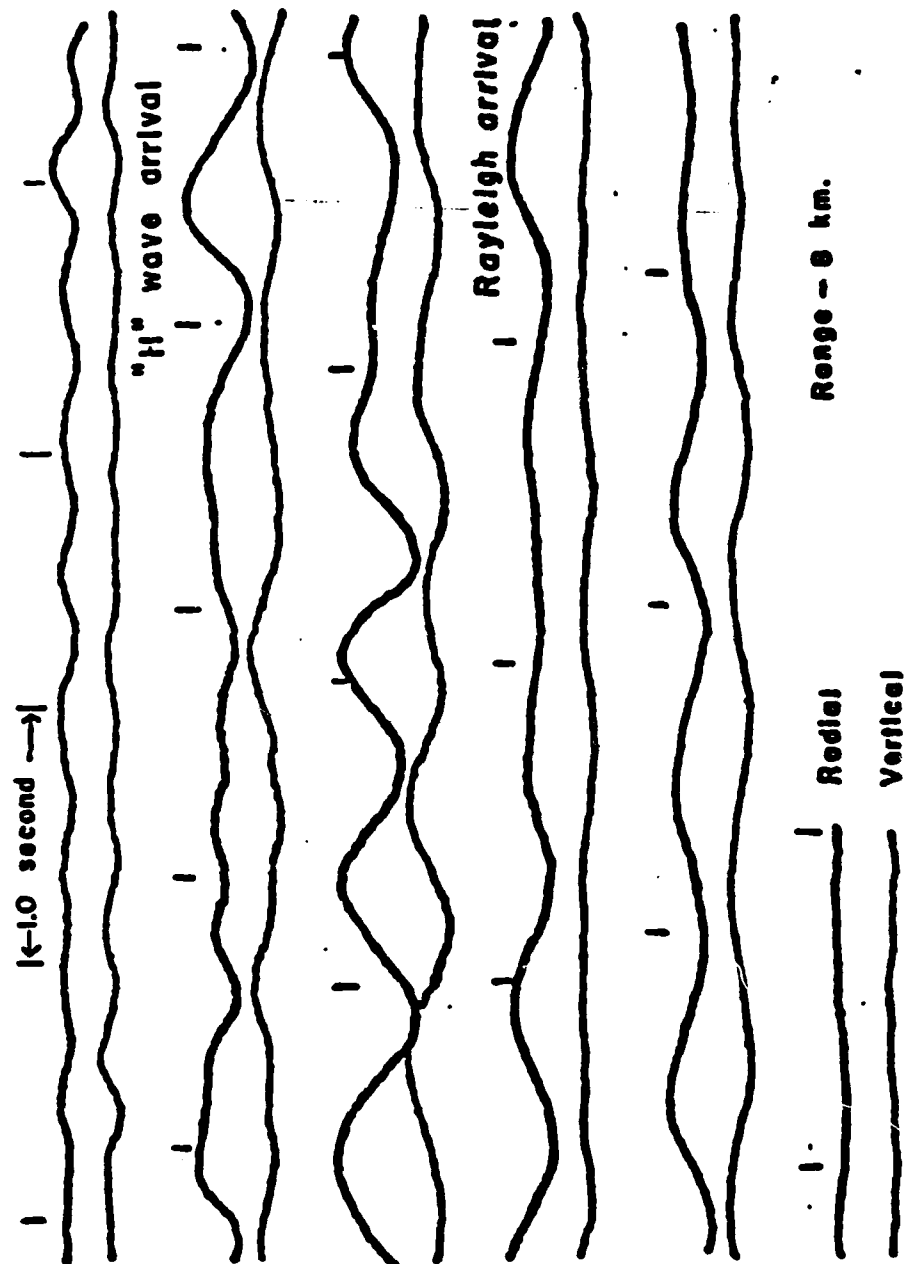
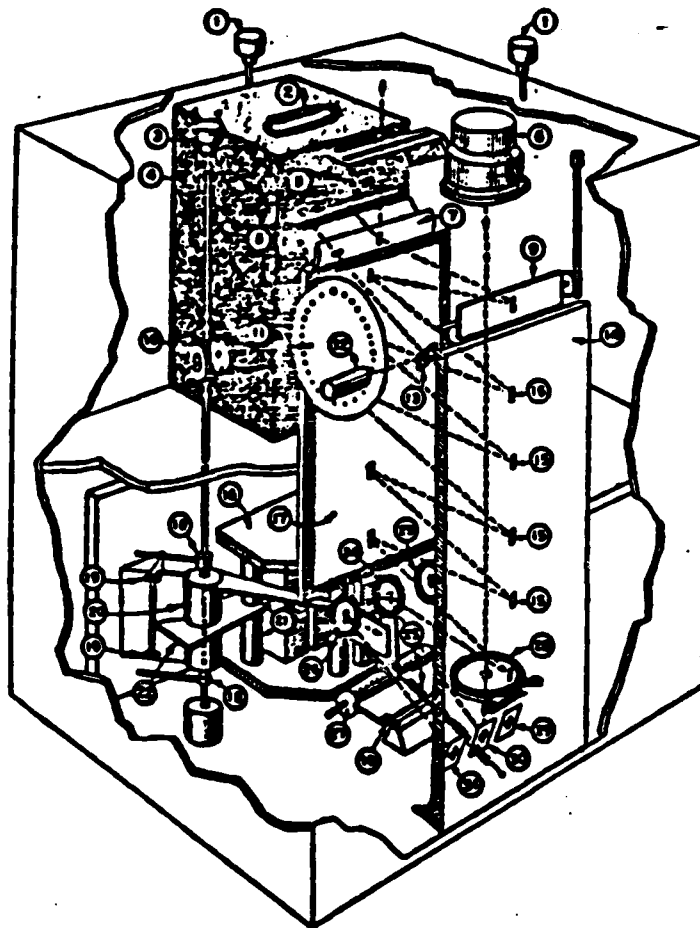


Figure 1. Seismic Station Map for MILL RACE



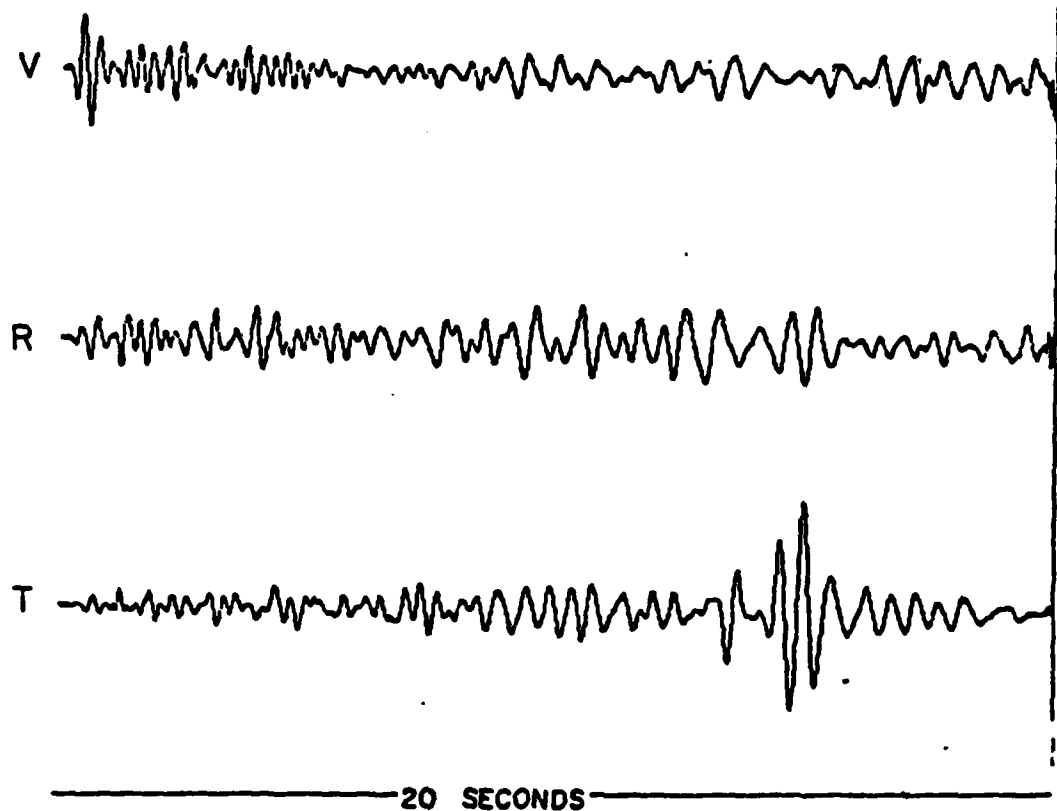
RECORD OF EARTH MOTION, TRINITY TEST, JULY 16, 1945
(from Leet, 1946)

Figure 2. Leet's Trinity Seismogram



Leet three-component portable seismograph. (1) Knobs controlling leveling feet; (2) camera handle; (3) knob for locking inertia member; (4) camera; (5) viewing slit; (6) light-source housing; (7) cylindrical lens; (8) half-silvered mirror; (9) adjustable mirror; (10) camera-drive clutch; (11) timing-line shutter; (12) timing-line light housing; (13) timing-line mirror; (14) and (17) plane mirrors; (15) point of reflection; (16) permanent magnet; (18) locking nut; (19) spring; (20) and (27) inertia members; (21) magnet poles; (22) damping vane; (23), (24) and (26) inertia member mirrors; (25) stabilizing spring; (28) condensing lens; (29), (30), and (31) fixed mirrors.

Figure 3. Drawing of Leet Seismograph



MILL RACE LEET STATION (NORTH)
RANGE 8.0km

Figure 4. Seismograms from North Digital Recorder

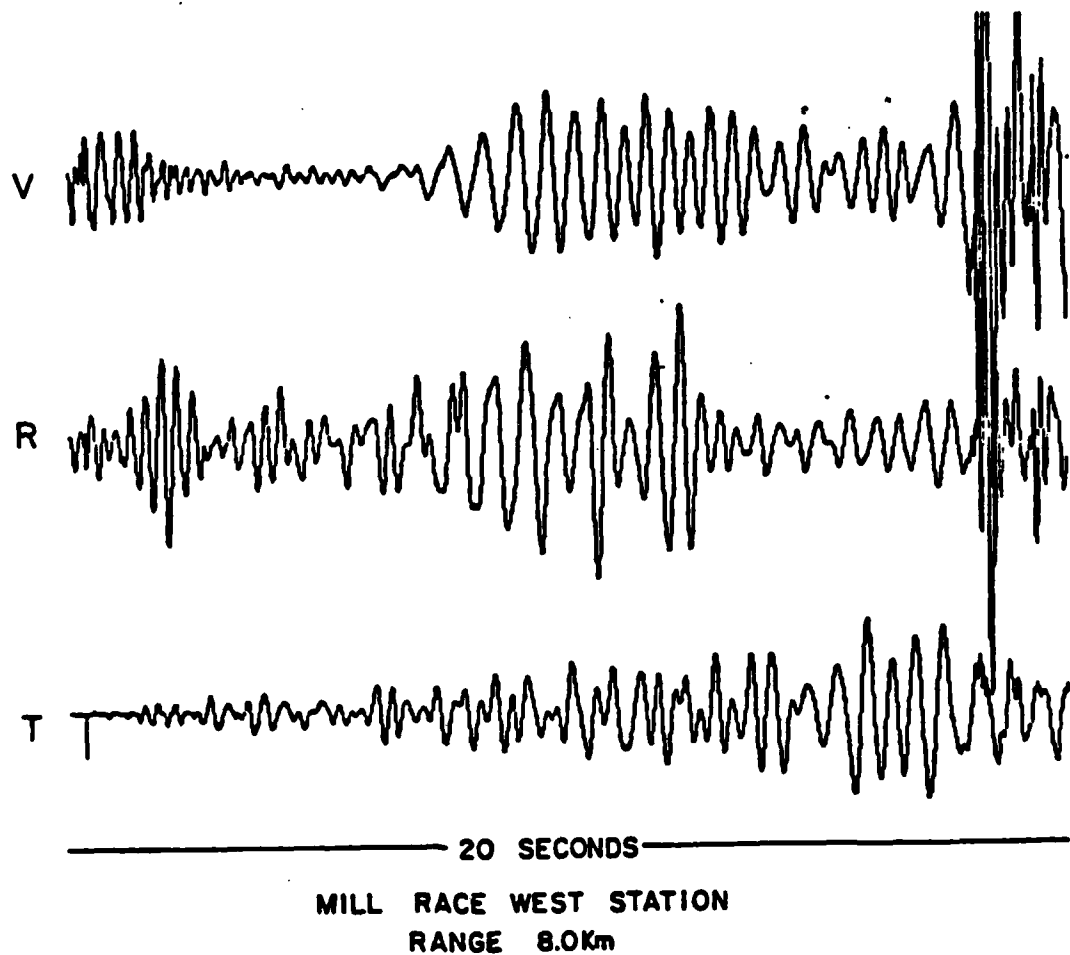
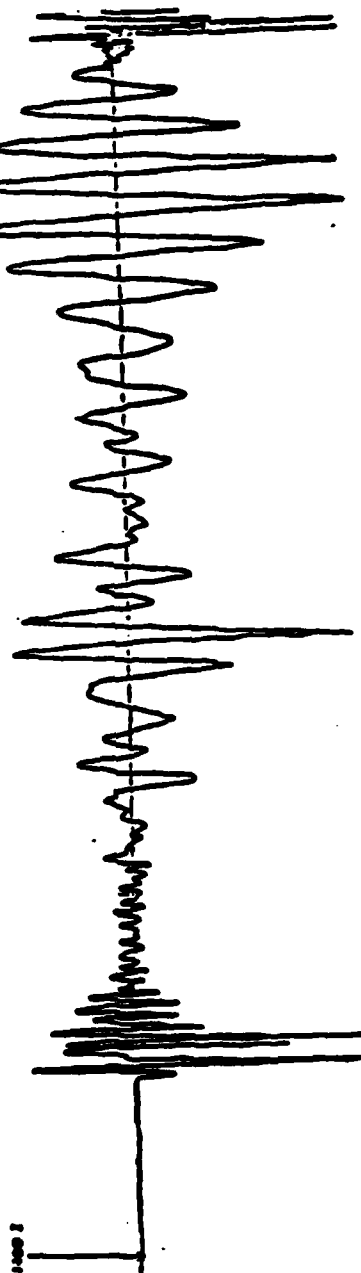


Figure 5. Seismograms from West Digital Recorder

DICE THROW 500 TON
SMU VERTICAL 7.5 km.

2 SEC



Vertical component. SMU station.
Dice Throw, October 6, 1976.

Figure 6. Seismogram from 7.5 km North of DICE THROW

FILM
10-8